

**A Contribution to Sustainable Forest Management in
Patagonia**

**Object-oriented Classification and Forest Parameter Extraction
based on ASTER and Landsat ETM+ Data**

Dissertation

zur
Erlangung der naturwissenschaftlichen Doktorwürde
(Dr. sc. nat.)

vorgelegt der
Mathematisch-naturwissenschaftlichen Fakultät
der
Universität Zürich

von
Sandra Eckert
von
Leuggern AG

Begutachtet von
Prof. Dr. Klaus I. Itten
Dr. Thomas Schneider

Zürich, 2006

Die vorliegende Arbeit wurde von der Mathematisch-naturwissenschaftlichen Fakultät der Universität Zürich auf Antrag von Prof. Dr. Klaus I. Itten und Prof. Dr. Robert Weibel als Dissertation angenommen.

Erklärung

Hiermit erkläre ich, Sandra Eckert, dass bei der Abfassung der Dissertation unter dem Titel „A Contribution to Sustainable Forest Management in Patagonia - Object-oriented Classification and Forest Parameter Extraction based on ASTER and Landsat ETM+ Data“ keine anderen Hilfsmittel als die darin angegebenen benützt worden sind.

Zürich, den 1. Februar 2006

S. Eckert

Publikationsmodus

Gewünschter Publikationsmodus ist c):

Publikation als Verlagsausgabe.

Verlag ist das Geographische Institut der Universität Zürich, im Rahmen der Remote Sensing Series (Editorial Board: Prof. Dr. K. I. Itten, Prof. Dr. D. Nüesch, Dr. T. W. Kellenberger, Dr. E. Meier, and Dr. M. Kneubühler)

Summary

This thesis deals with the current situation of unsustainable forest management of the Subandean native forests in Patagonia, Argentina. The research area is situated in the west of the Province of Chubut on the trailing edge of the Andes. The goal is to provide the CIEFAP, the Patagonian forest research centre and the DGBYP, the Department of Forests and Parks of the Patagonian Province of Chubut with an improved bio-geographical information database of the area in order to support them in establishing an optimized, sustainable forest management, accounting for limited fundings, guaranteed reproducibility and continuation of the established database.

First, a digital elevation model (DEM) is generated from near-infrared ASTER satellite data. The establishment of a stable stereo model with accurate, differentially corrected GCPs is discussed and a semi-empirical post-processing method is presented, which successfully eliminates erroneous peaks and sinks. An accuracy assessment follows where the established DEM is compared to SRTM data and to several differentially corrected independent check points.

Comparing the ASTER DEM and the SRTM DEM results in a RMSE of 39.48 m. The differential image shows that errors at mountainous regions are between ± 100 m. In the foothills of the Andes and the steppe area, the DEMs correspond reasonably well with each other, the variations are between ± 30 m.

The comparison of the ASTER DEM with ten independent check points, all of them located in the foothills of the Andes, results in a RMSE of 13.29 m.

Secondly, the preprocessing and mosaicking of ASTER and Landsat ETM+ datasets are discussed. They both contain systematic errors, which have to be corrected. The ASTER datasets contain a systematic banding while the Landsat ETM+ datasets contain lines with zero values and a high/low gain switch. Except for the gain switch all artefacts are successfully corrected. The applied methods and visual results are presented in this work. Geometric correction is done with a rigorous model [177]. The goal is to achieve a maximum RMSE below 15 m in X- and Y-direction to obtain conformity within all satellite data. With the availability of GCPs this is possible for all areas except for the mountainous western regions of the study area, where a maximum RMSE of about 30 m is achieved. For radiometric correction the ATCOR3 procedure is used [155]. Influences of topography, atmospheric absorption and scattering as well as radiance reflected from adjacent terrain is corrected. Moreover, an empirical BRDF correction is presented to account for the partial overcorrection in the mountainous areas in the datasets.

Thirdly, an object-oriented classification method is applied to account for the vegetation cover characteristics and relationships in the research area. The theoretical aspects are discussed in detail, followed by some segmentation pre-tests focussing on the appropriate choice of scale parameter, criterion and bands as well as the reproducibility of the segmentation. The developed class hierarchy and rule base is presented, where some of the tree types, such as Ñire and Caña Colihue, are successfully classified. Moreover, attempts were made to classify the vegetation types growing in two transition zones bordering pure natural forests. The accuracy assessment is performed by using the weighted kappa to account for the error severity of some classes. With this method, an overall accuracy of 82.04% and a weighted kappa coefficient of 0.82 was achieved. Some fundamental thoughts about the evaluation of fuzzy classification results conclude the chapter.

In the section on forest parameter estimation, first a theoretical overview of different forest parameter determination methods is given. A detailed comparison of the measured and modelled parameters LAI, tree density, DBH, basal area, volume and biomass and their relationships with spectral measurements follows. The findings of forest parameter determination shows that LAI can be estimated with ASTER data at a relative RMSE around 12% compared to the measured LAI values. The best determination results were achieved for the forest parameters DBH and basal area with relative RMSE around 26% and 30% respectively. Tree density, volume and biomass were estimated with lower accuracies. Relative RMSE of 40%, 45% and 57% were achieved.

Additionally, a selection of descriptive parameters and their impact on spectral reflectances were analyzed and the effects of different forest management systems on Lenga forests have been identified. It is shown that total volume and therefore timber production vary according to site quality, stocking, growth phase and previous land management. At last forest parameter maps are presented, which were produced by applying the best performing models to the areas classified as Lenga forest. All established datasets and products were implemented in the GIS of CIEFAP and DGBYP.

This work has shown that a bio-geographical database can be established at low cost considering geometric resolution, accuracy and simplicity. The accuracies of the generated products are sufficient to provide valuable informations on the forest situation in the research area, which allows for sustainable forest management. The detailed analysis of the unique Lenga forest parameter measurements allowed for further findings in the field of sustainable forestry and remotely sensed reflectance research.

Zusammenfassung

Diese Arbeit befasst sich mit der derzeitigen Situation der nicht nachhaltigen Bewirtschaftung der subandinen Wälder Patagoniens. Das Untersuchungsgebiet liegt im Westen der argentinischen Provinz Chubut an den ostabfallenden Hängen der Anden. Das Ziel der Arbeit ist es, für das CIEFAP, einem Patagonischen Wald-Forschungszentrum, und das DGBYP, das Departement für Wald und Nationalparks der Provinz Chubut eine verbesserte bio-geographische Informationsdatenbank der Naturwaldflächen der Provinz zu erstellen, um die beiden Institutionen bei der Planung und Überwachung einer optimierten, nachhaltigen Waldbewirtschaftung zu unterstützen. Die Durchführung dieses angewandten Forschungsprojekts unterliegt dabei diversen Rahmenbedingungen, wie den limitierten finanziellen Mitteln, der Notwendigkeit der Reproduzierbarkeit der entwickelten und angewandten Methoden sowie der Gewährleistung der selbstständigen laufenden Fortführung und Aktualisierung der erstellten GIS-Datenbank durch die Verantwortlichen des CIEFAP und des DGBYP.

Als erstes wurde aus den beiden nahinfraroten Stereo-Bändern der ASTER Satellitendaten ein digitales Höhenmodell (DEM) berechnet, wobei die Auswirkungen der Verteilung und Menge der differentiell korrigierten Passpunkte zur Erstellung eines stabilen Stereo-Modells sowie deren Auswirkungen auf die Genauigkeit dargelegt werden. Zudem wird eine semi-empirische Nachbearbeitungsmethode vorgestellt, die erfolgreich fehlerhafte Artefakte aus dem Höhenmodell filtert und mit Umgebungswerten realistisch interpoliert. In der darauffolgenden Genauigkeitsanalyse wird das generierte Höhenmodell mit SRTM Daten und mit differentiell korrigierten unabhängigen Checkpunkten verglichen.

Im Vergleich zwischen dem erstellten ASTER DEM und dem SRTM DEM resultiert ein RMSE von 39.48 m. Das Differenzbild zeigt, dass die Fehler im gebirgigen, steilen Gelände im Bereich von ± 100 m liegen. Im Gebiet der Andenausläufer sowie in den flachen Steppenregionen stimmen die beiden Oberflächenmodelle gut überein, die Unterschiede liegen im Bereich von ± 30 m.

Der Vergleich des ASTER DEM mit den zehn unabhängigen differentiell korrigierten Checkpunkten im vorandinen Gebiet ergab einen RMSE von 13.29 m.

Im zweiten Kapitel wird auf die Vorverarbeitung und die Mosaikierung der ASTER und Landsat ETM+ Daten eingegangen. Sie weisen beide systematische Fehler auf, welche vorgängig korrigiert werden müssen. Die ASTER Szenen enthalten ein systematisches Banding, während die Landsat ETM+ Daten einen Zeilenausfall sowie einen *High/Low-Gain-Switch* aufweisen. Abgesehen vom *Gain-Switch* können alle Artefakte erfolgreich korrigiert werden. Alle angewendeten Lösungsansätze inklusive deren Resultate werden in dieser Arbeit vorgestellt und illustriert. Die durchgeführte geometrische Korrektur der Daten basiert auf einer Mischung eines strengen, parametrischen und eines nicht-parametrischen Ansatzes [177]. Die Genauigkeit dieser geometrischen Korrektur soll dabei für alle Passpunkte einen maximalen Fehler von 15 m in X- und Y-Richtung nicht überschreiten, damit die Übereinstimmung der ASTER mit den Landsat ETM+ Daten gewährleistet ist. In Gebieten wo genügend Passpunkte vorhanden sind, kann dies problemlos erreicht werden, hingegen in den gebirgigen Regionen im Westen des Untersuchungsgebiets liegt der maximale Fehler teilweise bei ca. 30 m. Die radiometrische Korrektur, welche topographische, atmosphärische sowie umgebungsbedingte Effekte korrigieren soll, wird mit Hilfe von ATCOR3 [155] durchgeführt. Zusätzlich wird eine empirische BRDF-Korrektur vorgestellt, welche der partiellen Überkorrektur im Gebirge Rechnung tragen soll.

Anschliessend wird eine neuartige, objekt-orientierte Klassifikationsmethode angewendet, um

den vegetationspezifischen Charakteristiken und Zusammenhängen im Untersuchungsgebiet Rechnung zu tragen. Dabei wird als erstes in die theoretischen Grundlagen und Aspekte der objekt-orientierten Klassifikation mit eCognition eingeführt. Es folgen mehrere Voranalysen, die sich mit der Segmentierung und der optimalen Wahl der Skalierungsparameter, den Segmentierungskriterien, der Kanalwahl und -gewichtung, sowie mit der Reproduzierbarkeit der Segmentierung auseinandersetzen. Anschliessend wird das entwickelte Klassifikationsregelwerk und die Klassenhierarchie, mit welchen erfolgreich einige bisher schwierig zu klassifizierende Baumarten, wie Ñire und Caña Colihue unterschieden werden können, präsentiert. Bei der Klassifikation wurde zusätzlich versucht die Vegetationsgesellschaften in den Übergangszonen zu den reinen Naturwaldbeständen zu definieren und zu klassieren. In der Genauigkeitsanalyse wird das Genauigkeitsmass *weighted kappa* eingeführt, um der Fehlergewichtung je nach Klasse Rechnung zu tragen. Mit dem angewandten objekt-orientierten Klassifikationsansatz wird eine Gesamtgenauigkeit von 82.04% und ein *weighted kappa* -Koeffizienten von 0.82 erreicht. Eine Diskussion der Evaluation von auf *fuzzy-logic*-Methoden beruhenden Klassifikationsresultaten schliesst das Kapitel ab.

Im Kapitel, welches sich mit der Bestimmung von Forstparametern befasst, wird als erstes eine Übersicht über diverse Berechnungsmethoden der Parameter gegeben. Ein detaillierter Vergleich der gemessenen und hergeleiteten Parameter LAI, Bestandesdichte, Brusthöhendurchmesser (BHD), basale Fläche, Volumen und Biomasse sowie deren Beziehung zu spektralen Messungen folgt. Die Erkenntnisse der Forstparameter-Extraktion zeigt, dass der Parameter LAI mit Hilfe von ASTER Daten mit einer Genauigkeit von 12% relativem RMSE, im Vergleich zu den gemessenen LAI-Werten, bestimmt werden kann. Die besten Forstparameter-Modellierungen können für die Parameter BHD und basale Fläche erzielt werden, mit je einem relativen RMSE von ca. 26% und 30%. Die Parameter Bestandesdichte, das Volumen und die Biomasse werden mit etwas schlechteren Genauigkeiten von 40%, 45% und 57% modelliert.

Zusätzlich wird eine Auswahl von beschreibenden respektive qualitativen forstlichen Parametern analysiert. Die Auswirkungen der unterschiedlichen Waldbewirtschaftungssysteme auf die Qualität der Lengawälder werden anhand dieser Parameter festgestellt. Es zeigt sich dabei, dass das Volumen und somit die Holzproduktion je nach Qualität, Bestockung, Wachstumsphase und Bewirtschaftungsverfahren an einem Standort stark variieren kann.

Schliesslich werden anhand der besten Forstparameter-Modelle Waldparameter-Karten für die klassierten Lengawaldflächen erstellt und präsentiert. Alle hergeleiteten Produkte und Datensätze sind Bestandteile des vom CIEFAP und DGBYP aufgebauten GIS der bewaldeten Flächen der Provinz Chubut.

Diese Arbeit zeigt, dass eine bio-geographische Datenbasis unter Berücksichtigung der notwendigen geometrischen Auflösung und Genauigkeit, der Einfachheit und Übertragbarkeit der Methoden auch mit limitierten finanziellen Mitteln hergestellt werden kann. Die Genauigkeiten der erzeugten Kartenprodukte sind genügend gut, um wertvolle Informationen über die derzeitige forstliche Situation im Untersuchungsgebiet zu liefern. Sie soll zukünftig die Basis einer nachhaltigen Planung der Waldbewirtschaftung sein. Die detaillierte Analyse der erstmals für Lengawälder erhobenen forstlichen Messungen liefern neue Erkenntnisse in den Forschungsbereichen der angewandten Fernerkundung und der nachhaltigen Waldbewirtschaftung patagonischer Naturwälder.

Resumen

Esta tesis trata la situación actual del manejo no sustentable del bosque nativo en la Patagonia, Argentina. El área de estudio está situada en el Oeste de la Provincia de Chubut, en la precordillera andina. El objetivo es proveer al CIEFAP, Centro de Investigación y Extensión Forestal Andino Patagónico y la DGBYP, Dirección General de Bosques y Parques de la Provincia de Chubut, una mejor base de datos con información bio-geográfica del área, con el fin de sustentar el establecimiento de un sistema optimizado de manejo sustentable, teniendo en cuenta la limitación de recursos económicos como así también la reproducción garantizada y la continuación del establecimiento de la base de datos.

En primer lugar se generó un modelo digital de elevación (MDE) a partir de estereo-imágenes satelitales ASTER infrarrojo cercano. En la discusión se aborda la generación de un modelo estéreo estable a partir de puntos control del terreno (GCPs) precisos diferencialmente corregidos y se presenta un método de post-procesamiento semi-empírico, que elimina satisfactoriamente las elevaciones y depresiones erróneas. Posteriormente se realizó un análisis de la precisión, donde el MDE generado se compara con los datos SRTM a través de varios puntos de chequeo independientes tomados con corrección diferencial.

De la comparación del modelo digital de elevación ASTER con el MDE SRTM se obtuvo un Error Medio Cuadrático (EMC) de 39,48 m. La imagen diferencial muestra que los errores en zonas montañosas se encuentran entre ± 100 m. En la zona de transición y la estepa, existe una buena correspondencia entre los MDE encontrándose errores entre ± 30 m. De la comparación del MDE ASTER con 10 puntos de chequeo independientes situados en la zona de transición entre los Andes y la estepa, se obtuvo un EMC de 13,29 m.

En segundo lugar se discute el procesamiento y generación de mosaicos del conjunto de datos ASTER y Landsat ETM+. Ambos tipos de datos contienen errores sistemáticos, los que han sido corregidos. Los datos ASTER contienen 'banding' sistemático, mientras que los datos Landsat ETM+ contienen líneas con valores nulos e intermitencia de ganancias alta y baja. Exceptuando la intermitencia en ganancias, todos los errores fueron corregidos satisfactoriamente. Los métodos utilizados y los resultados visuales son presentados en este trabajo. La corrección geométrica fue realizada con un modelo riguroso, paramétrico [177]. El objetivo es lograr un EMC máximo inferior a 15 m en dirección de X y Y, y así lograr la correspondencia entre todos los datos satelitales. Por la disponibilidad de GCPs esta precisión fue posible lograrla para toda el área, excepto para las regiones montañosas al Oeste del área de estudio donde se obtuvo un EMC de alrededor de 30 m.

Para la corrección radiométrica se utiliza el procedimiento ATCOR3 [155]. La influencia de la topografía, absorción atmosférica y refracción, así como también la radiación reflejada por el terreno adyacente, es corregida. Además, se presenta un modelo de corrección empírico BRDF que contrarresta la sobrecorrección parcial de los datos en las áreas montañosas.

En tercer lugar se emplea un método de clasificación orientado a los objetos para tener en cuenta las características y relaciones de la vegetación en el campo de investigación. Los aspectos teóricos son discutidos en detalle, seguido de algunas segmentaciones preliminares, focalizando en la correcta elección de los parámetros de escala, criterio y bandas, como así también en la reproducción de la segmentación. Se presenta la jerarquía de clases desarrollada y la base de reglas, donde algunos de los tipos de vegetación, tales como Ñire y Caña Colihue, son clasificados satisfactoriamente. Además se intentó clasificar tipos de vegetación en zonas de transición contiguas a los bosques naturales puros. La estimación de la precisión se efectuó usando el

coeficiente kappa ponderado para considerar la severidad del error de algunas clases. Con este método, se logró una precisión general de de 82,04% y un coeficiente kappa ponderado de 0,82. Se presentan al final del capítulo algunas consideraciones fundamentales sobre la evaluación de los resultados de la clasificación 'fuzzy'.

En la sección sobre la estimación de parámetros del bosque, primero se presenta una revisión sobre los diferentes métodos para la estimación de los mismos. A esto le sigue una comparación entre los parámetros medidos y modelados del Índice de Área Foliar (LAI), densidad, DAP, área basal, volumen, biomasa y sus relaciones con valores espectrales. Los resultados de la determinación de parámetros forestales muestran que el LAI puede ser estimado con datos ASTER con un EMC de 12% aproximadamente comparado con los valores registrados del LAI. Los mejores resultados se lograron para la determinación del DAP y área basal con un EMC relativo de alrededor del 26% y 30% respectivamente. La densidad, volumen y biomasa se estimaron con precisiones menores. Se lograron EMC relativos de 40%, 45% y 57% respectivamente.

Además se analizó una selección de parámetros descriptivos y su impacto sobre la reflectancia espectral y se identificaron los efectos de diferentes tipos de manejo en bosques de Lenga. Se ha demostrado que el volumen total y por consiguiente la producción de madera varía de acuerdo a la calidad de sitio, densidad, fase crecimiento y manejo previo. Por último se presentan mapas de parámetros forestales, los cuales fueron producidos aplicando los mejores modelos a las áreas clasificadas como bosque de Lenga. Todo el conjunto de datos y productos se implementaron en el SIG del CIEFAP y la DGBYP.

Este trabajo ha demostrado que una base de datos bio-geográfica puede ser establecida a bajo costo respecto a resolución geométrica, precisión y simplicidad. La precisión de los productos generados es suficiente para proveer información valiosa sobre la situación forestal en el área de estudio, que permitan un manejo sustentable del bosque. El análisis detallado de mediciones de parámetros forestales para el caso de Lenga, permitió encontrar resultados adicionales en el campo del manejo sustentable de bosques y en la investigación de la percepción remota.

Table of Contents

Summary	I
Zusammenfassung	III
Resumen	V
Table of Contents	VII
List of Figures	XI
List of Tables	XV
1. Introduction	1
1.1 Problem Description	1
1.2 Structure of this Thesis	2
2. Forestry in Patagonia	5
2.1 The Forests in the Province of Chubut, Patagonia	5
2.1.1 Lenga (<i>Nothofagus pumilio</i>)	6
2.1.2 Coihue (<i>Nothofagus dombeyi</i>)	8
2.1.3 Ñire (<i>Nothofagus antarctica</i>)	9
2.1.4 Ciprés de la Cordillera (<i>Austrocedrus chilensis</i>)	10
2.1.5 Caña Colihue (<i>Chusquea culeou</i>)	11
2.2 History and Silvicultural Development in Patagonia	12
2.3 Silvicultural Situation in the Province of Chubut	12
2.3.1 Deficits and Problems	13
2.4 Forest Inventories in Patagonia	14
2.5 Remote Sensing in Patagonian Forestry	15
3. Study Area	17
3.1 Introduction	17
3.2 Location & Topography	17
3.3 Climate	18
3.4 Soils	18
3.5 Regional Vegetation Patterns	19
4. Data Base	21
4.1 Introduction	21
4.2 Remote Sensing Data	21
4.2.1 ASTER	21
4.2.2 Landsat ETM+	22
4.2.3 Datasets	22
4.3 Land Cover Data	25
4.4 GCP Database	25
4.5 LAI-Measurements	26
4.5.1 Theory	26
4.5.2 Hemispherical Camera	28
4.5.3 Measurement Plan	30
4.6 Forest Parameter Measurements	30

4.7	Plot Measurement Evaluation	32
5.	Preprocessing & Digital Elevation Model Generation	33
5.1	Introduction	33
5.2	Quality Analysis	34
5.2.1	ASTER System Correction	34
5.2.2	ASTER Post-System Correction	35
5.2.2.1	Damaged Line Correction	35
5.2.2.2	Systematic Vertical Banding	35
5.2.3	Landsat ETM+ Post-System Correction	36
5.3	Digital Elevation Model Generation	37
5.3.1	Image Data & Stereo Capability	38
5.3.2	Ground Control Points Collection	38
5.3.3	Extracting Elevation Parallax	39
5.3.4	Quality Control	39
5.3.4.1	Semi-empirical postprocessing method	40
5.4	Results	40
5.4.1	ASTER DEM mosaic	40
5.4.2	Postprocessing	42
5.4.3	Accuracy Assessment and Validation	43
5.5	Geometric Correction	46
5.6	Mosaicking	47
5.7	Radiometric Correction	49
5.7.1	ATCOR 3	50
5.7.1.1	Input Parameter Determination	51
5.7.2	Empirical BRDF Correction	52
5.7.3	Results	53
5.8	Discussion	57
6.	Object-oriented Classification	59
6.1	Introduction	59
6.2	The eCognition Approach	61
6.2.1	Knowledge-based image interpretation	61
6.2.1.1	Scale	61
6.2.1.2	Image Semantics & Hierarchical Dependencies	61
6.2.2	Segmentation	61
6.2.2.1	Definition of Heterogeneity	62
6.2.3	Hierarchical Object Network	63
6.2.4	Classification in eCognition	64
6.2.4.1	Fuzzy Classification	64
6.2.4.2	Nearest Neighbor Classifier vs. Membership Function	66
6.3	Classification Project Design	67
6.3.1	Classification Image Database	67
6.3.2	Training Area	67
6.3.3	Segmentation Evaluation	68
6.3.3.1	Band Weighting, Scale Parameter and Criterion Test	68
6.3.3.2	Segmentation Reproducibility Test - Border Problem	70
6.4	Results	71
6.4.1	Classification Rule Base	71
6.4.1.1	Feature Selection	71

6.4.1.2 Class Hierarchy	72
6.4.2 Accuracy Assessment	75
6.4.3 Vegetation Cover Map	82
6.5 Discussion	82
7. Forest Parameter Estimation.....	85
7.1 Introduction	85
7.2 Introduction to Forest Parameter Retrieval	85
7.3 Methodology of Forest Parameter Retrieval	87
7.4 Results	89
7.4.1 Analysis of LAI Measurements	89
7.4.2 Determination of LAI	90
7.4.3 Conclusions on LAI Determination	95
7.4.4 Determination of Forest Parameters	95
7.4.4.1 Tree Density	98
7.4.4.2 DBH	100
7.4.4.3 Basal Area	101
7.4.4.4 Volume	103
7.4.4.5 Biomass	104
7.4.5 Conclusions on Forest Parameter Determination	105
7.4.6 Descriptive Forest Parameter Analysis	107
7.4.6.1 Forest Cultivation	107
7.4.6.2 Regeneration and Vitality	110
7.4.6.3 Coverage	113
7.4.6.4 Dominant Height	115
7.4.6.5 Stand Structure	115
7.4.6.6 Conclusions on Descriptive Forest Parameter Analysis	117
7.5 Application to the Remote Sensing Data	117
7.5.1 Forest Parameter Maps	117
7.6 Discussion	120
8. Conclusion, Final Discussion and Outlook	123
8.1 Conclusions and Final Discussion	123
8.1.1 Digital Elevation Model Generation	123
8.1.2 Preprocessing of the ASTER and Landsat ETM+ Data	124
8.1.3 Object-Oriented Vegetation Classification	125
8.1.4 Parameter Estimation by Regression Analysis	127
8.1.5 LAI Measurement and Determination	127
8.1.6 Forest Parameter Determination	128
8.1.7 Costs and Time Account	129
8.2 Outlook	131
References	133
Appendix	147
Acknowledgements	153

List of Figures

Figure 2.1	Vegetation profile of the Patagonian forest towards the Andean-Patagonian steppe ([77] modified).	5
Figure 2.2	Photographs of the different ecosystems and ecotones. Top left: deciduous temperate forest consisting of Lenga (in the background) and Ñire (in the foreground of the image); top right: evergreen and deciduous temperate mixed forest; bottom left: Andean-Patagonian steppe with mallin; bottom right: transition zone dominated by Ciprés stands.	6
Figure 2.3	Decay affected Lenga trees.	7
Figure 2.4	Lenga stand, photograph taken from helicopter (top left), cultivated large Lenga stand (top right), Lenga leaves (bottom left), Shrublenga stand (bottom right).	8
Figure 2.5	Coihue	9
Figure 2.6	Vast Ñire stand, next to Lenga and a dry meadow, photograph taken from helicopter (top left), pure Ñire stand (top right), Ñire leaves (bottom left), Ñire krummholz stand (bottom right)	10
Figure 2.7	Ciprés de la Cordillera.....	10
Figure 2.8	Ciprés de la Cordillera, photograph taken from helicopter (left), Ciprés stand (right)..	11
Figure 2.9	Caña Colihue.	11
Figure 3.1	Topographical map of Argentina including an approximate outline of the study area. The study area is represented by a mosaic of four ASTER scenes.	17
Figure 3.2	Climate diagram for Esquel, Years: 1931-1998. NCDC (National Climatic Data Centers)	18
Figure 3.3	Major vegetation zones of southern South America (Veblen [186], modified). The cool temperate Nothofagus forest and woodland is outlined in green.	19
Figure 4.1	GCP measurement at a river bending (left) and localization in the nadir-looking NIR band (right).....	26
Figure 4.2	Hemispherical photograph.	29
Figure 4.3	Scheme of the field sampling on a forest plot.	31
Figure 5.1	Workflow of all preprocessing steps for the DEM generation derived from the ASTER datasets and the produced ASTER mosaic.	33
Figure 5.2	Workflow of the Landsat ETM+ mosaic generation.....	34
Figure 5.3	Systematic vertical banding and noise lines before (left) and after (right) Fourier filtering.	35
Figure 5.4	Sensor calibration differences caused by high/low gain switch during data measurement (left) and its correction (right). A wedge-shaped artefact consisting of low and high gain DNs remained in band 4 (bottom).....	37
Figure 5.5	Shaded mosaic of the four generated DEMs from ASTER data.....	41

Figure 5.6	ASTER DEM before (left) and after semi-automatic postprocessing (right). Blunders are eliminated and the systematic grid pattern smoothed.....	42
Figure 5.7	ASTER DEM before (left) and after semi-automatic postprocessing (right). The border of the mosaicked scenes is still apparent in the DEM (upper images) as well as some bigger blunders (lower images).	43
Figure 5.8	Difference image of ASTER DEM - SRTM C-band DEM. Extreme differences greater than ± 100 m are due to missing data in the SRTM DEM or cloud coverage in the ASTER DEM mosaic.....	44
Figure 5.9	Diagram of calculation of overlap area (left) and illustration of the Hermite Cubic algorithm (right).	48
Figure 5.10	Adjusting the two Landsat ETM+ pan tiles by 3rd order polynomial transformation. Accuracy requirements for the GCPs is <15 m pixel size.	49
Figure 5.11	Radiation components taken in to account in the ATCOR3 model [155].....	51
Figure 5.12	Subset of the generated ASTER DEM (top left), the derivatives aspect and slope (lower left and lower right) and sky view factor (top right).	53
Figure 5.13	Subset of the uncorrected ASTER dataset (top left) and the atmospherically/topographically corrected ASTER dataset (bands 3, 2, 1) (top right). On the bottom left the uncorrected and on the bottom right the atmospherically/topographically corrected Landsat ETM+ dataset (bands 3, 2, 1).	54
Figure 5.14	Regression analysis of illumination and at-sensor radiance before atmospheric/topographic correction (left image), illumination and reflectance after atmospheric correction but without BRDF correction (middle image), and illumination and BRDF corrected atmospherically corrected reflectance values. The graphs present the correlation of ASTER band 3 and Landsat ETM+ band 4 respectively. For both dataset two different predominantly forested subsets were chosen, see Fig. 5.15 and Fig. 5.16.	55
Figure 5.15	ASTER DEM (top left) and illumination (top middle) subset and at-sensor radiance dataset (top right). ASTER reflectance dataset with no BRDF correction (lower left), suboptimal BRDF correction threshold angle 50° (lower middle) and optimized threshold angle of 30° (lower right image).	56
Figure 5.16	ASTER DEM (top left) and illumination (top middle) subset and at-sensor radiance dataset (top right) of Landsat ETM+. Landsat ETM+ reflectance dataset with no BRDF correction (lower left) and optimized threshold angle of 50° (lower right image).....	57
Figure 6.1	Workflow of an eCognition classification project.....	60
Figure 6.2	Overview of the multiresolution segmentation criteria in eCognition.	62
Figure 6.3	Scheme of a hierarchical network of classified image objects on different segmentation levels ([184], (modified)).	63
Figure 6.4	Membership function describing the plausibility of object class \tilde{N} ire subject to height asl [m]. To obtain a wider area of high stability the parable shaped membership function was adjusted (circles).....	65
Figure 6.5	Overlap of class descriptions based on membership functions in a two-dimensional feature space ([184], (modified)).	66

Figure 6.6	Screenshot of arcview, showing the training subset. Displayed is a false color composite of ASTER bands 1, 2, 3 overlaid with the vegetation cover ground reference layer....	68
Figure 6.7	Preliminary segmentation and classification result showing a realistic (left) and an unrealistic (right) pattern. Left image criterion: color: 0.8, smoothness: 0.9, right image criterion: color: 0.2, smoothness: 0.1. Both images represent a scale factor of 9, which represents realistically groups of homogeneous tree types. The criterion represented in the left image was chosen in the final classification project.....	69
Figure 6.8	Kappa accuracies of the different eCognition test projects varying by their segmentation criteria and scale parameter. The nomenclature "xy_0201" can be explained as follows: weight of shape = 0.2, weight of compactness = 0.1.	70
Figure 6.9	Differences of two overlapping datasets are apparent (circles).	71
Figure 6.10	Developed class hierarchy.....	73
Figure 6.11	Ground reference bitmap (grey) and randomly selected sample units (black).....	76
Figure 6.12	Classification result of the training subset.	78
Figure 6.13	Classification stability of the training subset. The graphical output displays the value for each image object in a range from dark green (1.0, nonambiguous) to red (0.0, absolutely ambiguous).	81
Figure 7.1	Measured LAI versus modelled LAI from ASTER reflectances and vegetation indices respectively. The lowest right plot shows the result from linear multiple regression. Each cross corresponds to a measurement plot. The diagonal line represents the 1:1 relationship.	93
Figure 7.2	Measured LAI versus modelled LAI from Landsat ETM+ reflectances and vegetation indices respectively. Each cross corresponds to a measurement plot. The diagonal line represents the 1:1 relationship.....	94
Figure 7.3	The relationship between tree density and forest stand structure and its impacts on the band ETM4 (n=38).....	96
Figure 7.4	The relationship between ASTER3 and ASTER9 respectively, volume and its understory situation for each plot measurement (n=38).....	98
Figure 7.5	Measured tree density versus modelled tree density. Only best performing vegetation indices were plotted. Each cross corresponds to a measurement plot. The diagonal line represents the 1:1 relationship.....	99
Figure 7.6	The relationship between the vegetation indices MVI E, NDVI E and PVI E respectively, tree density and its understory situation for each measurement plot (n=38).	99
Figure 7.7	Measured DBH versus modelled DBH. Only best performing vegetation indices are plotted. Each cross corresponds to a measurement plot. The diagonal line represents the 1:1 relationship.	100
Figure 7.8	The relationship between the vegetation indices OSAVI E, NDVI E and PVI E respectively and DBH and its understory situation for each measurement plot (n=38).....	101
Figure 7.9	Measured basal area versus modelled basal area. Only best performing vegetation indices were plotted. Each cross corresponds to a measurement plot. The diagonal line represents the 1:1 relationship.	102

Figure 7.10	Measured volume versus modelled volume. Best performing vegetation indices were plotted. Each cross corresponds to a measurement plot. The diagonal line represents the 1:1 relationship.	103
Figure 7.11	Measured biomass versus modelled biomass. Only best performing results were plotted. Each cross corresponds to a measurement plot. The diagonal line represents the 1:1 relationship.	105
Figure 7.12	The relationship between the different forest parameters and their best estimator in respect of the forest cultivation situation for each measurement plot (n=38).	109
Figure 7.13	The relationship between the different forest parameters and their best estimator in respect of the regeneration situation of each measurement plot (n=38).	111
Figure 7.14	The relationship between the different forest parameters and their best estimator in respect of the vitality of each measurement plot (n=38).	112
Figure 7.15	The relationship between the different forest parameters and their best estimator in respect of the percent coverage of each measurement plot (n=38).	114
Figure 7.16	The relationship between the different forest parameters and their best estimator in respect of its forest cultivation situation for each measurement plot (n=38).	115
Figure 7.17	The relationship between the different forest parameters and their best estimator in respect of stand structure for each measurement plot (n=38).	116
Figure 7.18	Regional-scale variation of LAI in the south-western Lenga forests.	118
Figure 7.19	Regional tree density variations in Lenga forests. Not cultivated areas are denser (circles) than cultivated forests (rectangles).	118
Figure 7.20	Regional-scale variation of DBH.	119
Figure 7.21	Regional variation of basal area due to higher precipitation in the west and varying elevation and exposition.	120
Figure 7.22	Regional-scale variation in biomass. Left image shows a cultivated Lenga forest, whereas the right image shows an uncultivated Lenga forest at Lago Baguilt.	120

List of Tables

Table 2.1	Existing Forest Inventories of Patagonian Provinces.....	14
Table 4.1	ASTER sensor specifications [103].	21
Table 4.2	Landsat 7 ETM+ specifications [103].	22
Table 4.3	Specifications and quicklook: ASTER scene 1	23
Table 4.4	Specifications and quicklook: ASTER scene 2	23
Table 4.5	Specifications and quicklook: ASTER scene 3	23
Table 4.6	Specifications and quicklook: ASTER scene 4	24
Table 4.7	Specifications and quicklook: Landsat ETM+ scene 1	24
Table 4.8	Specifications and quicklook: Landsat ETM+ scene 2	24
Table 4.9	Number of the measured GCPs for each ASTER scene. Some GCPs had to be neglected due to a) destabilization of the stereo-model, b) questionable localization in the scene or c) low accuracy of GPS signal.	26
Table 4.10	Levels at which errors can be introduced in digital hemispherical canopy photography [149].	29
Table 4.11	Summary statistics for all measured forest parameter variables (n=38).	32
Table 5.1	Parameters used for gain conversion of band 4 [105].	36
Table 5.2	Residual results for the used ground control points for ASTER DEM generation. These residuals are valid for the VNIR bands 3N and 3B.	40
Table 5.3	Statistical analysis of the difference image ASTER DEM - SRTM C-band DEM.....	45
Table 5.4	Geolocation and height differences between the independent check points and the ASTER DEM.	45
Table 5.5	Residual results of the georectified satellite datasets. For the ASTER scenes the results of the VNIR subsystem are listed.	47
Table 5.6	Residual results of the georectified ASTER SWIR datasets.....	47
Table 5.7	Applied calibration coefficients for the ASTER- and Landsat ETM+ -mosaic. Gain and offset are in $[w/m^2 \cdot sr \cdot \mu m]$	50
Table 5.8	Parameters contained in the atmospheric database, stored as look-up tables [155].	51
Table 5.9	Applied radiometric correction parameters.....	52
Table 5.10	Determined and applied empirical BRDF correction parameters.	53
Table 6.1	Identifiable objects of interest.	68
Table 6.2	Chosen criteria for the conducted segmentation tests (see Fig. 6.2 for the definition of the segmentation criteria).	69

Table 6.3	Class separation matrix. Bands in grey color indicate low separation between classes. Bands in black may have minor spectral overlaps between classes.....	74
Table 6.4	Assigned weights to the errors of classification.....	77
Table 6.5	Accuracy statistics containing user- and producer accuracy for each class as well as overall accuracy, kappa coefficient and weighted kappa.....	79
Table 6.6	Fuzzy logic membership statistics for each object.....	80
Table 7.1	Investigated vegetation indices calculated from ASTER and/or Landsat ETM+ bands.	88
Table 7.2	Tasseled cap coefficients for Landsat 7 ETM+ at-sensor reflectance [76].	89
Table 7.3	Correlation coefficients r for linear relationships between LAI, LAI _{uw+dw} (incl. upward and downward measurements) and the ASTER- and Landsat ETM+ bands ($n = 38$). Correlation coefficients in bold are statistically significant at the 0.01 level (2-tailed).....	90
Table 7.4	Parameter estimates for regression models: LAI = $a + b \cdot VI$ and respective shrinkage. Validation of linear LAI models ($n = 15$): Coefficient of determination (R^2) and relative RMSE. R^2 in bold signify statistically significant correlation coefficients ($p = 0.01$ (2-tailed)).....	91
Table 7.5	Correlation coefficients r for the linear relationships in-between LAI and the measured forest parameters ($n = 38$). Correlation coefficients in bold are statistically significant at the 0.01 level (2-tailed).....	95
Table 7.6	Correlation coefficients r for linear relationship between the measured forest parameters and the spectral reflectances of ASTER and Landsat ETM+ data ($n = 38$). Correlation coefficients in bold are statistically significant at the 0.01 level (2-tailed).....	96
Table 7.7	Parameter estimates for regression models: Tree density = $a + b \cdot VI$ and Shrinkage. Validation of linear tree density models ($n = 15$): Coefficient of determination (R^2) and relative RMSE.....	98
Table 7.8	Parameter estimates for regression models: DBH = $a + b \cdot VI$ and Shrinkage. Validation of linear DBH models ($n = 15$): Coefficient of determination (R^2) and relative RMSE..	100
Table 7.9	Parameter estimates for regression models: Basal area = $a + b \cdot VI$ and Shrinkage. Validation of linear basal area models ($n = 15$): Coefficient of determination (R^2) and relative RMSE.....	101
Table 7.10	Parameter estimates for regression models: Volume = $a + b \cdot VI$ and Shrinkage. Validation of linear volume models ($n = 15$): Coefficient of determination (R^2) and relative RMSE.....	103
Table 7.11	Parameter estimates for linear and quadratic regression models: Biomass = $a + b \cdot VI$ and Biomass = $a + b \cdot VI + c^2 \cdot VI$ and Shrinkage. Validation of linear and quadratic biomass models ($n = 15$): Coefficient of determination (R^2) and relative RMSE.....	104
Table 7.12	Summary of the best performing estimators and the most suitable wavelength's, the required correlation and the achieved accuracy for Lenga stands.....	106
Table 7.13	Forest parameter derived from the provincial forest inventory dataset. 57 virgin, 17 cultivated and 8 heavily cultivated forest stands where observed. Biomass measurements were derived from a different study in the south of Province of Chubut.....	108
Table 8.1	Approximate costs and production time calculation for the main procedure steps of this research project, conducted by experienced staff.....	129

Chapter 1

Introduction

1.1 Problem Description

The subantarctic native forests of Patagonia are on the verge of extinction due to the lack of awareness of the essential role they play in the fragile ecosystem. The pressure on these forests is constantly growing and the conservation is threatened by not only natural induced fires but also by increasing intentional forest fires, illegal or uncontrolled timber and wood extraction, domestic animal overgrazing, human encroaching activities, and the replacement of native trees by fast-growing exotic species. The economic crisis in Argentina that started in 2001, deteriorated the situation even further.

Patagonia requires a forest measuring and monitoring system that responds to the forest department authorities to report on sustainable forest development to ensure a sustainable development inside and outside national parks. The creation of products for forest inventories, monitoring sustainable forest management, landscape management and forest carbon accounting has to be established. Despite growing interest in, and general concern for sustainable forest management, many interested parties are ill-equipped to judge if the current management practices are sustainable. It's argued that in order to effectively manage resources, three elements must be present, i.e. information about the natural forest resources, clear policies on how the forests can be managed and participation of the people with an interest in the native forests. Accordingly, first quantitative and qualitative information must be gathered, managed and updated. Due to physical remoteness, lack of funds and personnel, spatially referenced datasets for the forested areas of Patagonia are either nonexistent or out of date and thus unreliable. Satellite remote sensing can be an efficient and cost-effective way to acquire up-to-date and accurate land cover and topographic information.

The Remote Sensing Laboratories of the University of Zurich (RSL), in partnership with the Centro de Investigación y Extensión Forestal Andino Patagónico, Esquel (CIEFAP) and the Dirección General de Bosques y Parques, Esquel (DGBYP) have decided to share their specific knowledge and resources to reduce the information deficits and take a step forward towards sustainable forest management in the Province of Chubut.

At the beginning of this research project, the economic development in Argentina was uncertain. Trust in the policy makers was lost, and as a result thereof finding funding for the research project became almost impossible. The fact that limited fundings were available to acquire remote sensing data was an aggravated circumstance. Nevertheless, confidence in the scientific and ecological value of this research project was strong and the enthusiasm to achieve the defined objectives enormous. The objectives of this work are:

- To establish a topographic information database to ensure reliable and accurate results of future projects dealing with land use classifications, environmental modelling and resource management in the partially mountainous Province of Chubut;
- To produce an accurately orthorectified and radiometrically corrected remote sensing database which can be used as geospatial information on forest cover, forest productivity and as input to the provincial forest inventory as well as information input to other land use projects;
- To apply and evaluate an advanced classification methodology to provide a detailed forest classification map with emphasis on tree type discrimination and accounting for the difficult mapping of mixed forest vegetation in the transition zone of the Patagonian forest ecosystem

- towards the steppe ecotone;
- To retrieve biophysical forest parameters from the remote sensing database and provide new informations on the vast pure *Nothofagus pumilio* forests in the Province of Chubut;
 - To provide the CIEFAP and DGBYP with the established database, products, all developed methodologies and know-how.

Taking account of limited fundings, it was decided that the remote sensing datasets would consist of the low-cost scientific sensor ASTER and Landsat ETM+ data provided free of charge by the Argentine Space Agency. Additional scientific objectives of this project are:

- The evaluation of the accuracy of DEM generation from ASTER stereo data;
- The suitability of object-oriented classification methodology to classify tree species in pure and mixed forest stands;
- The potential of ASTER and Landsat ETM+ data for object-oriented forest classification and tree type discrimination;
- And the establishment of biophysical forest parameter relationships from ASTER and Landsat ETM+ data.

All objectives of this research project together with their theoretical background provide a bio-geographical information database and adapted methodology to support the forest authorities of Patagonian Provinces in realizing sustainable forest management.

1.2 Structure of this Thesis

This thesis deals with the current problem of unsustainable forest management due to the lack of accurate and up-to-date quantitative and qualitative forest information and how remote sensing can help to fill these information gaps. A bio-geographical database is established in deriving different mapping products from multispectral remote sensing data. The structure of this thesis represents the sequence of the defined objectives to be solved, where intermediate cognitions and products often serve as input to the following task. The methodical chapters are thematically selfcontained, thus they comprise their theoretical part, an analysis and development part followed by the results, an evaluation or accuracy assessment of the result and a discussion.

First, Chapter 2 gives an overview of the ecology of Argentinean *Nothofagus* forests and its history and silvicultural development. The silvicultural situation as well as deficits and problems of forest management in the Province of Chubut are highlighted. At last an overview of the existing forest inventories and applications of remote sensing to date to improve forest information and management in Patagonia is then given.

In Chapter 3 the study area in the Province of Chubut is presented and an overview of the geographical and climatological characteristics of the area, as well as its vegetation pattern is provided.

The database, consisting of remote sensing data and ground reference data, including GPS, LAI and forest parameter measurements, is presented in Chapter 4. The methodology of hemispherical LAI measurement is described and the developed measurement plan for all parameters adapted to *Nothofagus pumilio* forest is described.

Chapter 5 deals with the digital elevation model (DEM) generation with an explanation on a semi-empirical post-processing method. The geometric and radiometric preprocessing of the remote sensing data, including mosaicking and an empirical BRDF correction is also discussed.

Chapter 6 details the object-oriented classification approach. The theory of the approach is discussed in detail, followed by a segmentation evaluation, the developed rule base and the class hierarchy. Finally, the achieved classification result - the vegetation cover map - and a detailed accuracy assessment are discussed.

Chapter 7 addresses the forest parameter estimation from the remote sensing database. First an overview of the subject is given, followed by the methodology. An interpretation of the relationships between the remote sensing data and the measured forest parameters is given, followed by the presentation of all forest parameter estimation results and a detailed analysis of the descriptive parameters. The chapter concludes with the interpretation of the produced forest parameter maps.

Finally, Chapter 8 provides a summary of all the objectives given and a discussion of the gained cognitions. An outlook describing the consequences of this work and future activities of the local authorities as well as possible improvements in similar projects finalize this thesis.

Chapter 2

Forestry in Patagonia

2.1 The Forests in the Province of Chubut, Patagonia

The Andes of southern Chile and southwestern Argentina are a major determinant of climate and vegetation patterns in southern South America. Patagonian forests in Argentina are growing along the eastern trailing edge of the Andes from Río Colorado at 38° S until Beagle Channel at 54° 53' S. As mean annual temperatures and the length of the growing season decline along the north to south gradient, so do species richness and total biomass in the rain forests. The presence of the forests is mainly determined by precipitation. The forests are present in the Provinces of Neuquén, Río Negro, Chubut, Santa Cruz and Tierra del Fuego. The forested area appears in a long strip along the Andes which in places is 30 to 80 km wide and approximately 2100 km long [82], [83], [84], [85].

The deciduous, temperate forest ecotone in the north of Patagonia is dominated at high-elevation and/or xeric sites by deciduous Lenga (*Nothofagus pumilio*). The mean annual temperatures are 5 to 9° C and precipitation ranges from 500 to 1500 mm per year [78]. At 42° S the deciduous Lenga forests are mainly growing at heights between 900 and 1600 m above sea level. At these elevations Ñire (*Nothofagus antarctica*) is also present. It covers poor soils and grows often as bush. On better soils Ñire can reach heights of 5-10 m. At mesic mid-elevation sites the evergreen Coihue, which can occur as rich, pure stands (*Nothofagus dombeyi*) appears at rather humid sites near lakes and rivers. Drier, rocky areas in-between, mostly steep slopes with shallow soils are covered by Ciprés de la Cordillera (*Austrocedrus chilensis*). Ciprés can form pure stands in dry, rocky areas or appear together with Radal (*Lomatia Hirsuta*) and Maitén (*Maytenus Boaria*) [167], [186].

Evergreen temperate forests are dominated by Coihue (*Nothofagus dombeyi*) and do occur between 38 and 44° S. This ecotone belongs to the Valdivian rain forest and is found mainly in the inner Andean valleys and on the western side of the Cordillera. Coihue forests do prefer areas with a mean annual temperature of 5 to 8° C and mean annual precipitation of 1500 to 4000 mm. Its upper limits are at around 1100 m above sea level [77], [78]. The Coihues often advance towards Ciprés and Lenga (*Nothofagus pumilio*) stands. The understories of Coihue forests are typically dominated by Caña Colihue (*Chusquea culeou*), a bamboo specie.

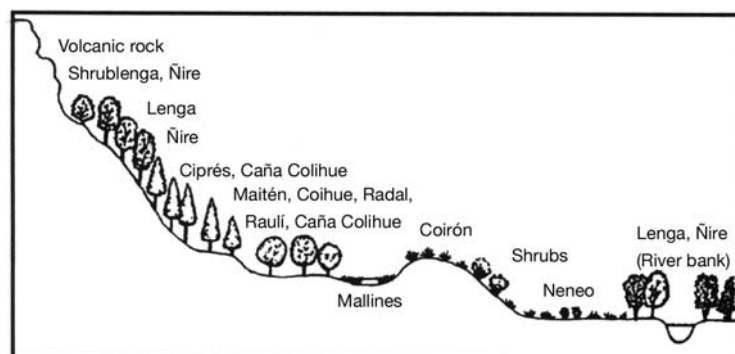


Figure 2.1 Vegetation profile of the Patagonian forest towards the Andean-Patagonian steppe ([77] modified).

The transition zone between the steppe and the temperate forest is dominated by Ciprés de la Cordillera (*Austrocedrus chilensis*). This ecotone occurs between 36 and 44° S [78]. Mean yearly

temperatures range between 7 and 10° C and precipitation ranges from 600 to 1000 mm per year, mainly falling during winter. Ciprés stands "enlighten" from west to east and grow as single trees towards the Patagonian steppe. They prefer heights between 300 and 1500 m above sea level. Ciprés stands were decimated in the last 100 years by forest fires and intense logging [78]. Some of the ecosystems present in the Province of Chubut are illustrated in Fig. 2.2.

The eastern part of the research area belongs to the Andean-Patagonian steppe. It occurs from 38 to 47° S and is characterized by a temperature range of 8 to 13° C and mean annual precipitation of 200 to 600 mm [165]. The Patagonian steppe is dominated by shrubs and grass species. Intensive grassland, called *mallines*, exists near rivers.



Figure 2.2 Photographs of the different ecosystems and ecotones. Top left: deciduous temperate forest consisting of Lenga (in the background) and Ñire (in the foreground of the image); top right: evergreen and deciduous temperate mixed forest; bottom left: Andean-Patagonian steppe with mallin; bottom right: transition zone dominated by Ciprés stands.

2.1.1 Lenga (*Nothofagus pumilio*)

Lenga is known as the most important tree species in Patagonia. It covers large areas and plays an important role in soil- and water-conservation functions. Furthermore, its wood is of good quality and plays an important economical role for the local silviculture industry [112].

Lenga occurs from 35° 35' to 55° S in Chile and Argentina in both the Andes and the Coastal Cordillera. It ranges in elevation from sea level to 2'000 m. North of 41° S it occurs only in the sub alpine zone and commonly forms the upper tree limit, but in the southern part of its range it occurs at both high and low elevations. Near the center of its distribution, at 41° S, mean annual precipitation is more than 5000 mm on the western side of the Andes and less than 800 mm at the easternmost localities of Lenga in Argentina [186].



Figure 2.3 Decay affected Lenga trees.

At low elevations Lenga can reach heights of 30 m. Its strongest trunks can reach a diameter of 1.5 m. Lenga is often affected by white (*Phellinus andinopatagonicus*) and brown decays (*Postia pelliculosa* and *Piptoporus portentosus*), which can influence timber quality substantially [Fig. 2.3]. Trunks with a DBH of 60 cm consist of 50% of decay and consequences are that although high volumes are harvested only a small amount can be used for production [128].



Figure 2.4 Lenga stand, photograph taken from helicopter (top left), cultivated large Lenga stand (top right), Lenga leaves (bottom left), Shrublenga stand (bottom right).

Lenga occurs at cooler and drier sites than Coihue and typically forms extensive pure stands. Understories on wet sites and lower elevations are usually dominated by Caña Colihue. Lenga krummholz often occurs in a ten to fifty meter wide ecotone with alpine vegetation. At many sites, however, presumably those less affected by strong winds, dense stands of erect Lenga form the timberline [186]. On dry sites at timberline and at low elevations Ñire is often associated with Lenga. In autumn the leaves of the Lenga tree become red and can then be optically separated from Coihue trees.

2.1.2 Coihue (*Nothofagus dombeyi*)

Coihue occurs in Argentina from 38°30' to 44° S [176]. The largest of the South American *Nothofagus* species often attains heights greater than 50 m and trunk diameters in excess of 2 m. It ranges from near sea level to 2500 m in elevation and occurs only in moist habitats. On the Argentinean/Chilean border, at 40° to 43° S, where the mean annual precipitation is 1800 to 2500 mm, Coihue forms extensive pure stands. These monotypic forests have relatively open main canopies, 30 to 40 m tall. Understories are dominated by Caña Colihue, which forms nearly impenetrable three to six meter tall thickets. Further east, as mean annual precipitation declines to less than 1800 mm, Coihue forms mixed stands with Ciprés, which are growing on the rockier and drier areas, mainly on steep slopes [186]. Coihue is an evergreen tree specie and keeps its green leaves for several years.



Figure 2.5 Coihue

2.1.3 Ñire (*Nothofagus antarctica*)

Ñire occurs in the Andes and the Coastal Cordillera from 36°30' to 56° S. In elevation it ranges from near sea level in the south to 2000 m in the north. Among South American *Nothofagus*, it occurs in the widest range of habitat types: areas of poor drainage at low to high elevations, exposed sites of unstable substrate at alpine timberline, topographic depressions (*mallines*) subject to cold air drainage, steep slopes with shallow soils, and dry sites near the Patagonian steppe. In general, it is common at sites that are too harsh for most other tree species [186]. It is also the first tree species that grows after a forest fire.

Ñire most commonly occurs in association with Lenga, both at the alpine timberline and at the lower timberline near the ecotone with the Patagonian steppe. At the alpine timberline, Ñire often occurs in krummholz vegetation, either in pure patches or interspersed with Lenga. Near the ecotone with the steppe south of 45°, Ñire forms extensive woodlands, sometimes intermixed with Lenga but generally occurring on edaphically less favourable sites. It occurs both as a tree and as a shrub. At 40 to 43° S on the eastern side of the Andes, it forms dense thickets on steep xeric slopes with shallow soils [186]. In autumn, before losing its leaves, Ñire leaves become red similar to the Lenga leaves. Fig. 2.6 indicates an erect Ñire forest as well as the widely distributed krummholz form.



Figure 2.6 Vast Ñire stand, next to Lenga and a dry meadow, photograph taken from helicopter (top left), pure Ñire stand (top right), Ñire leaves (bottom left), Ñire krummholz stand (bottom right)

2.1.4 Ciprés de la Cordillera (*Austrocedrus chilensis*)

Ciprés de la Cordillera is the main native deciduous tree specie along the Andes. It occurs at very dry sites and shallow soils but also grows at deep soils where it can reach heights of 20 to 25 m.



Figure 2.7 Ciprés de la Cordillera.

It is common near the Patagonian steppe. Timber of Ciprés is very popular and has been logged for quite some time. Nowadays Ciprés logging is strongly regulated and monitored by the Directorate General of Forest and Parks (DGBYP). The main problems endangering Ciprés stands face are wildfires and a still unknown cause which induces a whidespread mortality of Ciprés [117]. Due to global change Ciprés is expanding its occurrence towards the habitats of Coihue and the Patagonian steppe.



Figure 2.8 Ciprés de la Cordillera, photograph taken from helicopter (left), Ciprés stand (right).

2.1.5 Caña Colihue (*Chusquea culeou*)

Caña Colihue is a bamboo specie and typically dominates the rain forest understories in the north but is absent in the south of around 48° S. Caña Colihue forms nearly impenetrable 3 to 6 m high thickets [186]. Due to its profound rhizomes it can withstand forest fires better than other tree species and is, together with Ñire, the first plants after a forest fire to grow. Due to its thick growth Caña Colihue makes it almost impossible for other plants to grow [77].

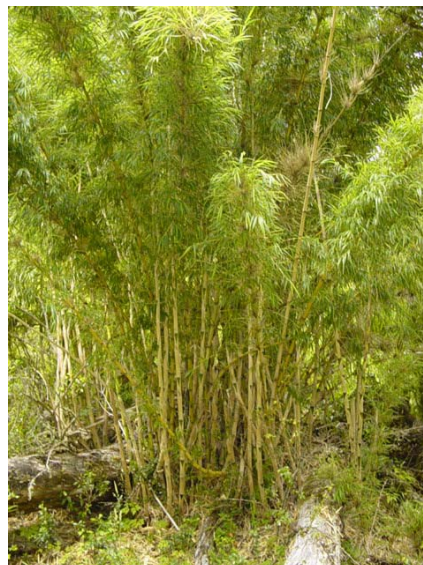


Figure 2.9 Caña Colihue.

2.2 History and Silvicultural Development in Patagonia

The *Nothofagus* forests of southern Argentina have been more subject to destructive exploitation than to effective management. Exotic pines have been extensively planted in Argentina along the ecotone between *Nothofagus* forests and Patagonian steppe. Conversion of *Nothofagus* forest to plantations of exotic trees has not been extensive, and the recent rate of forest degradation through destructive logging practices has not been high [186].

Significant areas of *Nothofagus* forest were destructively logged or burned during the first half of the twentieth century. However, since the mid-seventies substantial silvicultural research has been conducted in South American *Nothofagus* forests, but relatively little of the resulting knowledge has been put to use in forest management [9]. The minimal attention given to management of native forests in Argentina is unfortunate given the potential inherent in the timber quality and rapid growth of these forests. The traditional form of forest exploitation on *Nothofagus* forests in southern Argentina has been "high grading" in which the best formed individuals of the most valuable timber species are extracted. This removal of the more commercially valuable species has degraded the timber quality of the resource. In mixed-species rain forests, selective logging has also favoured the regeneration of shade-tolerant tree species at the expense of the more valuable *Nothofagus*. The relatively small canopy openings created, are filled by the advanced regeneration of the shade-tolerant tree species and chusquea bamboos [185]. In the mixed-species forests of the Argentinean Lake Districts, the best regeneration of *Nothofagus* has occurred where the silvicultural intervention was more intensive, for instance, after the cutting of patches of several hectares [186].

Large areas of *Nothofagus* forest are protected in numerous national parks and reserves. Although the number of reserves and their surface areas are impressive, the protection of *Nothofagus* forests is not necessarily adequate. It is unclear whether the areas in parks and reserves encompass a sufficiently large and diverse mosaic of environments to adequately protect *Nothofagus* ecosystems. Regional- and landscape-scale studies are needed in order to assess the sufficiency of present parks and reserves [186]. For example, it is not known whether individual parks are large enough to encompass the "minimum dynamic area" [142], which includes all successional stages of the present plant communities. Furthermore, in many cases the forests were burned or logged prior to the creation of the reserve, and there have been serious invasions of the disturbed areas by exotic species [15]. In most parks and reserves the impacts of introduced animals such as livestock, deer and beavers are severe. Some species and forest types are not adequately represented in reserves. Information of the amount and distribution of genetic diversity is also fundamental for planning the conservation of *Nothofagus* species [141].

2.3 Silvicultural Situation in the Province of Chubut

In the Province of Chubut approx. 897 000 ha of natural forest exists [11]. Only 131 850 ha of this area has been declared as productive forest. The productive forests consist of 90% Lenga forests, 10% consist of Ciprés and Coihue [42]. 90% of productive forest belongs to the Province of Chubut [11].

Economically the most important products from Lenga are round timber and the mean lumbering amounts to 9000 m³ per year but due to quality- and production reasons only 3500 m³ can be converted [91].

Every year timber is being harvested on an area of 800 ha of the productive part of the natural forests. Harvesting follows management plans only after a short five year period [11]. This leads to insecurity of timber supply for the sawmills [92] which in turn leads to a short-term maximization of timber harvesting. In combination with browsing livestock in the forests the

quality of the rejuvenescence of the *Nothofagus* forests sinks substantially [112].

In the Province of Chubut natural forests are being managed by the DGBYP. The Directorate gives away concessions after previous acceptance of a forest management plan handed in by the sawmills. The selling prices for timber per m³ are established by the DGBYP. Private landowners of forested areas are only the possessors of the land, the timber growing on this land belongs to the Province. Exempted from this law are landowners who settled on their land prior to 1955. However, they are also obliged to hand in a forest management plan if they like to harvest their forests with an economical interest [112].

10 000 ha of the natural forests are being economically used. 26% of these forests are privately owned, 21% are for sale, for 43% thereof livestock grazing concessions were granted, and 10% are owned by the Province. Only 10% of the whole forested area are not influenced by browsing of livestock. The negation of economical use of the forest by the settlers is one of the main conflicts [19].

Béron et al [11] developed a management plan for the whole Province to establish sustainable forest management in the Province of Chubut. The forest inventory of 1996 as well as a forest cover map with a scale of 1:100 000 provided the basis for this work. In consideration of the 14 existing sawmills, fourteen different catchment areas and a potential yearly yield for each sawmill were defined. Even though the data basis is of low geometrical resolution and needs improvements, it was the first step towards forest management on a provincial scale [112].

Several environmental organisations are also focussing on future enlargements of existing national parks and are planning the development of new park areas in Patagonia.

2.3.1 Deficits and Problems

In Patagonia several problems exist which hinder sustainable management of the *Nothofagus* forests substantially: These are:

- The presence of livestock in the forest,
- The lack of forest yield data and precise inventory data in order to develop sustainable forest management plans,
- Economical problems of the sewing industries due to forest bioremediation which is caused by decay,
- The lack of solid multiple use planning of the forests. At the moment the sewing industry is deciding where and when trees are being harvested.
- The lack of an efficient operational forest monitoring system to ensure sustainable development on a provincial level,
- Unclear law concerning ownership and right of use, and
- Forest fires.

The situation with the second most important *Nothofagus* specie, Ñire, is similar. Ñire forests play an important role in soil protection and water regulation. Still Ñire forest are being burned to create pasture land. Although it is prohibited it is still practised due to its strong traditional significance. Ñire was often destructively logged and replaced by exotic plantations such as Ponderosa pine (*Pinus ponderosa*). Moreover, Ñire is used as firewood by the local people. Béron [12] says that 39 000 ha of Ñire are being harvested per year, which is 4.3 times the amount of Lenga being harvested.

Tourism is a growing branch in Patagonia in contrast to farming. But it is difficult to balance the need to protect the environment with the promotion of economic development. Tourism has promoted the growth of urban centers and lead to a considerable amount of litter in the environment as a result of the tourists' lack of environmental awareness. Fauna and flora is being disturbed and forest fires have increased. Hunting tourism is growing as well and has recently lead

to conflicts. No tourism management plan exists on provincial level.

Mining is another industry which heavily burdens the ecology in the Province of Chubut. In recent years, multinational companies have settled down near or at forested areas to exploit precious metals such as silver and gold. Mining concessions are distributed by the national government in Buenos Aires [27]. The local people and governments who are directly affected by the ecological consequences have no influence in the decisions made by the policy makers in Buenos Aires. Their will and interest to protect the native forests from being destroyed by the mining companies [112] are mostly passed over. Again, the balance of environmental protection with the economic development is difficult to keep, but protests against proposed mining projects are growing.

Economical changes in the past years have put the native forests in Patagonia into public interest. On one side ecotourism has gained an importance and local authorities and farmers have noticed that sustainable forest management can be a key to secure their economical existence. On the other side international mining and forestry companies are currently putting enormous pressure on different regions in the Province of Chubut and offering the local people financially rewarding jobs. Therefore it is of great importance that future forest planning is based on accurate quantitative and qualitative forest informations. Forest planning has to include interests of all involved parties, the policy makers and the local people, to be accepted by the local people and thus to ensure their support and environmental engagement.

2.4 Forest Inventories in Patagonia

In 1986 forested areas in the Provinces Río Negro, Chubut, Santa Cruz and Tierra del Fuego were mapped for the first time. As database, airphotos were used. The developed map "*Precarta Forestal*" was published at 1:500'000 scale. It is the first forest inventory in Patagonia and still the most reliable and accurate database though some forest areas and lakes have changed due to fires and water power plant constructions [113]. However, the database was never topographically corrected and contains geographic distortions. The forest cover map is only available as hard copy.

In 1999 the Valdivian Forest ecosystem was mapped and classified into forest types and is based on visual interpretation of Landsat TM images. The satellite images were not topographically corrected before interpretation. The map encloses Chile and the Patagonian Provinces Neuquén, Río Negro and Chubut and was published digitally and analogically at 1:500'000 scale.

From 1995 to 1997 a national forest inventory of potential productive forests, based on Landsat TM images, was established. The final map was produced at 1:100'000 scale but never published and did not bring any qualitative improvements in comparison to the 1986 forest inventory [113].

Table 2.1 Existing Forest Inventories of Patagonian Provinces.

Year	Data Base	Classes	Scale
1986	Airphotos Landsat TM	tree types	1:500'000
1995-1997	Landsat TM	tree types	1:100'000
1999	Landsat TM	tree types	1:500'000
1998-1999	Landsat TM Topographical Data	productive forest, tree types	1:250'000

During 1998-1999 two Canadian timber companies, in association with an Argentinean

company, produced a map of potential productive forests in Province Chubut based on Landsat TM and topographical data. The products with 1:250'000 scale are heavily influenced by economical and not sustainable forest management interests and are therefore subjective [113].

2.5 Remote Sensing in Patagonian Forestry

Application of remote sensing to sustainable forest management can be divided into four categories, as follows:

- classification of forest cover type,
- estimation of forest structure,
- forest change detection,
- and forest modelling.

So far remote sensing was only sparsely applied in Patagonian forestry. The established forest inventories and forest cover maps base on airphoto or satellite imagery but were in any case only interpreted visually, do not imply topography, represent only few forest types and products are of small scale.

In 2001 a first research study with the goal to develop a forest management plan for native forests at the La Plata and Fontana lake region in the Province of Chubut based on SPOT 4 and Landsat TM data was developed [112]. During his project, Dr. José Lencinas then founded a Remote Sensing Laboratory at the Andine-Patagonean Forest Research and Extention Centre (CIEFAP). The laboratory is concentrating on remote sensing for sustainable forest management in Patagonia and has done research in the area of forest mapping, stand volume estimation [112] and carbon reservoirs modelling [13].

Chapter 3

Study Area

3.1 Introduction

In this chapter the study area in the Province of Chubut is presented. First the geographical location and its topography are briefly described, followed by a description of the climatic conditions and the soil characteristics for the study area. Last a short overview of the regional vegetation pattern, strongly influenced by the extreme climate gradient in the area, is given.

3.2 Location & Topography

The study area is situated in the west of the Argentine Province of Chubut ($70^{\circ} 45' - 71^{\circ} 35' W$, $40^{\circ} 58' - 43^{\circ} 32' S$) in Patagonia; on the eastern trailing edge of the Andes, with a large elevation gradient towards the east.

Topographically the study area is dominated by the eastern trailing edge of the Andes in the west and the Patagonian Plains in the east. The highest summits run along the west of the study area, over the mountains Cerro Carreras, 2350 m asl, in the north to Cerro Ventisquero Sur, 2070 m asl, in the south. The study site stretches towards the very dry eastern planes with heights of approximately 350 m asl. It includes parts of Los Alerces National Park, that protects a small part of the native forest belt along the eastern flanks of the Andes as well as the great grassland plains to the east. The area encompasses approximately 14 400 km².

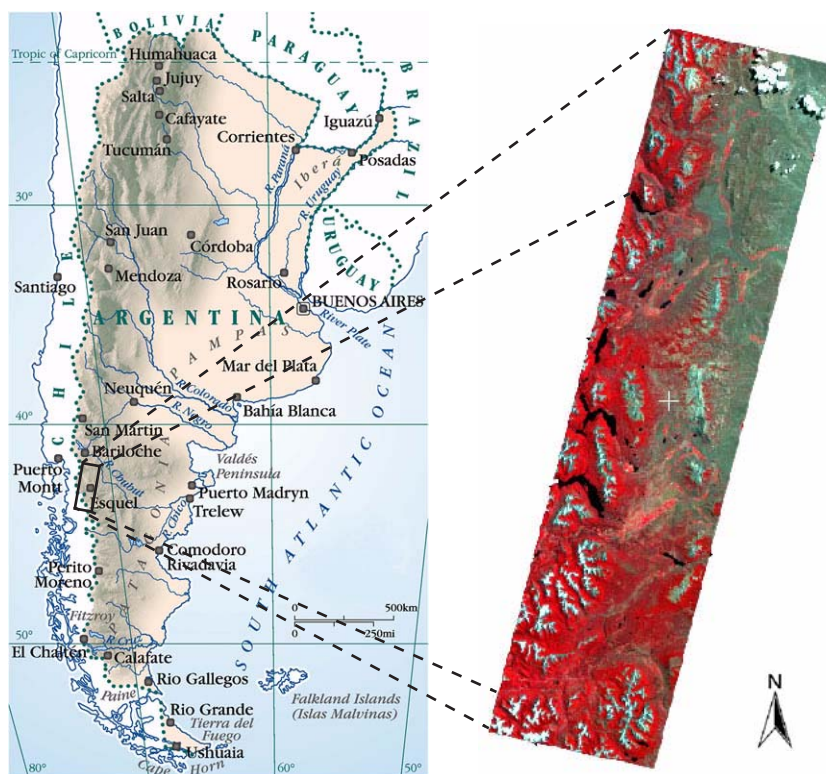


Figure 3.1 Topographical map of Argentina including an approximate outline of the study area. The study area is represented by a mosaic of four ASTER scenes.

3.3 Climate

The climate of the mid-latitudes of southern South America is directly controlled by the mid-latitude westerlies with their cyclonic storms, the south-east Pacific subtropical high-pressure cell, and the topographic barrier of the Andes [127], but also shows significant relationships to higher-latitude circulation patterns and southeastward movement of maritime and continental subtropical air masses [174], [188]. The Andean Cordillera in the west of the study area reaches elevations of more than 2000 m asl and is an effective barrier to moisture-laden storms that flow westerly from the Pacific into the continent. Most of the precipitation is discharged in the coastal mountains of Chile, and on western slopes of the Andes. In the rain shadow of the Andes, precipitation declines dramatically from west to east. For example, at 41° S mean annual precipitation declines along a nearly 100 km west-east transect from about 4000-6000 mm in the Chilean Andes, in the west, next to the study area, to about 200-300 mm in the Patagonian plains, in the east of the study area [8]. Temperatures in the study area are moderate, though the influence from the Pacific temperatures can fall in the winter season towards -20° C.

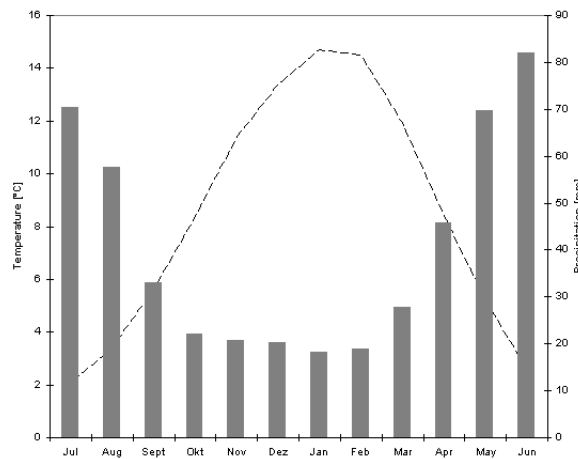


Figure 3.2 Climate diagram for Esquel, Years: 1931-1998. NCDC (National Climatic Data Centers)

3.4 Soils

The Andes were extensively glaciated during the Pleistocene. Many of the glaciated surfaces have been covered by extensive andesitic volcanic deposits of recent origin. Glaciers scoured large lakes in the Andean foothills [186]. Due to these glacially influenced geomorphological developments and the climatic situation, different soil types exist in the study area.

In higher elevations as well as on steep slopes Lithosols and rocky soil types without humus are dominant. They are generally sparsely or not vegetated. In the lower and flatter regions alluvial and volcanic ash deposits lead to the development of very fertile soils. They are characterised by a stable and high porosity, a slight acid ph-value and a high water storage capacity. The more humid the area, the more rich in humus the soils [32].

In lower, humid areas water-logged soils are existent. These soils lead to humid, marshy meadows, the *mallines*, which are mostly agriculturally used as grazing land. In the eastern, very dry Patagonian plains rocky, alluvial soils are dominant.

3.5 Regional Vegetation Patterns

The vegetation pattern in the study area mirror mainly the west-to-east climatic gradients. Rain forest is followed by mesic forest, xeric forest, open woodland and tall shrubland, grassland and low shrub-steppe [187].

In the west of the study area the montane rain forests at 900 - 1600 m elevation are dominated by extensive pure stands of the deciduous Lenga. At the timberline, Lenga krummholz often occurs in a few meter wide ecotone with alpine grass and shrub vegetation. Mean annual temperatures are 5 - 9° C and precipitation ranges from 500 - 1500 mm per year [78].

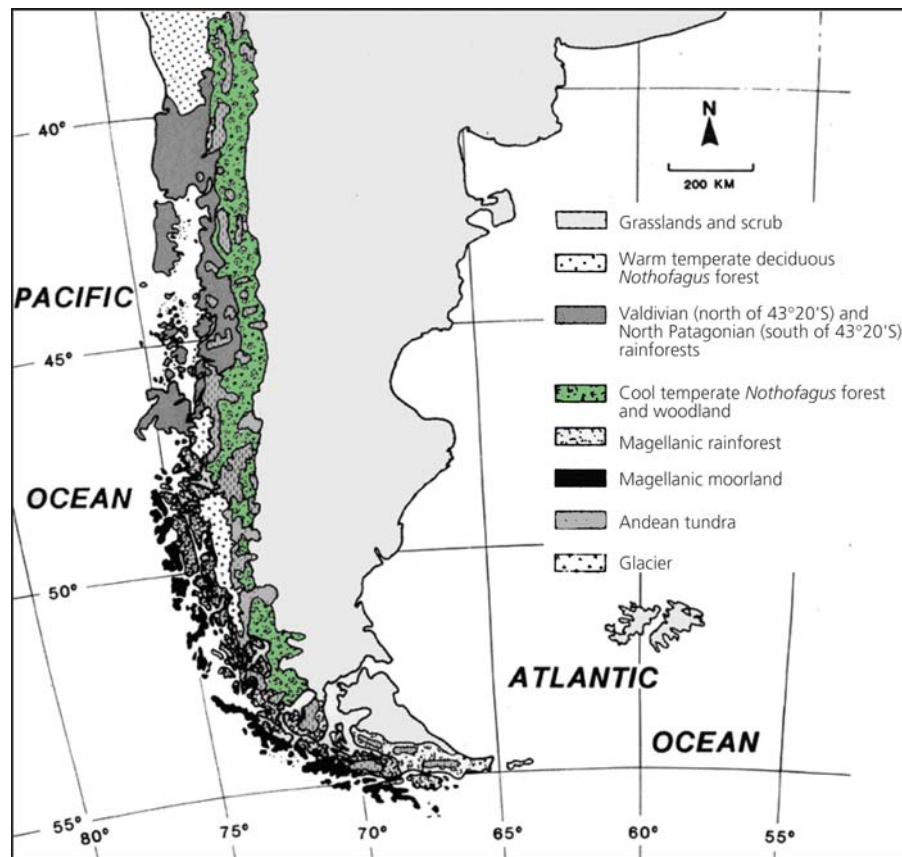


Figure 3.3 Major vegetation zones of southern South America (Veblen [186], modified). The cool temperate *Nothofagus* forest and woodland is outlined in green.

This deciduous forest ecotone is followed at approximately 700 - 1000 m elevation by 40 m tall evergreen Coihue forests. This ecotone belongs to the Valdivian rain forest and occurs mainly in the inner andine valleys and on the western side of the Cordilleras. Coihue forests prefer areas with a mean anual temperature of 5 - 8° C and mean annual precipitations of 1500 - 4000 mm. It's upper limits are at around 1100 m asl [77], [78]. Typically these forests have dense understories of 3 - 6 m tall bamboo, called Caña Colihue.

With increasing aridity, the conifer Ciprés forms mixed stands with Coihue and then pure conifer stands. Understories become less dense as Caña Colihue is replaced by xeric shrubs and small trees such as Maqui (*Aristotelia chilensis*) and Radal (*Lomatia hirsuta*). Near the ecotone with the steppe, Ciprés stands form open woodlands with bunch grasses and low shrubs such as Neneo (*Mulinum spinosum*) and *Discaria articulata* [187]. Mean yearly temperatures range between 7 and 10° C and precipitation ranges from 600 - 1000 mm per year, mainly falling during

winter. They prefer heights between 300 and 1500m asl [78].

The small deciduous tree, Ñire, often dominates sites that are unfavorable for development of tall forests including (1) relatively xeric sites that are transitional to the steppe; (2) bottoms of broad valleys that have more finely textured soils and a high probability of cold-air drainage resulting in temperature inversions; (3) sites along streams and bogs with elevated water tables; (4) mid-dry during the summer; and (5) high-elevation sites exposed to strong winds that prevent a protective snow cover from forming [125], [164]. Open woodlands of 4 - 6 m tall Ñire are most common in broad valleys in the transition toward steppe [187]. On midslopes from 800 - 1100 m, at intermediate positions along the precipitation gradient, Ñire forms dense 2 - 4 m tall shrublands with xerophyllous tree or shrub species such as Laura (*Schinus patagonicus*), Radal (*Lomatia hirsuta*), Notro (*Embothrium coccineum*), Retamo (*Diostea juncea*), Maitén (*Maytenus boaria*), and/or the bamboo Caña Colihue [156], [164].

Adjacent to the Andean Forests the grassland steppe is dominated by the grass *Festuca palleescens*, locally called Coirón blanco and comprises 50 - 90% of the vegetation cover of the area [40]. Intensive humid grassland patches, *mallines*, exist near rivers. The andino-patagonian steppe is characterised by a temperature range of 8 - 13° C and mean annual precipitations of 200 - 600 mm [165].

Chapter 4

Data Base

4.1 Introduction

In this chapter the database, composed of remote sensing data and ground reference data, also known as ground truth data, is discussed. First a short introduction into the sensor specifications is given, followed by the presentation of the applied satellite scenes. Secondly, the field data is presented consisting of GPS (Global Positioning System) measurements, mapped ground reference information, LAI (Leaf Area Index) and forest parameter measurements. A detailed description of the hemispherical LAI measurement methodology and forest parameter calculations are presented. In addition, the measurement scheme of all parameters are outlined.

4.2 Remote Sensing Data

4.2.1 ASTER

ASTER (Advanced Spaceborne Thermal Emission and Reflection Radiometer), a Japanese sensor flying on the Terra satellite, was launched in December 1999, as part of NASA's Earth Observing System (EOS) [198]. The ASTER instrument consists of three separate instrument subsystems, i.e. the visible and near infrared (VNIR) system with a geometric resolution of 15 m, the shortwave infrared (SWIR) with a resolution of 30 m and the thermal infrared (TIR) subsystem with a resolution of 90 m.

The VNIR subsystem features two telescopes, one nadir-looking with a three-spectral-band detector, and the other backward-looking with a single-band detector. The backward-looking telescope provides a second view of the target area for stereo observations [103]. An overview of the technical specifications of the ASTER instrument is given in Tab. 4.1.

ASTER datasets can be downloaded from the Earth Observing System Data Gateway [46]. ASTER Level 1A and 1B data were free of charge until 12 August 2002 but due to high demand an administrative charge of 55 US\$ has been levied since then.

Table 4.1 ASTER sensor specifications [103].

Characteristic	VNIR	SWIR	TIR
Spectral Range [μm]	1: 0.52 - 0.60	4: 1.600 - 1.700	10: 8.125 - 8.475
	2: 0.63 - 0.69	5: 2.145 - 2.185	11: 8.475 - 8.825
	3N: 0.76 - 0.86	6: 2.185 - 2.225	12: 8.925 - 9.275
	3B: 0.76 - 0.86	7: 2.235 - 2.285	13: 10.25 - 10.95
		8: 2.295 - 2.365	14: 10.95 - 11.65
	9: 2.360 - 2.430		
Ground Resolution [m]	15	30	90
Data Rate [Mbits/sec]	62	23	4.2
Cross-track Pointing [deg]	± 24	± 8.55	± 8.55
Cross-track Pointing [km]	± 318	± 116	± 116
Swath Width [km]	60	60	60
Quantization [bits]	8	8	12

4.2.2 Landsat ETM+

The 33 year record of data acquired by the Landsat satellites constitutes the longest continuous record of the earth's continental surfaces. Landsat 7 was launched in April 1999. The earth observing instrument on Landsat 7, the Enhanced Thematic Mapper Plus (ETM+), replicated the capabilities of the highly successful Thematic Mapper 4 and 5 [103]. New features with ETM+ are: 1) an additional panchromatic band with 15 m spatial resolution, 2) a thermal infrared band with 60 m spatial resolution and 3) an on board, full aperture, 5 % absolute radiometric calibration. The Landsat 7 ETM+ instrument specifications are listed in Tab. 4.2.

Since May 2003 Landsat 7 ETM+ has had a scan line corrector defect with the result that all newly gap-filled products, available since Fall 2004, are of limited scientific use. As an alternative Landsat 5 data can be used.

Table 4.2 Landsat 7 ETM+ specifications [103].

Characteristic	VIS/TIR	PAN
Spectral Range [μm]	1: 0.45 - 0.52 2: 0.52 - 0.61 3: 0.63 - 0.69 4: 0.78 - 0.90 5: 1.55 - 1.75 6: 10.4 - 12.5* 7: 2.09 - 2.35	Band8: 0.52 - 0.90
Ground Resolution [m]	30/60*	15
Data Rate [Mbits/sec]	150	150
Swath Width [km]	185	185
Quantization [bits]	8	8

4.2.3 Datasets

In total six datasets were processed in this research project i.e. four ASTER Level 1A scenes acquired on 18 January 2002 and two Landsat ETM+ Level 1G scenes taken on 21 February 2000.

The four ASTER Level 1A data products contain the raw reconstructed, unprocessed instrument digital counts with geometric correction coefficients and radiometric calibration coefficients appended but not applied. The radiometric calibration coefficients consisting of offset and sensitivity information are generated for all detectors from a database.

The two Landsat ETM+ Level 1G scenes are radiometrically and geometrically system corrected. The radiometric correction coefficients *gain* and *bias* are appended in a metafile. The Landsat ETM+ scenes were provided for free by the Argentinean National Space Program (CONAE - Commission National de Actividades Espaciales).

Table 4.3 Specifications and quicklook: ASTER scene 1

Parameter		Quicklook
Acquisition Date	18 January 2002	
Acquisition Time	14:43:39	
Scene-No.	AST_L1A.003:2005839464	
Height [km]	722.538	
Sun Zenith [deg]	34.9	
Sun Azimuth [deg]	62.2	
Central Longitude	-71.103957	
Central Latitude	-41.987542	

Table 4.4 Specifications and quicklook: ASTER scene 2

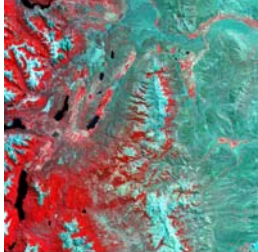
Parameter		Quicklook
Acquisition Date	18 January 2002	
Acquisition Time	14:43:48	
Scene-No.	AST_L1A.003:2005839468	
Height [km]	722.779	
Sun Zenith [deg]	35.2	
Sun Azimuth [deg]	61.7	
Central Longitude	-71.286895	
Central Latitude	-42.514060	

Table 4.5 Specifications and quicklook: ASTER scene 3

Parameter		Quicklook
Acquisition Date	18 January 2002	
Acquisition Time	14:43:57	
Scene-No.	AST_L1A.003:2005839474	
Height [km]	723.019	
Sun Zenith [deg]	35.6	
Sun Azimuth [deg]	61.2	
Central Longitude	-71.472368	
Central Latitude	-43.040420	

Table 4.6 Specifications and quicklook: ASTER scene 4

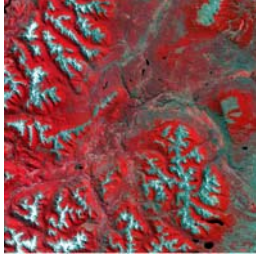
Parameter		Quicklook
Acquisition Date	18 January 2002	
Acquisition Time	14:44:06	
Scene-No.	AST_L1A.003:2005839476	
Height [km]	723.258	
Sun Zenith [deg]	35.9	
Sun Azimuth [deg]	60.7	
Central Longitude	-71.660467	
Central Latitude	-43.566507	

Table 4.7 Specifications and quicklook: Landsat ETM+ scene 1

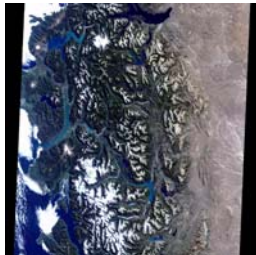
Parameter		Quicklook
Sensor	ETM+	
Acquisition Date	21 February 2000	
Acquisition Time	14:22:30	
Scene-No.	L71232089_08920000221	
Path/Row	232/089	
Height [km]	722.7	
Sun Zenith [deg]	46.3	
Sun Azimuth [deg]	59.4	
Central Longitude	714403.4204	
Central Latitude	414539.0426	

Table 4.8 Specifications and quicklook: Landsat ETM+ scene 2

Parameter		Quicklook
Sensor	ETM+	
Acquisition Date	21 February 2000	
Acquisition Time	~14:24:00	
Scene-No.	L71232090_09020000221	
Path/Row	232/090	
Height [km]	722.7	
Sun Zenith [deg]	~47.3	
Sun Azimuth [deg]	~58.4	
Central Longitude	721246.5161	
Central Latitude	431109.9600	

4.3 Land Cover Data

To date the forest cover map derived from the first forest inventory, conducted in 1986 and based on geometrically uncorrected airphotos and Landsat TM data, is the most detailed and accurate, two dimensional information on the forest cover in the study area. However, its scale, age and inaccuracy due to topographic distortion does not fulfill the needs for this research study. Accordingly, three field campaigns took place between 2001 and 2004, mainly during the summer seasons when the remote areas in the mountainous Andes were accessible by car. One goal was to visually delineate pure as well as mixed forest stands of the major tree types growing in the study area. For accessibility reasons most data was collected in Los Alerces National Park. During the summer of 2004 there was an option to join the local fire brigade on their daily helicopter control flights to take digital photographs of inaccessible areas, which improved the ground reference database substantially. However, of some areas still no detailed land cover information is available. Reasons are diverse, a) the inaccessible terrain, b) the sparse road network, c) destroyed roads or d) hedged and locked or guarded privately owned land.

The ground reference was mapped on plastified satellite composites and then transferred to a GIS (Geographical Information System) database.

4.4 GCP Database

In order to geometrically correct the satellite data and extract digital elevation models from stereo data, precise ground control point (GCP) measurements are required. Sources can be accurate topographical maps or GPS based point measurements.

The available topographical maps at a scale of 1:50 000 from the Argentine military in the early 1950's were not utilised, since the planimetric and height accuracy averages to approximately 50 m – 100 m. It is for this reason that a GPS based GCP database was established. The GCPs were collected using two Trimble Geoexplorer II GPS receivers, working in differential correction mode. The horizontal positional error in differential correction mode averages to 3 m and the vertical error to 5 m.

In the first instance ASTER data were stretched in contrast for better visualisation and with the help of the topographical maps potential measurement points were localized. The GCPs had to be identifiable in both, the nadir and backward-looking near infrared band, in order to ensure a distinct localization and, at a later stage, stable stereo-model generation. The collection of GCPs was concentrated near the sparse road network consisting basically of unsealed roads, which are subject to seasonal and periodic closure due to flooding of river crossings. Clear localization and accurate measurements of points were achieved at:

- road crossings and intersections,
- bridges,
- river confluences or bendings,
- characteristic lakeshores and
- some outstanding, characteristic vegetation structures.



Figure 4.1 GCP measurement at a river bending (left) and localization in the nadir-looking NIR band (right).

Still some areas remained without any GCPs, mainly mountainous areas which were inaccessible by 4x4 cross-country vehicle and needed to be explored on expedition by horse, boat and foot lasting several days. Also privately owned land, called *Estancias* are usually inaccessible because they are hedged and crossing roads blocked with gates. Prior arrangements and agreements with the owners to get hold of the keys for the gates are necessary and can be a time consuming task.

For the whole study area, 146 GCPs, preferably equally distributed in planimetry and height, were measured. The GCPs localization was documented with photographs or sketches as well as high resolution screenshots taken from the ASTER datasets [Fig. 4.1]. Thus a GCP database was established containing the coordinates in WGS 84, the local datum Campo Inchauspe as well as the X- and Y-pixel coordinates of the corresponding ASTER scene.

Table 4.9 Number of the measured GCPs for each ASTER scene. Some GCPs had to be neglected due to a) destabilization of the stereo-model, b) questionable localization in the scene or c) low accuracy of GPS signal.

ASTER Scene	Total Number of measured GCPs	Total Number of used GCPs for stereo modelling & georectification
1	29	23
2	31	29
3	44	41
4	41	35

4.5 LAI-Measurements

4.5.1 Theory

Several definitions of leaf area index (LAI), depending on the technique used, have been suggested. In this research study LAI is defined as one half the total leaf area per unit ground surface area as first defined by Watson in 1947 [193]. LAI is dimensionless.

LAI can be measured directly or indirectly. Indirect methods, in which leaf area is inferred from observation of another variable, are generally faster, amendable to automation, and thereby allow for a larger spatial sample to be obtained. Indirect methods can be divided into two categories: (1)

indirect contact LAI measurements and (2) indirect non-contact measurements. These are ground-based measurements that usually integrate over one single stand only. Indirect non-contact measurement techniques/instruments can again be divided into two main groups: (1) instruments based on *gap fraction* analysis and (2) instruments based on *gap size distribution* analysis [89]. The hemispherical camera measurement method is based on gap size distribution. Documented research has proven these instruments to be very efficient and reliable in forest environments [195]. A characteristic of the gap fraction-based approach is that it does not distinguish photosynthetically active leaf tissue from other plant elements such as stem, branches or flowers. Alternative terms for leaf area index have therefore been proposed, among them *Vegetation Area Index* (VAI) [50], *Plant Area Index* (PAI) [131], and *Foliage Area Index* (FAI) [196].

Chen and Black [23] used the term *effective LAI* (L_e) to describe LAI estimates derived optically. This nomenclature seems most appropriate because it recognizes that conventional inversion models are incapable of measuring the surface area contributed solely by green leafy material, and that they are unable to compensate for the non-random positioning of canopy elements.

The last step in the interpretation of gap fraction for these methods in terms of LAI is based on relationships between gap fraction and canopy geometry. These relationships are derived from light extinction models, which link LAI and canopy architecture to the penetration of solar radiation through the canopy. Gap fraction, as a function of zenith angle, is the essence of such mathematical formulas and models [133], [22], [196] and can be determined as follows:

$$T(\vartheta, \alpha) = \frac{P_s}{P_s + P_{ns}} \quad (\text{Eq. 4.1})$$

where $T(\vartheta, \alpha)$ is the gap fraction for a range of zenith angles ϑ and azimuth angles α ; P_s is the fraction of sky in a region (ϑ, α) and P_{ns} is the fraction of vegetation in a region (ϑ, α) .

Light extinction models describe the probability of interception of radiation within canopy layers, as well as the probability of sun flecks at the bottom of the canopy. Sun flecks correspond to gaps in the canopy when viewed along the direction of the direct solar beam. The *Poisson* model requires the assumption of random spatial distribution of the canopy, assuming that projections of leaves are randomly located in the plane of the projection [195]. The model divides the canopy in N statistically independent horizontal layers in which leaves are uniformly and independently spread. These layers are sufficiently thin $\Delta L = L/N$ to make the probability of having more than one contact between incoming light rays and vegetation within one layer small compared to the probability for one contact. The probability of a contact in layer ΔL :

$$G(\theta, \alpha) \frac{\Delta L}{\mu} \quad (\text{Eq. 4.2})$$

where $G(\theta, \alpha)$ is the mean projection of the leaf area unit in a plane perpendicular to the sunrays; and the probability of no contact is:

$$(1 - G(\theta, \alpha)) \frac{\Delta L}{\mu} \quad (\text{Eq. 4.3})$$

As N is allowed to approach infinity, the probability of a ray making exactly n contacts is described by a *Poisson* distribution. The gap fraction or probability for not having contact is then given by Eq. 4.4 [131]:

$$P_0(\vartheta) = \exp\left(-G(\vartheta, \alpha)\frac{LAI}{\mu}\right) \quad (\text{Eq. 4.4})$$

where $P_0(\vartheta)$ is the gap fraction at zenith angle ϑ ; α the azimuth angle of leaves; $G(\vartheta, \alpha)$ the mean projection of the leaf area unit in a plane perpendicular to the sunrays; μ stands for $\cos\vartheta$.

However, this definition is not entirely valid for canopies with clumped leaf distributions, as is usually the case in natural systems. Canopies with clumped or more regularly distributed leaves can be described more accurately by binomial models, respectively, using negative or positive binomial probability functions [131]. Markov models [132] are also appropriate. To compensate for clumping effects a combination of local linear averaging with larger-scale logarithmic-linear averaging of transmittance data was proposed [107]. On the other hand, it was also indicated that for isolated canopies in open tree stands, the inversion kernel might be more complicated than the one defined by Eq. 4.4 [133]. All models, however, require some information on the distribution of leaf angles and leaf azimuths within the canopy, with the binomial and Markov models also necessitating an additional parameter to describe the canopy orderliness. Given these inputs, plus the solar elevation, the models then estimate the solar radiation regime within the canopy if LAI is given, or they invert the procedure and compute the LAI from the radiation regime (e.g. the sun fleck probability). It is evident that with all input parameters available, LAI may be derived from the inversion of Eq. 4.4 [89].

With regard to the practical application, it has been shown that most instruments based on gap fraction assess the effective LAI (L_e) under the assumption of random spatial distribution of leaves [44]. It is, however, primarily foliage clustering at the shoot level that invalidates this assumption, resulting in an underestimation of LAI [129]. As a conclusion on the gap fraction measurement devices, it appears that hemispherical cameras offer the greatest potential, if high spatial resolution and large signal dynamics of well registered visible and NIR bands are available [89].

4.5.2 Hemispherical Camera

Hemispherical canopy photography is a technique for studying plant canopies via photographs obtained through a hemispherical (fish-eye) lens from beneath the canopy (oriented towards zenith) or placed above the canopy looking downward. A hemispherical photograph provides a permanent record and is therefore a valuable source of information for position, size, density and distribution of canopy gaps. It is able to capture the species-, site- and age-related differences in canopy architecture, based on light attenuation and contrast between features within the photo (sky versus canopy). Hemispherical photographs provide an extreme angle of view, generally with a 180° field of view. In essence hemispherical photographs produce a projection of a hemisphere on a plane [150]. The exact nature of the projection varies according to the used lens. The simplest and most common hemispherical lens geometry is known as the polar or equi-angular projection [73], [60]. In a perfect equi-angular projection of a 180° field of view, the resulting circular image [Fig. 4.2] shows a complete view of all sky directions, with the zenith in the centre of the image and the horizons at the edges [89].

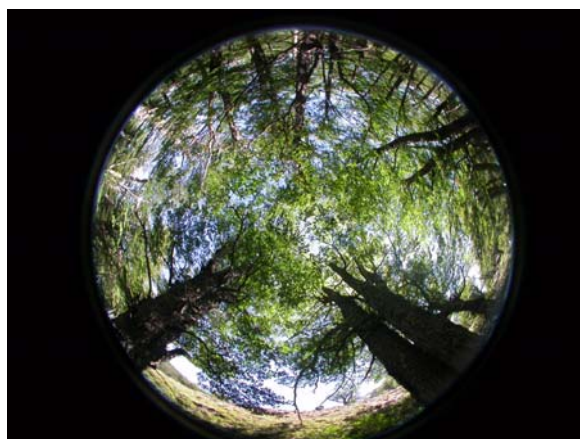


Figure 4.2 Hemispherical photograph.

Measurements were done with a digital camera, which in comparison to analog cameras, have better radiometric image quality, linear response, greater dynamic range and wider spectral sensitivity range [99]. They offer some practical advantages: (1) digital images make the expense and time associated with photographic film, film development, and scanning unnecessary and thereby eliminating errors that may occur during this procedure; (2) the potential of real time processing and assessment in the field; and finally (3) the unlimited image treatment possibilities. The digital camera and lens used was a NIKON Coolpix 4500 (4.0 million pixels) with NIKON Fish-eye Converter FC-E8 and the software package used for hemispherical image processing was CAN-EYE [194]. The software version utilized did not yet account for foliage clumping and non-photosynthetic material. Thus *plant area index* was actually calculated and applied in the developed models. In this work it is referred to PAI as LAI.

As with remote sensing technique, errors can occur at any stage of image acquisition or analysis. Reoccurring methodological errors have been discussed in several studies [135], [151] and are listed in Tab. 4.10. Strict protocols should be followed to ensure a systematic data acquisition.

Table 4.10 Levels at which errors can be introduced in digital hemispherical canopy photography [149].

Levels	Errors
Image acquisition	Camera positioning Horizontal/vertical position Exposure Evenness of sky lighting Evenness of foliage lighting (reflections): direct sunlight Optical distortion
Image analysis	Distinguishing foliage from canopy openings Assumed direct sunlight distribution Assumed diffuse skylight distribution Assumed surface of interception Image editing/enhancement Consideration of missing areas
Violation of model assumptions	Assessment of G-function variations Leaf angle variability Consideration of clumping

4.5.3 Measurement Plan

A ground survey of 42 forest plots in **Lenga** (*Nothofagus pumilio*) stands was carried out between 28 January 2004 and 13 February 2004. Every effort was made to measure plots varying in geographic location, exposition, elevation and silvicultural characteristics, though measurement plot distribution was influenced by accessibility and time restrictions.

LAI measurements based on hemispherical canopy photography can be made at diffuse or direct illumination conditions any time of the day. Measurements usually started at approximately 9:30 AM and ended at around 5:30 PM local time. Nine measurements were taken per forest plot to provide an average single value at each plot. For each measurement an upward and downward directed photograph was taken. The camera was kept above head for the upward image, and at hip height for the downward image. Slope adjustments were considered at photograph takes to minimize measurement errors. All measurements were made by the same person to guarantee a degree of consistency.

The measurement scheme of a plot is illustrated in Fig. 4.3. The plots measure an area of 45 by 45 m and are randomly distributed in Lenga stands accessible by either car or foot. In total, data of 42 plots were measured. At each plot 9 LAI measurements were taken and a mean LAI for each plot was calculated.

4.6 Forest Parameter Measurements

The LAI measurement setup [Fig. 4.3] was determined with consideration of the LAI measurement technique of averaging nine single LAI measurements to provide a single LAI value for each plot. The pixel size of both the ASTER and Landsat ETM+ data is 15 m whereby the Landsat ETM+ data were resampled beforehand with the cubic convolution method to 15 m pixel size. For each plot and sensor scene an averaged reflectance value based on a 3x3 pixel window was extracted.

To collect the forest parameters a circle of 12.62 m in radius in all forest plots was outlined. The circle represents an area of 500 m² [Fig. 4.3] and inside this circle several forest parameters were measured or calculated, i.e.

- tree density,
- basal area,
- tree height,
- diameter at breast height,
- dominant tree height,
- volume,
- biomass.

Moreover some descriptive parameters of the plots were recorded such as:

- regeneration,
- understory,
- coverage,
- forest stand structure,
- vitality,
- forest cultivation status (pristine, cultivated).

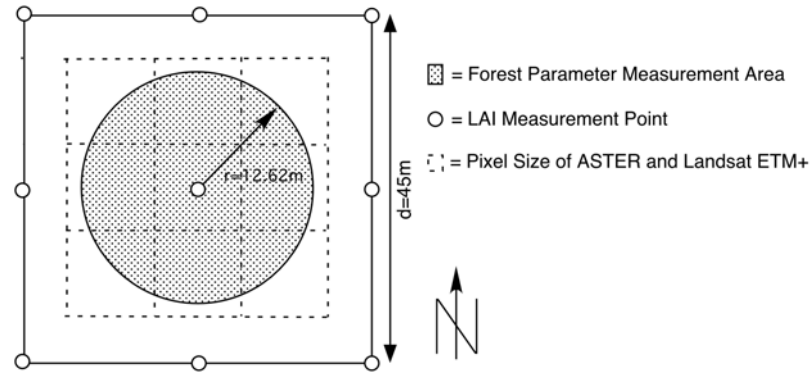


Figure 4.3 Scheme of the field sampling on a forest plot.

DBH was measured at a height of 1.3 m, using a tree caliper. To measure tree trunk/stem circumference a flexible measuring tape was used.

Tree height was measured, using a *Vertex* hypsometer. The method of height calculation is based on using the two angles (to the tip of the tree and to the transponder, which is held at a predefined height of 1.3 m) and the distance from the transponder. The *Vertex* uses ultrasonic pulses that assist to determine the distance from the hypsometer to the transponder. The instrument must be calibrated daily as the speed of sound in air depends on several factors such as temperature, humidity and atmospheric pressure. Once calibrated, the hypsometer has a built-in temperature sensor which compensates for changes in temperature. It is very important to allow the instrument sufficient time to stabilise to the ambient air temperature before calibration.

Once the diameter at breast height and the merchantable height of all trees have been measured, dominant tree height, tree density and basal area per ha were calculated. Merchantable volume V was calculated with the two-parametric equation [Eq. 4.5] developed by Antequera [2]:

$$V = DBH^2 \cdot h \cdot 0.0000520342 - h \cdot 0.008761 - DBH \cdot 0.002757 + 0.0711988 \quad (\text{Eq. 4.5})$$

where h is the tree height.

Biomass sampling can be done either by destructive methods, where plant material is actually collected from the site and weighed, or by nondestructive techniques, in which an alternate measure related to weight, such as length, height, or biovolume, has been calibrated using a subsampling of destructive plant samples measuring weight, and the two quantitative variables related by regression. In this research biomass was calculated by applying previously developed formulas for Lenga in Tierra del Fuego [118]. The empirical formulas look as follows:

$$BIOM_{leaf} = -0.139025203 + 0.005041522 \cdot DBH^{0.868515963} \cdot h^{1.184906810} \quad (\text{Eq. 4.6})$$

$$BIOM_{stem} = -10.77321293 + 0.02445014 \cdot DBH^{1.82698029} \cdot h^{1.1128900} \quad (\text{Eq. 4.7})$$

$$BIOM_{branch} = 9.373116783 + 0.017034830 \cdot DBH^{1.329011662} \cdot h^{1.120232356} \quad (\text{Eq. 4.8})$$

$$BIOM_{root} = 0.335841524 \cdot DBH^{1.391627694} \cdot h^{0.331357362} \quad (\text{Eq. 4.9})$$

$$BIOM_{ag} = 0.027096529 \cdot DBH^{1.776039101} \cdot h^{1.176318280} \quad (\text{Eq. 4.10})$$

Biomass was calculated for roots [Eq. 4.9], leaves [Eq. 4.6], branches [Eq. 4.8] and stems [Eq. 4.7] as well as for total above ground biomass [Eq. 4.10].

4.7 Plot Measurement Evaluation

After careful evaluation of the 42 Lenga plots, four plots had to be excluded from further analysis. Three of the four plots were geographically wrong geolocated and one plot was too close to an adjacent bare soil area which highly influenced the corresponding satellite reflectances. A statistical summary of all measured forest parameters is displayed in Tab. 4.11.

Table 4.11 Summary statistics for all measured forest parameter variables (n=38).

Parameter	Min	Max	Mean	Std.dev	Std.error	Range
LAI []	1.00	2.60	1.90	0.44	0.07	1.60
Dom. Height [m]	10.92	25.60	17.85	3.92	0.64	14.68
DBH [cm]	21.49	69.07	41.67	12.75	2.07	47.58
Basal area [m ² /ha]	7.16	89.50	47.34	18.78	3.05	82.34
Density [trees/ha]	20.00	1280.00	439.21	305.82	49.61	1260.00
Volume [m ³ /ha]	105.01	1306.37	474.35	238.56	38.70	1201.36
Biomass [t/ha]	39.416	477.794	189.922	90.340	14.655	438.379

Preprocessing & Digital Elevation Model Generation

5.1 Introduction

In this chapter the geometric and radiometric preprocessing of the ASTER and Landsat ETM+ satellite data is presented as well as the digital elevation model extraction from the ASTER nadir and backward-looking NIR bands 3N and 3B. All processing steps for the ASTER datasets are illustrated in Fig. 5.1.

Fig. 5.2 shows the workflow of all preprocessing steps for the two Landsat ETM+ datasets.

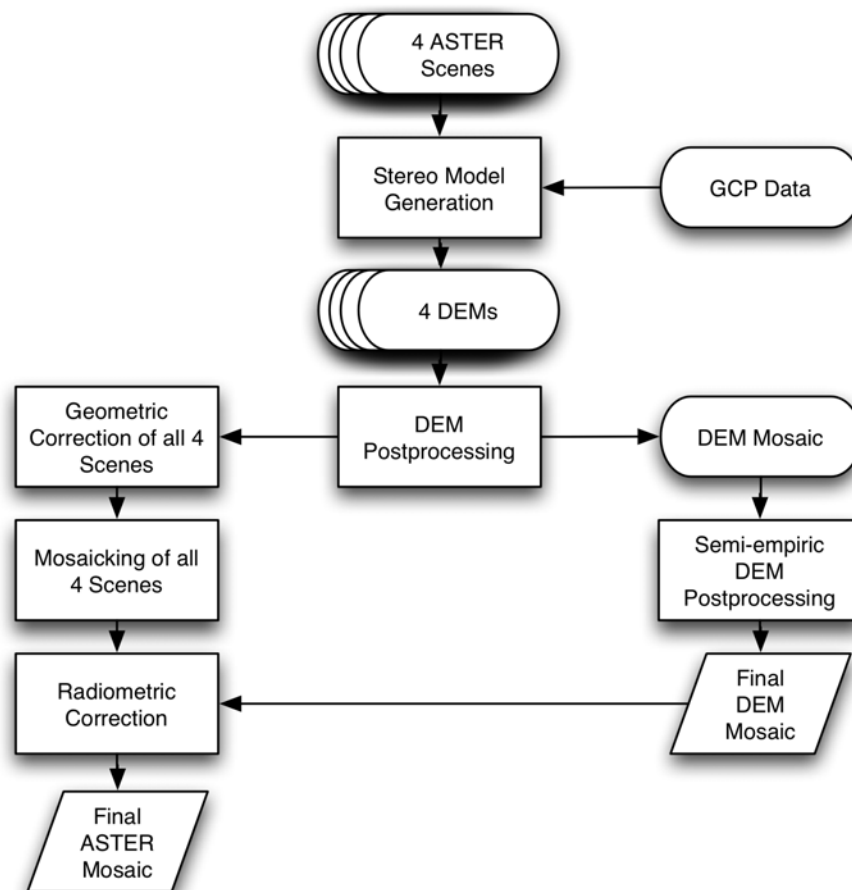


Figure 5.1 Workflow of all preprocessing steps for the DEM generation derived from the ASTER datasets and the produced ASTER mosaic.

First the preprocessing of the ASTER datasets is presented followed by an insight into the digital elevation model theory. In the results section an accuracy assessment of the generated ASTER DEM mosaic as well as a developed semi-empirical postprocessing algorithm are presented. Thereafter the performed preprocessing steps and the workflows of the two Landsat

ETM+ mosaics are discussed.

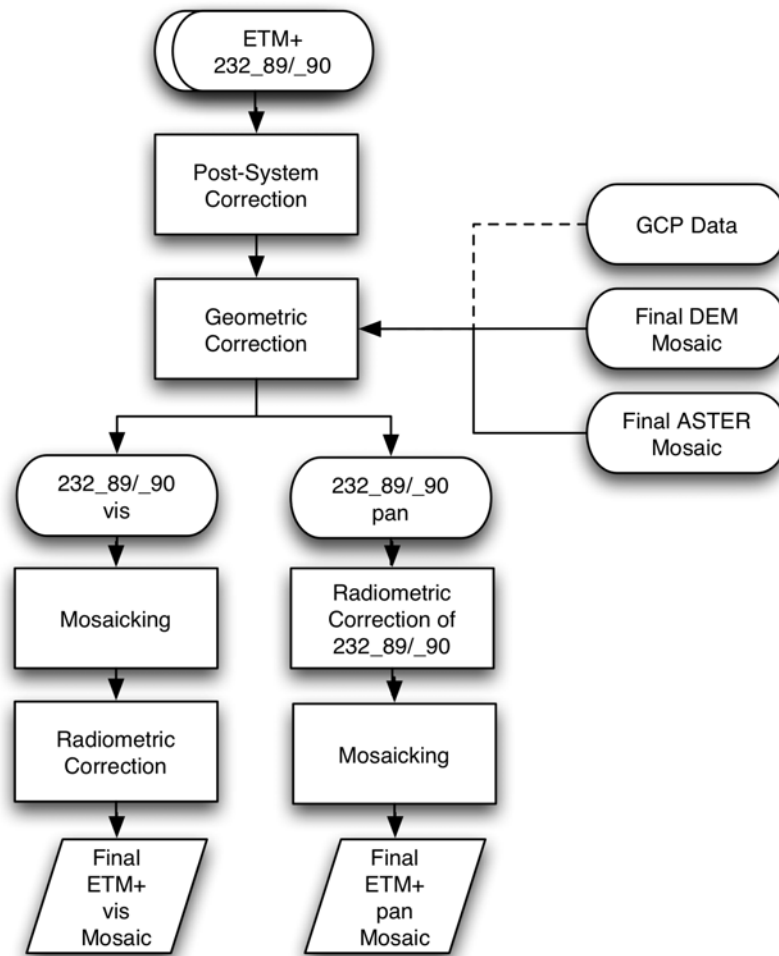


Figure 5.2 Workflow of the Landsat ETM+ mosaic generation.

5.2 Quality Analysis

5.2.1 ASTER System Correction

ASTER is a scientific sensor. The data products vary substantially in quality and each dataset has to be checked for radiometric and geometric system-specific errors.

The raw reconstructed, unprocessed ASTER level 1A data has not yet been radiometrically and geometrically system-corrected. The data contain vertical banding and have not yet been band-to-band co-registered. The radiometric correction coefficients, consisting of offset and sensitivity coefficients as well as the geometric correction data are delivered together with the dataset. The radiance values of Level 1 products can be calculated from the output voltage as follows [181]:

$$L = a \cdot \frac{v}{g} + d \quad (\text{Eq. 5.1})$$

where

L = Radiance,
 a = Amplification,
 v = raw DN value,
 g = gain,
 d = offset.

After radiance value calculation, band-to-band co-registration was performed for each of the four scenes.

5.2.2 ASTER Post-System Correction

5.2.2.1 Damaged Line Correction

Scene 3, in the SWIR bands 4, 5, 6 and 8, contained two lines with no data. The zero pixel values were replaced with the mean values of the lines above and below the damaged lines. Good visual results were achieved with this method.

5.2.2.2 Systematic Vertical Banding

Banding refers to a striping-like noise that can for example be aggravated by bright scene elements, such as clouds, that cause detector saturation for parts of the scan, and depends on the scan direction. All four ASTER scenes contain a systematic vertical banding in some of the SWIR bands. In particular, bands 7 and 8 are affected by vertical banding.

A common method to delineate and filter systematic noise is to convert the data from the spatial domain to the frequency domain performing a Fourier transform [66]. The approach is to examine the amplitude or power spectrum of the image to locate the noise frequency components. A filter can be specified in a graphic bitmap by masking and consequently eliminating the now visible and definable noise. When the inverse Fourier transformation is performed on the filtered image, the result is the original image with the noise frequencies removed.

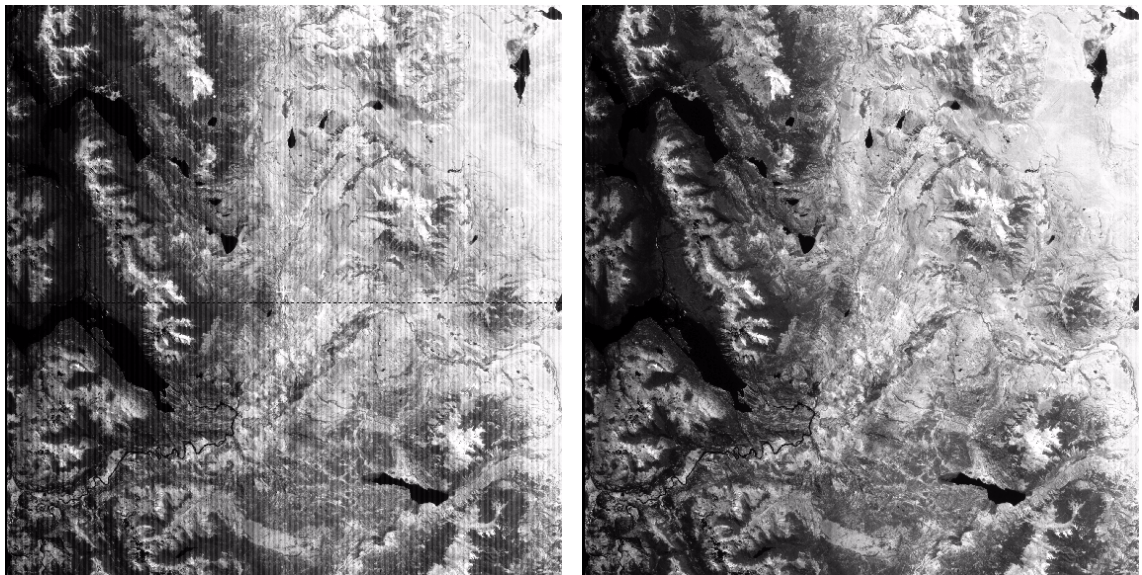


Figure 5.3 Systematic vertical banding and noise lines before (left) and after (right) Fourier filtering.

5.2.3 Landsat ETM+ Post-System Correction

All of the Landsat ETM+ bands have an adjustable gain setting, which allows the Mission Operations Center to maximize the instrument's radiometric resolution for each band without saturating the detectors. In general, acquisition of a scene in low gain allows a higher dynamic range with less risk of saturation over bright areas. Acquisition in high gain will provide better radiometric resolution or sensitivity respectively [104].

Band 4 of the raw image scene 232_89 was switched gradually from low to high gain at about image line 5058. The low and high gain areas of band 4 had to be individually converted to radiance units and afterwards the whole scene was converted to DNs with high gain settings.

The applied formula to convert DNs to radiances looks as follows:

$$L_{\lambda} = gain \cdot QCAL + offset \quad (\text{Eq. 5.2})$$

which is also expressed as:

$$L_{\lambda} = ((LMAX_{\lambda} - LMIN_{\lambda}) / (QCALmax - CALmin)) \cdot (QCAL - QCALmin) + LMIN_{\lambda} \quad (\text{Eq. 5.3})$$

where:

L_{λ} = spectral radiance at the sensors aperture in $[\text{w}/\text{m}^2 \cdot \text{sr} \cdot \mu\text{m}]$,

$gain$ = rescaled gain, contained in the Level 1 product header data record in $[\text{w}/\text{m}^2 \cdot \text{sr} \cdot \mu\text{m}]$,

$offset$ = rescaled bias, contained in the Level 1 product header data record in $[\text{w}/\text{m}^2 \cdot \text{sr} \cdot \mu\text{m}]$,

$QCAL$ = quantized calibrated pixel value in DN,

$LMIN_{\lambda}$ = spectral radiance that is scaled to $QCALMIN$ in $[\text{w}/\text{m}^2 \cdot \text{sr} \cdot \mu\text{m}]$,

$LMAX_{\lambda}$ = spectral radiance that is scaled to $QCALMAX$ in $[\text{w}/\text{m}^2 \cdot \text{sr} \cdot \mu\text{m}]$,

$QCALMIN$ = minimum quantized calibrated pixel value in DN,

$QCALMAX$ = maximum quantized calibrated pixel value in DN [105].

Table 5.1 Parameters used for gain conversion of band 4 [105].

Parameter	low gain	high gain
$QCAL$	respective pixel values in DN	respective pixel values in DN
$LMIN_{\lambda}$	- 4.5	- 4.5
$LMAX_{\lambda}$	235.0	157.5
$QCALMIN$	1	1
$QCALMAX$	255	255

Since the changes from low to high gain took place gradually an artefact in wedge-shape was generated by the correction method. This irregular artefact can only be corrected manually by converting each distinctive pixel with its correct gain setting to high gain. This correction would be very time consuming and was in this case not performed. Fig. 5.4 shows the gain changes in band 4, the corrected band and the remaining artefact after correction.

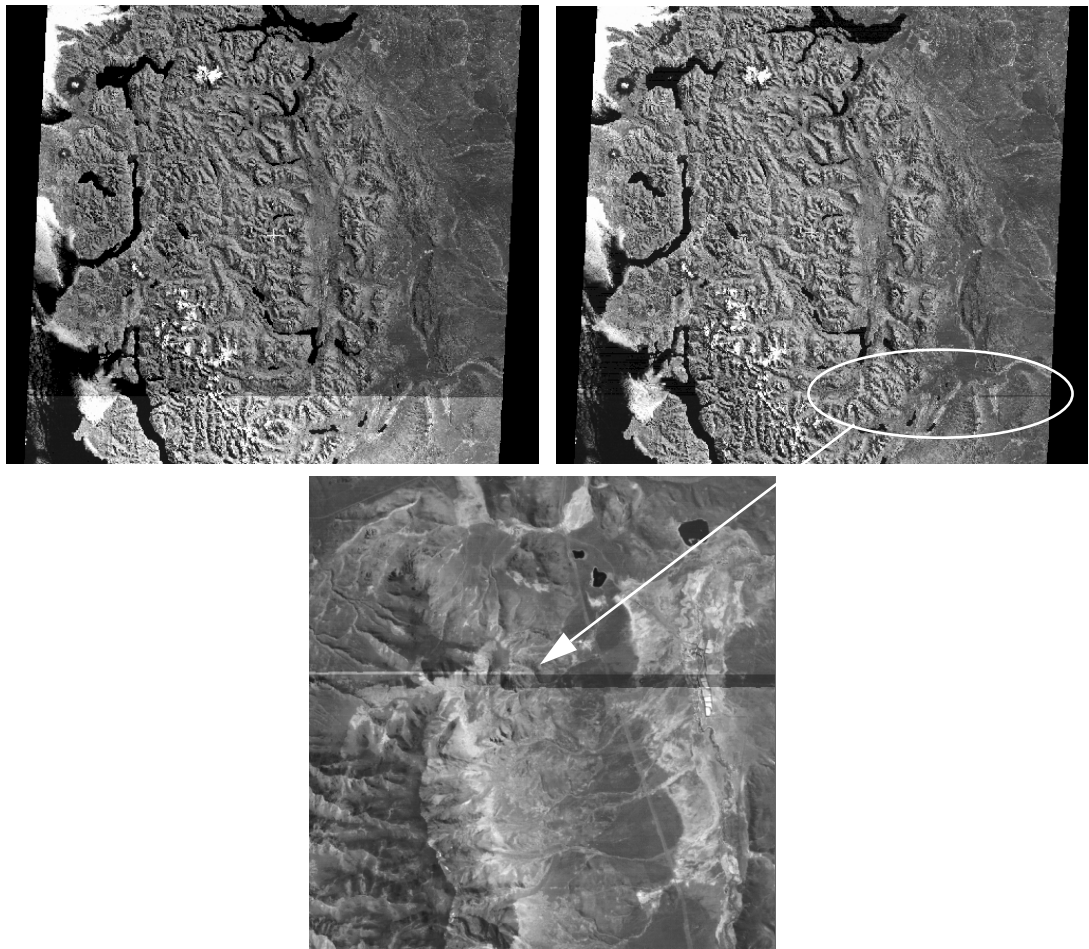


Figure 5.4 Sensor calibration differences caused by high/low gain switch during data measurement (left) and its correction (right). A wedge-shaped artefact consisting of low and high gain DN's remained in band 4 (bottom).

5.3 Digital Elevation Model Generation

A DEM provides an essential base layer for further analysis, as well as a common framework for the georeferencing and orthorectification of additional remote sensing datasets. For environmental modelling, resource management or land use classifications in mountainous regions, DEMs are essential to ensure reliable and accurate results [200]. Spectral response patterns in mountainous areas are strongly dominated by topographic effects [56]. Even more essential, the inclusion of topographic data in the classification process significantly improved forest type separability in the same ecoregion further south in Province of Chubut [112].

There are a number of production strategies to collect digital elevation data in modern scientific technologies, including manual profiling from photogrammetric stereo models, stereo model digitizing of contours, digitizing topographic contour maps, converting hypsographic and hydrographic tagged vector files and performing autocorrelation via automated photogrammetric systems. Using satellite data to produce DEM has been a recent development research topic. Efforts, based on digital matching and additional image processing techniques, have been made in digital photogrammetry to develop automatic methods for surface reconstruction [5], [4] and software packages have been developed by several companies to reconstruct the surface and

automatically generate DEMs using suitable optical remote sensing data [1]. To mention only a few: PCI Geomatica (OrthoEngine), ERDAS (OrthoBASE Pro), LH Systems/Leica (Helava/Socetset) and others.

The different processing steps to produce DEMs using stereo images can be described in broad terms as follows:

- 1) to acquire the stereo image data with supplementary information such as ephemeris and attitude data if available;
- 2) to collect GCPs to compute or refine the stereo model geometry;
- 3) to extract the elevation parallax;
- 4) to compute the 3-D cartographic coordinates using 3-D stereo intersection; and
- 5) to create and postprocess the DEM (smoothing, filtering, 3-D editing, etc.) [178].

5.3.1 Image Data & Stereo Capability

In the stereoscopic space perception, two major cues are used: the convergence and the binocular disparity. Convergence is the ability to focus the optical axes of the eyes on to a single object. The sensing of the amount of muscular tension in the eyes, as a result of different convergence angles provides a cue to the absolute distance to the viewed point. The binocular disparity (or parallax) is the disparity or the difference between the images of an object projected on to each retina. The degree of disparity between the two projected images depends on the convergence angle. The binocular disparity is considered the most important perception cue over medium distance, and is the only one used in stereo photo- or radargrammetry for quantitative elevation extraction. To obtain stereoscopy with images from satellite scanners, two solutions are possible:

- the along-track stereoscopy from the same orbit using fore and aft images
- the across-track stereoscopy from two different orbits [178].

To obtain good geometry for better stereo plotting, the intersection angle should be large in order to increase the stereo exaggeration factor, or equivalent to the observed parallax, which is used to determine the terrain elevation. One of the parameters from which the quality of a stereo pair can be judged is the base-to-height (B/H) ratio, i.e. the ratio of the distance between two satellite passes and the satellite altitude. B/H ratios of 0.6 to 1.2 are a typical value to meet the requirements of topographic mapping [114]. ASTER's VNIR subsystem consists of a nadir- and a backward-looking telescope, generating along-track stereo images with a B/H ratio of 0.6 and an intersection angle of 27.7° degrees.

With optical satellite images two types of data can be used: raw images with normalization and calibration of the detectors only, or georeferenced images, corrected for the systematic distortions due to the sensor, the platform and the Earth rotation and curvature. Raw 1A imagery is preferred by photogrammetrists for use in digital stereo-workstations because the geometry of the satellite image is preserved for highest accuracy satellite geometric modelling [179].

5.3.2 Ground Control Points Collection

Geometric modelling solutions, which have been adapted to suit the geometry of scanner imagery, employ the well-known co-linearity and co-planarity equations. With parametric modelling, few GCPs are required. In an operational environment their number will vary as a function of their accuracy and they should preferably be spread at the border of the stereo pair to avoid extrapolation in planimetry and cover the full elevation range of the terrain. Different types of GCPs can be used:

- full control points with known XYZ co-ordinates;
- altimetric points with known Z co-ordinate; and

- tie points with unknown cartographic co-ordinates.

The last two types are useful to reinforce the stereo geometry and fill in gaps where there is no XYZ-GCP. Furthermore, GCPs displayed only on one image in or outside the stereo pair can also be acquired as complementary points to the stereo GCPs. Combined with tie points they can also help to avoid extrapolation in planimetry in areas where there is no stereo GCP [178]. The final accuracy of the stereo geometry is mainly dependent on the GCPs cartographic and image co-ordinates.

5.3.3 Extracting Elevation Parallax

In digital photogrammetry elevation parallax is extracted through image matching. When working with airphotos, computer-assisted visual matching on analytical stereo-workstations is principally used, and where digital images are the basis, automated image matching is common.

Before elevation extraction, the images are resampled into an epipolar or quasi-epipolar geometry to remove the y-parallax. Any matching procedure for determining homologous points can be restricted to the rows of the images which results in smaller search space and a reduction in computation time. The two main matching techniques are area based and feature based matching. The latter is discussed more in detail.

The idea is to compare the grey level distribution of a small image patch, with its counterpart in the other image. The template is the image patch which usually remains in a fixed position in one of the images. The search window refers to the search space within which the image patches are compared with the template [162]. Image matching can be performed with several methods of which cross-correlation is considered to be the most accurate [108] and is largely used with remote sensing images [178].

Cross-correlation techniques have a long tradition for finding conjugate points in photogrammetry. The idea is to measure the similarity of the template with the matching window by computing the correlation factor. The cross-correlation factor is determined for every position r,s of the matching window within the search window. Next is to determine the position u, v , which yields the maximum correlation factor. If the search window is constrained to the epipolar line, then the correlation factors can be plotted in a graph, the maximum is found by fitting a polynomial through the correlation values [162]. With PCI Geomatics Orthoengine a mean normalized cross-correlation technique is utilized, where the zero mean sum of squared differences are used. This estimate is independent on the differences of brightness and contrast due to the normalization [74].

5.3.4 Quality Control

After the automatic extraction of digital elevation models there is always a need for postprocessing. The models may contain blunders due to mismatching or missing data. A detailed quality control is necessary to guarantee the reliability of the DEM. Postprocessing can be very crucial as for it does not only affect the quality of the DEM but also the economy of an automated approach [162]. Most software packages include standard procedures to edit and smooth digital elevation models. With PCI Geomatica's Orthoengine (Version 8.0) two filters can be applied to identify failed pixel values and their surrounding pixels.

The first filter calculates the average and variance of the eight elevation values directly surrounding each pixel, excluding failed and background pixels. If the center pixel is more than two standard deviations away from the average it is replaced with the failed value. The second filter counts the number of failed values directly surrounding each pixel. If five or more failed pixels border the center pixel, then the center pixel is also set to a failed value. The failed values are interpolated with an estimate weighted by the distance calculated from the valid pixels surrounding the failed pixels. Afterwards the DEM can be smoothed with a Gaussian filter that

calculates the weighted sum of all the pixels in a 3x3 pixel frame and assigns the value to the center pixel in the frame [138].

5.3.4.1 Semi-empirical postprocessing method

Sometimes the software-implemented postprocessing procedures are not sufficient. Medium sized artificial peaks and sinks usually remain in the DEM. In order to derive reliable products such as slope and aspect the DEMs have to be further corrected, and in this regard a semi-empirical postprocessing method is presented [45]:

With this method all pixels are masked that show an elevation difference of more than 100 m within a 5x5 sample area. The two parameters elevation difference and window size are area dependent and have to be adjusted individually. The masked areas are then buffered by 2 pixels to ensure that no outliers would later influence the morphology-dependent interpolation algorithm [20]. The input image around each pixel with the background value is searched in eight directions for the location of the two nearest encoded contour lines. Each pixel is classified morphologically as residing on a slope, a depression or a peak. The interpolation algorithm used depends on this classification. The algorithm requires that contour lines be encoded into the input image using four-connected lines, (lines are all connected by pixels in four directions, up, down, left, and right, but not along diagonals). If lines are eight-connected rather than four-connected, the algorithm might miss a contour line when searching in the diagonal directions. In order to reduce the number and severity of artefacts produced by the algorithm, a conic search is used. It searches along 22.5° cones, instead of along diagonal lines. The conic method uses previously calculated data, to provide extra smoothing, and can be used with eight-connected contour lines [139]. All DEMs are finally smoothed using a 3x3 Gaussian filter to eliminate edges at interpolated areas.

5.4 Results

5.4.1 ASTER DEM mosaic

The commercial software package PCI Geomatica (Version 8.0) was used to reconstruct the surface and calculate the DEMs. Once the GCPs were collocated in both images and the geometric model computed, they were reprojected into a quasi-epipolar projection and then the DEM was calculated. Elevation points were extracted for every second image pixel. With ASTER data this led to a final resolution of 30 m for the generated DEM.

Several attempts were made to find out what GCP distribution yielded maximum quality. The question of whether or not tie points would improve the DEM was also addressed. It was observed that tie points can sometimes have a negative impact on the DEM accuracy [45]. Nevertheless, they have been used due to the lack of GCPs in some areas of the study site. For optimal results, the GCPs should be regularly distributed all over the scene and collected at different elevations [45], [178].

Table 5.2 Residual results for the used ground control points for ASTER DEM generation. These residuals are valid for the VNIR bands 3N and 3B.

Scene	Pixel Size [m]	No. of Stereo GCPs	Mean RMSE [m]		Max. RMSE [m]		
			in x	in y	in x	in y	in z
ASTER1	15	23	6.24	7.12	15.02	14.13	21.23
ASTER2	15	29	5.58	6.74	12.48	11.09	14.44

Table 5.2 Residual results for the used ground control points for ASTER DEM generation. These residuals are valid for the VNIR bands 3N and 3B.

Scene	Pixel Size [m]	No. of Stereo GCPs	Mean RMSE [m]		Max. RMSE [m]		
			in x	in y	in x	in y	in z
ASTER3	15	41	13.35	14.25	15.24	17.12	19.41
ASTER4	15	35	14.87	14.05	20.27	22.85	21.13

For the four ASTER scenes, between 23 and 41 GCPs were used to generate the digital elevation models. Afterwards, the four single DEMs were mosaicked using Arc/Info.



Figure 5.5 Shaded mosaic of the four generated DEMs from ASTER data.

5.4.2 Postprocessing

After mosaicking a quality control of the ASTER DEM mosaic was performed. The ASTER DEM mosaic contained blunders due to mismatching and in the north of the study area a cloud had to be masked. Another phenomenon which was detected, was a systematic pattern, as seen in Fig. 5.6, which had to be removed, as well as ridges and mismatches at the borders of the four mosaicked DEMs. It is assumed that the systematic pattern is introduced during the DEM generation by the software package PCI Geomatica [64]. The ASTER DEM mosaic was finally smoothed using a 3x3 Gaussian filter to eliminate edges at interpolated areas. At last all major lakes were masked and their specific water level height inserted.

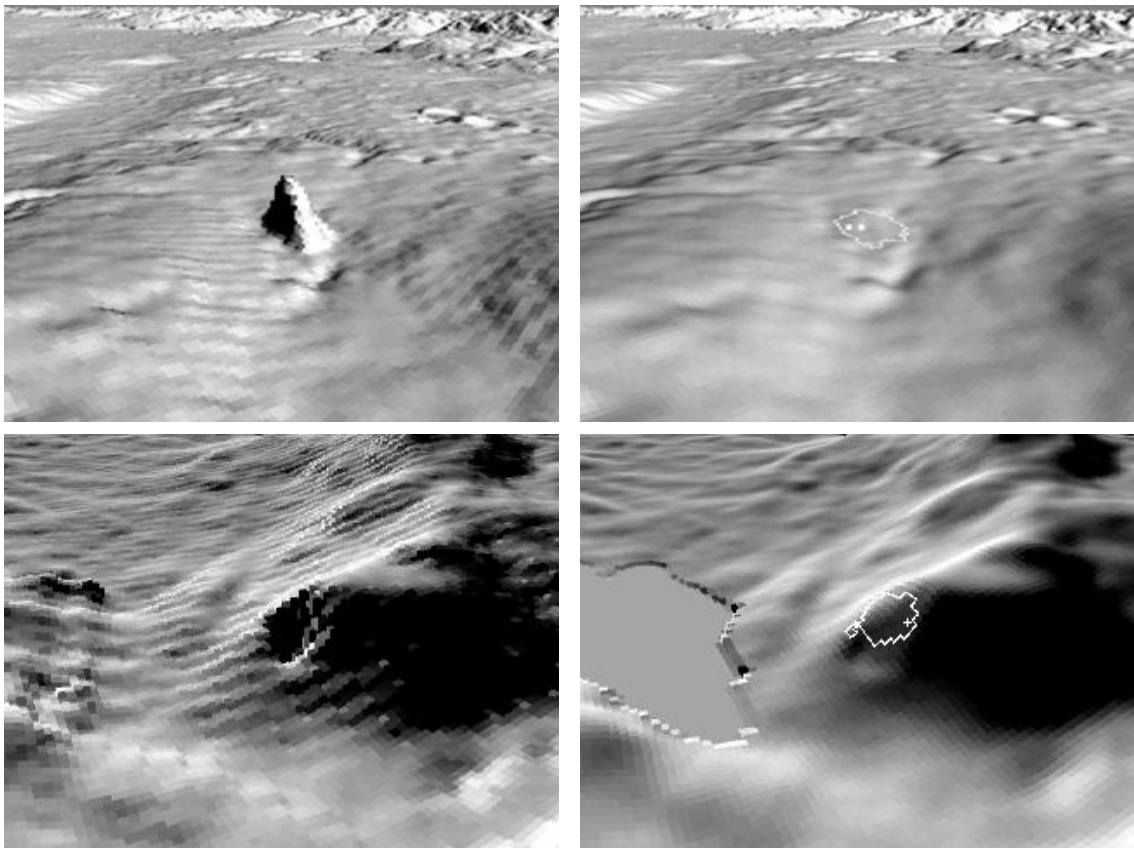


Figure 5.6 ASTER DEM before (left) and after semi-automatic postprocessing (right). Blunders are eliminated and the systematic grid pattern smoothed.

Fig. 5.6 shows that the quality could be greatly improved by applying the presented postprocessing steps to the ASTER DEM mosaic. The applied masking selects only small diameter peaks and sinks to minimize contamination of authentic peaks and sinks. Large errors are not eliminated and remain in the ASTER DEM mosaic as seen in Fig. 5.7.

Generally large errors were found in forested, shadowed or snow and ice covered areas as well as at steep cliffs and narrow valleys. Furthermore it was observed that exposition can influence the quality of a DEM due to advantageous illumination and viewing angles. In a comparable study with ASTER data it was detected that slopes with southern exposition achieved good accuracies compared to reference data of about ± 10 m [45].

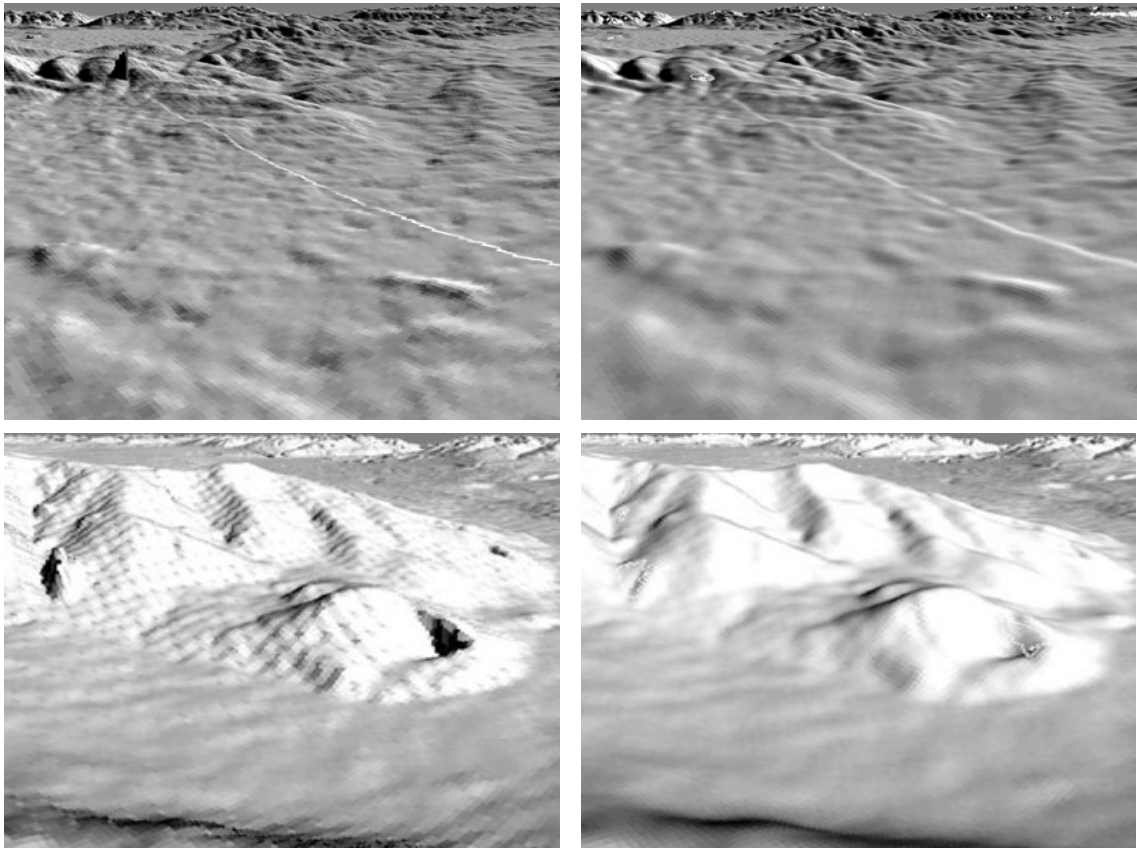


Figure 5.7 ASTER DEM before (left) and after semi-automatic postprocessing (right). The border of the mosaicked scenes is still apparent in the DEM (upper images) as well as some bigger blunders (lower images).

5.4.3 Accuracy Assessment and Validation

The accuracy was tested by comparing the generated ASTER DEM mosaic to a) the recently published and freely available Shuttle Radar Topography Mission (SRTM) C-band data and b) ten independent check points.

The SRTM is a joint project of the National Aeronautics and Space Administration (NASA), the German Aerospace Center (DLR), the U.S. National Imagery and Mapping Agency (NIMA) and the Italian Space Agency (ASI). Using C-band Spaceborne Imaging RADAR (SIR-C) and X-band Synthetic Aperture RADAR (X-SAR), SRTM collected data during a shuttle flight in February 2000. The SIR-C/X-SAR is a multifrequency, multipolarization imaging RADAR system, complemented by additional antennas located at the end of a 60 m long mast which deployed from the shuttle after reaching orbit. This configuration produced single-pass interferometry and during the mission, SRTM imaged all of the Earth's land surface between 60° N and 50° S. The C-band SRTM data is being processed into DEMs on a continent-by-continent basis. (Data from the X-band RADAR are used to create slightly higher resolution DEMs but without the global coverage of the C-band data.) It was expected that the entire world DEM based on C-band data would have been processed and available by July 2004 at a resolution of 30 m over the U.S. and 90 m over the rest of the world. The absolute horizontal and vertical accuracy is told to be 20 m and 16 m respectively. In addition, a C-band RADAR image mosaic is produced at 30 m resolution. At present the data being released is considered by NASA to be of "research quality", suitable for scientific investigations and development. The DEMs contain

significant null areas, as well as spikes and wells, that require further processing and editing before being useful to the wider community. The DEMs contain numerous voids (areas without data), water bodies do not appear flat and coastlines are ill defined [172], [173]. These errors have to be considered when interpreting the difference image, Fig. 5.8, and its statistical results, Tab. 5.3.

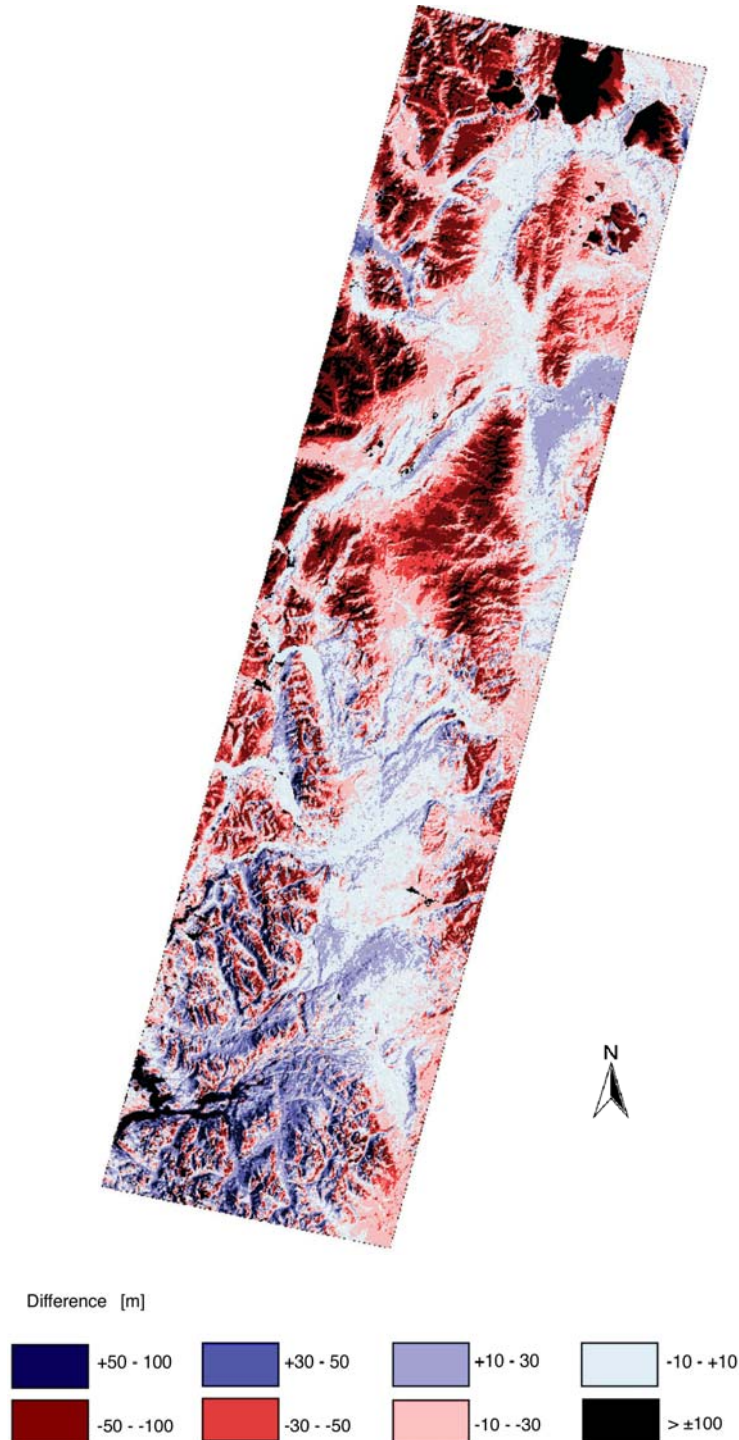


Figure 5.8 Difference image of ASTER DEM - SRTM C-band DEM. Extreme differences greater than ± 100 m are due to missing data in the SRTM DEM or cloud coverage in the ASTER DEM mosaic.

The comparison of the ASTER DEM mosaic and the reference DEM was performed by calculating the differences between the generated ASTER DEM mosaic and the SRTM C-band DEM. Errors at mountainous regions are between ± 100 m, which is considered as rather high. It can be observed that the SRTM DEM is systematically higher than the ASTER DEM, especially in the north of the study site. In the south-west of the study site exposition differences are clearly visible. Western exposed slopes defer in the range of plus 30-50 m and eastern exposed slopes defer in the range of minus 30-50 m. This effect was already observed in [45]. In the foothills of the Andes and the mainly flat steppe area the DEMs correspond well with each other, the variations are between ± 30 m.

Since both DEMs contain notable errors, a final accuracy statement of the established ASTER DEM mosaic is difficult to issue. Considering the errors in both DEMs, an overall standard deviation of 40.56 m and an RMSE of 39.48 m seems to be realistic.

Table 5.3 Statistical analysis of the difference image ASTER DEM - SRTM C-band DEM.

Parameter	[m]
Minimum	-783
Maximum	407
Standard deviation	40.56
Mean	-12.13
RMSE	39.48

Table 5.4 Geolocation and height differences between the independent check points and the ASTER DEM.

ID	Image X [m]	Image Y [m]	Image Z [m]	GPS Z [m]	Δ Height [m]
329	1574849	5257169	784.3461	798.00	-13.65
330	1554894	5247907	563.0714	554.00	9.07
332	1552056	5246936	572.1948	557.00	15.19
334	1558382	5255453	883.5342	868.00	15.53
339	1553274	5250486	792.0853	786.00	6.09
342	1528251	5227041	483.407	502.00	-18.59
344	1541079	5239024	644.9503	643.00	1.95
345	1546117	5224378	377.8704	369.00	8.87
10	1540554	5220954	350.1642	373.00	-22.84
20	1548584	5238966	574.8321	568.52	6.31

In the second validation, 14 differentially measured GPS points were compared to the heights in the ASTER DEM mosaic. The check points are all located in the foothills of the Andes and unfortunately do not represent the accuracies achieved in the steep areas of the study area. Mislocation errors of the GPS points as a result of the partially imprecise geometric correction in the mountainous western part of the research area is below a pixel size of 15 m in the foothills of the Andes and can thus be neglected. The results of the comparison are summarized in Tab. 5.4. With a mean absolute height error of 11.81 m, a RMSE of 13.29 m good accuracies were achieved in the foothills of the Andes. The maximum error amounts to 22.84 m. The quality of the ASTER DEM mosaic is considered just sufficient to do atmospheric, topographic and geometric

corrections to satellite data with resolutions of up to 15 m. Keeping in mind that no alternative DEM with a better accuracy in X-, Y- and Z-direction is currently available for the research area.

Slope and aspect may be derived to enlarge the GIS database of CIEFAP and DGBYP of the Province of Chubut.

After extracting several DEMs from ASTER data, it can be concluded that a successful automatic generation of a DEM from optical satellite imagery depends on the following main factors:

- Image source/geometric resolution,
- spectral sensitivity,
- acquisition date gap,
- base-to-height ratio (B/H-ratio),
- number of GCPs,
- horizontal and vertical GCP distribution,
- image matching technique,
- surface fitting technique,
- postprocessing methods and
- quality control.

5.5 Geometric Correction

Sensor, platform or scene-induced geometric measurement errors have to be removed in such a way that the data conform to a required projection. This process involves the creation of a new digital image by resampling the input data. Each pixel of the image is given the correct place on Earth which is known as geocoding, i.e. matching pixel coordinates with the proper Earth coordinates in the required projection.

For rectification, a rigorous model, developed by Toutin [177], was applied. It compensates distortions such as

- sensor geometry,
- satellite orbit and altitude variations,
- earth shape,
- rotation and relief.

The computed mathematical model calculates the position and orientation of the sensor at the time when the image was taken. It is based on co-linearity condition, which represents the physical law of transformation between the image space and the ground space. The model reflects the physical reality of the complete viewing geometry as well as all the distortions generated during the image formation, such as those caused by:

- the platform (position, velocity and orientation),
- the sensor (orientation, integration time and field of view),
- the earth (geoid, ellipsoid and relief),
- the cartographic projection.

As a result of this integration, the modelling equations are simple and straightforward with few unknowns. Each of the unknowns is the combination of several correlated variables of the viewing geometry, so the number of unknowns is reduced to an independent set. The equations are then solved with a few well distributed ground control coordinates.

Table 5.5 Residual results of the georectified satellite datasets. For the ASTER scenes the results of the VNIR subsystem are listed.

Scene	Pixel Size [m]	No. of GCPs	Mean RMSE [m]		Max. RMSE [m]	
			in x	in y	in x	in y
ASTER1	15	23	6.24	7.12	15.39	13.98
ASTER2	15	28	5.58	6.74	11.74	11.83
ASTER3	15	41	7.06	6.63	15.64	15.74
ASTER4	15	35	11.01	9.26	24.18	20.51
ETM+ vis 89	30	36	15.30	12.60	28.50	25.80
ETM+ pan 89	15	39	6.90	7.20	13.35	14.25
ETM+ vis/pan 90	15	76	5.72	5.27	14.87	14.05

For resampling the satellite scenes, the cubic convolution method was used. It determines the gray level from the weighted average of the 16 closest pixels to the specified input coordinates and assigns that value to the output coordinates. The resulting image is slightly sharper than the one produced by bilinear interpolation and it does not have the disjointed appearance produced by nearest neighbor interpolation.

The ASTER SWIR data obtain a geometric resolution of 30 m. For georectification the already defined GCPs for the VNIR bands were adapted. Pixel and line values were simply divided by a factor of two and then carefully checked and adjusted. The goal was to achieve a mean RMSE below 15 m to obtain conformity with the VNIR dataset. This was not always possible, particularly in the western, mountainous regions.

Table 5.6 Residual results of the georectified ASTER SWIR datasets.

Scene	Pixel Size [m]	No. of GCPs	Mean RMSE [m]		Max. RMSE [m]	
			in x	in y	in x	in y
ASTER1	30	22	17.38	7.52	30.64	20.77
ASTER2	30	33	12.88	6.06	31.61	12.53
ASTER3	30	50	11.35	9.25	30.79	19.31
ASTER4	30	47	13.47	10.73	27.65	25.26

5.6 Mosaicking

Mosaicking is the process of joining two or more independent images to form one single image. When you mosaic images, areas of overlap are stitched together resulting in *edges* in the continuous data. Two different software packages were used to mosaic the DEM and the satellite imagery due to different handling of the transition zones.

The four digital elevation model tiles were mosaicked in Arc/Info because the software offers a mosaicking algorithm suitable for digital elevation model data. The algorithm uses a weighted average method to calculate values of cells in the overlapping area, taking input from two or more input grids. The proximity analysis algorithm applied to determine cell values over the overlapping areas is called the Hermite Cubic and can be described by the following formula:

$$H_3(s) = 1 - 3s^2 + 2s^3 \quad (\text{Eq. 5.4})$$

where, s is the normalized distance (ranging values from 0 to 1) of the width of the overlapping area (it may be oriented horizontally or vertically). The cell values for the output C grid, being the mosaic of grids A and B on the overlapping area x [Fig. 5.9] are calculated according to this formula:

$$C = AH + B(1 - H) \quad (\text{Eq. 5.5})$$

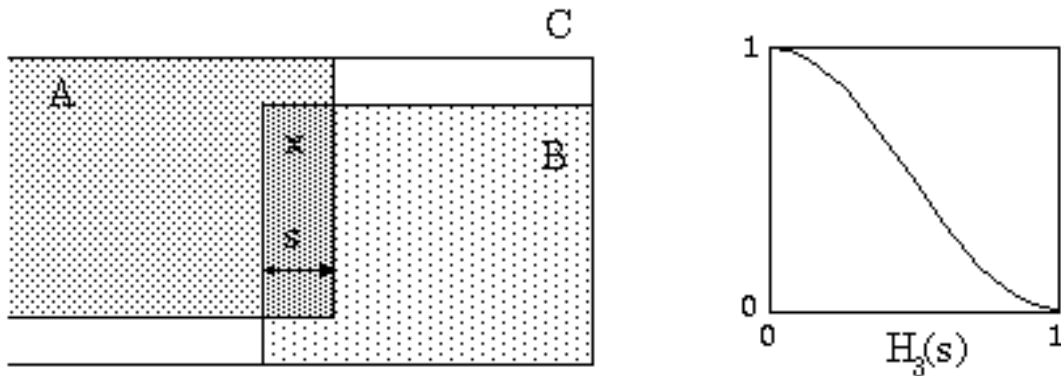


Figure 5.9 Diagram of calculation of overlap area (left) and illustration of the Hermite Cubic algorithm (right).

The diagram on the right [Fig. 5.9] shows graphically how the applied weighted average method works on the overlapping area. The ratio of weights of the overlapping grids changes within the width s of the x area [59]. The method worked well, however, the ridges are apparent [Fig. 5.7] when shading the ASTER DEM mosaic.

The ASTER and Landsat ETM+ satellite imagery were mosaicked using PCI Geomatica's Orthoengine (Version 8.0). Radiometric differences between the images at the overlap areas were balanced by generating histograms for the overlapping areas in the mosaic and then performing a least squares analysis to determine the optimum radiometry for the final mosaic. For each image a transformation was calculated before the image was added to the mosaic [139].

The mosaicking of the two Landsat ETM+ pan datasets caused some problems due to prior geocoding. At the overlap area the two scenes did not fit together geometrically, which resulted in non-fitting lake borders. The mismatch was solved as follows: first two GCP points were set at the upper left and right corners of the northern tile to fix it; the northern part itself served as reference. Then 14 GCPs were defined in the overlap area. For these points the southern part of the Landsat ETM+ tiles served as reference. The two scenes were consequently adjusted to one another by applying a 3rd order polynomial transformation. All GCPs had an RMSE below 15 m pixel size; mean RMSE in x-direction is 5.91 m and in y-direction 3.73 m.

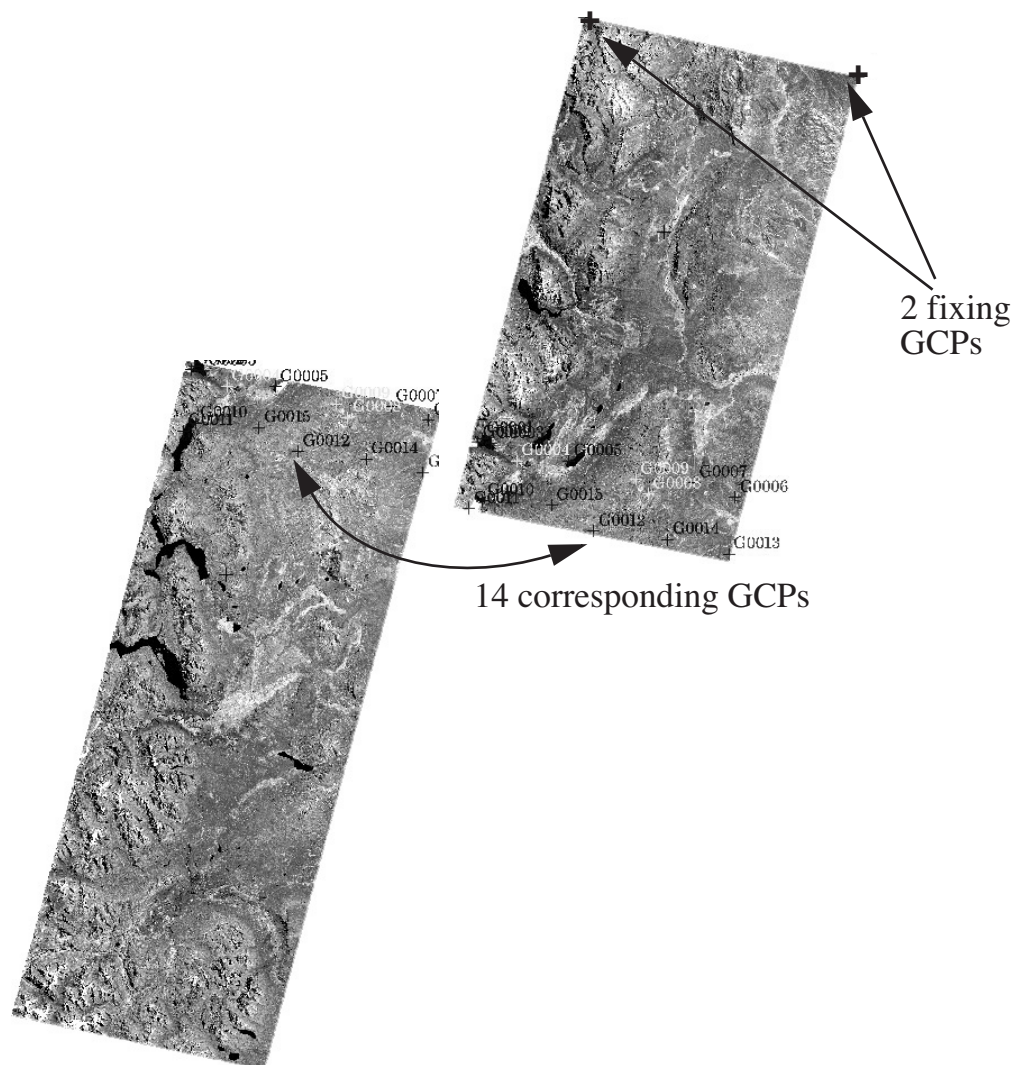


Figure 5.10 Adjusting the two Landsat ETM+ pan tiles by 3rd order polynomial transformation. Accuracy requirements for the GCPs is <15 m pixel size.

5.7 Radiometric Correction

Particular radiometric measurement errors of the sensor detectors have to be calibrated and corrected. A typical error that may affect the actual radiance measurement of a sensor is the brightness intensity variation across the image plane. For sensor data in the optical range, the data in the nadir is usually brighter than off-nadir data as a result of varying path length and BRDF (bidirectional reflectance function) effects (not considering illumination effects) and thereby reducing the contrast of the image. Another error source may result from the fact that an output signal of a particular detector cell is not exactly proportional to the brightness intensity of the input signal. All radiometric corrections are performed on the digital gray value of the pixels of an image, resulting in *calibrated gray values*.

Atmospheric correction is applied to sensor data in order to separate and eliminate the atmospheric path radiance contribution from the ground-reflected signal. Path radiance is energy that may originate from the surface outside the field of view (FOV); it is scattered into the beam

by the atmosphere. In the visible region and at shorter wavelengths, Rayleigh scattering caused by density fluctuations in atmospheric gases is the dominant contributor to path radiance. Light scattered by particles or aerosols, creates both path radiance as well as extinction.

The algorithms employed are based on model assumptions about the atmospheric state and on supplementary measurements. So far only approximate methods are available. The application of atmospheric correction to sensor data allows the comparison of different data sets of the same or different sensors, measured at different times. Though if atmospheric condition is unknown or the calibration coefficients at the acquisition date are not available or not plausible, atmospheric correction can be an element of uncertainty and introduce an error in calculating surface reflectance.

Atmospheric correction was performed after the mosaicking step to achieve a homogeneous radiometrically corrected data mosaic. In Tab. 5.7 the calibration coefficients for the ASTER- and Landsat ETM+ scenes are listed. Gain and offset values for all datasets were retrieved from the meta-files delivered together with the datasets.

Table 5.7 Applied calibration coefficients for the ASTER- and Landsat ETM+ -mosaic. Gain and offset are in [$w/m^2 \cdot sr \cdot \mu m$].

Acquisition Date Sensor	Band	Gain Mode	Gain ($c0$)	Offset (ASTER: $c0 = -c1$)
18. Jan. 2002 ASTER	1	Low 1	2.25	-2.25
	2	Low 1	1.89	-1.89
	3N/b	Low 1	1.15	-1.15
	4	High	0.1087	-0.1087
	5	High	0.0348	-0.0348
	6	High	0.0313	-0.0313
	7	High	0.0299	-0.0299
	8	High	0.0209	-0.0209
	9	High	0.0159	-0.0159
21. Feb. 2000 ETM+	1		0.7756863	-6.2
	2		0.7956863	-6.4
	3		0.6192157	-5.0
	4		0.6372549	-5.1
	5		0.1257255	-1.0
	7		0.0437255	-0.35
	pan		0.9717647	-4.7

5.7.1 ATCOR 3

The ATCOR3 approach is an extension to the model ATCOR2 with which ground reflectance and surface brightness temperature (thermal band) for a flat terrain [152], [153] can be calculated. ATCOR3 is able to handle horizontally varying optical depths and contains a statistical haze removal algorithm. A radiative transfer code is required to compute the atmospheric transmittance, direct and diffuse solar flux, and path radiance. In ATCOR3, these quantities are summarized as atmospheric correction functions and were calculated with the MODTRAN 4 code for several sensors including ASTER and Landsat ETM+. A database has been compiled for a wide range of typical atmospheric conditions. It covers terrain elevations from 0 to 2.5 km asl., values for

elevation regions above 2.5 km are obtained with extrapolation [155]. All numerical values are stored as look-up tables and account for the influence of atmospheric absorption and scattering. The main variable atmospheric parameters that affect the radiative transfer in the atmospheric window regions are water vapor content as well as the type of aerosol and the optical depth. In Tab. 5.8 the parameters taken into account are summarized.

Table 5.8 Parameters contained in the atmospheric database, stored as look-up tables [155].

Parameter	Range
Water vapor content [g/cm^2]	0.8-4.75
Aerosol type	rural, urban, maritime, desert
Visibility [km]	5-150
Ground elevation [km asl]	0 - 8.5
Solar zenith angle [$^\circ$]	0 - 70
different view and azimuth angles for tilt sensors	

Furthermore, ATCOR3 also considers radiance reflected from adjacent terrain and the range dependence of the adjacency effect caused by atmospheric scattering, and a special processing in areas of low illumination, where strong anisotropic reflectance effects may appear [154]. Fig. 5.11 shows a schematic sketch of the four radiation components taken into account in the applied atmospheric correction model. The equations for these radiation components are described in detail in [155].

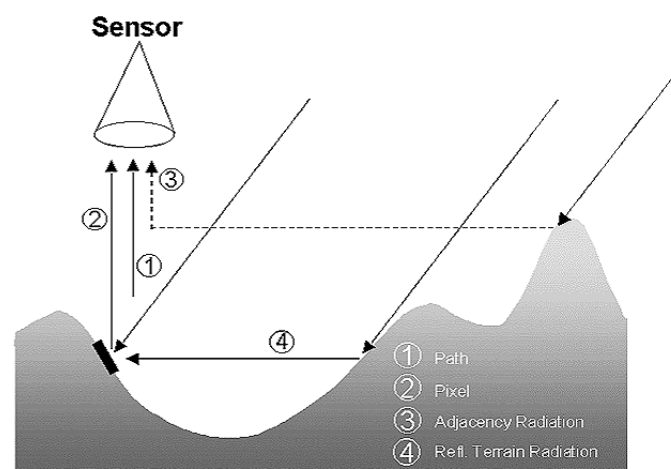


Figure 5.11 Radiation components taken in to account in the ATCOR3 model [155].

5.7.1.1 Input Parameter Determination

The choice of the atmospheric and aerosol model was determined by the geographic location of the study site and its rural character. All datasets are taken at clear sky conditions and are marginally affected by water vapor. The visibility for the radiometric corrections are based on the observations made by the only meteorological station in the study site at Esquel Airport. For the ASTER scenes a visibility of 25 km and for the Landsat ETM+ of 40 km was estimated.

The atmospheric correction of the Landsat ETM+ data resulted in negative or small reflectances in band 1. There are several possibilities for this behavior: (a) incorrect solar zenith angle, (b) inappropriate visibility, (c) inappropriate aerosol type or (d) wrong radiometric calibration coefficients. It is assumed that the radiometric calibration coefficient for band 1 is incorrect, still

it was preferred to overcome this problem by adjusting the visibility parameter to obtain a decrease of the path radiance and therefore raise the reflectance values. Visibility for the Landsat ETM+ dataset was adjusted from 40 km to 150 km. Actually, based on our own experiences and observations it is thought that the visibility estimates are too low for the research area. Its geographic location, specially its remote and rural character allow for much higher visibilities on clear and cloudless days with low air humidity.

Solar azimuth and zenith angle were calculated for the center longitude and latitude of the mosaic and a mean acquisition time for all four ASTER datasets and two Landsat ETM+ datasets respectively. The applied mosaic specific parameters are summarized in Tab. 5.9.

Table 5.9 Applied radiometric correction parameters.

Parameter	ASTER	ETM+
Atmospheric model	midlatitude summer	midlatitude summer
Aerosol model	rural	rural
Visibility [km]	25	150
Adjacency effect [km]	1.00	1.00
Solar azimuth [°]	61.4	58.9
Solar zenith [°]	35.4	46.8

5.7.2 Empirical BRDF Correction

Many surface types exhibit anisotropic reflectance behavior, i.e. the reflectance depends on the viewing and illumination geometry [102], [97], [98]. The relationship is described by the BRDF (bidirectional reflectance distribution function). An approximation of the BRDF is given by the bidirectional reflectance function BRF, also called biconical reflectance function, which is measured for finite solid angles of incoming and reflected radiation.

For high spatial resolution sensors with a small field-of-view, the solar/viewing geometry is approximately constant in a flat terrain. Therefore, the reflectance image calculated with the assumption of an isotropic (Lambert) reflectance law contains the BRDF properties for this geometry and BRDF variations for a certain cover type because geometry changes are small.

However, in mountainous terrain with slopes as large as 30°- 50° and a solar zenith angle of $\theta_s = 40^\circ$, the range of incident angles will be $\beta = 0^\circ - 90^\circ$. For this extreme range, most surface types show anisotropic reflectance properties.

For moderate incident angles $\beta < 60^\circ$, BRDF deviations from the flat case ($\beta = \theta_s$) are often less than 30%, whereas for $\beta = 70^\circ - 80^\circ$ deviations may rise to a factor of 2-6 [102], [97]. There is a further difficulty: in regions of significant slope the BRDF is no longer symmetrical about the principal plane [161] and measurements performed on a flat area do not apply. In addition, BRF measurements of tilted natural land surfaces are not available. To aggravate problems, the spatial resolution of available DEMs is often not appropriate.

The following empirical function G serves to reduce the high reflectance values in regions of extreme geometry to get reflectance values closer to those of adjacent areas with moderate incident angles. G ranges between a specified lower boundary g and 1, i.e. $g \leq G \leq 1$. Only areas of extreme incidence and/or exitance angles are involved, starting with a threshold angle β_T :

$$G = \frac{(\cos \beta_i)^{0.5}}{(\cos \beta_T)} \quad (\text{Eq. 5.6})$$

Most of the high spatial resolution sensors have view angles close to nadir, whereas the sun is usually at a greater distance from nadir. Therefore, the incident angles are more likely to enter the critical region $\beta_i = 60^\circ - 90^\circ$ and Eq. 5.6 can be applied [155].

Tab. 5.10 comprises the input parameters g and βT . They were determined by visual check of the illumination file and statistical regression analysis, which is discussed in detail in Chapter 5.7.3.

Table 5.10 Determined and applied empirical BRDF correction parameters.

Parameter	ASTER VNIR	ASTER SWIR	ETM+ vis	ETM+ pan
g	0.100	0.100	0.100	0.250
βT [°]	30	30	50	65
% modified	36.4307	35.8372	14.9503	3.59396

5.7.3 Results

Fig. 5.12 shows a subset of the ASTER DEM and the calculated derivatives slope, aspect and sky view factor. The sky view factor was computed with the horizon line algorithm employing 32 azimuth directions. Aspect and slope were calculated with the software ENVI.

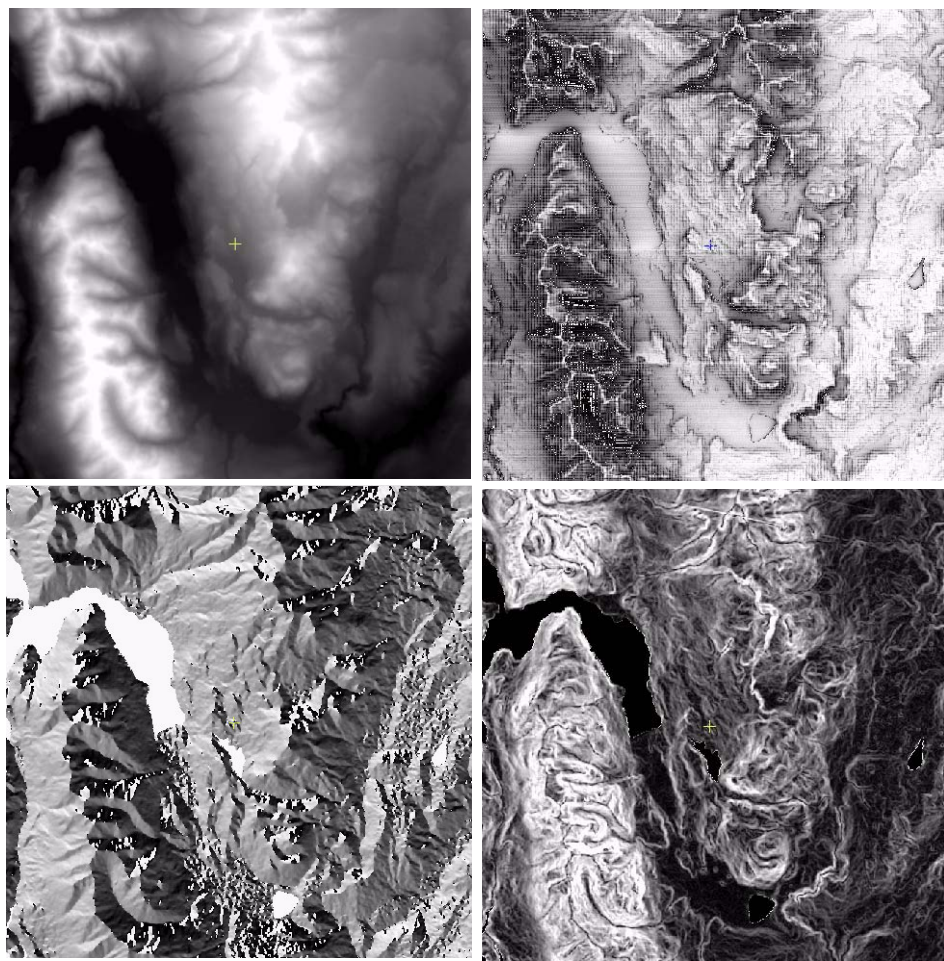


Figure 5.12 Subset of the generated ASTER DEM (top left), the derivatives aspect and slope (lower left and lower right) and sky view factor (top right).

The two right images of Fig. 5.13 show the results of the radiometric correction, including BRDF correction. After topographic correction the illumination effect is strongly reduced causing the impression of a flat terrain. A slight overcorrection of the westward oriented slopes is visible in the ASTER dataset. The tendency of overcorrection may be caused by BRDF effects and/or multiple reflection of radiation between opposite slopes. They were corrected by applying an empirical BRDF correction algorithm. The left image in Fig. 5.14 shows the result of the regression analysis of ASTER band 3 with the illumination angle $\cos\beta$ before atmospheric/topographic correction. A correlation coefficient of 0.6699 is obtained. The result of atmospheric and topographic correction was an extreme overcorrection, visible in the top middle graph of Fig. 5.14 as well as in the bottom left image of Fig. 5.15. Therefore, an empirical BRDF correction was employed with a threshold angle $\beta_T = 30^\circ$ and a lower bound of $g = 0.100$. A substantially reduced correlation coefficient of -0.2208 is obtained in this case demonstrating the successful removal of topographically induced bright patches in the dataset. The visual result of the optimized selection of β_T and g is shown in the bottom right image in Fig. 5.15. The bottom middle image shows the result for a suboptimal choice of β_T where not all effects are corrected.

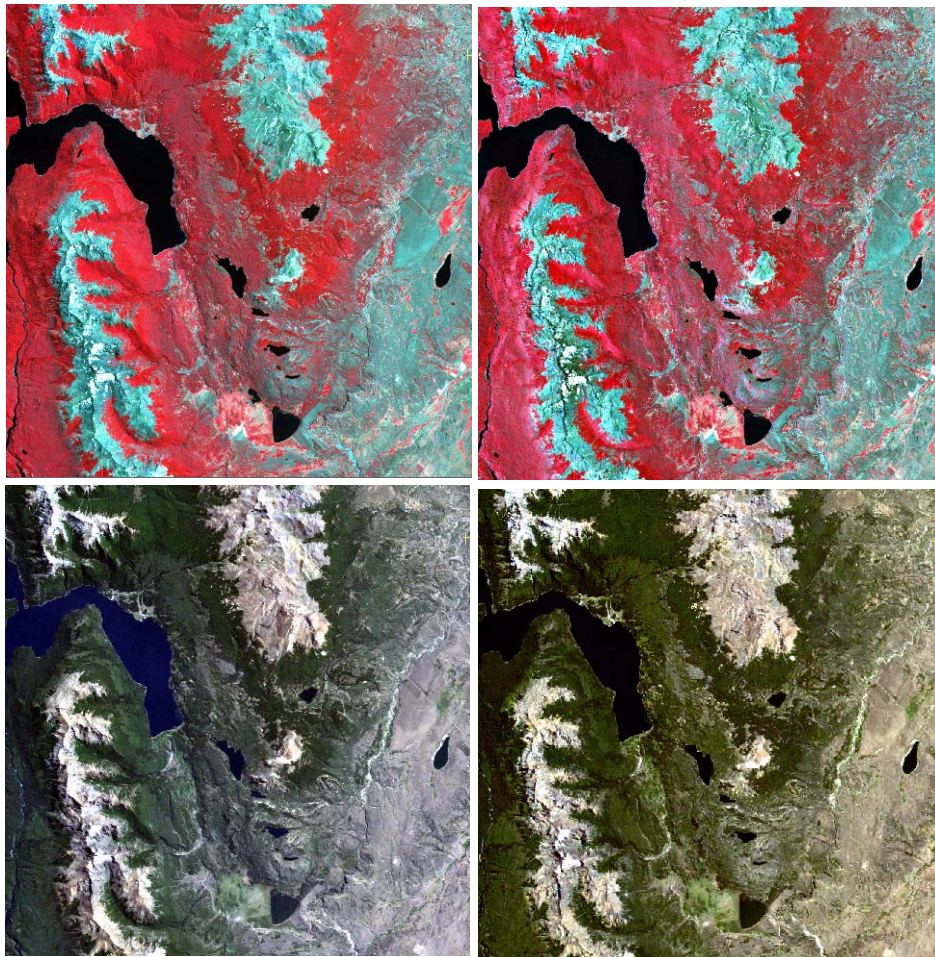


Figure 5.13 Subset of the uncorrected ASTER dataset (top left) and the atmospherically/topographically corrected ASTER dataset (bands 3, 2, 1) (top right). On the bottom left the uncorrected and on the bottom right the atmospherically/topographically corrected Landsat ETM+ dataset (bands 3, 2, 1).

As mentioned in Chapter 5.7.1.1 the atmospheric correction of the Landsat ETM+ band 1 resulted in very low reflectances. By adjusting visibility this effect was minimized, however, the

adjustment could not completely compensate the effect which results in a greenish color composite [Fig. 5.13].

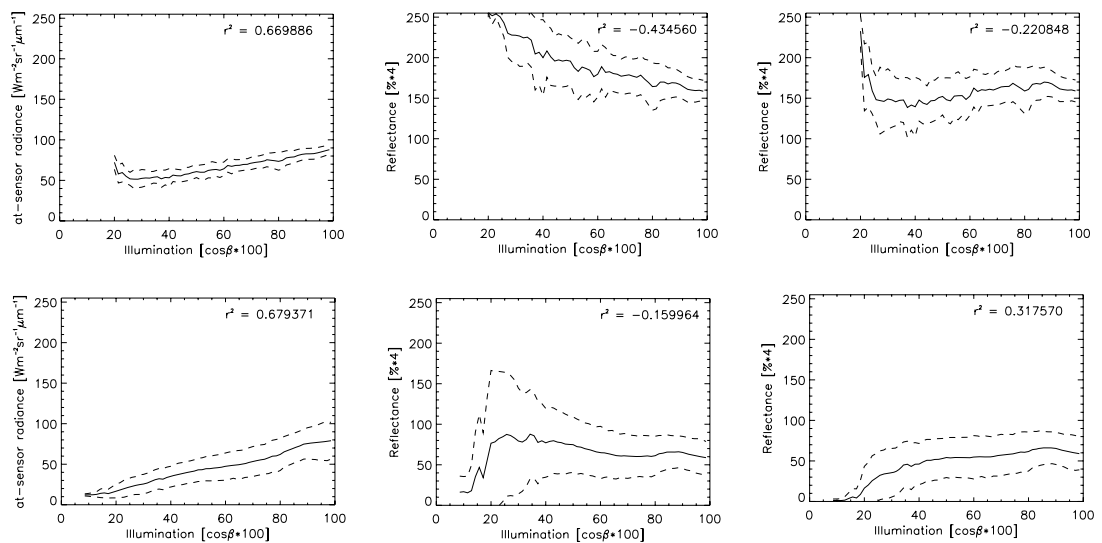


Figure 5.14 Regression analysis of illumination and at-sensor radiance before atmospheric/topographic correction (left image), illumination and reflectance after atmospheric correction but without BRDF correction (middle image), and illumination and BRDF corrected atmospherically corrected reflectance values. The graphs present the correlation of ASTER band 3 and Landsat ETM+ band 4 respectively. For both dataset two different predominantly forested subsets were chosen, see Fig. 5.15 and Fig. 5.16.

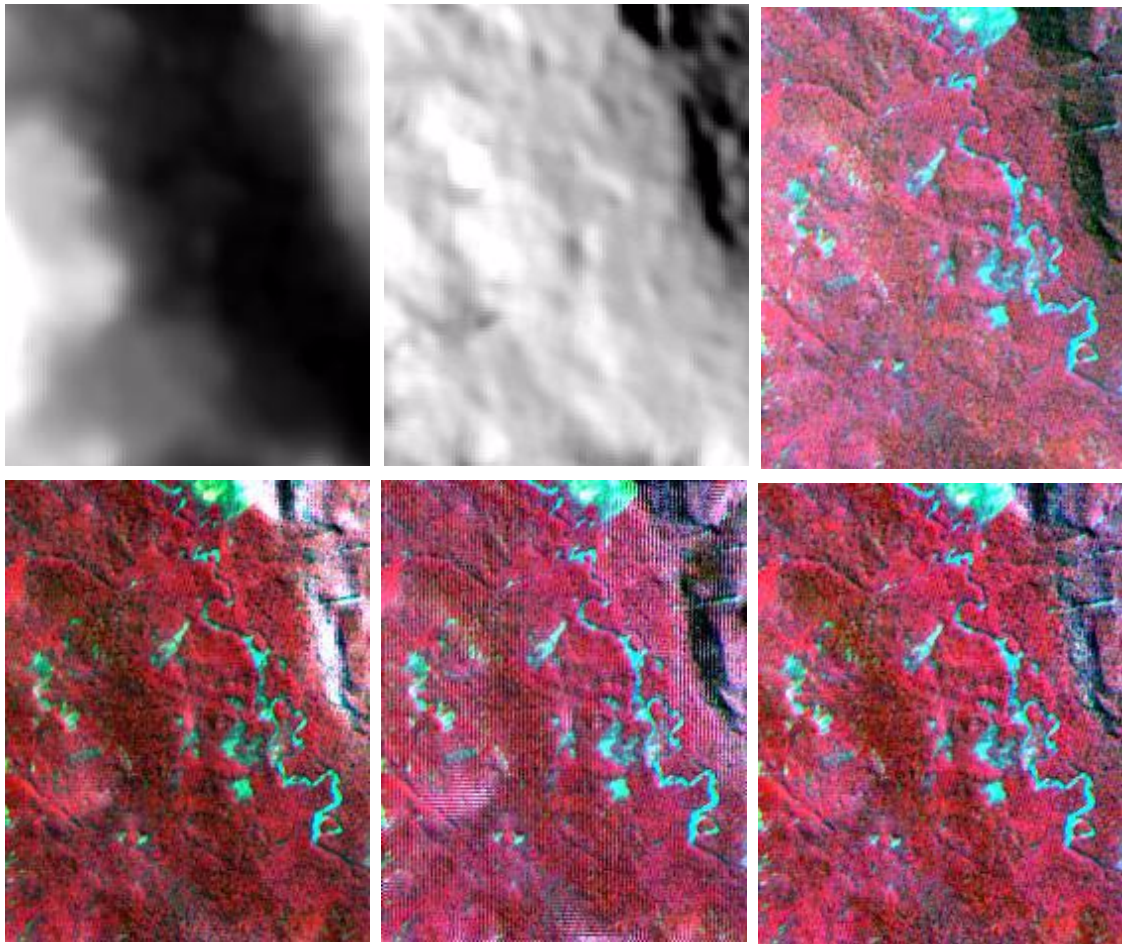


Figure 5.15 ASTER DEM (top left) and illumination (top middle) subset and at-sensor radiance dataset (top right). ASTER reflectance dataset with no BRDF correction (lower left), suboptimal BRDF correction threshold angle 50° (lower middle) and optimized threshold angle of 30° (lower right image).

After performing radiometric correction to the at-sensor radiances dataset of Landsat ETM+, the effect of overcorrection was less apparent compared to the ASTER dataset. Still the empirical BRDF correction was applied to minimize the negative correlation of reflectances with illumination which is apparent in the lower middle image of Fig. 5.14, and to eliminate some bright patches appearing at $\beta T > 50^\circ$ as shown in Fig. 5.16 in the bottom left image. Applying BRDF correction lead to an equalization of reflectance values in all illumination angle ranges, with slightly lower values for small angles. The effect of bright patches could be reduced, as shown in the bottom right image in Fig. 5.16. They now contained reflectance values closer to those of neighboring areas.

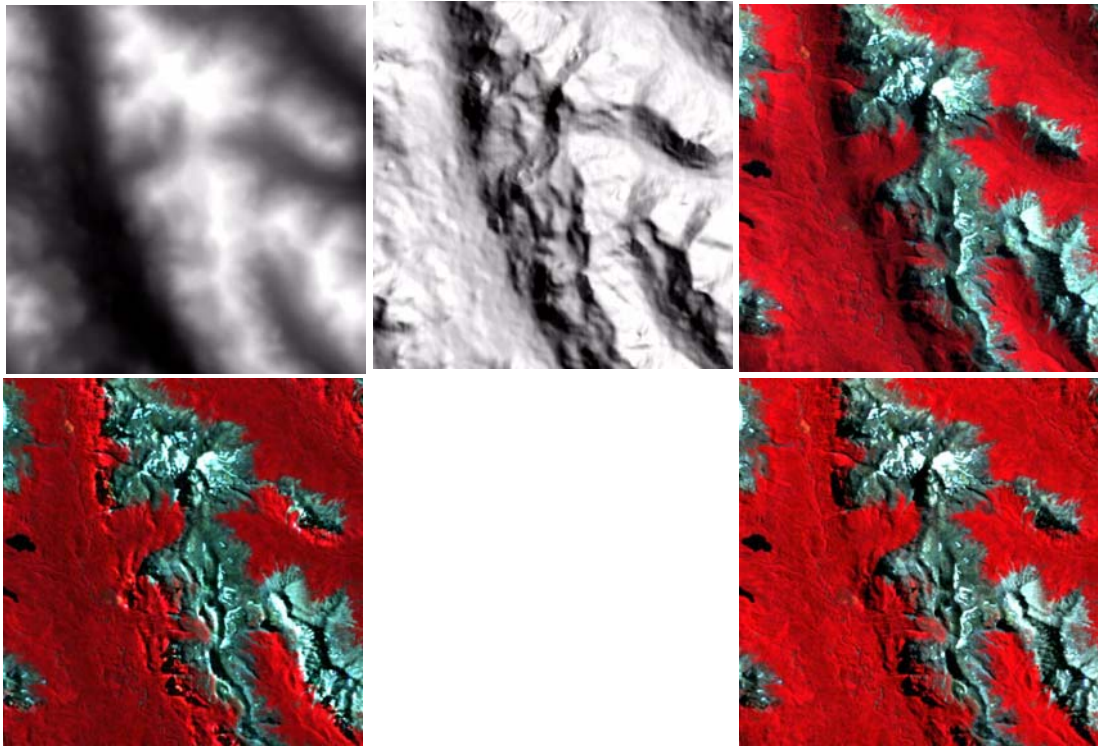


Figure 5.16 ASTER DEM (top left) and illumination (top middle) subset and at-sensor radiance dataset (top right) of Landsat ETM+. Landsat ETM+ reflectance dataset with no BRDF correction (lower left) and optimized threshold angle of 50° (lower right image).

5.8 Discussion

All datasets were first successfully system and/or post-system corrected. Damaged lines and a non-systematic banding in the ASTER datasets were eliminated. One Landsat ETM+ scene contained in band 4 a gain switch, which resulted in a wedge-shaped irregular artefact. It was corrected partially.

Digital elevation model extraction from ASTER data was successfully performed. It was observed that GCP distribution can highly influence the stability of the model and thus accuracy and quality of the DEM. The developed semi-empirical post-processing method improved the quality substantially. Post-processing is an important step in digital elevation model generation and should not be neglected. Nevertheless, most large blunders remained, either due to the stereo data (exposition, illumination and viewing angle) or due to unstable stereo modelling or matching failure. These errors indicate that the automatic surface reconstruction techniques used in OrthoEngine still exhibit weak performance in certain coverages and fail in finding the corresponding pixels on the stereo images: errors appear in forested, snow covered, and shady areas since all are spectrally homogeneous. Preprocessing the stereo images, e.g. with a filter, could improve the quality of the resulting DEMs. Other difficulties became apparent at steep cliffs and deep river valleys or creeks. A solution would be to pre-classify shaded areas and exclude them from matching, and either interpolate them or substitute for those missing values using other sources. Another effect is the growth of the error with increasing slope [45], which is related to the effects of bidirectional reflectance. Correcting these two effects on ASTER stereo images before ultimate DEM generation would improve matching performance and therefore elevation accuracy.

The nature of the stereo images themselves is a limiting factor to accuracy. The completely different perspectives of the two images, which actually makes the extraction of the parallax possible, also have a large inherent disadvantage. "Backside" slopes of ridges tend to completely disappear in certain perspectives. This results in a lack of corresponding pixels in one of the stereo pair images and the difference in imaging geometries can lead to a mismatching of non-corresponding pixels.

Geometric correction based on a rigorous model was applied successfully. The goal was to achieve a maximum RMSE below 15 m to obtain conformity within all satellite data. This was possible for all areas except for the mountainous western regions of the study area, where a maximum RMSE of about 30 m was achieved. All datasets were resampled to 15 m pixel size by applying the cubic convolution method, afterwards all satellite scenes were successfully mosaicked.

The most critical point for the radiometric correction is the spatial resolution of the DEM [67], the calculation of slope and aspect from digital terrain data [21] and bidirectional reflectance effects. The last item is to some degree coupled to the DEM accuracy. Artefacts might arise when the DEM resolution is coarser than the resolution of the imaging satellite sensor [155]. It would be desirable to have a spatial resolution of the DEM of at least four times better than the pixel size of the satellite data [67], which is for most areas of the world not available. ATCOR3 uses a number of simplifications to achieve the objective of fast image processing for the correction of radiometric effects over rugged terrain. Radiance contributions reflected from neighboring terrain are included with a simple spatial average and the BRDF correction method is based on empirical test series [155]. Hence radiometric correction is sensor and scene specific and intermediate and final results have to be validated visually and statistically. Evaluating the ASTER and Landsat ETM+ dataset individually, visually and statistically, acceptable results, considering the following analysis were achieved for the ASTER dataset. However, some north-eastern exposed slopes in the south-west of the ASTER mosaic were overcorrected.

The radiometric correction of the Landsat ETM+ dataset caused some problems. After radiometric correction reflectances in band 1 were negative or very low. A well known problem with Landsat ETM+ data. Although it is assumed that the radiometric calibration coefficients provided by USGS are most probably incorrect, it was decided that it was more plausible to adjust the visibility input parameter for the Landsat ETM+ scene rather than the provided calibration coefficients, which finally lead to positive and well distributed reflectances for all bands.

After the radiometric correction Landsat ETM+ reflectances are lower for the bands 1 to 4 compared to the respective ASTER reflectances, also for presumably stable objects such as dark objects or water bodies. Reasons could be differences between the sensor calibration and calibration coefficients or the applied atmospheric input parameters and the actual atmospheric conditions at the acquisition time. But without any reference reflectance measurements taken at both acquisition dates it is difficult to judge the two corrected dataset results. However, in many projects these kind of measurements are not available.

However, as long as investigations on both datasets are based on single ratio calculations, such as vegetation indices or on monotemporal classification analysis, the varying reflectance behaviors have no negative consequences on the results. For multitemporal analysis, however, these datasets must be handled with care. In order to improve radiometric preprocessing and achieve an absolute radiometric correction ground reference reflectance measurements should be collected in the research area.

Object-oriented Classification

6.1 Introduction

The basic processing units of object-oriented image analysis are segments, so-called image objects, and not single pixels. Advantages of object-oriented analysis are meaningful statistic and texture calculation, an increased uncorrelated feature space using shape (e.g. length, number of edges, etc.) and topological features (neighbor, super-object, etc.), and the close relation between real-world objects and image objects. This relation improves the value of the final classification and cannot be fulfilled by common, pixel-based approaches. Since at least two decades, processing power of affordable computers allows image processing and image segmentation. Therefore, these methods have become applicable for operational remote sensing image analysis [10]. First major advantages in this area were derived in studies for sea-ice analysis [38], object-oriented agricultural land use classification [126], object-oriented image matching [72] and certain approaches for data compaction [63].

The first general object-oriented image analysis software on the market was eCognition [184]. This software product was produced by Definiens¹⁾. Although eCognition is, of course, a specific combination of different contributing procedures, there are some basic characteristics of the underlying object-oriented approach which are independent of the particular methods. The network of these image objects is directly connected to the representation of image information by means of objects. Whereas the topological relation of single, adjacent pixels is given implicitly by the raster, the topology and interaction of adjacent image objects must be explicitly worked out in order to address neighbor objects. In consequence, the resulting topological network has a big advantage, as it allows the efficient propagation of many different kinds of relational information [10].

In many cases a complete classification task consists of subtasks which have to operate on objects of different sizes. This multi-scale analysis is possible with eCognition. The system allows representation of image information in different scales simultaneously by different object layers [10].

It is achieved by a hierarchical network of image objects. Besides its neighbors, each object also knows its sub-objects and super-objects in such a strict hierarchical structure. This allows a precise analysis of the substructures of a specific region and the shape of super-objects can be changed based on sub-objects.

For successful information extraction, an iterative application of segmentation and classification is applied.

¹⁾ Definiens Imaging GmbH, Trappentreustrasse 1, 80339 Munich, Germany.

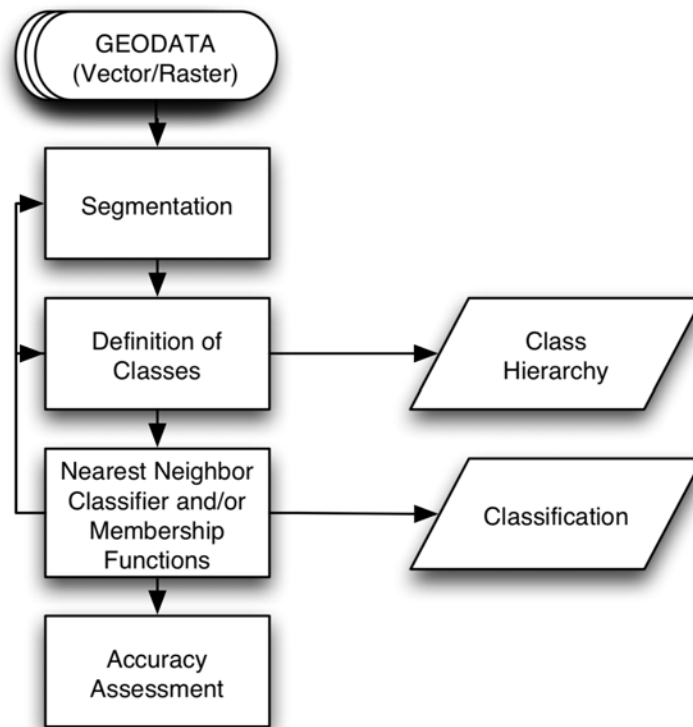


Figure 6.1 Workflow of an eCognition classification project.

Initial segmentation relies on low-level information, e.g. the pixel values and basic features of the intermediate image objects. The initial (multi-scale) segmentation provides image object primitives with a certain spectral behavior, shape and context. These object features enable a preliminary classification. Subsequently, the classification result can be used as high-level input for segmentation, a so-called classification-based segmentation. Typically, objects of interest are extracted by these iterative loops of classification and processing. Thereby, image objects as processing units can continuously change their shape, classification and mutual relations. This circular processing results in a sequence of intermediate states, with an increasing differentiation of classification and an increasing abstraction of the original image information [10]. In each step of abstraction, new information is extracted and knowledge generated and can be beneficially used for the next analysis step. It is interesting that the result of such a circular process is by far not only a spatial aggregation of pixels to image regions, but also a spatial and semantic structuring of the image content. Whereas the first steps are more data driven, more and more knowledge and semantic differentiation can be applied in later steps. The resulting network of classified image objects can be seen as a spatial, semantic network. The image analysis, based on a hierarchical object network, leads from mainly data-driven analysis to scene understanding [10].

6.2 The eCognition Approach

6.2.1 Knowledge-based image interpretation

The design of successful image analysis systems requires knowledge about the underlying problem solving processes. The better the knowledge about the process and the better this knowledge can be represented in the system, the more useful the extracted information will be [10].

Main requirements of the information extraction process in a state-of-the-art image analysis system are:

- Understanding of the sensor characteristics,
- understanding of appropriate analysis scales and their combination,
- identification of typical context and hierarchical dependencies,
- consideration of the inherent uncertainties of the whole information extraction system, starting with the sensor, up to fuzzy concepts for the requested information [10].

The choice of the appropriate scales and their combination as well as understanding object context and hierarchical dependencies are two crucial factors in determining successful image analysis. They are discussed in detail in Chapter 6.2.1.1 (scale) and Chapter 6.2.1.2 (image semantics and hierarchical dependencies).

6.2.1.1 Scale

Scale is a crucial aspect of image understanding. Although in the domain of remote sensing a certain scale is always presumed based on pixel resolution, the objects of interest often have their own inherent scale. Scale determines the occurrence or absence of a certain object class. The same type of objects appears differently at different scales [10].

Vice versa, the classification task and the respective objects of interest directly determine a particular scale of interest. There is an important difference between scale and resolution: as resolution commonly expresses the average area dimensions a pixel covers on the ground, scale describes the magnitude or the level of aggregation (and abstraction) on which a certain phenomenon can be described [10].

6.2.1.2 Image Semantics & Hierarchical Dependencies

One of the most important aspects of understanding imagery, is information about image context. In human perception, processing of context information is in most cases consciously or subconsciously present and contributes essentially to the great capabilities of humans in image analysis [10].

In order to receive meaningful context information, image regions of appropriate scale must be brought into relation and thus allows for handling image semantics. It results in a knowledge-based, hierarchical image object network. Establishing such a network requires profound understanding of relations between objects on different levels of scale, such as the reality, intermediate scales and on image scale. The more object specific characteristics and relations on the established level of scales are known, the more robust a classification rule can be established.

6.2.2 Segmentation

Objects are created by image segmentation, which is the subdivision of an image into separate regions. Image segmentation is a long lasting research topic in the area of image analysis [158], [122], [123], [137].

In eCognition, the segmentation approach adopted is multiresolution segmentation, which is a bottom up region-growing technique starting with one-pixel objects. In numerous subsequent

steps, smaller image objects are merged into bigger ones. Throughout this pairwise clustering process, the underlying optimisation procedure minimizes the weighted heterogeneity of resulting image objects. In each step, that pair of adjacent image objects is merged which stands for the smallest growth of the defined heterogeneity. If the smallest growth exceeds the threshold defined by the scale parameter, the process stops. In doing so, multiresolution segmentation is a local optimization procedure.

The procedure simulates the simultaneous growth of segments over a scene in each step to achieve adjacent image objects of similar size and thus of comparable scale. Thus, the procedure starts at seed points in the image with one-pixel objects. A treatment sequence, based on a binary counter, guarantees a regular spatial distribution of treated objects. However, such a sequence leads to slightly varying results dependent on the history of treated pixels and objects [10].

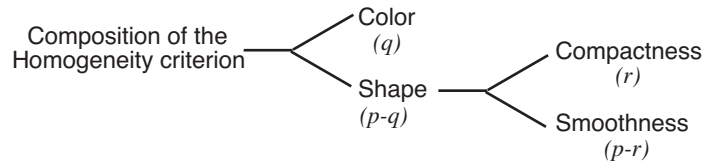


Figure 6.2 Overview of the multiresolution segmentation criteria in eCognition.

6.2.2.1 Definition of Heterogeneity

Heterogeneity in eCognition considers as primary object features color c and shape s . The increase of heterogeneity f has to be less than a certain threshold.

$$f = w_c \cdot \Delta h_c + w_s \cdot \Delta h_s, w_c \in [0,1], w_s \in [0,1], w_c + w_s = 1 \quad (\text{Eq. 6.1})$$

The weight parameters w_c, w_s allow adapting the heterogeneity definition to the application. The spectral heterogeneity (color) allows multi-variant segmentation by adding a weight w_b to the image bands b_x . Difference in spectral heterogeneity Δh_c is defined as following:

$$\Delta h_c = \sum_c WC((n_m \cdot \sigma_{cm}) - (n_{o1} \cdot \sigma_{co1} + n_{o2} \cdot \sigma_{co2})) \quad (\text{Eq. 6.2})$$

with n_m number of pixels within merged objects, n_{o1} number of pixels in object 1, n_{o2} number of pixels in object 2, σ_c standard deviation within object of band b_x . Subscripts merge refer to the merged object, object 1 and object 2 prior to merge, respectively.

The shape heterogeneity Δh_s (shape) is a value that describes the improvement of the shape with regard to smoothness (*smooth*) and compactness (*com*) of an object's shape.

$$\Delta h_s = w_{com} \cdot \Delta h_{com} + w_{smooth} \cdot \Delta h_{smooth} \quad (\text{Eq. 6.3})$$

with

$$\Delta h_{smooth} = n_m \cdot \frac{l_m}{b_m} - (n_{o1} \cdot \frac{l_{o1}}{b_{o1}} + n_{o2} \cdot \frac{l_{o2}}{b_{o2}}) \quad (\text{Eq. 6.4})$$

$$\Delta h_{com} = n_m \cdot \frac{l_m}{\sqrt{n_m}} - \left(n_{o1} \cdot \frac{l_{o1}}{\sqrt{n_{o1}}} + n_{o2} \cdot \frac{l_{o2}}{\sqrt{n_{o2}}} \right) \quad (\text{Eq. 6.5})$$

l is perimeter of object, b is perimeter of object's bounding box.

Thus, the smoothness heterogeneity equals the ratio of the de facto border length l and the border length b given by the bounding box of an image object parallel to the raster.

The compactness heterogeneity equals the ratio of de facto border length l and the square root of the number of pixels forming this image object.

The weights w_c , w_s , w_{smooth} , w_{com} are parameters, which can be selected in order to get suitable segmentation results for a certain image data stack and a considered application.

The scale parameter is the stop criterion for the optimization process. Prior to the fusion of two adjacent objects, the resulting increase of heterogeneity f is calculated. If this increase exceeds a threshold t determined by the scale parameter, $t = \Psi$ (scale parameter), then no further fusion takes place and the segmentation stops [10].

The result of automatic segmentation has to be validated by the expert and adjusted depending on the classification task. A successful classification or rather discrimination of meaningful object, possibly implying image semantics, depends highly on the establishment of a reasonable hierarchical image object network based on expedient levels of segmentation.

6.2.3 Hierarchical Object Network

All segmentation procedures provided by eCognition operate on arbitrary levels in a strong hierarchical network. Since the level of pixels and the level of the whole image always exist by definition, each segmentation of a new level is a construction in between a lower and an upper level. To guarantee a definite hierarchy over the spatial shape of all objects the segmentation procedures follow some important rules:

- Object borders must follow borders of objects on the next lower level.
- Segmentation is constrained by the border of the object on the next upper level.
- Structures of different scales can be represented simultaneously and thus classified in relation to each other.
- Different hierarchical levels can be segmented based on different data information. Thus different data types can be analyzed in relation to each other.
- Object shape correction based on regrouping of sub-objects is possible [10].

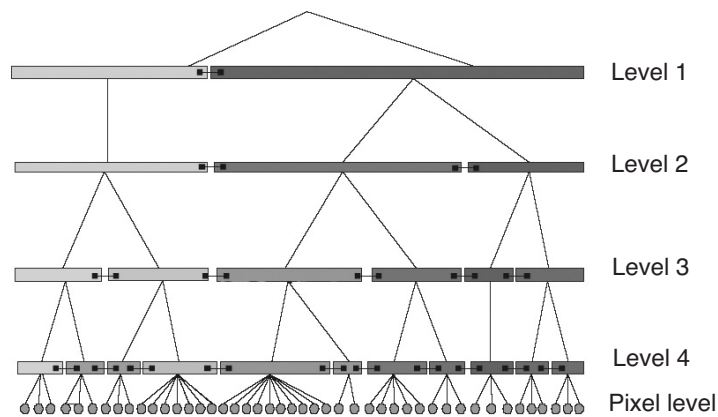


Figure 6.3 Scheme of a hierarchical network of classified image objects on different segmentation levels ([184], (modified)).

6.2.4 Classification in eCognition

Classification is the process of connecting the classes in a class hierarchy with the image objects in a scene. After the process of classification, each image object is assigned to a certain class, or remains unclassified, and thus connected with the class hierarchy. With the assignment of a class to an image object, the relations to other classes formulated in the specific class description are transferred to the image object. The result of the classification is a network of classified image objects with concrete attributes, concrete relations to each other and concrete relations to the classes in the class hierarchy [184].

For the classification of the segments, two types of nearest neighbor expressions can be used in eCognition: the nearest neighbor (NN) and the standard nearest neighbor (Std. NN) expression. The NN expression and its feature space can be individually adjusted to classes, membership functions introduced and fuzzy rules applied, whereas the Std. NN expression works with a defined feature space for selected classes. Actually the denomination "nearest neighbor" can be misleading since classes are assigned to image objects based on minimum distance measurements as typically does a minimum distance classifier. In Chapter 6.2.4.1 fuzzy classification in eCognition is discussed in detail.

The fuzzy realization of the nearest neighbor approach used in eCognition automatically generates multidimensional membership functions. They are suitable for covering relations in high-dimensional feature space. The nearest neighbor classifies image objects in a given feature space and with given samples for the class of concern. The principle for the nearest neighbor is to declare a representative set of sample objects for each class. Then the algorithm starts to search for the closest object in the feature space for each image object.

In comparison to pixel-based training, the object-based approach of the nearest neighbor requires fewer training samples. One representative sample can already cover many typical pixel samples and their variations [184].

6.2.4.1 Fuzzy Classification

Fuzzy classification consists of an n -dimensional tuple of membership degrees, which describes the degree of class assignment μ of the considered object obj to the n considered classes.

$$f_{class,obj} = [\mu_{class_1}(obj), \dots, \mu_{class_n}(obj)] \quad (\text{Eq. 6.6})$$

Crisp classification would only give the information of which membership degree is the highest, whereas this tuple contains all information about the overall reliability, stability and class mixture.

Fuzzy classification requires a complete fuzzy system, consisting of fuzzification of input variables resulting in fuzzy sets, fuzzy logic combinations of these fuzzy sets and defuzzification of the fuzzy classification result to get the common crisp classification for map production.

Fuzzy logic is a multi-valued logic quantifying uncertain statements. The basic idea is to replace the two boolean logical statements *true* and *false* by the continuous range of $[0, \dots, 1]$, where 0 means *false* and 1 means *true* and all values between 0 and 1 represent a transition between true and false. Avoiding arbitrary sharp thresholds, fuzzy logic is able to approximate real world in its complexity much better than the simplifying boolean systems do. Fuzzy logic can model imprecise human thinking and can represent linguistic rules.

Hence, fuzzy classification systems are well suited to handle most sources of vagueness in remote sensing information extraction. The mentioned parameter and model uncertainties are considered by fuzzy sets, which are defined by membership functions. An example describing a membership function describing the plausibility of the tree type *Nire* subject to height *asl* is

illustrated in Fig. 6.4. To obtain a wider area of high stability the standard shape of the parabolic shaped membership function was manually adjusted (see circles). This was done for most applied parabolic shaped memberships, since the default shaped parabola allocates only a narrow area with high stability to a class, which first, does not represent the memberships of the defined classes well and second, leads to a destabilisation of the classification rule.

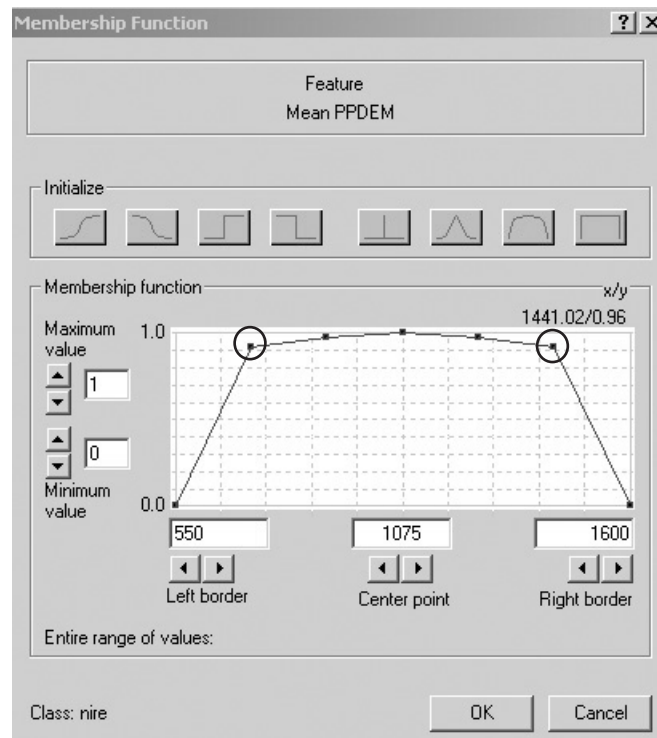


Figure 6.4 Membership function describing the plausibility of object class Ñire subject to height asl [m]. To obtain a wider area of high stability the parable shaped membership function was adjusted (circles)

For successful classification a deliberate choice and parameterization of the membership function is crucial. The function has to model the underlying relation between object features and classification as good as possible. The design is one of the most important steps to introduce expert knowledge into the system. Therefore, the better the knowledge about the real system is modelled by the membership functions, the better the final classification result [26].

It is possible to define more than one fuzzy set on one feature, e.g., to define the fuzzy sets low, medium and high for one object feature. The more the memberships overlap, the more objects are common in the fuzzy sets and the more vague the final classification. And - the higher the membership degree for the most possible class, the more reliable is the assignment.

Equal membership degrees of an object to several classes indicate an unstable classification. Within the resolution cell, and based on the provided class definition, the classes cannot be distinguished. If the membership value is high and the system is well designed, this result indicates a class mixture within the resolution cell. If the membership value is low, the assignment is unreliable and the object will be flagged for quality assurance in subsequent processing steps. A threshold for the required membership degree is defined and if this threshold is not reached, the object remains *unclassified*.

The possibility of a fuzzy classification provides important input for classification validation and, in particular, for information fusion in current and future remote sensing systems dealing with multi-sensor sources and ancillary data. The reliability of class assignments for each sensor for

instance can be elicited to find the best class assignment.

To produce results like maps for standard land cover and land use applications, the fuzzy results have to be translated back to a crisp value. To this end, the maximum membership degree of the fuzzy classification is used as crisp class assignment [10].

6.2.4.2 Nearest Neighbor Classifier vs. Membership Function

With membership function, the rule base development to form multidimensional dependencies is very clear and an adaptation is easily possible. However, if one combines one-dimensional membership functions, the form of the resulting multi-dimensional membership functions is restricted and often does not match the necessary class description closely enough. Therefore, if a class can be separated from other classes by just a few features or only one feature, the application of membership functions is recommended otherwise the nearest neighbor classifier is suggested [184].

Fig. 6.5 shows that the factual distribution of class A and B do not overlap. However, note that the membership functions describing the class A create an overlap with the membership function describing the class B. The area of these overlaps in the feature space increases with its number of dimensions. When using two features to describe the classes A and B, the areas defined by the range of one dimensional membership functions produce an enormous overlap. This overlap can be reduced if multidimensional membership functions are directly designed. Thus the actual distribution of class B can be approximated much better. The application of a nearest neighbor to define these multidimensional membership functions is advisable if several object features are to be used to describe a class. The reasons are:

- NN evaluates the correlation between object features favorably.
- Overlaps in the feature space increase with its dimension and can be handled much easier with NN.
- NN allows very fast and easy handling of the class hierarchy for the classification (without class-related features).

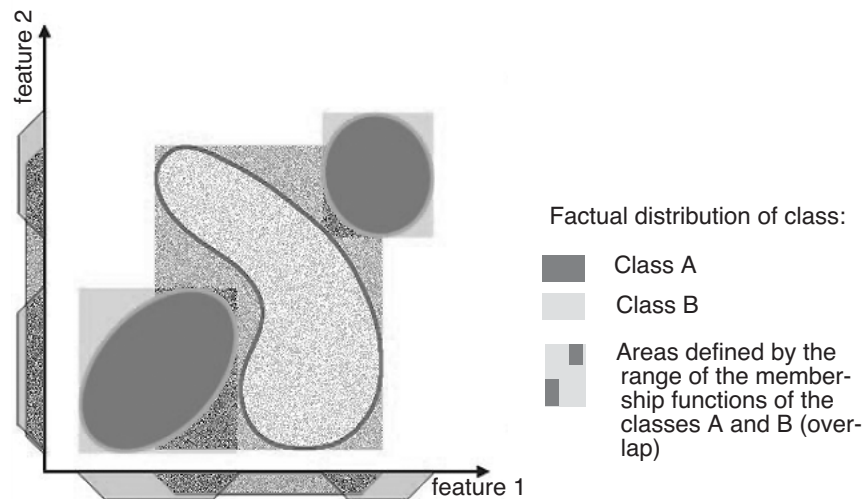


Figure 6.5 Overlap of class descriptions based on membership functions in a two-dimensional feature space ([184], (modified)).

However, if a reasonable number of sample objects for each class has to be kept, the feature space should be kept as small as possible for a nearest neighbor classification.

6.3 Classification Project Design

6.3.1 Classification Image Database

The classification database consisted of both, the ASTER and Landsat ETM+ datasets. Additionally, ancillary data as classification evidence, were also included. The normalized difference vegetation index (NDVIA) (for definition see Tab. 7.1), calculated from the ASTER mosaic (NDVIA), was imported as well as the tasseled cap derivatives brightness (BRIGHT), greenness (GREEN) and wetness (WETN) (for definition see Tab. 7.2). Moreover the generated ASTER DEM (DEM) and its calculated derivatives slope (SLP) and aspect (ASP) were included in the database. Additionally, a vector layer (PLANTATIONS) was added to the eCognition project containing all coniferous plantations of an age between 5 and 30 years. The vector dataset was provided by the CIEFAP. It was not weighted in the segmentation process and small discrepancies between plantation borders of very young plantations, which are hardly visible in the satellite data, and the generated segments based on the selected weighted ASTER bands were knowingly accepted.

Image band derivatives and ancillary data sources can provide useful information to help distinguish between spectrally inseparable vegetation classes and lead to more effective vegetation classification [124]. Environmental factors, such as elevation, slope or aspect are widely used ancillary data. According to the habitat characteristics of vegetation, location specific conditions can function as limiting factors to the spacial distribution of some species. For this reason, elevation (DEM), slope (SLP) and aspect (ASP) were incorporated into the eCognition classification database. Other site specific maps, e.g. a soil map, do not exist for the research area.

NDVI reportedly improves vegetation classifications by partially compensating for variation in illumination due to terrain [115], and is well correlated to vegetation biophysical parameters [182]. The tasseled cap transformation is a method for enhancing spectral information content [36]. It optimizes data viewing for vegetation studies and is calculated from the six Landsat ETM+ bands (excluding the thermal band). The resulting brightness, greenness and wetness indices can improve vegetation classifications because they are sensitive to phenological changes. Thus the indices can be used to distinguish green vegetation with soil from green vegetation with brown vegetation. In addition, the wetness band correlates with shadows and forest stand density. These correlations improve the separation of fields from forest, and between forest classes [37].

6.3.2 Training Area

The development of the classification was performed on a smaller subset in the research area. It comprises "Los Alerces National Park" as well as the city of Esquel and represents all vegetation classes and terrain reliefs present in the research area. The training area is illustrated in Fig. 6.6. This smaller training area was chosen because most ground reference data was collected in the subset area due to good accessibility and cooperation with the national park representatives.

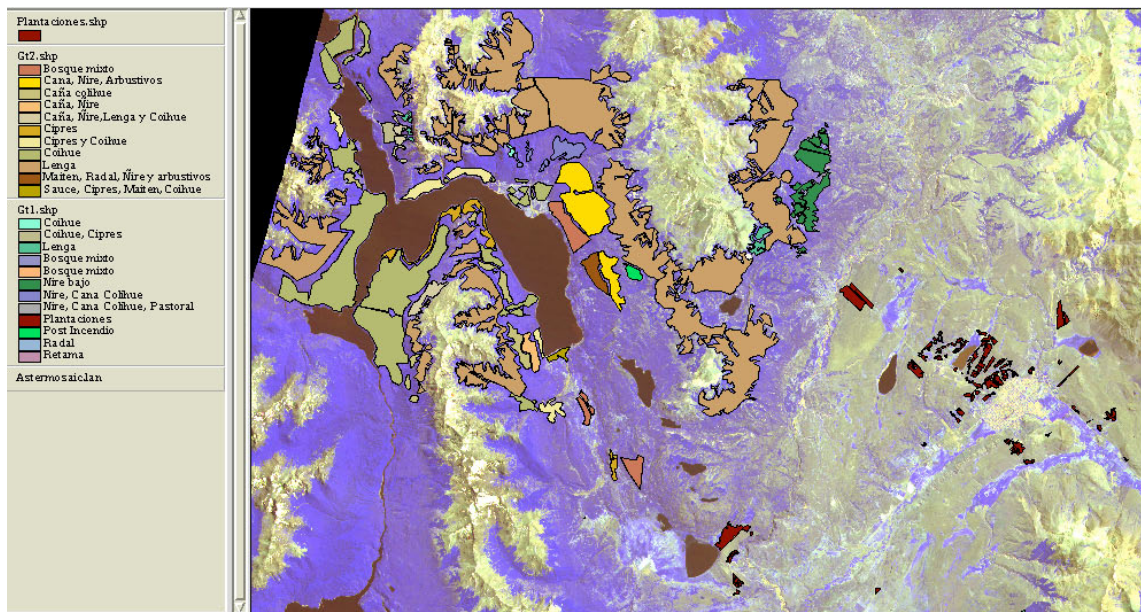


Figure 6.6 Screenshot of arcview, showing the training subset. Displayed is a false color composite of ASTER bands 1, 2, 3 overlaid with the vegetation cover ground reference layer.

6.3.3 Segmentation Evaluation

6.3.3.1 Band Weighting, Scale Parameter and Criterion Test

The choice of the appropriate scale parameters on each level is the most crucial task in an eCognition project. Scale is mainly defined by the geometric resolution of the geodatabase and the physical entities that have to be classified. The objects of interest in this research project can be divided into two groups. They are listed in Tab. 6.1.

Table 6.1 Identifiable objects of interest.

Scale Level	Objects of Interest
Middle	Groups of trees, bushes
	Grass patches
	Single buildings /roads
Low	Forest stands
	Mallines
	Urban area

The layer selection and weighting was performed empirically, based on visual inspection of different segmentation results. Several segmentation tests were performed including either bands with both 15 m and 30 m geometric resolution (e.g. ASTER band 1, 2,3 and 4 to 9) or only bands with 15 m geometric resolution (e.g. ASTER band 1, 2, and 3). Finally, it was decided to incorporate mainly the bands with the highest geometric resolution since they represented the defined objects of interest better.

- The ASTER bands 1, 2 and 3 were given a weight of 2 and
- the vegetation index NDVI, derived from ASTER bands 2 and 3, was given a weight of 1.

Finding the optimum scale and criterion parameters for extracting the defined objects of interest, a segmentation evaluation was performed. The geodatabase was segmented in four different eCognition projects using different scale parameters and all possible criterion combinations [Tab. 6.2]. The four projects and every criterion combination was visually evaluated. For statistical comparison purposes, the more detailed segmentation level of each project was classified into the main tree type classes growing in the research area and statistically evaluated by comparing the classification results with the corresponding ground reference dataset.

Table 6.2 Chosen criteria for the conducted segmentation tests (see Fig. 6.2 for the definition of the segmentation criteria).

Criteria	Parameters
Project 1-4 with 2 scale levels each	6/9, 9/12, 12/15, 15/18
Color/Shape	all possible combinations: 0.9/0.1 to 0.1/0.9
Smoothness/Compactness	all possible combinations: 0.9/0.1 to 0.1/0.9

Visual differences depending on the chosen segmentation criteria are evident and represent the shapes of the vegetation patches growing in the research area more or less realistically, as seen in Fig. 6.7. Visual interpretation of the different segmentations resulted in the following conclusions:

- Compactness and shape should be low to achieve realistic objects representing groups of trees and tree stands.
- The larger the scale parameter the higher the generalization.
- A high color value seems to achieve better results than a low color value.

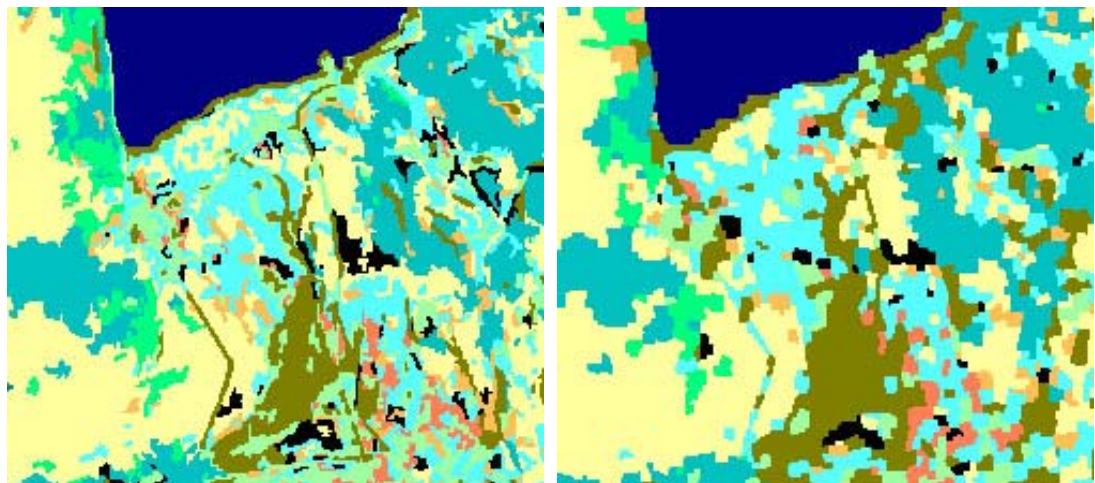


Figure 6.7 Preliminary segmentation and classification result showing a realistic (left) and an unrealistic (right) pattern. Left image criterion: color: 0.8, smoothness: 0.9, right image criterion: color: 0.2, smoothness: 0.1. Both images represent a scale factor of 9, which represents realistically groups of homogeneous tree types. The criterion represented in the left image was chosen in the final classification project.



Figure 6.8 Kappa accuracies of the different eCognition test projects varying by their segmentation criteria and scale parameter. The nomenclature "xy_0201" can be explained as follows: weight of shape = 0.2, weight of compactness = 0.1.

The analysis of the different classified segmentations resulted in little differences. Fig. 6.8 illustrates the summarized kappa accuracies depending on the scale parameter of the project and the chosen color/shape criteria. Again it can be seen that color should be weighted more than the shape criterion. It also achieves better result than a 50% weighting of each color and shape criterion. The smoothness/compactness criteria can not be judged by the accuracies. They should be chosen depending on the shape of the classifiable objects of interest.

The definition of these parameters requires detailed knowledge of the vegetation patterns in the research area. Based on this knowledge, the classification results and the visually best representation of the defined objects of interest the scale parameter and weighting criteria were chosen.

- Scale parameter: 9
- Color: 0.8
- Shape: 0.2,
- Smoothness: 0.9,
- Compactness: 0.1

6.3.3.2 Segmentation Reproducibility Test - Border Problem

With the release of eCognition Version 3.0 the segmentation algorithm became enhanced with respect to reproducible object shapes for comparable scenes. This is of great importance if large datasets are classified since due to hardware restrictions datasets often have to be tiled and processed in several smaller eCognition projects. The classified subsets have to be merged again after classification and therefore segmentation should be identical. Unfortunately this is not the case in border areas. Fig. 6.9 shows an upper and a lower tile of the dataset with a large overlapping area. Both tiles were segmented with identical scale parameters and weighting criteria and afterwards checked for conformity. It can be seen that about 150 pixels from the border are not segmented into identical segments. Hence an overlapping area of 300 pixels for each tile was defined to account for this effect.

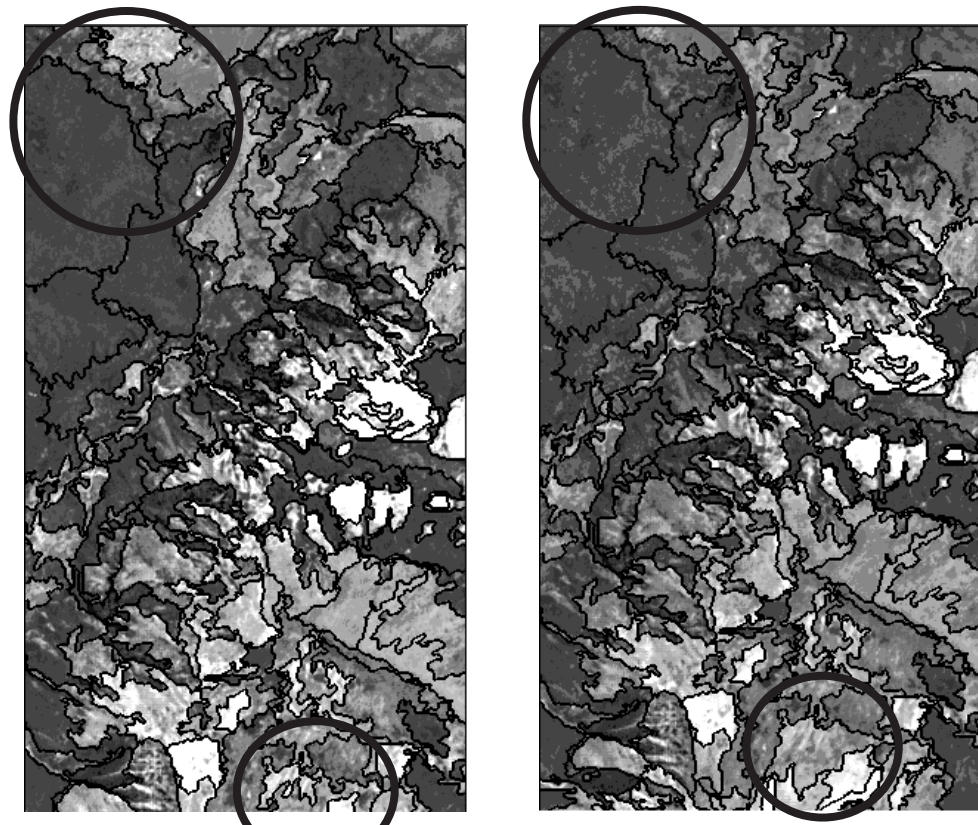


Figure 6.9 Differences of two overlapping datasets are apparent (circles).

6.4 Results

6.4.1 Classification Rule Base

6.4.1.1 Feature Selection

Features of each object, used in this analysis, were calculated from the 24 spectral and ancillary bands. 30 features were generated which can be divided into four categories:

- 1) 22 means of all layers and the standard deviation of the DEM respectively were calculated for each image object.
- 2) Two features for the fuzzy class description: brightness and maximum difference. Brightness is defined as the total of the mean values of the layers containing spectral information divided by their quantity computed for an image object (mean value of the spectral mean values of an image object). The brightness of all generated feature layers have been calculated. The maximum difference is calculated by subtracting the minimum mean value belonging to an object from its maximum value and the result divided by the brightness. These two features are generated automatically.
- 3) Two shape features: compactness, defined as the product of the length and the width of the corresponding object, divided by the number of its inner pixels, and the length/width ratio for each object.
- 4) Four neighborhood relation features: relative border to brighter neighbors for the bands ASTER7, ASTER8, ETM5 and NDVIA

Unlike in the classification of urban areas, geometric features did not significantly contribute to this vegetation/land cover classification in light of the absence of human-made features and the level of image resolution.

By applying a feature space optimization tool provided by eCognition the features standard deviation of the DEM and the four neighborhood relation features were selected to best classify the first six overall classes listed in the following chapter. These features were only used in the St. NN classification step.

6.4.1.2 Class Hierarchy

After the visual evaluation of the tested segmentation levels it was decided that classification would be performed on one segmentation level only. After segmentation, training objects were identified for each class and a combination of Std. NN and fuzzy membership classification rule was developed. Fig. 6.10 shows the established class hierarchy.

First six overall classes, covering large areas, were separated. The classes

- high¹⁾ vegetation,
- low vegetation,
- plantations,
- water,
- snow/bright rock and
- border

were easily classified by Std. NN and/or membership function. Std. NN was applied on the first class hierarchy level only, except for the class Intense Grassland/Mixed Trees, where the combined application of Std. NN and membership functions achieved the best representation of the reality. All other classes were classified based on membership functions.

The main focus was directed to the subclassification of the class high vegetation; it includes the forested areas as well as high vegetative grasslands and thick shrubs or bushes. The subclassification of the class low vegetation, was of less interest. Nevertheless, the class includes some dumose representatives of *Lenga* and *Ñire* growing in harsh conditions, the identification of which were first attempted in a land cover classification in Patagonia. The used features and the applied fuzzy rule are listed in the Appendix Table 1.

¹⁾ "high" vegetation and "low" vegetation signifying high and low vegetation amount respectively.

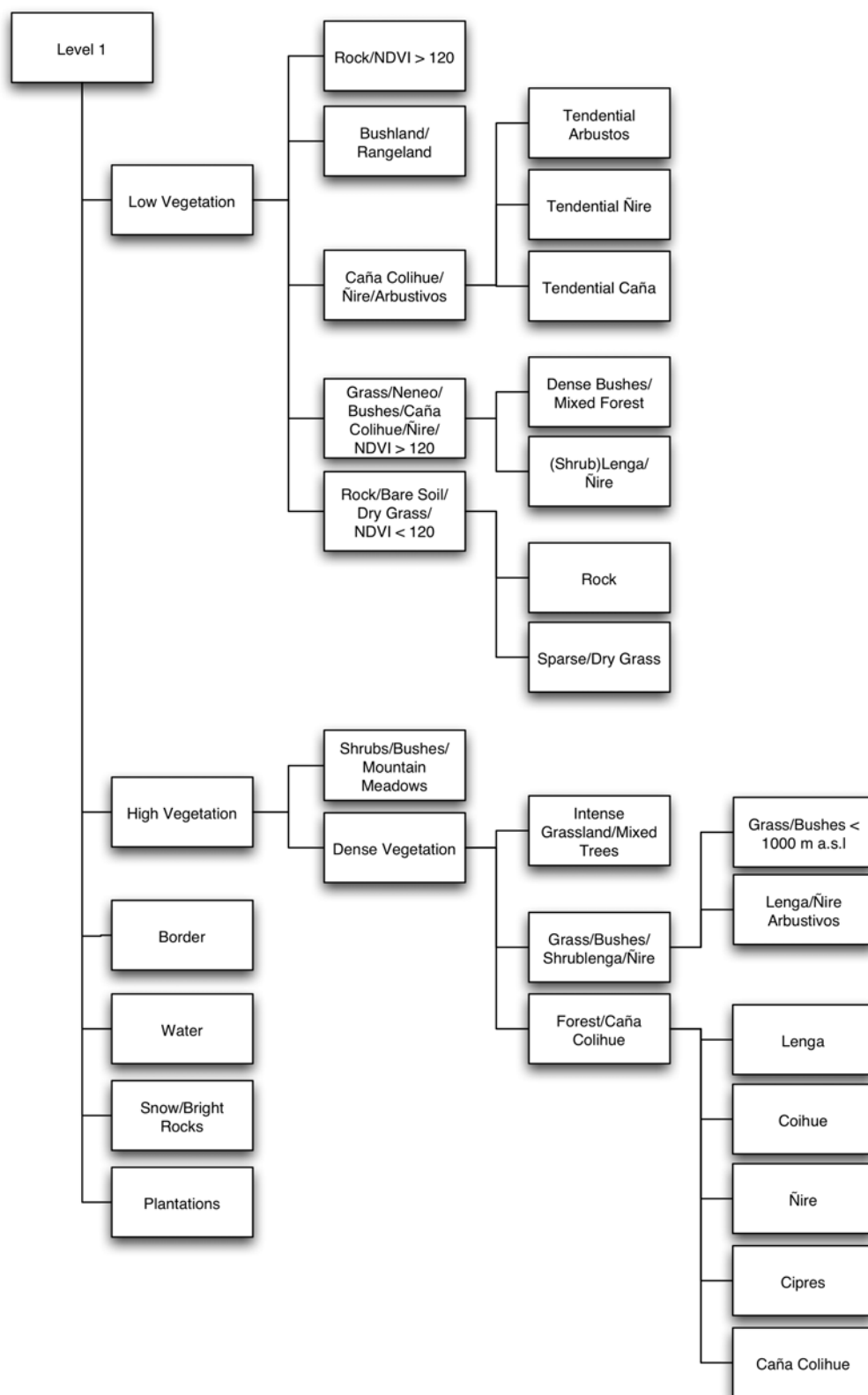


Figure 6.10 Developed class hierarchy.

The class **High Vegetation** was subdivided in two classes: **Shrubs/Bushes/Mountain Meadows** and **Dense Vegetation**. They were separated by the feature NDVIA. Dense Vegetation was further subclassified in three classes representing Forests/Caña Colihue, Grass/Bushes/Shrubs/Ñire and **Intense Grassland/Mixed Trees**. The Intense Grassland/Mixed Trees class represents mainly the agriculturally important meadows and acres near mallines and rivers mainly present in a narrow strip between the Patagonian mountainous forests and the Patagonian steppe. It was only successfully classified by combining the ST. NN classifier and the feature DEM. The classes **Forests/Caña Colihue** and **Grass/Bushes/Shrubs/Ñire** were separated by applying the features NDVIA, DEM and ETM5. The mid-infrared band seemed to improve the separation of forests and grass/shrubs/bushes. The Grass/Bushes/Shrubs/Ñire class was further subdivided into **Grass/Bushes < 1000 m a.s.l.** and **Lenga/Ñire Arbustivos**. They represent the different types of grass communities growing in the area depending on the elevation they are growing and were thus divided by the feature DEM. The class **Forests/Caña Colihue** was subdivided into the main five tree type classes representing the Patagonian native forest. **Lenga, Coihue, Ñire, Ciprés** and **Caña Colihue**. Their discrimination was significantly more difficult, thus a class matrix was established to identify the bands where the tree type classes differed most [Tab. 6.3].

The tree type **Lenga** is growing in large homogenous stands in higher elevations and was mainly separable from Coihue, Ñire, Ciprés and Caña Colihue by applying the features DEM, ASTER4 and ASTER2. The separation of the classes **Ciprés** and **Coihue** caused some problems. They showed similar spectral characteristics and grow in similar elevations. The feature ASTER2 was applied to separate the two tree types. Although the separation of **Ñire** and **Caña Colihue** was performed by the features ASTER4 and ASTER5, there remain, in respect of both classes, overlapping areas in both bands. The features ASTER1, ASTER2, ASTER4, and ASTER5 as well as the Landsat ETM+ based features ETM5, ETM7, WETN and BRIGHT proved, besides the elevation feature DEM to work best to separate the tree type classes from each other.

Table 6.3 Class separation matrix. Bands in grey color indicate low separation between classes. Bands in black may have minor spectral overlaps between classes.

	Lenga	Coihue	Ñire	Ciprés
Lenga				
Coihue	ASTER4 DEM			
Ñire	ASTER2 ETM2 ETM3 DEM	ASTER1 ASTER2		
Ciprés	ASTER2 ASTER4 DEM	ASTER2 ETM3	ASTER4 ETM5	
Caña Colihue	ASTER2 DEM	ASTER4 ETM5 ETM7	ASTER4 ASTER5	ETM2 ETM5 BRIGHT WETN

The class **Low Vegetation** was first subdivided into **five subclasses**, which represent low synthetically active vegetation classes depending on different elevation and precipitation regimes. They were mainly discriminated by applying the DEM and the NDVIA feature. The transition zone class **Caña Colihue/Ñire/Arbustivos** was furthermore tried to subdivide. Dumose Ñire, Caña Colihue and other bushes were tried to separate. A possible separation between the three

classes was found in the feature *ratio of ASTER4*, still the classification results have to be handled with care. Therefore the classes were named as **Tendential Ñire**, **Tendential Caña Colihue** and **Tendential shrubs**.

6.4.2 Accuracy Assessment

Accuracy assessment requires the development of a statistically rigorous sampling design of the location, distribution and type of samples to be taken or collected. Several considerations are critical to the development of a robust design to support an accuracy assessment that is truly representative of the map being assessed. Important design considerations include the following:

- What are the map classes and how are they distributed? How a map is sampled for accuracy will partially be driven by how the categorical information of interest is spatially distributed. These distributions are a function of how the features of interest have been categorized - referred to as the *classification scheme*.
- What is the appropriate sample unit? Sampling units are the portions of the landscape that will be sampled for the accuracy assessment.
- How many samples should be taken? Accuracy assessment requires that an adequate number of samples be gathered so that any analysis performed is statistically valid.
- How should the samples be chosen? The choice and distribution of samples, or sampling scheme is an important part of any inventory design [69].

The ground reference used in the assessment of classification accuracy is in itself just another classification which may contain errors. They may be thematic errors in which the class labels are erroneous but may also include other errors such as those due to mislocation. The attachment of a label to a class is often based on highly subjective interpretations. Variation in the confidence of the class labelling in the ground reference data can significantly influence the apparent accuracy of a classification. In the available ground reference data, as well as the developed class hierarchy, some discrepancies in class definitions have arisen. Therefore some classes in the ground reference data as well as the classification result had to be merged, excluded or reassigned to other classes.

The definition of the sampling design, sampling size and the specification and use of measures of accuracy were also defined.

A general rule of thumb is to use a minimum of 50 samples for each land cover class in the error matrix [34]. If the area is large or the classification has a large number of land cover classes, i.e., more than 12 classes, the minimum number of samples should be increased to 75 to 100 samples per class. To achieve statistically reliable results and to allow for the available ground reference data, simple random sampling was chosen. The sampling unit is defined as a 10x10 pixel block, which represents an area of 150 m x 150 m and a total of 1050 randomly distributed samples were stratified according to the class percentages in the classification.



Figure 6.11 Ground reference bitmap (grey) and randomly selected sample units (black).

In classical accuracy assessment all misallocations are equally weighted. Often, however, some errors are more severe than others. In many instances, the errors observed in a classification are between relatively similar classes and sometimes these may be unimportant, while other errors may be highly significant. The conventional hard allocation of sites to discrete classes is, therefore, an issue of concern in thematic mapping, particularly as it may sometimes be more appropriate to model continuous variations in land surface properties and allow for indeterminate boundaries. The assessment of the accuracy of these representations is, however, difficult [52]. Errors may range in magnitude from relatively minor confusion involving similar classes either side of an arbitrarily defined class boundary to the confusion of the very dissimilar classes located at the end points of the defined class boundaries. The importance of these different degrees of error may vary depending on the user's requirements but, in many instances, the assumption that errors are of equal severity is incorrect. This is unfortunate, as basic accuracy metrics such as the percentage of cases correctly allocated or the kappa coefficient effectively weighted errors equally. The utility of some measures of accuracy is limited by variations on the severity of error magnitude. Some accuracy assessment procedures may be adapted to accommodate known differences in error severity, for example the various possible thematic errors that can be encountered in a study may be assigned to differing scores of severity and a weighted kappa coefficient K_{ω} derived [52],[53]. It can be written as:

$$K_{\omega} = 1 - (\sum v_{ij} f_{oij}) / (\sum v_{ij} f_{cij}) \quad (\text{Eq. 6.7})$$

where v_{ij} is the weight associated with the error in the confusion matrix element ij , f_{oij} the observed frequency in element ij , and f_{cij} the frequency that could be expected to occur in element ij by chance [30], [171]. To indicate the quality of the classification for individual classes, the percentage correct allocation for each class from the users's (correctly classified pixels in the

classification compared to the classification data) and producer's (correctly classified pixels compared to the ground reference data) perspectives were also derived.

The weights for the errors were determined such that an error weight of 1 was associated with misallocations to a *very similar* class, a weight of 2 with misallocations between *similar* classes and the highest weight, 3, associated with an *unacceptable* misclassification. Tab. 6.4 contains the assignment of the weights to the specific errors of classification.

Table 6.4 Assigned weights to the errors of classification.

Weight	Correct Class	Misclassified as
1	Shrublenga/Ñire	Lenga or Ñire
	Ñire	Caña Colihue
	Tendential Arbustos	Caña Colihue, Ñire or Bushes/Mountain Meadow, Rock
	Rock	Bushes/Mountain Meadow
	Dry/Sparse Grass	Tendential Arbustos or Bushland/Rangeland
	Bushes/Mountain Meadow	Caña Colihue, Ñire, Shrublenga/Ñire
	Bushland/Rangeland	Tendential Arbustos or Dry/Sparse Grass, Rock
2	Tree classes	Similar tree classes
	Intense Grassland/Mixed Forest	Other tree classes and Plantations
	Rock	Ciprés or Shrublenga/Ñire
	Tendential Arbustos	Ciprés
	Bushland/Rangeland	Intense Grassland/Mixed Forest
3	Caña Colihue	Lenga or Plantations
	Ciprés	Intense Grassland/Mixed Forest and vice versa
	Lenga	Caña Colihue
	Ñire	Plantations
	Bushes/Mountain Meadow	Plantations
	Dry/Sparse Grass	Plantations
	Plantations	Bushland/Rangeland
	Water	Rock
	Rock	Caña Colihue or Lenga
	Tendential Arbustos	Coihue, Lenga, Intense Grassland/Mixed Forest or Plantations

The result of the object based classification of the training subset is shown in Fig. 6.12. Firstly the statistical accuracy assessment between the classification and the ground reference data will be discussed and secondly the fuzzy membership statistics. Accordingly, the stability of the classification is analyzed.

As can be seen in Tab. 6.5 the accuracy assessment achieved an overall accuracy of 82.04% and a kappa coefficient 0.8002. After weighting the misallocated errors according to their importance, a weighted kappa of 0.8185 was calculated. The tree type classes were concentrated on, followed by the Intense Grassland/Mixed Forest and the Shrublenga/Ñire classes whilst the classification rule was developed. The classes with less importance in accuracy were the low vegetation classes such as Bushland/Rangeland, Dry/Sparse Grass or Tendential Bush class.

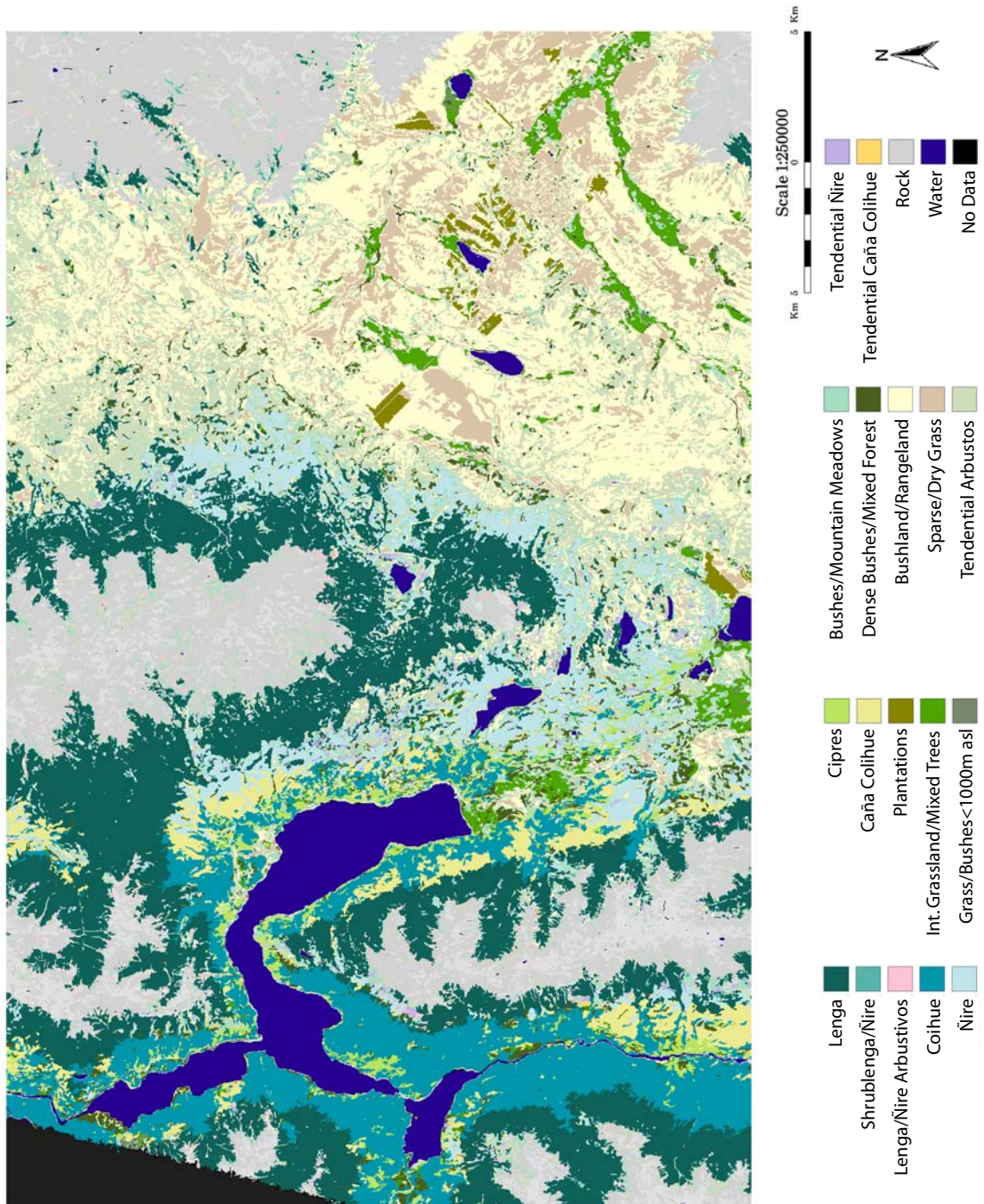


Figure 6.12 Classification result of the training subset.

Table 6.5 Accuracy statistics containing user- and producer accuracy for each class as well as overall accuracy, kappa coefficient and weighted kappa.

Class	User	Producer
Caña Colihue	0.563	0.8378
Ciprés	0.3961	0.6488
Ñire	0.7321	0.7157
Coihue	0.9168	0.709
Lenga	0.9592	0.8656
Intense Grassland/Mixed Forest	0.3847	0.8133
Bushes/Mountain Meadow	0.288	0.4776
Dry/Sparse Grass	0.9908	0.9505
Shrublenga/Ñire	0.3521	0.2342
Plantations	0.9542	0.9871
Bushland/Rangeland	0.9183	0.9477
Tendential Arbustos	0.7744	0.122
Rock	0.9839	0.9428
Water	0.9997	0.9987
Kappa Coefficient	0.8002	
Weighted Kappa Coefficient	0.8185	
Overall Accuracy	0.8204	

Looking at the producer and user accuracies of the **tree type classes**, it can be stated that they all reached an accuracy of at least 70% except for the coniferous tree type Ciprés. **Ciprés** was mostly misclassified as Coihue or Shrubs/Bushes/Mountain Meadow. The reasons for these misallocations are apparent. Ciprés is growing in heterogeneous, small stands mostly together with Coihue, preferring dry and rocky habitats. Ciprés has moreover a low spectral reflectance in the near-infrared (*nir*) compared to shrubs or bushes. The producer accuracy of the classified bamboo specie **Caña Colihue** reached an acceptable result, whereas the user accuracy is with 56.3% too low. Caña Colihue ground reference area was often misclassified as other tree types such as Lenga, Coihue, Mixed Forest or Ñire. This is mainly due to the fact that Caña Colihue is growing in the forest understory when the habitat is moist enough. Caña Colihue is also the first plant to grow after forest fires, so too Ñire. The misallocations of the other tree species with accuracies higher than 70% were mostly among each other or with the class Intense Grassland/Mixed Forest.

The classes **Intense Grassland/Mixed Forest**, **Bushes/Mountain Meadow**, **Shrublenga/Ñire** and **Tendential Arbustos** were rather difficult to classify and assess, since they are all a mixture of several plant species. Even so, it can be of high importance to the future users as these mixed classes, depending on the habitat, location and height, can give them a good idea of what kind of vegetation is most probably growing in a specific location. Always reminded that as to date no such vegetation information is available for the area. Intense Grassland/Mixed Forest was mostly misclassified as other forest classes or Caña Colihue. The classes representing different bush vegetation were mainly misclassified among each other. While establishing the ground reference database not many patches of these bush vegetation classes were mapped, which resulted in few ground reference area, that influenced the accuracies. This can clearly be seen by the very low producer accuracy the class Tendential Arbustos, Shrublenga/Ñire and Bushes/Mountain

Meadow achieved.

The remaining classes **Dry/Sparse Grass**, **Plantations**, **Rock** and **Water** reached rather high accuracies due to specific spectral characteristics of the classes. The class **Plantation** was classified with the help of an additionally imported plantation layer into the classification database. The layer was added after segmentation, thus the segmentation did not account for its boundaries, which resulted in a slightly reduced accuracy. The user and producer accuracies of these four classes reached at least 90%.

When using fuzzy classification methods, objects can belong to several classes but with different degrees of membership, which is the case when class descriptions overlap. Thus to evaluate the reliability or stability of classes it is necessary to survey the different degrees of membership of the classified objects. Objects whose feature values are within these overlapping ranges can be seen as ambiguous objects, because they fulfil the criteria of more than one class. Although fuzzy concepts make it possible to describe these ambiguities, the main aim of each classification should be to define classes as unambiguously as possible.

To quantify a class's quality regarding the statistics of its objects' degrees of membership is an appropriate method: the more objects that have a membership degree of 1 to just this class, the better the class is, and vice versa. In addition, the statistics and some parameters such as minimum, maximum, standard deviation and mean of the several degrees of membership, can give more evidence [184]. Tab. 6.6 shows the calculated fuzzy logic membership values for each of the object land cover classes for the training subset.

The maxima values can be interpreted as quite stable if they reach nearly 70% membership. Standard deviations do not exceed 0.2 and the mean values vary highly between 0.04 and 0.96. Again this is achieved by **all tree type classes** except for the class **Ciprés**. Lenga and Coihue were classified with the highest stability followed by Ñire, Caña Colihue and Ciprés.

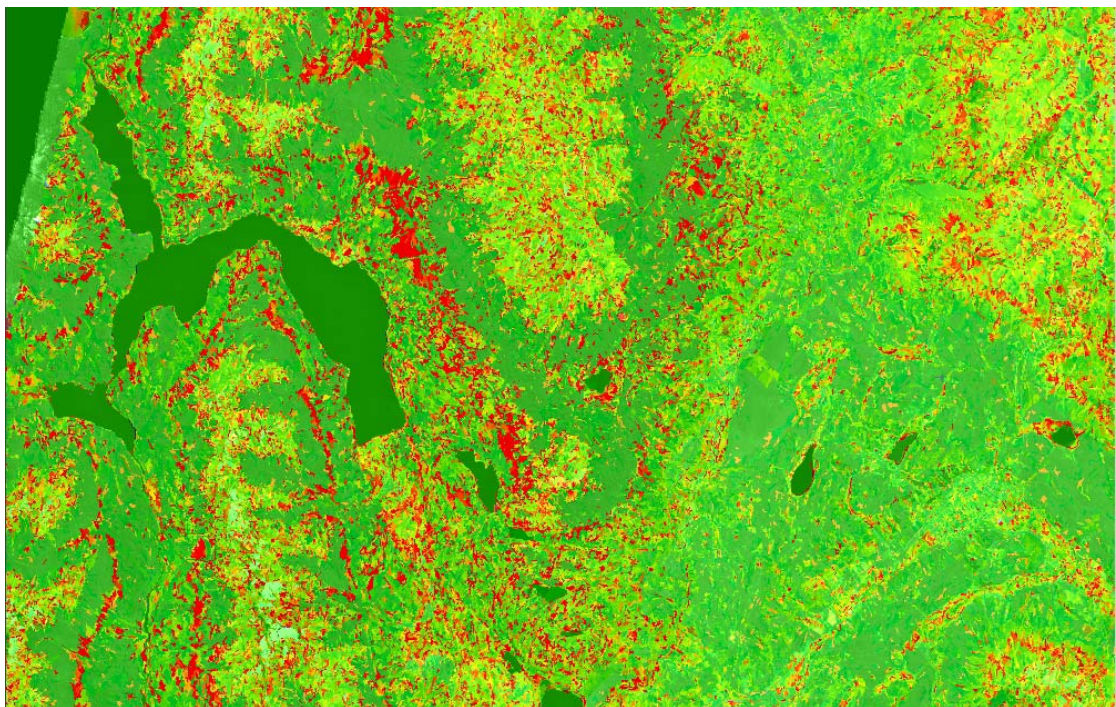
Table 6.6 Fuzzy logic membership statistics for each object.

Class	Objects	Mean	Stdv.	Min.	Max.
Caña Colihue	1571	0.26	0.19	0.00	0.68
Ciprés	1438	0.23	0.16	0.00	0.62
Ñire	4977	0.28	0.18	0.00	0.80
Coihue	6375	0.41	0.17	0.00	0.74
Lenga	14208	0.44	0.19	0.00	0.78
Grass/Bushes < 1000m	289	0.06	0.05	0.00	0.36
Lenga/Ñire Arbustivos	1276	0.12	0.09	0.00	0.86
Intense Grassland/Mixed Forest	2337	0.15	0.11	0.00	0.68
Bushes/Mountain Meadow	9791	0.16	0.12	0.00	0.69
Rock	15410	0.18	0.11	0.00	0.76
Dry/Sparse Grass	6741	0.36	0.18	0.00	0.88
Dense Bushes/Mixed Forest	2756	0.13	0.11	0.00	0.76
Shrublenga/Ñire	884	0.16	0.12	0.00	0.59
Plantations	662	0.37	0.14	0.09	0.79
Bushland/Rangeland	19129	0.38	0.17	0.00	0.93
Rock/NDVI > 120	3353	0.13	0.09	0.00	0.46
Water	1201	0.69	0.26	0.00	0.98
Border	1358	0.96	0.13	0.03	1
Snow/Bright Rocks	11022	0.19	0.16	0.00	1

Table 6.6 Fuzzy logic membership statistics for each object.

Class	Objects	Mean	Stdv.	Min.	Max.
Tendential Caña Colihue	450	0.04	0.07	0.00	0.76
Tendential Ñire	1322	0.00	0.00	0.00	0
Tendential Arbustos	19547	0.18	0.13	0.00	0.98

The membership stability for the **mixed tree classes with bush characteristics** such as Lenga/Ñire Arbustivos, Intense Grassland/Mixed Trees, Shrubs/Bushes/Mountain Meadow, Dense Bushes/Mixed Forest and Tendential Arbustos have maxima higher than 0.69 but also rather low mean values, which signifies that memberships are basically low. In an attempt to separate the classes **Tendential Ñire** and **Tendential Caña Colihue** from the large class **Tendential Arbustos**, resulted in a relatively unstable membership. The application of elevation information to the Arbustos classes is, however, still giving a hint what kind of bush vegetation most probably is growing at a specific location. If the knowledge of soil moisture is available this would discriminate the three tendential classes even more. The class **Grass/Bushes < 1000 m asl** has a very low stability due to high overlapping with the class Intense Grassland/Mixed Forest. This class is important though because it represents, together with the **Intense Grassland/Mixed Forest** class, the agriculturally important, intense grasslands, the *mallines*. The classes **Sparse/Dry Grass** and **Bushland/Rangeland** represent vast areas in the drier east of the subset and were classified with high stability. However, these classes are not as important as the tree type classes. Although the stability of the three different **Rock classes** are low, the classification accuracy assessment showed that the established classification rule works well and consolidates all non vegetated areas, except for some shadowed objects which have a low spectral reflectance. The classes **Water**, **Border** and **Plantations** were established with high stability which is also represented by the high accuracies previously analyzed.

**Figure 6.13** Classification stability of the training subset. The graphical output displays the value for each image object in a range from dark green (1.0, nonambiguous) to red (0.0, absolutely ambiguous).

eCognition also provides a classification stability map, where the differences in degrees of membership between the best and the second best class assignment of each object can be visually explored [Fig. 6.13]. It provides evidence regarding the ambiguity of an object's classification. The graphical output displays the value for each image object in a range from dark green (1.0, nonambiguous) to red (0.0, absolutely ambiguous). In Fig. 6.13 it can be seen that particularly on the transition zones between the tree types Lenga and Coihue, the memberships assigned to the two classes are identical because the two classes are basically discriminated by the elevation information. Another area with low stability is situated on the eastern shores of Lago Futalaufquen which is abundantly covered with the mixed post-fire regrowth species Ñire, Caña Colihue and Tential Arbustos. Moreover, medium stability can be observed on the non vegetated areas classified as one of the three Rock classes.

6.4.3 Vegetation Cover Map

Due to hardware restrictions the dataset size of an eCognition project is limited to a certain extent. Therefore the dataset mosaic was divided into 11 tiles having a size of 4600 pixel by 2000 pixels and containing overlapping areas of 150 pixels to guarantee segment conformity [see section 6.2.2 on page 61] between neighboring tiles. For every tile dataset, an eCognition project was generated.

After establishing the classification rule, the workflow was automated by setting up a protocol containing all relevant segmentation and classification settings, and was applied to the 11 projects. All classified tiles were checked for class conformity and subsequently minor adjustments had to be made. The class Water had to be adjusted as a result of misclassified shallow mountain lakes, where the rocky ground shone through (misclassified as Rock) or temporarily dried out lakes (actually correctly classified as Rangeland or Dry/Sparse Grass and not as Water). Additionally, the clouded and consequently shadowed areas in the north of the research area were masked out. In every tile a few objects were not classified at all; mostly very bright, atmospherically overcorrected object areas, shadowed bare soil areas or ambiguous vegetation objects. Otherwise the rule base was transferred automatically for all classes. The accuracies for the northern and southern adjacent tiles to the training subset are expected to be in the range of the accuracies of the training subset, since vegetation and ecotones do not change within the research area.

At last the tiled classification maps were mosaicked again. The final land cover classification map is displayed as appendix in a larger DIN A3 format.

6.5 Discussion

In an eCognition-based classification project the initial and most crucial task is to define the layer weighting, the scale parameters and the segmentation criterion. These parameters are only to be found empirically which has the great disadvantage that these parameters have to be adjusted every time a similar project is established. Moreover, this process is time consuming and requires some experience and expert know-how. In this project this process was tried to be improved by introducing some systematic testing and by first defining the meaningful objects that had to be classified. All segmentation and classification results were visually evaluated and compared to the available ground reference data and the consequently defined parameters were successfully applied.

The classification result of the subset area [Fig. 6.12] were verified accurately in the field. The developed rule base and defined classes have proven to represent the land cover characteristics most suitable. Beforehand, only pixel-based classifications had been established of the area, dealing with major problems in the range of forest type discrimination (Caña Colihue, Ñire, Ciprés) and the classification of the transition zone vegetation [134]. These vegetation species were hardly allowed for. Therefore, spectral characteristics and differences in these zones were

tried to be defined, which resulted in classes consisting of more than one species, representing a typical vegetation cover well known and understandable to the local interpreter of the resulting map. On the other hand, these class definitions might seem unusual to a person not familiar with the typical Patagonian vegetation species. However, the map serves its purpose and gives the local authorities a clear impression on the vegetation cover.

All calculated features mentioned in chapter 6.4.1.1 incorporated only when applying the St. NN algorithm. Looking at the defined membership functions it can be seen that the established land cover classification bases mainly on spectral and height information. The previously calculated layers SLP (slope) and ASP (aspect) didn't improve the exposition dependent vegetation patterns in the final classification, which could be explained with the previously conducted topographic correction of the satellite datasets that might have led to a certain elimination of exposition dependent vegetation pattern. Besides the elevation information DEM, the ASTER bands 1 and 2 as well as the mid-infrared bands ASTER4 and 5 as well as the Landsat ETM+ based mid-infrared bands ETM5 and 7 and the tasseled cap derivatives BRIGHT and WETN have been found to be very useful to discriminate the tree type classes. The importance of the mid-infrared bands in vegetation classification was again shown, where the ASTER bands separated the tree type classes better than the ETM+ bands. But the additional mid-infrared bands of ASTER (bands 6 to 9) did not provide additional differentiation due to high similarity to band 5. The near-infrared band ASTER3 was only used as part of the vegetation index NDVIA, which helped to separate the low vegetation from the high vegetation classes as well as differentiate in between the high vegetation grass communities and in between the low vegetation bush classes.

In the developed classification rule often the parabolic shaped membership function was applied. The shape of the parabola was for most classes manually adjusted and the area of high stability widened to achieve higher stabilities for the defined classes. The default shaped parabola instead allocates only a narrow area with high stability to a class, which could lead to a destabilisation of the classification rule.

With the applied accuracy assessment it was first tried to account for the limited ground reference by selecting a large amount of samples which represented a 10 x 10 pixel block and not only single pixels. Secondly, it was tried to account for the severity of the classification errors depending on the generated vegetation classes by introducing the weighted kappa coefficient. The resulting statistics identify well the accuracies and therefore the problems of class similarity and lack of large ground reference. Accuracy statistics always have to be interpreted with care and require knowledge of the defined classes, the used ground reference data and the sampling design and size.

When using fuzzy classification methods, objects can belong to several classes but with different degrees of membership. It is often criticized that fuzzy or "soft" classifiers lack of sufficient stability or reliability, but the advantage of smooth transitions of class membership accounts for mixed pixel information, especially apparent with medium-resolution satellite data. Certainly, in this research area most tree type classes for example are growing on specific characteristic locations differing in either elevation, succession, soil type or precipitation and can be fairly good delineated. But also these homogeneous tree type classes have border zones, where memberships are similar and transitions fuzzy. Vegetation cover changes rarely occur "on a straight line", notably with medium-resolution satellite data. The establishment of a fuzzy classification rule requires detailed knowledge of the vegetation patterns in the research area.

Applying an object-oriented classification approach including fuzzy membership functions accounts not only for the extremely variable but characteristic vegetation pattern of Argentinean Patagonia between 70 and 71° W and 38 to 44° S but also for the satellite data available to the CIEFAP and the provincial forest department, DGBYP. Its application to other research objectives addressed by the CIEFAP is promising and consequently will be continued and extended.

Forest Parameter Estimation

7.1 Introduction

Optical remote sensing imagery has to date mainly been used as an auxiliary data source in several forest inventory and monitoring applications. Auxiliary data, as such, may not be appropriate or sufficiently accurate for the specific forest inventory task, but are correlated with the true values of the interesting forest characteristics and can thus be used for the estimation of forest characteristics [175]. Two successful examples are the Finnish and the Swedish multi-source National Forest Inventories, where forest stand parameters, such as volume, are estimated by applying the k nearest neighbor estimation method [175], [148].

Remotely sensed data have also been successfully used to parameterize coarse-scale ecological models that predict the effects of primary environmental drivers such as temperature, precipitation, atmospheric CO², etc. and regional climate change on forest ecosystem function such as net primary productivity, carbon nutrient, and water cycling [197]. Due to the recent and growing demand of forest measurements as well as the increasing availability of a variety of ground-, air- and satellite-based sensors, improved methods are rapidly developing for remote sensing of forest canopy structure at all spatio-temporal scales.

Object-oriented classification of the ASTER and Landsat ETM+ data lead to detailed information about the forested areas and tree type distribution [see Chapter 6]. These are only two of the structural attributes of forest stands that are of interest as part of a general forest inventory. In this chapter, an introduction into forest parameters and its potential estimation by remote sensing data is given, whereafter the used vegetation indices and the applied statistical analysis are described followed by the presentation of the results of the leaf area index (LAI) and forest parameter estimation and the analysis of the descriptive parameters.

7.2 Introduction to Forest Parameter Retrieval

Delineation and forest composition are only two of the structural attributes of forest stands that are of interest as part of a general forest inventory. Some of the other forest attributes of interest might include:

- Tree density,
- Diameter at breast height (DBH),
- Basal area,
- Volume,
- Biomass, and
- Stage of development.

Some of these attributes can be considered as forest conditions to be estimated at some level of precision. Applications of remote sensing aimed at these continuous aspects of the forest inventory have been driven largely by empirical or semi-empirical model estimation [86], [146], [3], [180], [49], [47].

Empirical models might be constructed using the understanding derived from physically based models coupled with laboratory, field, and actual or simulated remote sensing data. The empirical approach is a data driven approach; learning proceeds from understanding the data, data

acquisition and the specific conditions under which models derived from those data were inverted. The form of the model can be inferred from physical considerations, while specific model parameters are estimated from empirical data. Unfortunately, purely empirical models can have the disadvantage of being highly site specific but with a few modifications, empirical methods used in one area to generate a relationship between spectral response and forest conditions, can be applied elsewhere. However, difficulties that can arise when using optical remote sensing data and linear regression techniques are:

- Typically low dynamic range of the data [49], [160];
- Extensive geometric and radiometric corrections are needed;
- Difficulty in reducing extraneous factors [144];
- Low spatial resolution relative to the objects under scrutiny - trees, and
- Generally, small sample sizes resulting in fewer degrees of freedom than required for extensive use.

The most important advantage of empirical modelling is the simplicity to establish the model. Finding the resources to complete the simple normative design that is required to establish a purely empirical relationship between spectral response and a forest parameter is easy, even in highly inaccessible areas.

Some of the physiological conditions that lead to, or are highly diagnostic of forest growth can be described by remote sensing measurements. LAI is an important structural attribute of forest ecosystems because of its potential to be a measure of energy, gas and water exchanges [56]. Physiological processes such as photosynthesis, transpiration and evapotranspiration are functions of LAI [140]. Remote sensing estimation of LAI is based on the knowledge that green leaves interact selectively with solar radiation [182]. Much of the near-infrared energy is reflected by foliage [101] and much of the visible energy, dominated in the red portion of the spectrum, is absorbed by photosynthetic pigments [191]. Vegetation indices can be used to capture the way in which red and near-infrared reflectance differ in a single measure. The common approach to LAI estimation is empirical or semi-empirical modelling, involving correlation of spectral indices with field estimates and the extension of such estimates over larger areas with regression [48], [24], [16]. Remotely sensed reflectance data is actually related to the fraction of incident photosynthetically active radiation (FPAR) absorbed by the canopy [68] and is only related to LAI to the extent that FPAR is related to LAI [24]. One simple LAI model assumes that light absorbed by the canopy can be approximated by the Beer-Lambert Law [192]. Light is attenuated by the canopy with an extinction coefficient k [87]:

$$LAI = (\ln I_z / I_o) / (-k) \quad (\text{Eq. 7.1})$$

where I_z is the PAR measurement under the canopy and I_o is the incoming solar radiation in open areas. This relationship flattens after reaching a threshold. Based on this model, the relation between LAI and any particular vegetation index based on reflectance will be curvilinear, flattening when LAI exceeds approximately 3 to 4 [170], [7].

Estimating forest LAI from satellite sensor data has been investigated by several researchers [24], [47], [190]. However, most of these studies were carried out in western coniferous forests [16], [24], [51].

Several studies established that multispectral satellite remote sensing data was related to tree density [39], basal area [146] and biomass [55], [199], diameter at breast height [160] and volume [3], [183]. These and other studies have led to the understanding that the effect of increasing or decreasing age, DBH, height, volume and so on, are actually all second- or third-order effects on remotely sensed image data. The principal influence on the intensity of the signal is the

illumination and the amount of vegetation viewed from above. Further factors such as stand composition, stand structure can influence the signal. As cover approaches full crown closure, the correlation between reflectance and these biophysical variables approaches zero [62]. In many forests crown closure will reach a maximum and basal area and structural complexity will continue to increase, but the remotely sensed signal is not significantly affected by these increases [55].

Biomass, an estimate of the total living/dead organic material, expressed as a weight per area, has been of greatest interest for studying productivity, carbon cycles, nutrient allocation, and fuel accumulation in terrestrial ecosystems [17], [118], [199]. Past studies have demonstrated that vegetation indices obtained from satellite data are useful predictors of biomass in deciduous as well as coniferous forest stands in temperate and tropical forests worldwide [109], [17], [86], [120], [199].

Volume prediction, using remote sensing, is strongly related to biomass prediction and, in fact, uses the same basic principles. In essence, what is sought is a remote sensing relationship with crown size and closure, and the desired volume or DBH estimate. Volume estimates from satellite imagery are based on the weak relationship between spectral response and stand structure, as captured by imagery, in the differences in illumination and shadowing of forest canopies. A few studies have attempted direct standing volume assessment from multispectral satellite sensor data; almost all have commented that the very low dynamic range (e.g. a range of three DN for all measured volumes in the *red* band [39]) in Landsat TM or SPOT satellite data is a significant factor limiting use for volume inventory at the level of detail required for forest management [41], [49], [160]. Even so, in areas without the resources to conduct forest volume inventory, rough or class-based volume estimates from satellite imagery can be very useful [58].

Forest age and tree height are difficult to estimate by optical satellite remote sensing data. Direct correlation of stand age and remote sensing spectral response approaches a "nonsense" correlation [41]. Age is a descriptor or surrogate of forest conditions but not itself an attribute [31]. The biophysical relationships between height and spectral response are rarely strong enough to justify model development. However, the uses of aerial photography in tree height estimation are well known to forest managers and remote sensing scientists [57].

7.3 Methodology of Forest Parameter Retrieval

After study of technical literature, a selection of vegetation indices (VI's) were computed from the atmospherically corrected ASTER and Landsat ETM+ data. The relations between single band reflectances, vegetation indices and LAI, tree density, DBH, basal area, volume and biomass were analyzed. The division of the forest stand attributes into distinct classes was also tested, but discarded since no estimation improvements were obtained.

Preliminary bivariate correlation analysis was performed to select promising spectral bands and vegetation indices for the following statistical analysis. For the preliminary correlation results using all measurement plot data see Appendix Table 2 and Appendix Table 3.

Linear and non-linear curve-fitting as well as multiple regression analysis was performed by applying the selected reflectances and vegetation indices as independent variables. The models were evaluated by cross-validation. The training and validation datasets were randomly selected. Two-thirds of the totally 38 measurement plots were used as training set ($n = 23$) and the remaining one-third ($n = 15$) of the measurement plots as validation set. The recorded descriptive parameters cultivation, regeneration, vitality, stand structure and understory were investigated qualitatively.

A summary of the selected vegetation indices is displayed in Tab. 7.1, where *nir* stands for the near-infrared wavelength range, *mir*₁ for the middle-infrared wavelength range between 1.56 μm - 1.75 μm and *mir*₂ for the middle-infrared range between 2.1 μm - 2.43 μm .

Table 7.1 Investigated vegetation indices calculated from ASTER and/or Landsat ETM+ bands.

Vegetation Index	Formula	Reference
mDVI _{mir1} , nir - modified Difference VI	$mir_1 - nir$	
mDVI _{mir2} , mir ₁ - modified Difference VI	$mir_2 - mir_1$	
SR - Simple Ratio VI	$\frac{nir}{red}$	[90], [16], [24], [47], [48], [94], [166]
SR _c - Corrected SR	$\frac{nir}{red} \cdot \left(1 - \frac{(mir_1 - mir_{min})}{(mir_{max} - mir_{min})}\right)$	[16], [144]
MVI - Mid-infrared VI	$\frac{nir}{mir_1}$	[51], [166]
MSI - Moisture Stress Index	$\frac{mir_1}{nir}$	[189], [48], [49]
GR - Green Ratio	$\frac{nir}{green}$	[88], [49]
GRVI - Green-Red VI	$\frac{green}{red}$	[95]
NDVI - Normalized Difference VI	$\frac{nir - red}{nir + red}$	[159], [160], [47], [48], [94], [166], [24], [190]
NDVI _{nir, mir₁/mir₂} - modified NDVI or Infrared Index	$\frac{nir - mir_1}{nir + mir_1}$ $\frac{nir - mir_2}{nir + mir_2}$	[71], [93], [48], [62]
NDVI _c - Corrected NDVI	$\frac{nir - red}{nir + red} \cdot \left(1 - \frac{(mir_1 - mir_{min})}{(mir_{max} - mir_{min})}\right)$	[130], [144]
OSAVI - Optimized VI	$\frac{nir - red}{nir + red + 0.16}$	[157], [48]
IPVI - Infrared Percentage VI	$\frac{nir}{nir + red}$	[35]
SAVI - Soil Adjusted VI ¹⁾	$\frac{nir - red}{nir + red + L} \cdot (1 + L)$	[79], [48]
PVI - Perpendicular VI ²⁾	$\frac{nir - (s \cdot red) - sli}{\sqrt{1 + s^2}}$	[6], [166], [33]
WDVI - Weighted Difference VI	$nir - s \cdot red$	[29],
EVI - Enhanced VI ³⁾	$G \cdot \frac{nir - red}{nir + c1 \cdot red - c2 \cdot blue + L}$	[80], [23], [190]
ARVI - Atmospherically Resistant VI ⁴⁾	$\frac{nir - (green - (c \cdot (blue - green)))}{nir + (green - (c \cdot (blue - green)))}$	[96], [48], [33]

1) where $L = 0.5$.2) where $s_{aster} = 0.064242$, $sli_{aster} = 135.717818$ and $s_{etm+} = 0.247384$, $sli_{etm+} = 30.651233$.3) where $G = 2.5$, $c1 = 6$, $c2 = 7.5$, $L = 1$ [80]. EVI was calculated with ETM+ bands only.4) where $c = 1$. ARVI was calculated with ETM+ bands only.

Besides the selected vegetation indices, the first five spectral bands of ASTER, the *vis-swir* bands of Landsat ETM+, including the PAN band, and the tasseled cap coefficients brightness, greenness and wetness were investigated. Tab. 7.2 gives the coefficients for the derived tasseled cap transformations based on Landsat ETM+ at-sensor reflectance. Brightness, the first feature, is a weighted sum of all 6 Landsat ETM+ bands and, as such, is a response to changes in total reflectance driven primarily by soil reflectance changes. Greenness contrasts the sum of the visible and *nir* bands and is thus a measure of the presence and density of green vegetation. Greenness has been shown to be moderately to well correlated to percentage canopy coverage, LAI and fresh biomass. Finally, wetness contrasts the sum of the visible and *nir* bands against the sum of the *mir* bands, providing a measure of soil moisture content and vegetation density [36], [37].

Table 7.2 Tasseled cap coefficients for Landsat 7 ETM+ at-sensor reflectance [76].

Index	Band 1	Band 2	Band 3	Band 4	Band 5	Band 7
Brightness	0.3561	0.3972	0.3904	0.6966	0.2286	0.1596
Greenness	-0.3344	-0.3544	-0.4556	0.6966	-0.0242	-0.2630
Wetness	0.2626	0.2141	0.0926	0.0656	-0.7629	-0.5388

LAI can also be estimated by WDV I according to the inverse of an exponential function, [28], [29], [18], Eq. 7.2:

$$LAI = -\frac{1}{\alpha} \cdot \ln\left(1 - \frac{WDVI}{\rho_{\infty}(\lambda_{nir})}\right) \quad (\text{Eq. 7.2})$$

where α and $\rho_{\infty}(\lambda_{nir})$ have to be determined empirically from a ground truth data set, e.g. the training set ($n = 23$). The model was mainly applied to LAI predictions from agricultural vegetation [100]. Even so, this model was tested in this study in addition to the simple linear model.

7.4 Results

7.4.1 Analysis of LAI Measurements

First, correlation coefficients r were computed for the overall relationships between LAI and the spectral bands of ASTER and Landsat ETM+ data.

ASTER3 and ASTER5 to ASTER9 as well as ETM2, ETM3, ETM4 and the second tasseled cap derivative, greenness, were significantly correlated with the upward LAI measurements [Tab. 7.3]. Less correlation existed with the total LAI (LAI_{uw+dw}), summarizing upward and downward LAI measurements. The influence of understory on the LAI-reflectance relationship seems to be less than expected despite the typically, rather sparse overstory situation in Lenga forest stands. Similar observations were made in sparse coniferous forests in Sweden [49]. It can be noted that correlation for ASTER bands were higher than for Landsat ETM+ bands.

For the calculation of mNDVI the *mir*₂ band ASTER5 was taken, even though Tab. 7.3 shows that ASTER6 would have been equally suitable due to similar strong correlation with LAI.

The definition of the nomenclature is as follows: If the investigated vegetation indices are based on ASTER bands an A is appended to the vegetation indices' name, if they are based on Landsat ETM+ bands an E is appended. For the modified difference VI's these abbreviations are applied too. The added numbers stand for the applied bands.

Table 7.3 Correlation coefficients r for linear relationships between LAI, LAI_{uw+dw} (summarizing upward and downward measurements) and the ASTER- and Landsat ETM+ bands ($n = 38$). Correlation coefficients in bold are statistically significant at the 0.01 level (2-tailed).

Band	LAI	LAI _{uw+dw}
ASTER1	-0.008	0.162
ASTER2	-0.145	0.008
ASTER3	0.685	0.697
ASTER4	-0.329	-0.185
ASTER5	-0.750	-0.587
ASTER6	-0.751	-0.656
ASTER7	-0.713	-0.609
ASTER8	-0.661	-0.559
ASTER9	-0.726	-0.660
ETM1	-0.384	-0.173
ETM2	-0.466	-0.259
ETM3	-0.571	-0.282
ETM4	0.548	0.374
ETM5	-0.283	-0.165
ETM7	-0.254	-0.045
ETM PAN	0.348	0.290
Brightness	0.231	0.184
Greenness	0.597	0.336
Wetness	0.328	0.155

7.4.2 Determination of LAI

Overall correlation, selecting all measurement plots, was performed first to identify potentially suitable vegetation indices to predict LAI [Appendix Table 2]. Statistically significant ($p \leq 0.01$) correlating spectral bands and vegetation indices were selected and regression analysis, based on cross-validation, performed.

Tab. 7.4 lists the results based on simple linear regression analysis for the ASTER and Landsat ETM+ derivatives and LAI. For every model shrinkage, the difference between the validation dataset R^2 and the training set R^2 , and R^2 were calculated. Additionally, root mean square error, RMSE (Eq. 7.3), and relative root mean square error, RRMSE (Eq. 7.4) were calculated.

$$RMSE = \sqrt{\frac{\sum_{i=1}^n (\hat{y}_i - y_i)^2}{n}} \quad (\text{Eq. 7.3})$$

$$RRMSE = 100 \cdot \frac{RMSE}{\bar{y}} \quad (\text{Eq. 7.4})$$

where y_i = measured value of variable y on plot i ; \hat{y}_i = estimated value of variable y on plot i ; \bar{y} = mean of the observed values and n the number of plots.

The smaller the shrinkage, the more confidence can be had in the generalizability of the established model equation. Hence, the models based on ASTER5, A5-A4, MSI E and mNDVI_(E4,E7) listed in Tab. 7.4 and previously defined in Tab. 7.1 should be implicitly used with caution.

Table 7.4 Parameter estimates for regression models: LAI = $a + b \cdot VI$ and respective shrinkage. Validation of linear LAI models ($n = 15$): Coefficient of determination (R^2) and relative RMSE. R^2 in bold signify statistically significant correlation coefficients ($p = 0.01$ (2-tailed)).

Band/VI	a	b	Shrinkage	R^2	RRMSE [%]
ASTER3	-1.819601	0.051997	-0.205	0.608	12.911
ASTER5	7.355676	-0.205758	0.213	0.424	18.179
ASTER6	6.770764	-0.215708	0.052	0.520	14.944
A4-A3	-0.586923	-0.053314	-0.132	0.630	13.271
A5-A4	2.179813	-0.152448	0.289	0.017	23.530
GR A	-2.095587	1.871999	-0.179	0.572	14.737
MVI A	-0.896501	0.96922	-0.304	0.707	11.281
MSI A	4.836071	-8.382739	-0.109	0.575	14.694
mNDVI _(A3,A4)	-1.866269	7.805989	-0.279	0.704	12.082
mNDVI _(A3,A5)	-1.442668	7.293025	0.080	0.604	15.049
PVI A	5.388144	0.053396	0.000	0.548	14.468
WDVI A lin.	-1.794601	0.052574	-0.204	0.612	12.930
ETM3	3.121521	-0.119890	0.098	0.272	17.584
E7-E5	2.195792	0.010023	0.001	0.006	21.48
MVI E	-0.636668	1.631424	-0.021	0.460	15.894
MSI E	4.761679	-4.403736	0.417	0.194	24.284
SR E	0.797044	0.162258	-0.072	0.480	15.064
NDVI E	-1.900373	5.208422	-0.006	0.508	14.814
mNDVI _(E4,E5)	0.733409	5.473081	0.025	0.429	17.269
mNDVI _(E4,E7)	-0.008556	3.323373	0.220	0.069	27.600
IPVI E	3.308049	-10.416844	-0.006	0.508	14.814
OSAVI E	-1.899686	5.218565	-0.007	0.510	14.815
ARVI E	-0.570311	3.880368	0.468	0.142	20.446
PVI E	1.225727	0.053396	0.000	0.145	19.912
WDVI E lin.	-0.870942	0.044375	0.048	0.324	18.454
Clevers WDVI A	$\alpha = 0.540985$ $\rho_{\infty}(\lambda_{nir}) = 109.830758$		0.100	0.284	27.752
Clevers WDVI E	$\alpha = 0.297340$ $\rho_{\infty}(\lambda_{nir}) = 144.991541$		0.058	0.304	18.535
Lin. mult. regr.	OSAVI E $\cdot 3.971 + \text{ASTER3} \cdot 0.03 - 3.429$		-0.029	0.674	19.702

The vegetation indices MVI A and mNDVI_(A3,A4) with an R^2 of 0.707 and 0.704 respectively, performed best followed by the developed linear multiple regression based on OSAVI E and

ASTER3 ($R^2 = 0.674$). A second group of vegetation indices achieving an $R^2 > 0.60$, consisted of A4-A3, WdVI A lin., ASTER3 and $mNDVI_{(A3,A5)}$. The best modelling result, based on Landsat ETM+ bands, was attained with OSAVI E ($R^2 = 0.510$). The results show that the vegetation indices, based on ASTER data, correlated stronger with LAI than the vegetation indices derived from Landsat ETM+ data, that can be explained by the lower overall correlations of Landsat ETM+ bands with LAI [Tab. 7.3].

Vegetation indices containing information from mir_1 bands, MVI A, $mNDVI_{(A3,A4)}$ and A4-A3, performed best. The mir_1 band in combination with the nir band seems to contain more information relevant to the characterization of LAI than the combination of red and nir bands. A closer relation of forest LAI to radiation in the mir , than to radiation in the visible domain, was also found by Boyd et al. [14] for tropical vegetation. The authors expected that this could be the case also with boreal forests. The results found in this study also support the suggestion by Fassnacht et al. [51] that mir bands may improve LAI estimations, particularly in more open forest stands. Lee et al. [110] and Schlerf et al. [166] found with imaging spectroscopy data that spectral bands in the red edge and mir regions correlated most with LAI of different biomes but particularly with forested sites. However, vegetation indices containing information from mir_2 , e.g. $mNDVI_{(A3,A5)}$ or A5-A4, achieved lower R^2 than vegetation indices derived from mir_1 bands.

For linear multiple regression analysis, all bands and vegetation indices served as input. Strongest correlation was found for a combination of Landsat ETM+ derived vegetation index OSAVI E and the ASTER band 3 with an R^2 of 0.674. Both variables correlated fairly strong with LAI, with simple linear regression models.

The linear relationship of WdVI and LAI was stronger than the non-linear relationship. Both, WdVI A and WdVI E achieved higher R^2 by applying the linear model to the vegetation indices. The non-linear relationship found by Clevers might apply to agricultural cultivars but less so to deciduous or coniferous forest vegetation [65]. The results also prove that soil background plays a minor role in Lenga forest stands as all soil correcting vegetation indices SAVI, PVI and WdVI achieved comparably lower R^2 except for OSAVI E.

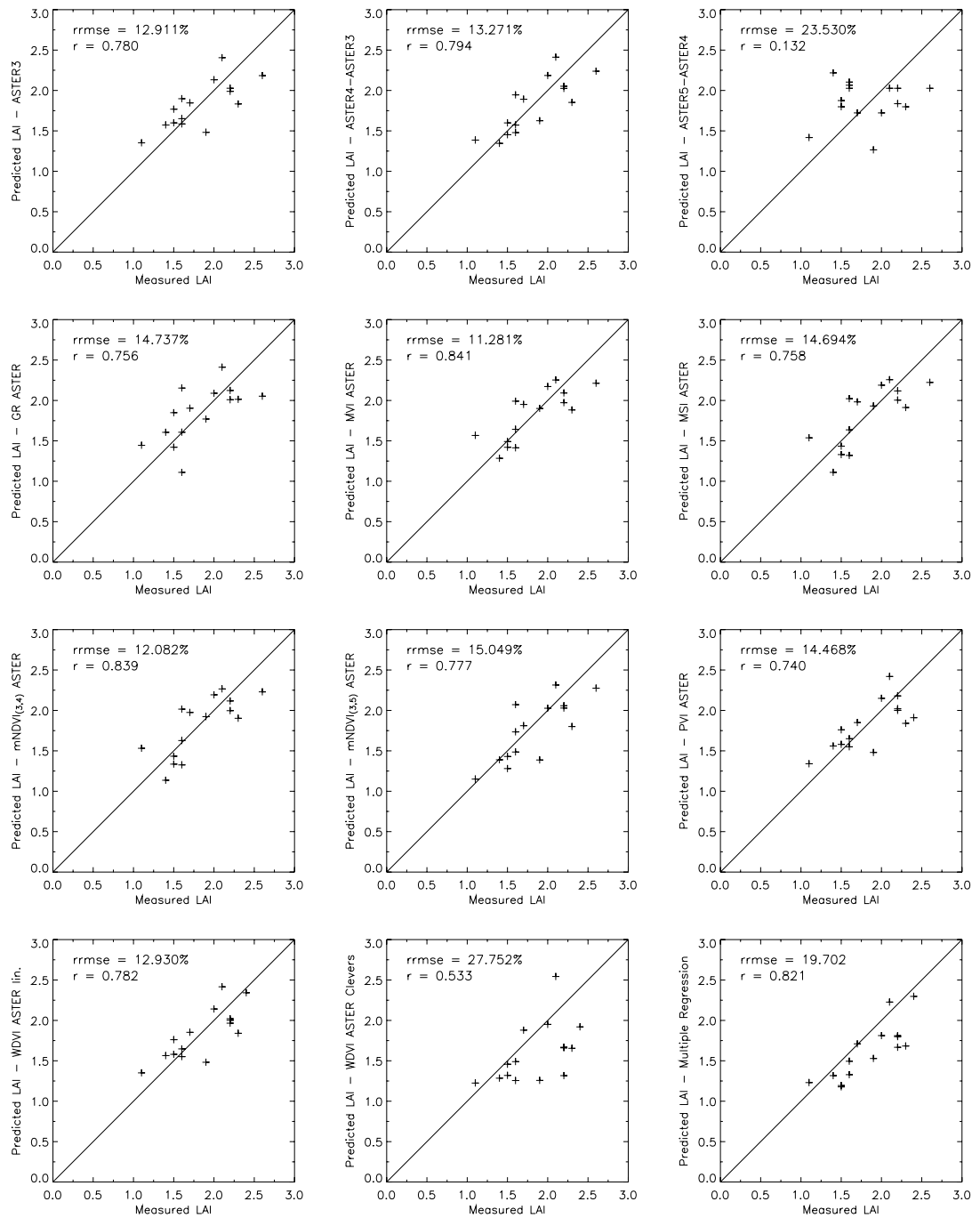


Figure 7.1 Measured LAI versus modelled LAI from ASTER reflectances and vegetation indices respectively. The lowest right plot shows the result from linear multiple regression. Each cross corresponds to a measurement plot. The diagonal line represents the 1:1 relationship.

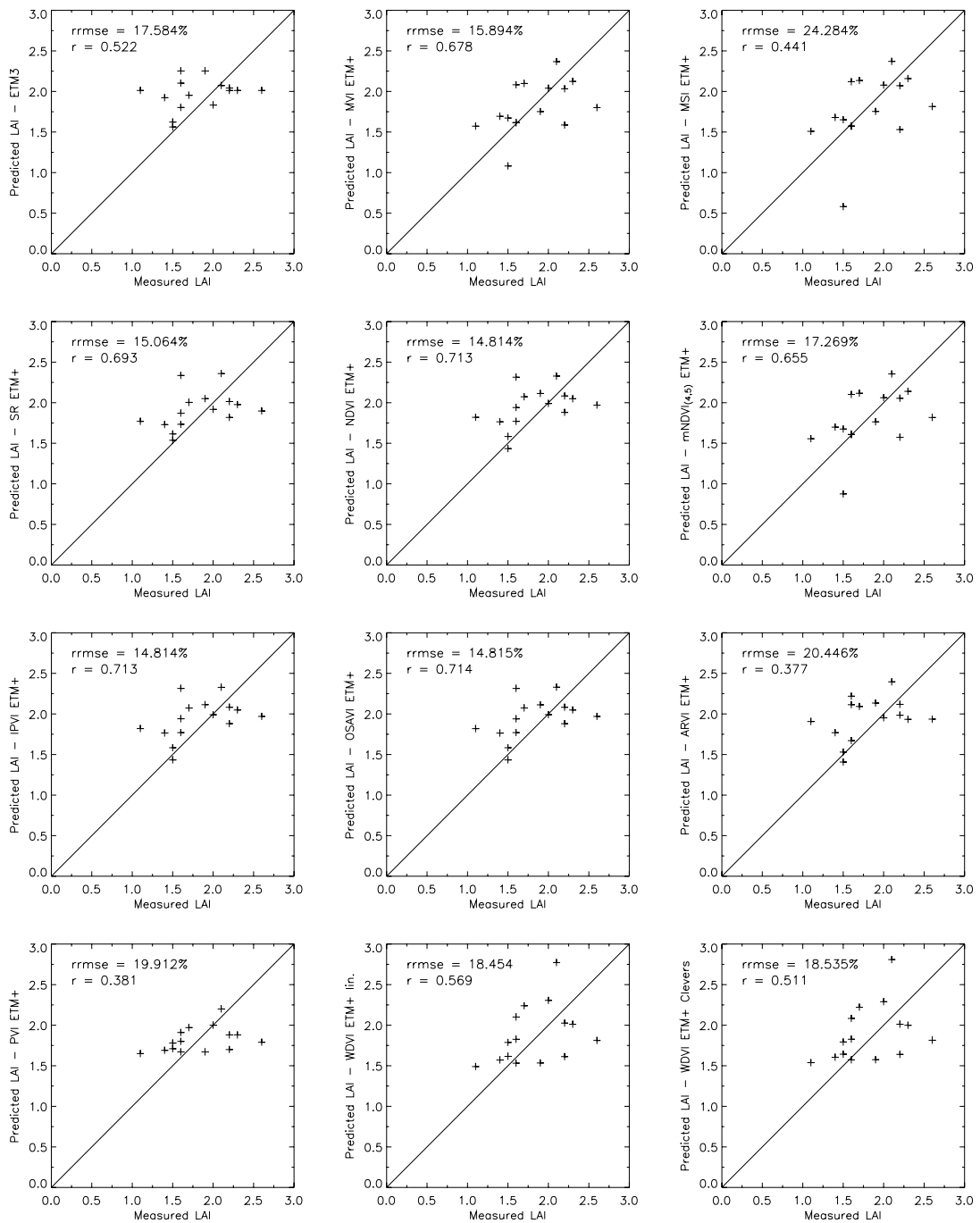


Figure 7.2 Measured LAI versus modelled LAI from Landsat ETM+ reflectances and vegetation indices respectively. Each cross corresponds to a measurement plot. The diagonal line represents the 1:1 relationship.

The two vegetation indices EVI and ARVI have been shown to minimize canopy background influence and reduce atmospheric variation by including information from the Landsat ETM+ blue and green bands [see Tab. 7.1] [81], [25]. But EVI did not correlate significantly with LAI measurements and ARVI was only weakly related to LAI. The findings of Brown et al. [16] that

soil-adjusted vegetation indices have a decreased sensitivity to forest LAI can thus be confirmed. Vegetation indices based on *nir* and *red* information furthermore correlated weakly with LAI. Information from the green band also did not improve the LAI estimations with an R^2 of 0.572 for the vegetation index GR E. A selection of the best cross-validation results for the ASTER derived vegetation indices and the linear multiple regression model is displayed in Fig. 7.1. Fig. 7.2 shows the strongest relationships between Landsat ETM+ derived vegetation indices and LAI. The estimation of LAI, utilizing the vegetation index with the highest R^2 , resulted in a RRMSE of 11.28% or an RMSE of 0.21.

7.4.3 Conclusions on LAI Determination

Determination of LAI for Lenga forest stands performs best with a vegetation index based on *mir*₁ and *nir* reflectances such as MVI A and mNDVI_(A3,A4). LAI can be estimated for Lenga forest stands with ASTER data at relative RMSE around 12%. Working with Landsat ETM+ data can lead to slightly higher RMSE due to different radiometric configuration and lower geometric resolution. Vegetation indices that account for canopy- or soil background, or atmospheric influences, do not improve RMSE.

7.4.4 Determination of Forest Parameters

The first step in the analysis of the measured forest parameters was to examine the relationships among themselves [Tab. 7.5]. Tree density was negatively correlated with dominant height and DBH. This relationship is clearly functionally related to growth. Basal area was only weakly correlated with DBH and dominant height, whereas biomass correlated well with dominant height and volume with both parameters, DBH and dominant height. All three parameters were derived from DBH and/or tree height. Biomass correlated positively with volume, which clearly illustrates that the more timber volume available in the forest stand, the more biomass exists. Surprisingly tree density did not significantly correlate with LAI and biomass.

LAI_{uw+dw} correlated stronger with the forest parameters than LAI. A strong positive relationship existed with the forest parameters basal area, volume and biomass.

Intercorrelations between LAI, basal area, volume and biomass can be explained in that young stands have low values for the four parameters, and values increase as forest stands develop to a mature condition.

Table 7.5 Correlation coefficients r for the linear relationships in-between LAI and the measured forest parameters ($n = 38$). Correlation coefficients in bold are statistically significant at the 0.01 level (2-tailed).

	LAI	LAI uw+dw	Tree Density	DBH	Dom. Height	Basal Area	Volume
LAI							
LAI uw+dw	0.809						
Tree Density	0.378	0.188					
DBH	-0.133	0.186	-0.751				
Dom. Height	-0.021	0.022	-0.448	0.390			
Basal Area	0.488	0.605	0.246	0.221	-0.099		
Volume	0.348	0.511	0.117	0.456	0.434	0.803	
Biomass	0.323	0.440	-0.060	0.357	0.416	0.779	0.954

Secondly, the relationship between the forest parameters and the remotely sensed data using

linear correlation analysis was examined [Tab. 7.6].

Tree density correlated most with ETM4, ETMPAN, greenness and brightness, derived from the Landsat ETM+ dataset. They were all positively correlated with tree density. Furthermore, all positive relationships with tree density were stronger for the Landsat ETM+ bands than for the ASTER bands. Similar relationships between *nir* bands and tree density were observed by Danson et al. [39] and Ekstrand [49] who examined the relationships for coniferous forests. The relationship can be explained as follows: the higher tree density, the less shadow influences and therefore the higher *nir* reflectances. With complex-structured old-growth stands, tree density is getting lower and consequently also *nir* reflectances; a positively correlated relationship is the corollary. Fig. 7.3 illustrates this effect in the observed Lenga plots. Old-growth and large timber stands have a low tree density and *nir* reflectance, whereas stands with small timber and mixed timber stages have medium to high tree densities and *nir* reflectances.

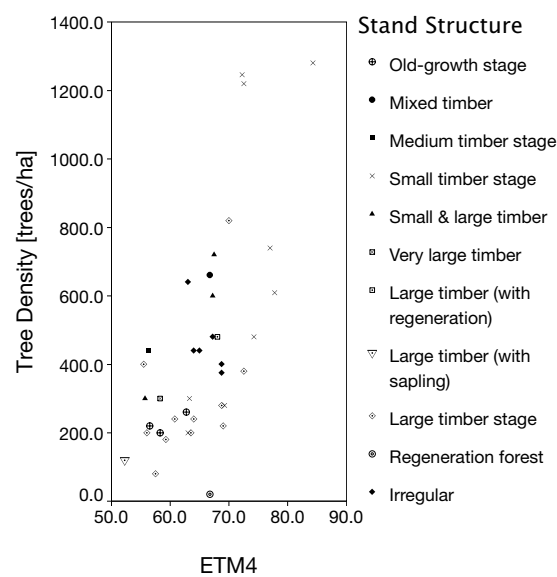


Figure 7.3 The relationship between tree density and forest stand structure and its impacts on the *nir* band ETM4 (n=38).

Greenness responded to the combination of high absorption in the visible bands and high reflectance in the near-infrared which is characteristic of green vegetation [36]. It has been shown to be a measure of vegetation density [37]. Brightness instead was responsive to changes in total reflectance and to those physical processes which affect total reflectance. Growing shadow influences tend to decrease brightness which makes it sensitive to forest stand structure [36]. This could explain the significant correlation with tree density in this study.

Table 7.6 Correlation coefficients r for linear relationship between the measured forest parameters and the spectral reflectances of ASTER and Landsat ETM+ data (n = 38). Correlation coefficients in bold are statistically significant at the 0.01 level (2-tailed).

	Tree Density	DBH	Dom. Height	Basal Area	Volume	Biomass
ASTER1	-0.050	0.063	-0.301	0.193	-0.049	-0.026
ASTER2	-0.299	0.293	-0.208	0.089	-0.026	-0.060
ASTER3	0.382	-0.203	-0.196	0.364	0.176	0.153
ASTER4	-0.265	0.162	-0.133	-0.176	-0.186	-0.109

Table 7.6 Correlation coefficients r for linear relationship between the measured forest parameters and the spectral reflectances of ASTER and Landsat ETM+ data ($n = 38$). Correlation coefficients in bold are statistically significant at the 0.01 level (2-tailed).

	Tree Density	DBH	Dom. Height	Basal Area	Volume	Biomass
ASTER5	-0.346	0.109	0.016	-0.490	-0.337	-0.279
ASTER6	-0.334	0.085	0.062	-0.535	-0.382	-0.322
ASTER7	-0.381	0.142	0.050	-0.526	-0.351	-0.304
ASTER8	-0.405	0.185	0.069	-0.578	-0.422	-0.392
ASTER9	-0.259	0.036	-0.123	-0.497	-0.444	-0.397
ETM1	-0.272	0.186	-0.093	-0.160	-0.146	-0.068
ETM2	-0.114	0.103	-0.138	-0.232	-0.291	-0.271
ETM3	-0.251	0.209	-0.086	-0.088	-0.102	-0.123
ETM4	0.657	-0.491	-0.268	0.165	-0.116	-0.109
ETM5	-0.095	0.073	0.009	-0.087	-0.084	-0.067
ETM7	-0.223	0.254	-0.109	0.024	0.029	0.047
ETMPAN	0.535	-0.398	-0.131	0.283	0.111	0.212
Brightness	0.417	-0.279	-0.377	0.133	-0.153	-0.166
Greenness	0.560	-0.502	-0.071	0.122	-0.035	-0.066
Wetness	0.180	-0.252	0.169	-0.081	-0.039	-0.040

DBH showed a similar relationship. It correlated negatively with greenness and ETM4. Again, Danson et al. [39] observed a similar behavior between DBH and *nir* bands. Moreover, a weaker relation between DBH and ETMPAN was observed.

To what was expected, dominant height did not correlate with any of the spectral bands, as biophysical relations between stand height and spectral reflectance are generally weak and can only be determined by visual interpretations of very high resolution images, as discussed in Chapter 7.2.

Basal area correlated strongly with the *mir*₂ bands of the ASTER dataset. All *mir* relationships with basal area were negatively correlated. A slightly weaker positive correlation between basal area and the ASTER *nir* band was detected. For basal area the ASTER bands correlated stronger than the Landsat ETM+ bands. Pühr et al. [146], Jakubauaskas [86] and Salvador et al. [160] observed negative relationships between basal area and the Landsat TM7 band. In this study ETM7 did not correlate at all with basal area.

Volume correlated significantly with the two *mir*₂ bands, ASTER8 and ASTER9. All other correlations were weak, including the correlation with ETM7. Salvador et al. [160] observed a strong correlation between volume and Landsat TM7 for deciduous tree stands, which corresponds to the ASTER bands 5 to 9 as well as some other studies, that have identified the *mir* region as being most sensitive to changes in forest wood volume with reflectance in this region being directly related to the extent of canopy closure [75], [180].

Moreover, it was shown that, with the exception of the *nir* region, the reflectances of Landsat TM and SPOT bands show a general negative correlation with wood-volume and volume-related parameters. In the *nir* region, however, correlation may be positive, negative or flat [180]; the latter was also the case in this study. Positive correlations generally occur at high LAI in closed canopy forests, while negative correlations occur in open-canopied forests when the understory has a higher *nir* reflectance than the canopy [170]. Furthermore, shadowing plays an important part in the response of all bands to changes in wood volume [3], and is thought to be at least as

important as canopy water content in determining the *mir* response [75]. In Fig. 7.4 the relationship between the *nir* band, the best correlating *mir* band and volume is shown, including the understory situation for each measurement plot. However, no significant difference of behavior of plots with either high or low understory situation is observable.

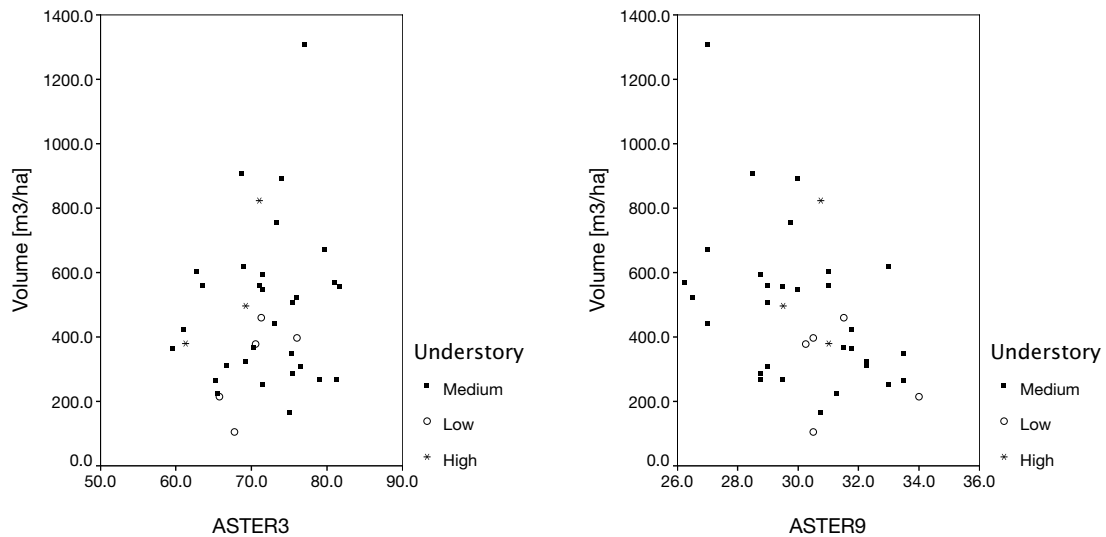


Figure 7.4 The relationship between ASTER3 and ASTER9 respectively, volume and its understory situation for each plot measurement ($n=38$).

Biomass did not correlate significantly with any of the spectral bands. Highest correlations were found for the ASTER *mir*₂ bands.

7.4.4.1 Tree Density

Statistically significant ($p \leq 0.01$ or $p \leq 0.05$) correlating spectral bands and/or vegetation indices were selected, and linear regression analysis, based on cross-validation, was performed. Only four vegetation indices were significantly correlated with tree density, they are listed in Tab. 7.7. The soil adjusted vegetation indices PVI and WDVI achieved the best R^2 . They are both based on *nir* and *red* reflectances and account for soil background effects, whereas MSI and MVI are based on *nir* and *mir*₁ reflectances. Very high tree densities were underestimated by all vegetation indices, whereas medium and low tree densities were both, under- and overestimated [Fig. 7.5].

Table 7.7 Parameter estimates for regression models: Tree density = $a + b \cdot VI$ and Shrinkage. Validation of linear tree density models ($n = 15$): Coefficient of determination (R^2) and relative RMSE.

Band/VI	a	b	Shrinkage	R^2	RRMSE [%]
MSI E	1732.570105	-2074.382431	0.029	0.340	93.647
MVI E	-1091.869019	945.056926	0.052	0.398	88.898
PVI E	-491.515378	32.164082	0.000	0.558	44.607
WDVI E lin.	-1207.740267	25.391583	-0.187	0.558	68.606

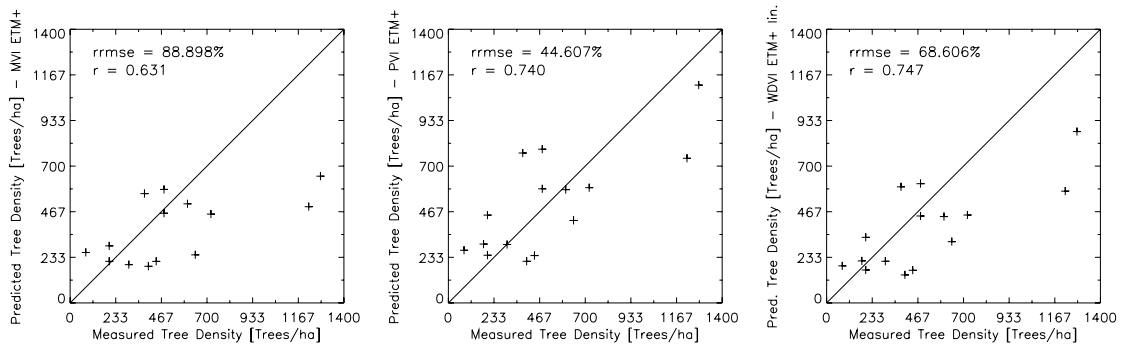


Figure 7.5 Measured tree density versus modelled tree density. Only best performing vegetation indices were plotted. Each cross corresponds to a measurement plot. The diagonal line represents the 1:1 relationship.

Native Lenga forests stands generally have larger gaps and a more open canopy than other deciduous forests where the background may have a larger influence on reflectance and consequently on its relation to tree density. Fig. 7.6 shows that high understory influences at low tree densities are corrected for the PVI E as opposed to the NDVI E and the MVI E. As a result, background effects related to soil and litter were reduced.

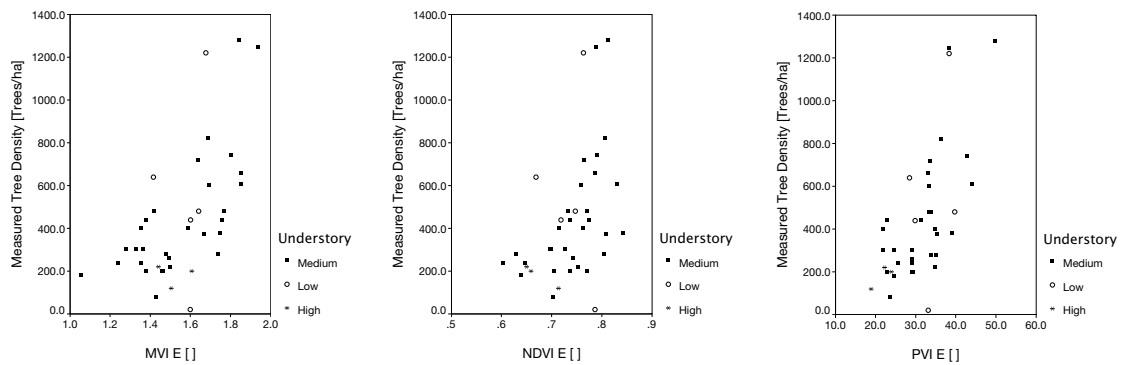


Figure 7.6 The relationship between the vegetation indices MVI E, NDVI E and PVI E respectively, tree density and its understory situation for each measurement plot (n=38).

Schlerf et al. [166] observed with hyperspectral image data that tree density of coniferous forests correlated most with the *nir* region, followed by the green peak, the *mir* region, and the chlorophyll absorption features in the red and blue wavebands. In this study, correlations with tree density were highest for the *nir* band ETM4, moderately for the *red* band ETM3 and weak for the *mir*₁ band ETM5. The ASTER bands correlated differently with tree density. The *mir*₂ and *nir* bands correlated strongest with tree density followed by the *red* band. The different behavior of the sensors reflectances can not be fully explained. Different band widths and positions as well as different geometric resolutions may be reasons for their diverse behavior.

Correlation trends should be in clear variance with each other to yield better results [49]. Still, it seems that the *nir-red* based vegetation indices as well as the *nir-mir*₁ combinations derived from Landsat ETM+ reflectances, describe the behavior of tree density best in this study.

The estimation of tree density utilizing the vegetation index with the highest R² resulted in a RRMSE of 44.61% or an RMSE of 226.01 trees/ha. Tree density estimation in Finland based on laser scanning data achieved RRMSE of 72.7%, and accordingly the estimation results of this

study are promising [121].

7.4.4.2 DBH

Correlations of DBH with spectral bands and vegetation indices were moderate. The four strongest statistically significant ($p \leq 0.05$) correlating spectral bands and vegetation indices were selected and linear regression analysis based on cross-validation, performed. The results are listed in Tab. 7.8. Highest R^2 was achieved by two single bands, greenness and ETM4, followed by the soil adjusted vegetation indices WDVIE and PVI E. As with tree density, the best estimations of DBH were obtained with Landsat ETM+ derived bands or indices. In Fig. 7.7 it can be seen that small DBH were rather underestimated while large DBH values were well modelled or only slightly underestimated. Both, greenness and ETM4 had a strong negative correlation with DBH.

Table 7.8 Parameter estimates for regression models: $DBH = a + b \cdot VI$ and Shrinkage. Validation of linear DBH models ($n = 15$): Coefficient of determination (R^2) and relative RMSE.

Band/VI	a	b	Shrinkage	R^2	RRMSE [%]
ETM4	102.029356	-0.908809	-0.092	0.299	25.934
Greenness	366.468593	-1.872857	-0.127	0.365	25.414
PVI E	68.404455	-0.898685	0.000	0.298	26.842
WDVIE lin.	98.89433	-0.894529	-0.083	0.298	25.958

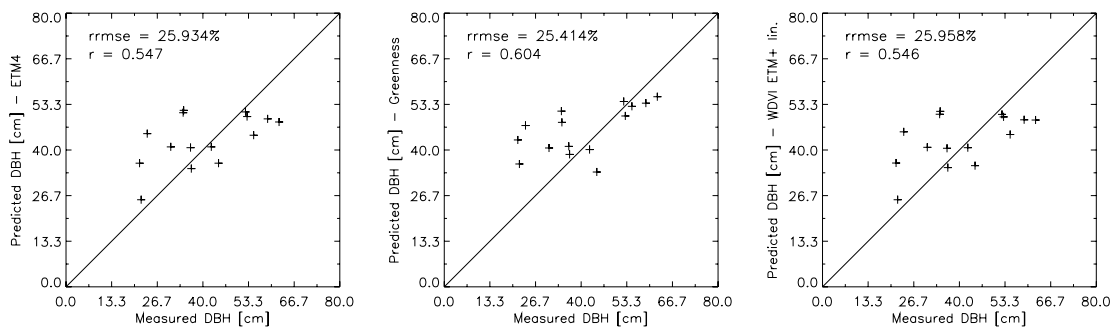


Figure 7.7 Measured DBH versus modelled DBH. Only best performing vegetation indices are plotted. Each cross corresponds to a measurement plot. The diagonal line represents the 1:1 relationship.

The higher DBH, the older are the trees and the more complex the stand structure. With complex stand structures shadow influences increase and consequently *nir* reflectance decreases, a negative relationship between DBH and *nir* region is the consequence. Schlerf et al. [166] found that the *nir* region of reflectance spectra revealed the strongest correlations with DBH, followed by the green peak and the *mir* region. Also, Danson et al., [39] detected strong correlations between a coniferous forest and the *nir* reflectances from a SPOT dataset. Due to its high sensitivity to vegetation density, greenness behaves similar to the *nir* band.

The regression models based on the vegetation indices WDVIE and PVI achieved the best approximations of DBH. Again, site-specific soil adjustment of WDVIE and PVI corrected for understory influences [Fig. 7.8], whereas simpler soil adjusted vegetation indices based on constant correction factors derived from literature did not seem to correctly adjust background influences and did therefore not correlate significantly with tree density and DBH.

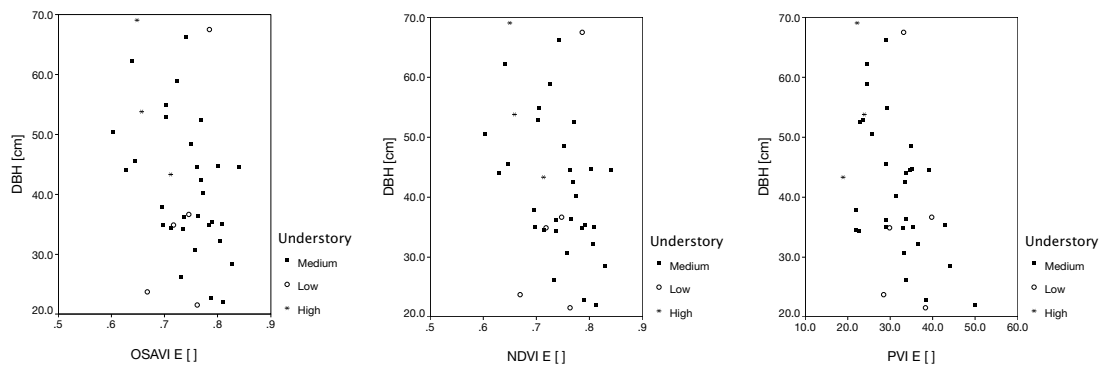


Figure 7.8 The relationship between the vegetation indices OSAVI E, NDVI E and PVI E respectively and DBH and its understory situation for each measurement plot ($n=38$).

The achieved RRMSE for the four best performing models do not vary much. RRMSE of 25.41% to 26.84% for DBH were obtained. Tuominen et al. [183] have reported RRMSE of 49.2% for DBH estimation in Finland working with airphotos and using the k nearest neighbor estimation method. When compared to the mentioned and other studies the results presented here are promising.

7.4.4.3 Basal Area

Basal area correlated strongly with several spectral bands and vegetation indices as well as the LAI. Statistically significant ($p \leq 0.01$ or $p \leq 0.05$) correlating spectral bands and vegetation indices were selected and linear regression analysis based on cross-validation, performed. Additionally, the suitability of LAI as estimator of basal area was analyzed. The results are presented in Tab. 7.9.

Table 7.9 Parameter estimates for regression models: Basal area = $a + b \cdot VI$ and Shrinkage. Validation of linear basal area models ($n = 15$): Coefficient of determination (R^2) and relative RMSE.

Band/VI	a	b	Shrinkage	R^2	RRMSE [%]
ASTER6	174.037130	-5.713072	-0.425	0.619	28.765
ASTER7	197.609975	-6.312061	-0.214	0.464	41.299
ASTER8	206.20452	-8.158384	-0.078	0.410	32.361
ASTER9	190.738768	-4.847484	-0.256	0.465	42.135
mNDVI _(A3,A4)	-13.028741	121.469501	-0.391	0.445	31.263
mNDVI _(A3,A5)	-33.816664	172.619636	-0.262	0.445	33.192
Lin. mult. reg.	ETM3 \cdot 3.515 + ASTER8 \cdot -11.362 + 234.167		-0.072	0.527	39.756
LAI	11.107128	18.102018	-0.272	0.460	30.378
LAI uw+dw	-6.779365	18.055259	-0.217	0.567	30.363

The ASTER mir_2 bands achieved the best estimations of basal area besides the linear multiple regression. ASTER6 performed best with an R^2 of 0.619. The best performing vegetation indices are mNDVI_(A3,A4) and mNDVI_(A3,A5) with an R^2 of 0.445. Also LAI_{uw+dw} did well in predicting basal area with an R^2 of 0.567. LAI reached a lower R^2 of 0.460.

Most estimators are based on ASTER mir_2 reflectances, some include information from the nir bands. The strong negative correlations of the mir_2 bands with basal area can be explained by higher shadow influences and less atmospheric scattering in complexly structured forest stands containing trees with high basal area [146]. The nir bands relation to basal area is inverse. The stronger the inverse, the better the relation to basal area and consequently the prediction [49]. The ASTER nir band correlated moderately with basal area whereas ETM4 hardly correlated with basal area. Still good results were reached, when taking into account the combinations $mNDVI_{(A3,A4)}$ and $mNDVI_{(A3,A5)}$ or the linear multiple regression with ASTER8.

The higher basal area, the more mir_2 reflectances are controlled by understory and the mir_2 - basal area relationship flattens off [146]. This could explain the slight underestimation of high basal area values in this study [Fig. 7.9].

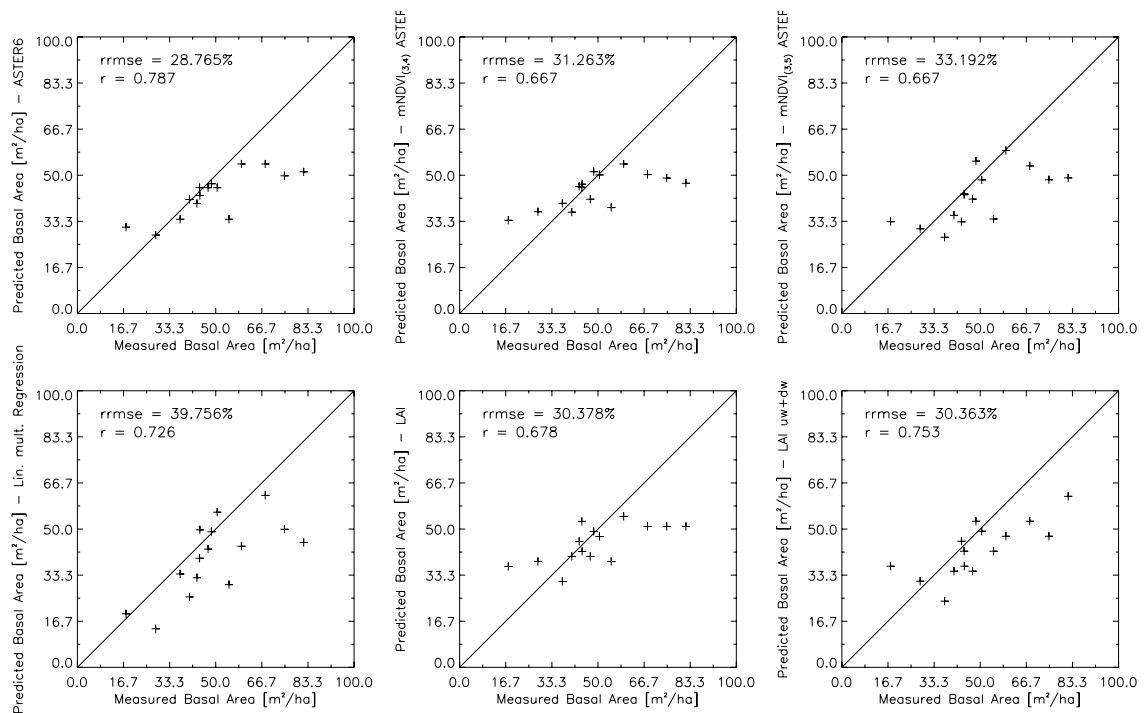


Figure 7.9 Measured basal area versus modelled basal area. Only best performing vegetation indices were plotted. Each cross corresponds to a measurement plot. The diagonal line represents the 1:1 relationship.

The calculated RRMSE in basal area estimation are between 28.77% and 41.30%. It should be noted that high R^2 does not automatically guarantee low RRMSE. For instance, the linear multiple regression model has a high R^2 but also rather high RRMSE and, ASTER8 has a low R^2 but also a low RRMSE. The estimated basal area results are comparable to results in other studies. Tuominen et al. [183], for example, modelled basal area with an RRMSE of 44.3% in mixed forests in Finland.

LAI and LAI_{uw+dw} are also suitable to model basal area. A slightly better result was achieved with the LAI_{uw+dw} . If LAI and LAI_{uw+dw} are modelled with their best estimator, MVI A for LAI and A4-A3 for LAI_{uw+dw} , the RRMSE changes only fractionally. RRMSE for the modelled basal area via the modelled LAI amounts to 31.335% with an R^2 of 0.416 ($p = 0.01$). The modelled basal area based on the modelled LAI_{uw+dw} amounts to 32.052% with an R^2 of 0.407 ($p = 0.05$).

7.4.4.4 Volume

Volume correlated mostly with the ASTER mir_2 reflectances, still correlations were low and only ASTER8 and ASTER9 correlated significantly at the 0.01-level. The modelled volume results, derived from ASTER8 and ASTER9, achieved very low R^2 , 0.158 and 0.174 respectively. Solely LAI_{uw+dw} and LAI yielded acceptable volume estimations; LAI_{uw+dw} with a simple linear model and a logarithmic model attained the best R^2 and RRMSE.

Similar studies applying a logarithmic instead of a linear regression analysis were conducted. For denser stands and canopy cover of 100%, basal area and biomass may continue to increase, while the signal recorded is not altered anymore, making a log transformation of the data or a logarithmic regression analysis necessary [55]. However, in this study, initial testing indicated slightly lower results for a logarithmic curve estimation because in native Lenga forests, canopy cover seldom reaches 100% and therefore a linear relationship is more appropriate.

The highest R^2 was 0.348 and is significant at the 0.05-level of confidence, as well as the second best model result with an R^2 of 0.309. RRMSE are between 35.48% and 37.62%. If LAI_{uw+dw} and LAI are modelled with their best estimator, the RRMSE changes reasonably. RRMSE for the modelled volume via the modelled LAI amounts to 38.48% with an $R^2 = 0.176$ ($p = 0.119$); and the modelled volume based on the linearly modelled LAI_{uw+dw} amounts to 39.55% where $R^2 = 0.144$ ($p = 0.163$).

Despite the low R^2 , RRMSE are comparable with the results from other volume estimation studies. Poso et al. [145] have reported volume RRMSE of 73% with Landsat TM data and the k nearest neighbor estimation method at plot level in Finland, and a recent study in North American conditions Franco-Lopez et al. [54] have reported RRMSE of approximately 65% for volume.

It has also been shown that with similar volume estimation results having a highly significant but weak relation to wood volume, estimates will only be accurate for large areas [55], [180]. Päivinen et al. [136] showed that volume RRMSE in Finland is descending and liability rising the larger the area size, because the variation of mean volume for small forest blocks is greater than that for large ones. For forest areas larger than 50 ha, RRMSE of 30% and smaller are reached.

Table 7.10 Parameter estimates for regression models: Volume = $a + b \cdot VI$ and Shrinkage. Validation of linear volume models (n = 15): Coefficient of determination (R^2) and relative RMSE.

Estimation Parameter	a	b	Shrinkage	R^2	RRMSE [%]
LAI	177.837909	161.138929	-0.115	0.223	37.619
LAI uw+dw lin.	-74.1367	192.42176	-0.056	0.348	35.481
LAI uw+dw log.	-34.689066	498.918846	-0.052	0.309	36.008

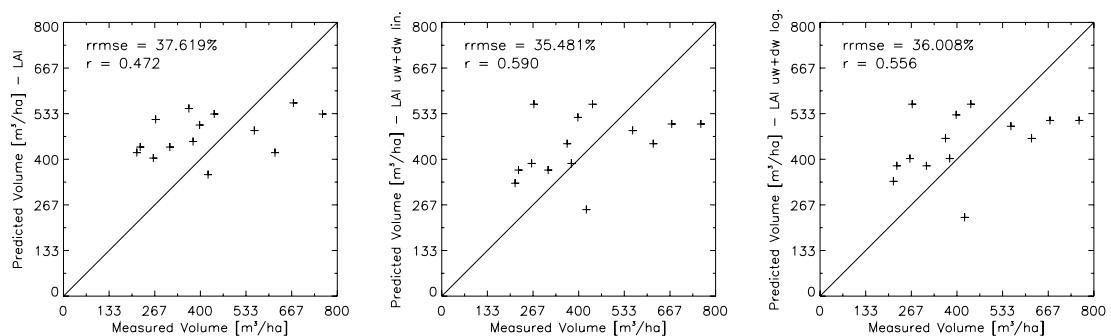


Figure 7.10 Measured volume versus modelled volume. Best performing vegetation indices were plotted. Each cross corresponds to a measurement plot. The diagonal line represents the 1:1 relationship.

7.4.4.5 Biomass

Biomass overall correlated weakly with all spectral bands and vegetation indices. Highest correlations were found for the ASTER mir_2 bands. A significant correlation was also found with LAI_{uw+dw} and the parameter basal area. The correlation with LAI was slightly weaker. Statistically significant ($p \leq 0.01$ or $p \leq 0.05$) correlating spectral bands, LAI_{uw+dw} and basal area were selected and linear as well as quadratic regression analysis was performed. Quadratic modelling achieved slightly better fittings for the spectral band ASTER9, whereas linear relationship with biomass was stronger for all other significantly related parameters. The results are presented in Tab. 7.11.

The only strong relationship of biomass was found with basal area. Since basal area was estimated with reasonable accuracy, the results of biomass modelling based on basal area achieved the highest R^2 and RRMSE. Of the spectral bands, ASTER9 attained the highest R^2 . LAI_{uw+dw} as the predicting parameter performed moderately with an R^2 of 0.56 and 0.43 respectively. Biomass models based on ETMPAN have a critical shrinkage and realized the lowest R^2 .

In Fig. 7.11 it can be seen that medium to high biomass measurements were underestimated by all predictors, whereas lower biomass values were well or slightly overestimated.

Table 7.11 Parameter estimates for linear and quadratic regression models: Biomass = $a + b \cdot VI$ and Biomass = $a + b \cdot VI + c^2 \cdot VI$ and Shrinkage. Validation of linear and quadratic biomass models (n = 15): Coefficient of determination (R^2) and relative RMSE.

Band/VI	a	b	c	Shrinkage	R^2	RRMSE [%]
ASTER8	524409.597	-17847.323		-0.228	0.349	60.159
ASTER9	555226.478	-12737.841		-0.398	0.500	61.695
ETMPAN	-170510.196173	5572.247653		0.205	0.000	65.100
LAI uw+dw	35742.460471	47720.356541		-0.308	0.432	58.194
Basal Area	38147.664	3010.186		-0.250	0.755	33.796
ASTER8	748447.852	114899.016	-3439.161	-0.138	0.268	60.039
ASTER9	941561.224	-38839.484	438.984	-0.428	0.530	61.600
ETMPAN	606854.585795	-18722.948377	187.726808	0.213	0.006	64.206
LAI uw+dw	350047.505005	-180165.817663	39643.567455	-0.409	0.560	54.030
Basal Area	21460.021	3898.269	-9.852	-0.213	0.721	35.777

Biomass correlated highly with basal area, followed by LAI_{uw+dw} and the ASTER mir_2 reflectances. The negative correlation of the mir_2 bands with biomass can be explained by higher shadow influences and less atmospheric scattering in complexly structured forest stands [146]. The nir relation with biomass is weak and should be inverse, which is the case for the ASTER measurements only. The stronger the inverse, the stronger the relation of vegetation indices to biomass and consequently biomass prediction [49].

Biomass estimation, based on optical remote sensing data, is recognized as very difficult to achieve [57], [166]. Some promising results were obtained in areas in which biomass accumulation is rapid, for instance tropical regeneration areas [120] or areas with naturally occurring low woody biomass levels and slow accumulation rates [111], which could also apply to Patagonian *Nothofagus* forests.

The calculated RRMSE for biomass are between 33.80% and 65.1%. If basal area and LAI_{uw+dw} are modelled with their best estimator, the RRMSE changes reasonably. RRMSE for the

modelled biomass via the linearly modelled basal area amounts to 58.72% with an $R^2 = 0.384$ and via the quadratically model to 57.08% with an $R^2 = 0.377$. The RRMSE based on the linearly modelled LAI_{uw+dw} amounts to 61.08% with an $R^2 = 0.244$. The RRMSE of the linear model amounts to 66.76% and an $R^2 = 0.154$. Consequently, the lowest RRMSE was achieved with the model based on modelled basal area, whereas the highest R^2 was found for the model based on ASTER9. Biomass map calculation was performed with the model based on ASTER9, due to the higher stability of the model.

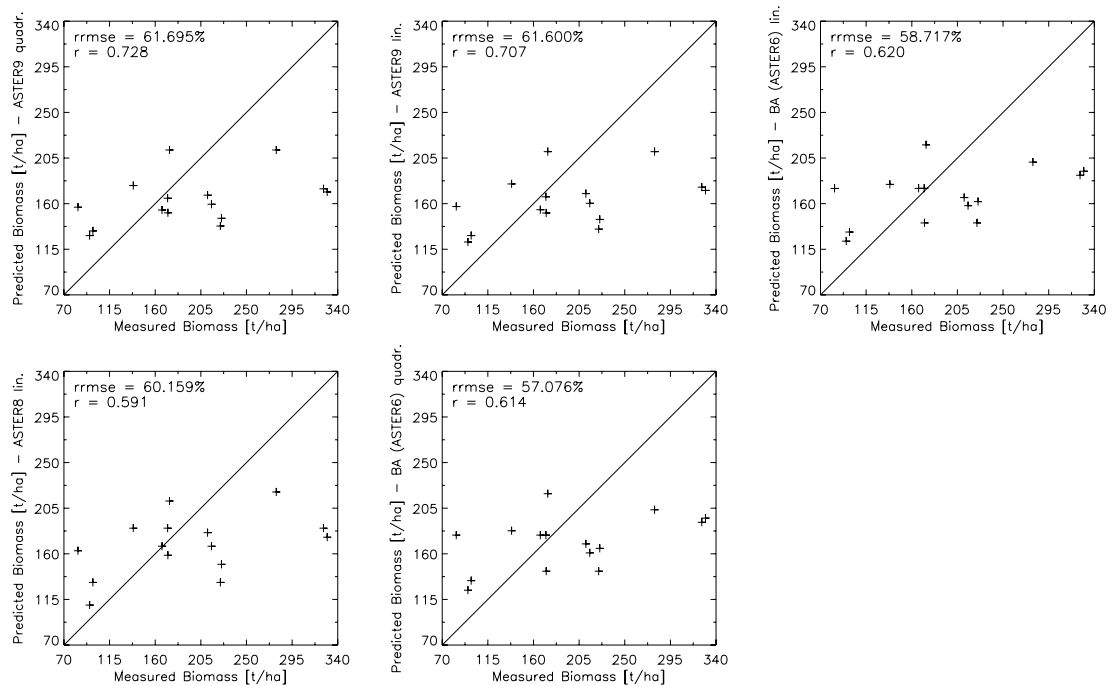


Figure 7.11 Measured biomass versus modelled biomass. Only best performing results were plotted. Each cross corresponds to a measurement plot. The diagonal line represents the 1:1 relationship.

Results from other studies applying similar methods based on optical satellite data are sparse. Most biomass estimations are based on radar or lidar data. Labreque et al. [106] compared three different biomass estimation methods based on Landsat TM data in Canadian boreal forests. Estimation results for deciduous trees applying the k nearest neighbor estimation method reached an RRMSE of 49.38%.

7.4.5 Conclusions on Forest Parameter Determination

Determination of **tree density** works best with the soil adjusted vegetation index PVI. It is based on *nir* and *red* reflectances and accounts for soil background effects. Lenga trees are growing in loose stands if they are cultivated or are growing in harsh conditions and the soil coverage can be very variable. Some Lenga stands are hardly covered by a herb layer and soils are bare and some have dense bushes and shrubs growing in the understory. These characteristics seem to be detected by the satellite data and thus the best approximation of the measured Lenga plots was achieved with a soil adjusted vegetation index.

Tree density can be estimated with Landsat ETM+ data at relative RMSE around 45% for Lenga forest stands. Working with other suitable vegetation indices such as WDV and satellite data can lead to much higher RMSE, as the results in Tab. 7.7 have shown. The model can be rated as stable, it explains 55.8% of the behavior of the dependent variable, tree density. The results are

promising when compared to results achieved by other studies and the determination of tree density can be stated as successful.

DBH was best estimated by a model based on the tasseled cap derivative greenness, followed by ETM4 and the soil adjusting vegetation indices PVI and WDV, all derived from Landsat ETM+ data. Relative RMSE for DBH estimation of Lenga stands are around 26%. The highest R^2 is low, the model explains only 29.8% of the behavior of the dependent variable, DBH. Even so, when looking at the small RMSE, the results are promising.

Determination of **basal area** works best with ASTER6, a mir_2 band. Basal area can be estimated with ASTER data at relative RMSE around 30% for Lenga stands if vegetation indices include information from mir and nir reflectances. The established model is strong, it explains 61.9% of the behavior of basal area. Compared to results from other studies, the determination of basal area for Lenga stands can be considered as successful.

The use of vegetation indices and spectral bands from ASTER and Landsat ETM+ is not successful in determining **volume** of Lenga forests. No significant correlation exists. LAI is the most suitable parameter, indirectly definable from remote sensing data, to estimate volume. Relative RMSE of volume determination are around 40%, if LAI is modelled with MVI derived from ASTER data. The R^2 is low, the model explains only 17.6% of the behavior of the dependent variable, volume. The results show that a logarithmic model can yield slightly better results than a linear model for Lenga forests. Compared to other studies of volume estimation, the achieved relative RMSE is good. However, the model based on modelled LAI is weak and the application of more promising methods such as the k nearest neighbor estimation method should be considered.

Determination of **biomass** performs best with modelled basal area, based on ASTER6 and reaches a relative RMSE of 57%. Biomass modelling based on spectral information performed only weakly. The best performing spectral estimators are based on ASTER mir_2 bands and reach a relative RMSE around 61% for Lenga forest stands. The highest R^2 is rather high, the model explains 75.5% of the behavior of biomass. The highest R^2 was found for the model based on ASTER9, whereas the lowest relative RMSE was achieved with the model based on modelled basal area. Consequently, biomass map calculation was performed with the model based on ASTER9, due to the higher stability of the model.

With biomass only few determination studies were performed, for example a study conducted in Canadian boreal forests reached slightly better relative RMSE [106]. Therefore the determination of biomass for Lenga forests can be considered as moderately. The application of other determination methods should be considered and investigated.

In Tab. 7.12 the best performing estimators for all analyzed forest parameters are summarized. The most suitable wavelength relationships and their required correlations with the corresponding parameters as well as the expectable accuracies are listed.

Table 7.12 Summary of the best performing estimators and the most suitable wavelength's, the required correlation and the achieved accuracy for Lenga stands.

Parameter	Best Estimator	Suitable Wavelength Relationships	Required Correlation	RRMSE [%]
LAI	MVI A, mNDVI(A3,A4)	$nir - mir_1$	nir +	11.281
			mir_1 -	12.082
Tree Density	PVI E	$nir - red$	nir +	44.607
			red -	
DBH	Greenness, ETM4	nir	-	25.414
			-	25.934

Table 7.12 Summary of the best performing estimators and the most suitable wavelength's, the required correlation and the achieved accuracy for Lenga stands.

Parameter	Best Estimator	Suitable Wavelength Relationships	Required Correlation	RRMSE [%]
Basal Area	ASTER6	mir_2	-	28.765
	mNDVI(A3,A4)	$nir - mir_1$	nir mir_1	31.263
Volume	LAI uw+dw lin		$+$ $(mir_2 -)$	35.481
Biomass	Basal Area		$+$	33.796
	ASTER8		mir_2 $-$	60.039

7.4.6 Descriptive Forest Parameter Analysis

At each Lenga measurement plot some additional descriptive forest parameters were assessed. Forest stand structure and its effects on the Landsat ETM+ *nir* band and tree density have already been discussed in Chapter 7.4.4. The influence of understory on spectral reflectances and its correction by selected vegetation indices was likewise analyzed. In the following sections the effect of forest cultivation, regeneration, vitality, coverage, dominant height and stand structure on the measured parameters of Lenga forests are discussed.

7.4.6.1 Forest Cultivation

Nine of the 38 measured plots are native forests with no human impact to date. In Fig. 7.12 the forest cultivation status for each measurement plot is displayed in relation to the measured forest parameters and its best estimator. Native forest plots have tendentially a higher LAI and biomass than cultivated plots and have medium to high basal area. Mean DBH of native forest plots instead are in the low to medium range. Tree density, dominant height and volume of virgin and cultivated forest plots do not differ.

The same trends were observed whilst analyzing the provincial forest inventory data from 1997 where it was shown that virgin Lenga stands have much higher basal area, tree density, volume and biomass. Dominant height and DBH instead are similar or slightly lower for cultivated stands but significantly higher for heavily cultivated stands.

The silvicultural system is based on selective cut of the best timber trees. This system is locally named as *floreo tradicional* and is incompatible with a sustainable forest management. It degrades forest quality and impoverishes the potential timber productivity in the stands. The analyzed forest inventory data are summarized in Tab. 7.13.

Native forest plots have tendentially higher vegetation indices and greenness values than cultivated plots, whereas the ASTER reflectances are tendentially lower for virgin plots, except for ASTER3 - the *nir* band.

Table 7.13 Forest parameter derived from the provincial forest inventory dataset. 57 virgin, 17 cultivated and 8 heavily cultivated forest stands were observed. Biomass measurements were derived from a different study in the south of Province of Chubut.

	Density [trees/ha]	DBH min/max [cm]	Dom. Height [m]	Basal Area [m ² /ha]	Volume [m ³ /ha]	Biomass [t/ha] ¹⁾
Virgin stands	373	27/80	18.9	53.8	354	256.05
Cultivated stands ²⁾	269	32/84	17	45.1	335	
Heavily cultivated stands ³⁾	170	35/86	21.6	37.2	256	157.12

¹⁾ Study site: Lago La Plata and Lago Fontana, Chubut.

²⁾ Cultivated stands: Traditional cultivation: Selective cut of the best timber trees.

³⁾ Heavily cultivated stands: Selective cut 2-3 times every 10 years. A regeneration time period of at least 35 years would be necessary to guarantee a sustainable cultivation.

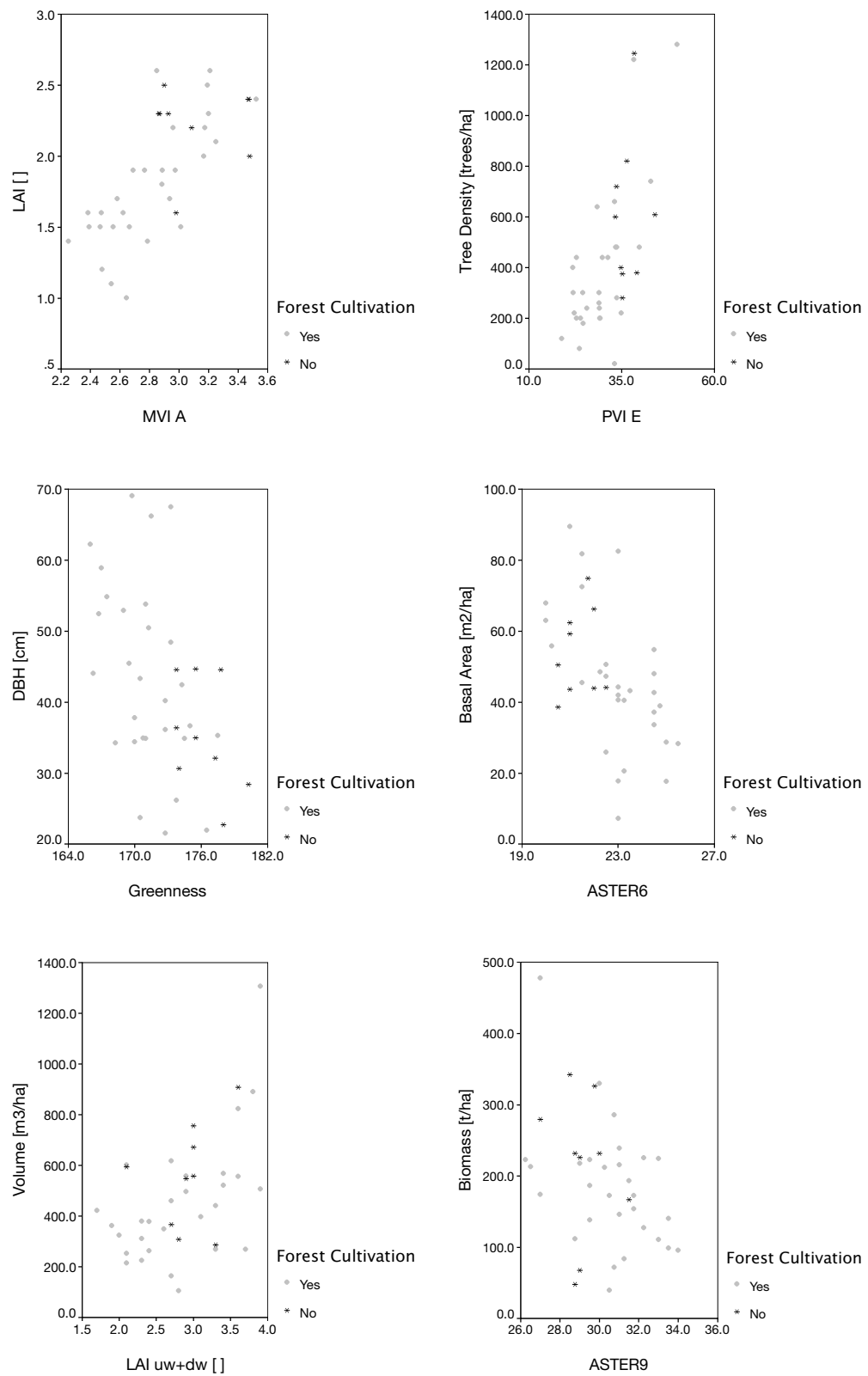


Figure 7.12 The relationship between the different forest parameters and their best estimator in respect of the forest cultivation situation for each measurement plot (n=38).

7.4.6.2 Regeneration and Vitality

Looking at the regeneration and vitality situation for each measurement plot in Fig. 7.13 and Fig. 7.14, the consequences of the traditional silvicultural system are clearly visible. LAI values are higher for the majority of the plots with medium to high regeneration and vitality.

Plots with low tree densities have a rather high regeneration situation due to a better light situation. These stands are generally cultivated. As already mentioned in Chapter 7.4.6.1, the traditional silvicultural system is based on selective cut of the best timber trees, the *floreo tradicional*, and is incompatible with a sustainable forest management. It degrades forest quality and impoverishes the potential timber productivity in the stands. The vitality of these stands is lower due to a selective cut of the better timber trees.

Plots with high regeneration and vitality contain a lot of young trees, they are regeneration stands or in the small timber stage, and have consequently lower DBH and volume. Plots with low to medium regeneration have higher DBH and volume. If the stands have low vitality, they consist of very old, medium or large sized trees, which results in higher DBH and wood volume for low vitality stands, for example old-growth stands or stands with very large or large timber stage.

Highest biomass values were measured for stands with low or medium regeneration and medium vitality. Basal area is not systematically distributed in relation to regeneration and vitality.

The three different regeneration situations are not systematically distributed in relation to reflectance or vegetation indices. Plots with low vitality have tendentially lower vegetation indices and plots with high vitality have higher vegetation indices. For the band ASTER6 the contrary is the case.

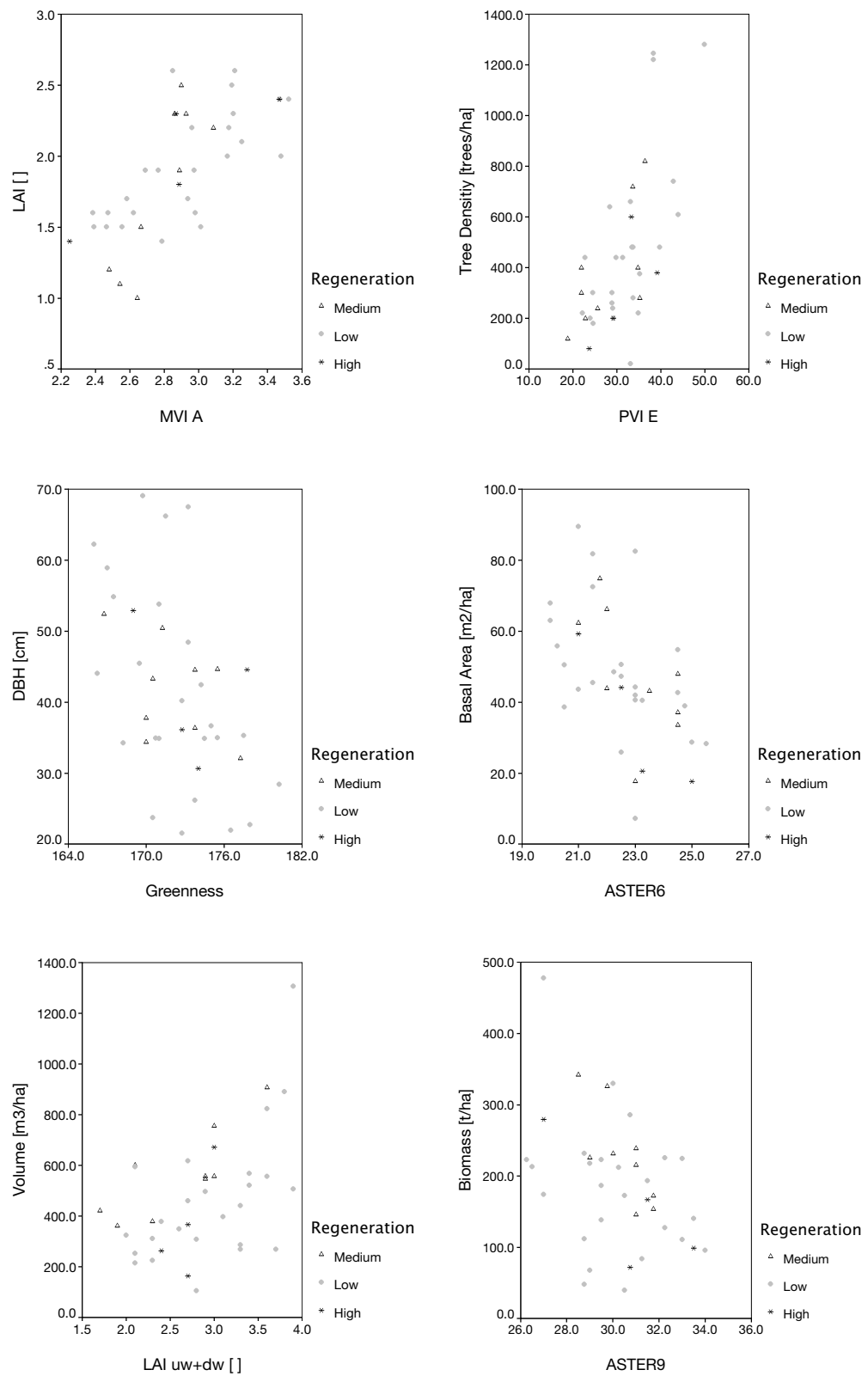


Figure 7.13 The relationship between the different forest parameters and their best estimator in respect of the regeneration situation of each measurement plot (n=38).

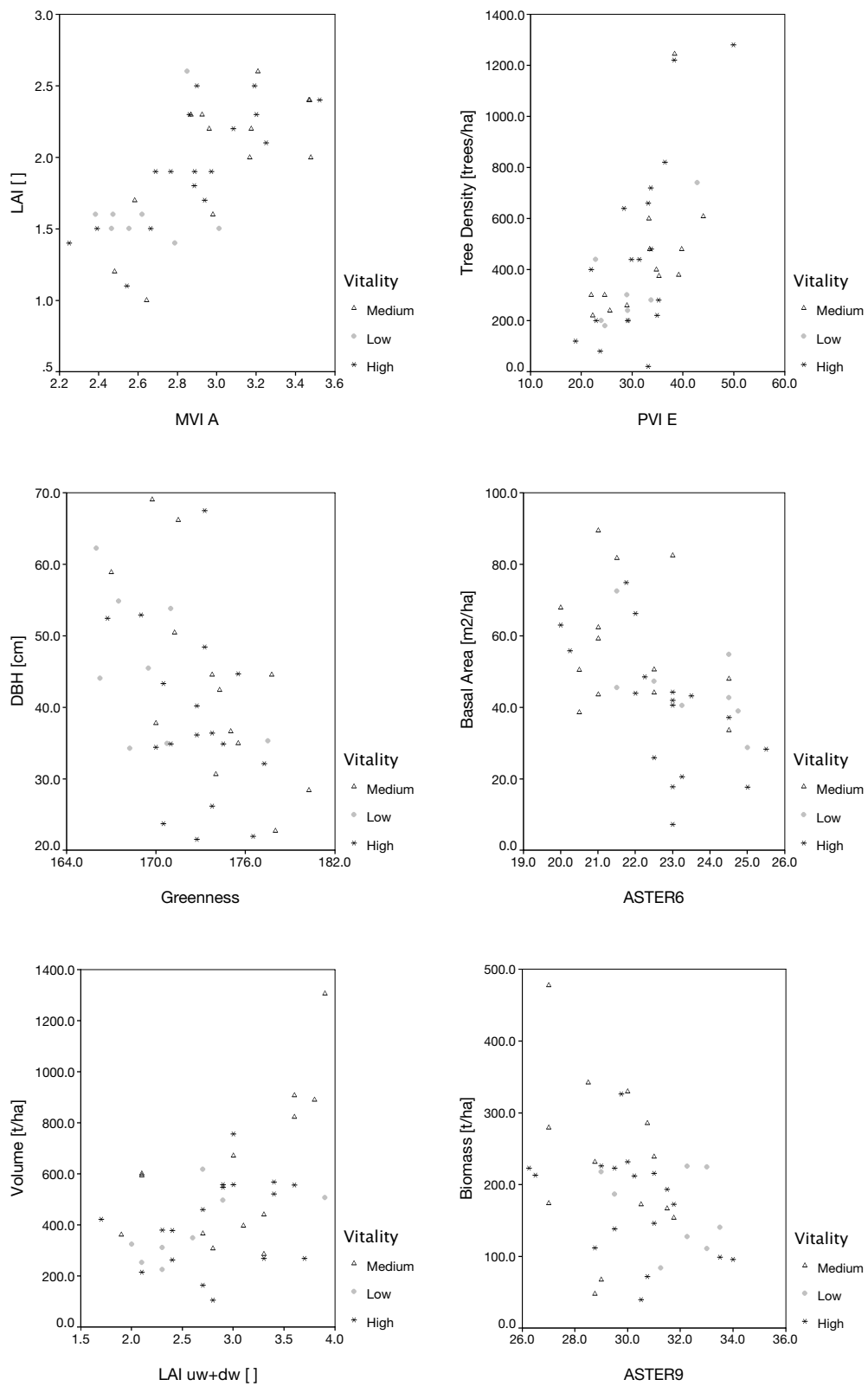


Figure 7.14 The relationship between the different forest parameters and their best estimator in respect of the vitality of each measurement plot (n=38).

7.4.6.3 Coverage

In Fig. 7.15 coverage and its relations to the forest parameters are displayed. As expected, LAI is rising with rising coverage. High coverage have rather low tree densities whereas lower coverages are evenly distributed along the density scale. The four parameters DBH, basal area, volume and biomass act similarly. High coverages lead to high parameter values. Medium coverages lead to medium to high DBH and volume and to a medium basal area and biomass. Stands with low coverage do also have rather low DBH, basal area, volumes and biomass.

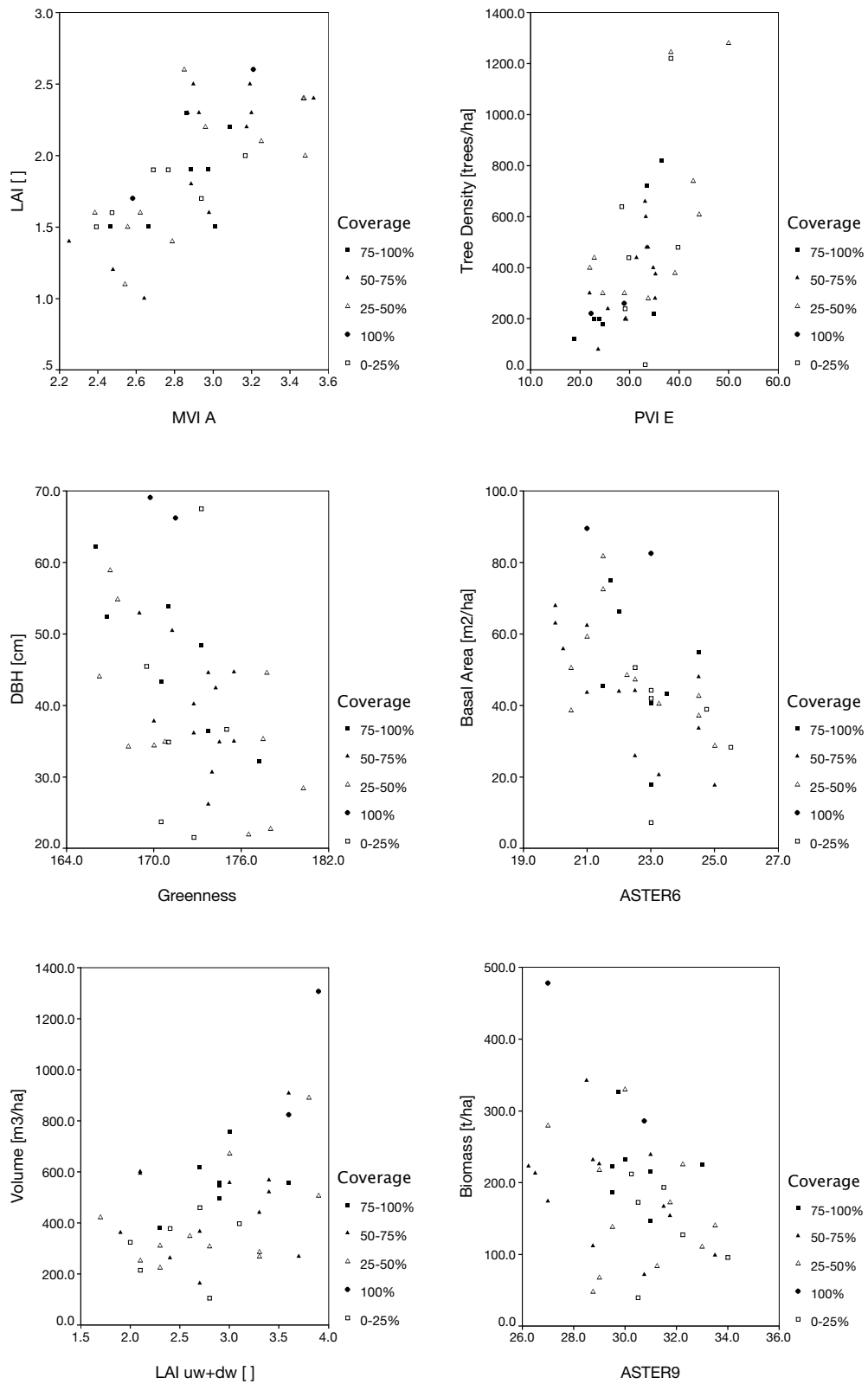


Figure 7.15 The relationship between the different forest parameters and their best estimator in respect of the percent coverage of each measurement plot (n=38).

7.4.6.4 Dominant Height

Although dominant height was numerically measured, it is discussed in the section of descriptive parameters, since regression analysis with LAI and reflectances derived from the satellite data indicated no relationship. However, some relations between dominant height and the made descriptive parameters are apparent and can be discussed as follows: Dominant heights are largest for stands with medium regeneration. Low and high regeneration plots have all kinds of dominant heights. Vitality seems not to have an effect on dominant height. No systematic relation can be detected. Coverage instead is again related to dominant height. Stands with coverages of 0-50% tendentially consist of low to medium-sized trees, whereas stands with coverages of 50-100% coverage consist of medium-sized to large trees [Fig. 7.16]. The relationship between dominant height and stand structure is discussed in Chapter 7.4.6.5.

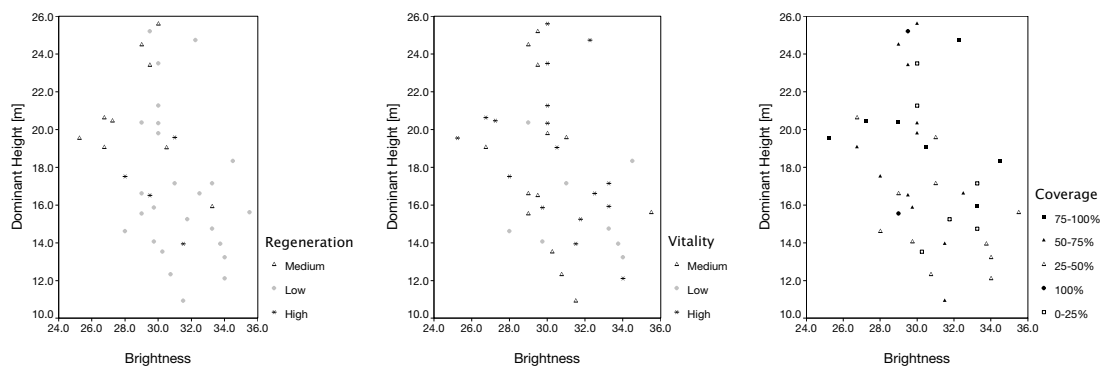


Figure 7.16 The relationship between the different forest parameters and their best estimator in respect of its forest cultivation situation for each measurement plot (n=38).

7.4.6.5 Stand Structure

In Fig. 7.17 stand structure is displayed for each forest parameter. Each image plot again reflects the analyses previously made. Old-growth and large timber stands have a rather low tree density whereas medium timber stands and mixed or irregular stands have a medium tree density and small timber stands a high tree density.

DBH and volume are high for old-growth, very large and large timber stands. Medium, mixed and irregular stands have medium sized DBH and medium volumes. Regeneration and small timber stands have low DBH and lower volumes consisting of mainly small, emerging trees.

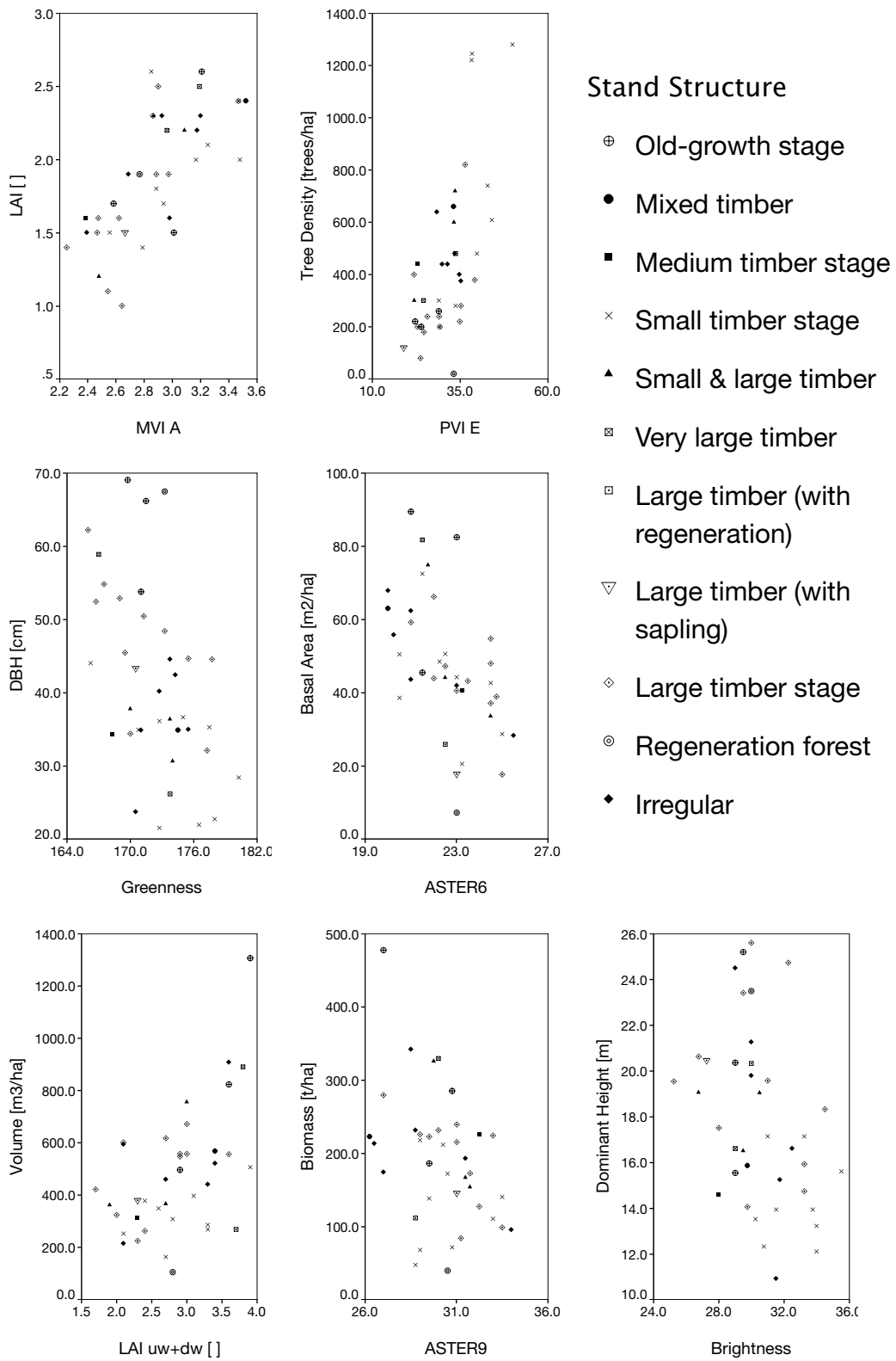


Figure 7.17 The relationship between the different forest parameters and their best estimator in respect of stand structure for each measurement plot (n=38).

Dominant heights are not only highest for large timber and old-growth stands but also for the only regeneration stand measured, which has to be considered as an exception. Medium heights are found mainly in irregular, medium timber and mixed stands, while lower heights are found in irregular and small timber stands.

Biomass varies for all stand structures but some tendencies can still be found. Old-growth, very large timber as well as irregularly structured stands have medium to high biomass rates. The mixed and medium timber stages have medium biomass rates. Stands with high regeneration and small timber stages have rather low biomass rates.

Basal area shows no systematic distribution in relation to stand structure.

PVI E, greenness and brightness are tendentially high for small timber stands. Irregular, mixed and small-and-large timber stands have medium values and large timber; very large timber and old-growth stands have low vegetation indices or reflectances. With MVI A, ASTER6 and ASTER9 no systematic distribution is visible except for a slight tendency of large timber towards lower values with MVI A and very large timber and old-growth stands towards lower values with ASTER6.

7.4.6.6 Conclusions on Descriptive Forest Parameter Analysis

The analysis of the descriptive stand parameters in combination with the measured forest parameters confirms that total volume, and therefore timber production, varies according to site quality, stocking, growth phase and previous land management. Accordingly, authorities of the provincial Forest Service and the CIEFAP promote the optimization of the forest management according to the site quality and stand conditions that influence the post-harvesting dynamics through the improvement of the yield harvesting system. Scientific evaluation of sustainable Lenga forest management systems is an important long-term research topic at the CIEFAP.

7.5 Application to the Remote Sensing Data

7.5.1 Forest Parameter Maps

One of the objectives of this thesis is to generate forest parameter maps for the Lenga forests, the main commercial woods in South Argentina and Chile. Remotely sensed data was linked to biophysical characteristics to be able to accurately extract biophysical forest parameters on a large scale without the need for elaborate fieldwork. The best regression models found for each of the estimated forest parameters were applied to the respective remote sensing dataset. Only image pixels classified as Lenga stands in the classification map [Chapter 6.4.3] were considered. The maps were printed in DIN A3 format and added as addendum in the appendix section.

Estimated values of **LAI** are in a reasonable range. The only measured LAI to date are on Tierra del Fuego and range from 1.7 to 2.8 for Lenga [70]. LAI values were classified into eight classes for cartographic reasons and a variation in LAI within the Lenga stands is clearly visible [see appendix and Fig. 7.18]. Reasons for the differences diverge according to site quality, stocking, growth phase and cultivation. These characteristics can vary within short distances and were clearly visible during fieldwork. A second, regional-scale variation in the south-western and southern Lenga forests in the research area also exists [Fig. 7.18]. It appears that, depending on exposition and slope, LAI diverges substantially. However, this pattern does not apply to all forested valleys in this region. Reasons for this effect are expected to be partially due to varying site quality, topography and thus solar radiation as well as to radiometric overcorrection of the ASTER dataset, regarding topographic correction and semi-empirical BRDF-correction. A third, large-scale variation in LAI can likewise be observed. LAI values are rising from the eastern stands towards the west as well as from stands in the north towards stands in the south-west. The variation

follows the geo-biographical pattern of Lenga growth in the Patagonian Andes between 40° N and 44° S, defined by the west-to-east climatic gradient [Chapter 3.5].

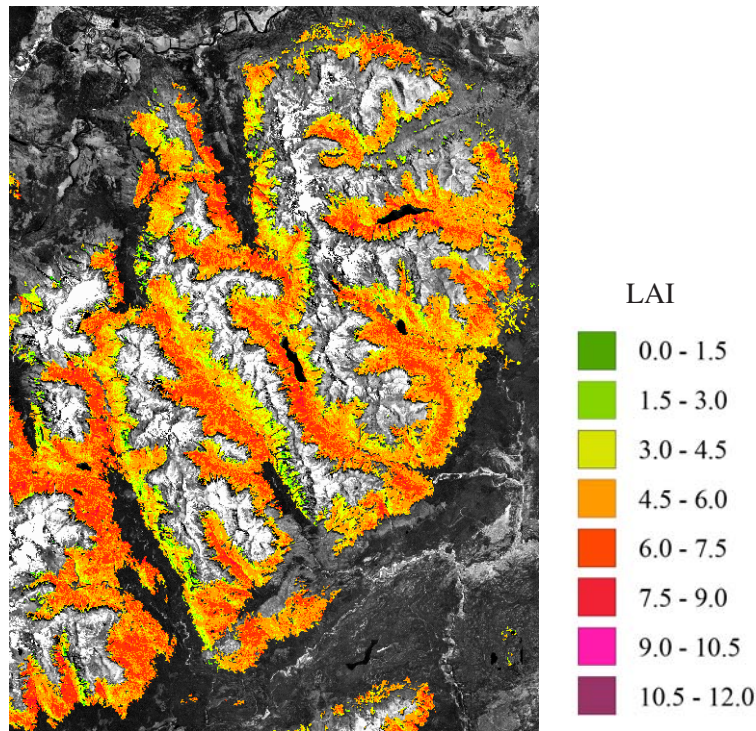


Figure 7.18 Regional-scale variation of LAI in the south-western Lenga forests.

Estimated **tree densities** are comparable to the densities measured by the provincial forest inventory of Chubut [Tab. 7.13]. In Fig. 7.19 it is clearly visible that native forests in the higher elevations and inaccessible valleys, which are not cultivated (see circles) are denser than the cultivated forests in the easily accessible, lower elevations (see rectangles). No systematic geographical pattern is visible as with LAI.

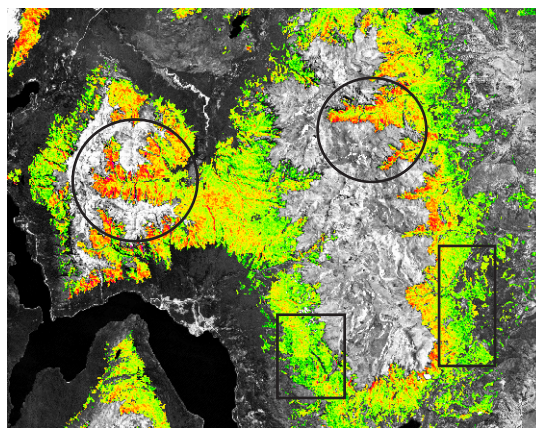


Figure 7.19 Regional tree density variations in Lenga forests. Not cultivated areas are denser (circles) than cultivated forests (rectangles).

Also the **DBH** map shows no systematic pattern caused by the preprocessing of the remote sensing data [see appendix]. Clearly higher DBH are apparent in the lower elevation, where native

forests are cultivated and accessible. In these stands healthy and qualitatively best trees with medium sized DBH are cut selectively and some very young and mainly old trees with large DBH remain. DBH are smaller in higher elevations and remote areas respectively, where accessibility is difficult and thus cultivation uneconomical [Fig. 7.20]. A slight large-scale variation is visible though. Forests near settlements or small towns in the north and eastern regions, being more cultivated, have higher DBH than the forests in the west towards the Andes.

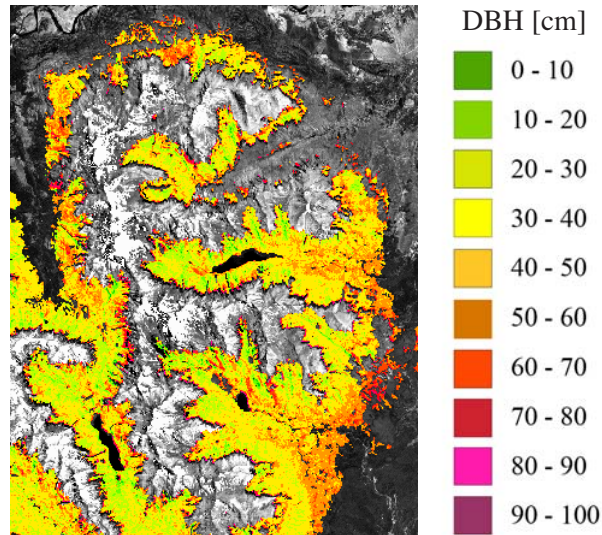


Figure 7.20 Regional-scale variation of DBH.

Determination of **basal area** achieved the highest R^2 and the range of values are comparable to the basal areas measured by the provincial forest inventory of Chubut [Tab. 7.13] and the basal areas reported by Schmidt and Urzúa [168]. Basal area varies with the availability of moisture [186], which is also reflected in the basal area map [see appendix and Fig. 7.21]. Basal area also varies consistently with elevation and exposition. Donoso [43] reported that, along an elevation gradient at 40° S in the Andes of south-central Chile basal area of *Nothofagus*-dominated forests increase from reduced levels in the lowlands to peak values at 700 - 900 m elevation and decline at higher elevations. Analyzing the generated basal area map a similar behavior is noticed where peak values are reached at 1100 - 1200 m elevation. How much the distribution pattern is influenced by atmospheric overcorrection of the ASTER dataset can not be clearly stated but it is expected to be minimal.

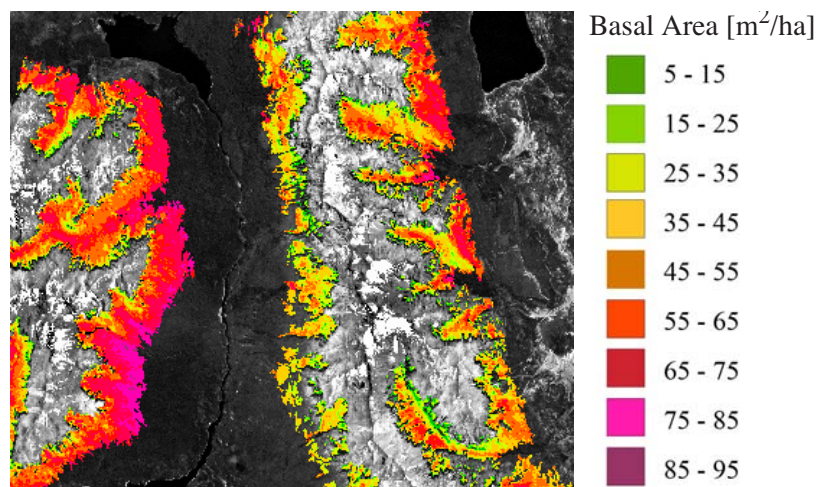


Figure 7.21 Regional variation of basal area due to higher precipitation in the west and varying elevation and exposition.

The selectively measured **volumes** by the provincial forest inventory range from 256 - 373 m³/ha and Schmidt and Urzúa [168] reported values of 400 - 600 m³/ha for old-growth stands at about 50 to 54° S where volumes are lowest for Lenga stands. The range of the estimated wood volumes in this study are realistic. Again a large-scale variation in volume can be observed as with basal area [see appendix]. Wood volumes are rising from the eastern stands towards the west as well as from stands in the north towards stands in the south-west.

The only comparable measured data on forest **biomass** are for the Lago La Plata and Fontana region in the south of Province of Chubut. The measurements range between 157 t/ha for cultivated stands and 256 t/ha for virgin Lenga stands. They clearly indicate that virgin Lenga stands have much higher biomass values than cultivated stands. This variation is also visible on the biomass map, modelled with ASTER9, when looking at the cultivated forests close to Los Alerces National Park near Cerro La Torta (circle) and the uncultivated native forests at Lago Banguilt (rectangle) [Fig. 7.22]. Biomass again varies with the availability of moisture. The generated biomass map in the appendix shows a large-scale variation defined by the west-to-east climatic gradient [Chapter 3.5], with highest biomass in the south-western Lenga forests. Biomass also varies consistently with elevation and particularly with exposition. How much the distribution pattern is influenced by radiometric overcorrection of the ASTER dataset cannot be clearly stated.

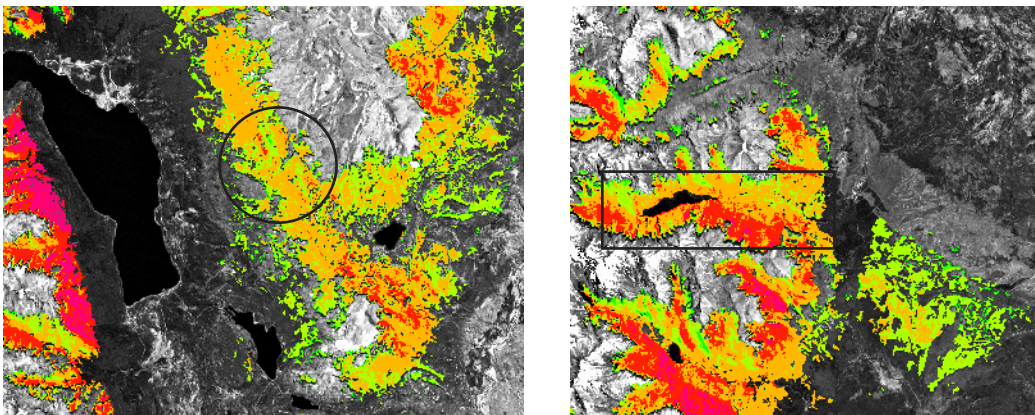


Figure 7.22 Regional-scale variation in biomass. Left image shows a cultivated Lenga forest, whereas the right image shows an uncultivated Lenga forest at Lago Banguilt.

All forest parameter maps are valuable, non-replaceable resources. They were integrated into the local GIS of CIEFAP and DGBYP. The generated maps will serve as input to future planning of Lenga forest management so as to guarantee sustainable forest management. For instance, a first consequence designated areas of so called virgin, protection and production Lenga forests will be defined by the CIEFAP in collaboration with DGBYP. A detailed validation of the maps will be carried out by the staff of CIEFAP and DGBYP.

7.6 Discussion

Forest parameter estimation from satellite sensor data has been a research topic for several years. Physically based or semi-empirical and empirical models respectively are constructed to estimate forest parameters at some level of precision. Of course, physically based models coupled with laboratory, field, and actual remote sensing data will probably lead to more accurate estimations,

which are site and time independent. However, they are very elaborate. The reality shows that most countries who are improving their forest statistics by combining field data with satellite data work with empirical data to train their established models and methods respectively. A widely and successfully applied method besides the linear regression technique is the k nearest neighbor method. For the parameters volume and biomass better accuracies were achieved with this method than with the regression technique in this study, especially if area size is larger than 50 ha. However, the disadvantage of the k nearest neighbor method is that it requires a large amount of samples in order to train it, which is not applicable in countries with large and mostly inaccessible forest areas or limited financial, human and technical resources. Thus, the linear regression technique is a simple, fast and comparably inexpensive alternative.

The achieved estimation results based on satellite data of the parameters LAI, DBH and basal area of Lenga forest stands are most promising. Relative RMSE of around 12%, 25% and 30% were achieved. The estimation accuracies of tree density, volume and biomass are rather low, compared to other studies. Further research should include the amplification and improvement of the established models. Also the integration and analysis of a dataset with high spectral resolution could provide information about suitable spectral regions for parameter retrieval.

The relationship analysis between the forest parameters and the multispectral bands showed that no vegetation index proved to be most suitable. A variety of vegetation indices, some of them soil-adjusted, and single spectral bands of either the near- or middle-infrared region achieved relatively high correlations depending on the forest parameter. Moreover, the results showed that the accuracies vary depending on the satellite data used. A larger forest parameter dataset is needed to confirm these results and cognitions of the relationships between the measured forest parameters and the satellite data reflectances. Future research at the CIEFAP will include the extension of the forest parameter dataset and the improvement of the models.

The analysis of the descriptive stand parameters in combination with the measured forest parameters confirms that timber volume and thus timber production varies according to site quality, stocking, growth phase and previous land management. Especially the impact of previous forest management can be severe and long lasting, which was recognized by analyzing long-term research results performed by the CIEFAP. As a result the provincial forest department, DGBYP is paying higher attention on the accomplishment of an adjusted forest management in the Province of Chubut.

Conclusion, Final Discussion and Outlook

8.1 Conclusions and Final Discussion

The overall objective of this work was to provide an improved bio-geographical information database to the forest authorities of Patagonian Province of Chubut. A digital elevation model of the area of interest was generated out of ASTER satellite data and a semi-empirical postprocessing method developed to allow for the topographic situation of the Andes. New scientific (ASTER) as well as established satellite data (Landsat ETM+) were geometrically and radiometrically preprocessed, to provide the projects image database. An accurate image database of this size and accuracy is to date unique for this area of highest interest. Extensive field work was conducted, measuring well distributed, accurate ground control points by differential GPS. Moreover several forest parameters as well as the LAI was measured for 42 different forest plots. They are to date the first and only LAI measurements of native Lenga growing in the Province of Chubut. A new, object-oriented, classification approach accounting for the heterogeneous vegetation situation in the research area was applied and a vegetation classification with emphasis on tree type discrimination established. For all measured forest parameters models were developed and forest parameter maps generated to provide valuable information on the current conditions of Lenga stands in the area. Conclusions are drawn on all defined objectives in Chapter 1 and critical aspects as well as first working experiences with the generated products are discussed.

8.1.1 Digital Elevation Model Generation

Digital elevation model extraction from ASTER data was successfully performed. However, the key to successful DEM generation is the amount, distribution and accuracy of GCPs. Evenly-distributed, sufficient and accurate GCPs strongly influence the quality of the DEM. Quality control of a DEM derived from optical satellite data is essential since it contains errors as a result of pixel mismatching. Accordingly, a semi-empirical post-processing method was developed to eliminate peaks and sinks as well as ridges at the borders of the four mosaicked DEMs. Accuracy assessment was performed by comparing the generated DEM with a) the SRTM digital elevation model and b) a selection of differentially measured independent GCP check points.

Comparing the ASTER DEM and the SRTM DEM resulted in a RMSE of 39.48 m in height. The differential image shows that errors at mountainous regions are between ± 100 m, which can be considered as rather high. In the foothills of the Andes and the steppe area, the DEMs correspond reasonably well with each other, the variations are between ± 30 m. It can be observed that the SRTM data is systematically higher than the ASTER DEM data. Since both DEMs contain notable errors, it is fairly difficult to interpret.

The comparison of the ASTER DEM with the ten independent check points, all of them located in the foothills of the Andes, resulted in a RMSE of 13.29 m. The maximum error is 22.84 m. After careful evaluation of the generated DEM mosaic it can be stated that the quality of the DEM mosaic is just sufficient to do atmospheric, topographic and geometric corrections to satellite data with resolutions of up to 15 m. Particularly in difficult topography the DEM may contain artefacts which can influence the preprocessing of the satellite imagery. Further products such as slope and aspect may be derived to enlarge and update the current GIS of CIEFAP and DGBYP, keeping in mind that they may contain minor artefacts and influence further GIS analysis, such as water runoff modelling.

Post-processing is an important step in digital elevation model generation and should not be

neglected. Nevertheless, most large blunders remained, either due to the stereo data (exposition, illumination and viewing angle) or due to unstable stereo modelling or matching failure. These errors indicate that the automatic surface reconstruction techniques used in PCI OrthoEngine still exhibit weak performance in certain coverages and fail in finding the corresponding pixels on the stereo images: errors appear in forested, snow covered, and shady areas since all are spectrally homogeneous. Preprocessing the stereo images, e.g. with a filter, could improve the quality of the resulting DEMs. Other difficulties became apparent at steep cliffs and deep river valleys or creeks. A solution would be to pre-classify shaded areas and exclude them from matching, and either interpolate them or substitute for those missing values using other sources. Another effect is the growth of the error with increasing slope [45], which is related to the effects of bidirectional reflectance. A possibility would be to correct these two effects on ASTER stereo images before the ultimate DEM generation to improve matching performance and therefore elevation accuracy. The nature of the stereo images themselves is a limiting factor to accuracy. The completely different perspectives of the two images, which actually makes the extraction of the parallax possible, also have a large inherent disadvantage. "Backside" slopes of ridges tend to completely disappear in certain perspectives. This results in a lack of corresponding pixels in one of the stereo pair images and the difference in imaging geometries can lead to a mismatching of non-corresponding pixels. Absolute DEM accuracy seems to be controlled by the software and the matching technique applied. Research improvements on the subject of pre- and post-processing are required. However, automatic surface reconstruction methods themselves require further refinement.

After the generation of the ASTER DEM it has soon become an important input dataset to other remote sensing based research studies at the CIEFAP, besides the SRTM DEM, which was published after the generation of the ASTER DEM. It is observed that for research areas situated in the flatter areas of Patagonia the SRTM DEM is more accurate in Z-direction than the ASTER DEM. Whereas in mountainous areas higher accuracies are achieved when applying the ASTER DEM due to a higher accuracy in Z-direction as well as less erroneous artefacts and data gaps.

8.1.2 Preprocessing of the ASTER and Landsat ETM+ Data

The scientific ASTER level 1A data was first system corrected. After quality analysis they had to be corrected for damaged lines and for systematic vertical banding in several bands. Successful correction of the banding was achieved by applying a suitable filter in the frequency domain. The Landsat ETM+ data was system corrected already but contained a gain switch in band 4 which had to be manually adjusted. Consequently a wedge-shaped artefact remained towards the right border of the dataset, but it did not influence the land cover classification. Moreover, the artefact affected an area in the east of the research area, representing the steppe ecotone.

Geometric correction was done with a "quasi-rigorous" model [177]. The goal was to achieve a maximum RMSE below 15 m to obtain conformity within all satellite data. This was possible for all areas except for the mountainous western regions of the study area, where a maximum RMSE of about 30 m was achieved. All datasets were resampled to 15 m pixel size by applying the cubic convolution method, afterwards all satellite scenes were mosaicked. The mosaicking method worked well for the ASTER and Landsat ETM+ datasets, which were both taken consecutive along the same path. Mosaicking images from different runs will probably require color balancing. With the mosaicked ASTER DEM small ridges at the borders of every single DEM become apparent when shading the DEM mosaic. However, this effect did not have any consequences for the classification and its product, the vegetation cover map.

For radiometric correction the ATCOR3 procedure was used [155]. Influences of topography, atmospheric absorption and scattering as well as radiance reflected from adjacent terrain were corrected. Moreover, an empirical BRDF correction was performed to a) account for

overcorrection and b) to reduce high reflectance values in regions of extreme incident angles and adjust them to those of adjacent areas with moderate incident angles.

Atmospheric correction of the Landsat ETM+ band 1 resulted in very low reflectances. Two possibilities could be applied to solve this problem: a) adjust the atmospheric input parameters, for example visibility or b) adjust the calibration coefficients provided by USGS. After some consideration it was decided to adjust visibility rather than experiment with the calibration coefficients. If spectral ground reference measurements of defined dark and bright objects would have been available for the area the calculation of new calibration coefficients suitable to this Landsat ETM+ scene could have been developed. Unfortunately such measurements are not available for the research area .

When comparing the two corrected datasets with each other it has to be noted that reflectances vary substantially for the visible and near-infrared bands, which is due to higher influence of the correction algorithm to these spectral regions than for the middle infrared region. Reasons could be differences between the sensor calibration and calibration coefficients or between the applied atmospheric input parameters and the actual atmospheric conditions at the acquisition time. Again, without any reference reflectance measurements it is difficult to judge the two corrected datasets.

However, as long as research combining both datasets is for example based on single ratio calculations, such as vegetation indices or on monotemporal classification analysis, the varying reflectance behaviors of both datasets have no negative consequences on the results. For multitemporal analysis, however, these datasets must be handled with care.

Moreover, the correction with ATCOR3 lead to a slight overcorrection of the westward oriented slopes, which was strong in the ASTER dataset and less apparent for the Landsat ETM+ scenes. This topographically induced illumination effect was partially reduced by applying an empirical BRDF correction. A topographic normalization approach, such as a Minnaert correction, yielded good results in reducing this effect in a similar project [147], and could be a solution to the problem.

Another critical point for the radiometric correction was the spatial resolution of the DEM, which resulted, due to overcorrection, in a sporadic pointwise artefact, representing the systematic raster pattern of the DEM but to date no DEM with a higher geometric resolution is available for the research area.

8.1.3 Object-Oriented Vegetation Classification

Segmentation evaluation showed that the choice of the appropriate scale parameters, segmentation criterion and layer weighting are a crucial task in an object-oriented classification. The successful creation of meaningful objects will decide on a successful classification. This task is time demanding and requires experience and detailed knowledge of the land cover characteristics such as the vegetation pattern and possible relationships between land cover types.

Several segmentation tests were performed first to visualize the effects of different scale parameters and criteria and second to find the best layer selection and weighting. The segmentation results and classification evaluation showed that different segmentation specifications resulted in little classification differences in this segmentation/classification project. Based on the visual inspection of the diverse segmentation configurations, the expert knowledge of the land cover characteristics in the research area and the visually best representation of the defined objects of interest all relevant segmentation input parameters were defined.

In eCognition segmentation reproducibility is warranted but conformity can vary towards image borders. Another segmentation test showed that about 150 pixels from the border are not identically segmented. An overlapping area of 300 pixels between all tiles had to be defined to successfully account for this tedious effect.

With the current class hierarchy and the selected features a stable rule base was developed.

Application of the rule base on other datasets will most probably need minor adjustments. Some of the tree type classes were successfully classified for the first time, such as Ñire and Caña Colihue. In addition, the class Lenga was divided in qualitatively varying subclasses. At high elevation and windy locations Lenga grows in a shrubby form called Shrublenga which was to date hard to distinguish from Ñire. It was attempted to somehow classify the vegetation types growing in the two transition zones bordering pure natural forests: a) the zone towards the steppe: pure Lenga forests-mixed forests-bushland-rangeland-*mallines* and b) the zone towards the limit of vegetation: pure Lenga forests-Shrublenga-Ñire-mountain meadows-bare soil. The classification of these transition zones and the tree types were accurately verified in the field and if necessary addition classes introduced or memberships adjusted. The development of the final rule base was thus an iterative process, incorporating expert knowledge and intermediate verification, which successfully improved the final result and is considered an important task in this project.

Looking at the rule base it can be seen that the St. NN algorithm was only applied on the first level, except for one class, which was simply better classified by St. NN than by membership function only. The used membership functions are mainly based on spectral and height information. The previously calculated layers SLP (slope) and ASP (aspect) didn't improve the exposition dependent vegetation patterns in the final classification. This could be explained with the previously conducted topographic correction of the satellite datasets, which might have led to a certain elimination of exposition dependent vegetation pattern. Besides the elevation information DEM, the ASTER bands 1 and 2 as well as the mid-infrared bands ASTER4 and 5 as well as the Landsat ETM+ based mid-infrared bands ETM5 and 7 and the tasselled cap derivatives BRIGHT and WETN have been found to be very useful to discriminate the tree type classes. The importance of the mid-infrared bands in vegetation classification was again shown, where the ASTER bands separated the tree type classes better than the ETM+ bands. Another important layer was the vegetation index NDVI based on ASTER bands 2 and 3. It helped to separate the low vegetation from the high vegetation classes as well as differentiate in between the high vegetation grass communities and in between the low vegetation bush classes.

In the developed classification rule often the parabolic shaped membership function was applied. The shape of the parabola was for most classes manually adjusted and the area of high stability widened to achieve higher stabilities for the defined classes. The default shaped parabola instead allocates only a narrow area with high stability to a class, which could lead to a destabilisation of the classification rule.

With the applied accuracy assessment it was first tried to account for the limited ground reference by selecting a large amount of samples which represented a 10 x 10 pixel block and not only single pixels. Secondly, it was tried to account for the severity of the classification errors depending on the generated vegetation classes by introducing the weighted kappa coefficient.

With this method an overall accuracy of 82.04% and a weighted kappa coefficient of 0.8185 was achieved. For all tree type classes accuracies of at least 70% were achieved, except for the coniferous Ciprés which was mostly misclassified as Coihue. Ciprés grows in small, loose groups of trees in-between pure Coihue stands on dry, rocky areas. The differentiation between Ciprés and Coihue seems to be problematic with medium resolution sensors such as ASTER and Landsat ETM+. The spectral influences of soil, rocks and Coihue trees on Ciprés pixels seems to be large and thus misclassification frequent. User accuracy reached 39.61% and producer accuracy 64.88%. The bamboo specie Caña Colihue achieved a user accuracy of 56.30% and a producer accuracy of 83.78%. Caña Colihue grows in the understory of Lenga and Coihue stands and grows together with Ñire as first tree types after forest fires. Therefore it is difficult with medium resolution sensors to detect Caña Colihue and moreover the mixed pixel information hinders the algorithm to allocate the correct class to the mixed Caña Colihue and Ñire pixels. The quantitative accuracies of the remaining vegetation classes have to be interpreted with care because of two reasons: a) for the class Shrublenga/Ñire only little ground reference was available and b) some of

the transition zone vegetation classes are radiometrically similar but are too distinct to be merged considering their habitat. During the above mentioned iterative development of the rule base intermediate classification results were discussed with the local authorities and thus adjusted and improved by defining these transition zone vegetation classes. As such an optimized vegetation map was produced. To date it is the most detailed vegetation and tree type map in the Province of Chubut covering an area of this size.

When using fuzzy classification methods, objects can belong to several classes but with different degrees of membership. Depending on the satellite data applied and the vegetation cover characteristics this can be an advantage by accounting for the mixed-pixel problem as well as for specific vegetation pattern in transition zones between classes. Still, it is important to evaluate the reliability or stability of classes it is necessary to survey the different degrees of membership of the classified objects. The membership stability for all tree type classes were again very high except for the conifer Ciprés. The membership stability for the mixed tree classes with bush characteristics have maxima higher than 0.69 but also rather low mean values which indicates that memberships are low by the majority. The classes Grass/Bushes < 1000 m asl and Intense Grassland/Mixed Forest have rather low stability due to overlapping. However, the two classes represent the agriculturally important intense grassland called *Mallines* very well. The classes Sparse/Dry class, Bushland/Rangeland, Rock, Water, Plantations and Border were classified with high stability.

The application of an object-oriented classification approach including fuzzy membership functions has shown that it accounts not only for the extremely variable but characteristic vegetation pattern of Argentinean Patagonia. Its application to other research objectives addressed by the CIEFAP is promising and consequently will be continued and extended.

8.1.4 Parameter Estimation by Regression Analysis

Correlation and regression analysis between the spectral bands and spectral vegetation indices proved to be an easy and fast method to estimate LAI and different forest parameters for Lenga stands, especially if only few forest measurement plots are available for training. The accuracies and inaccuracies are comparable with other studies' results, though most of them applied the k nearest neighbor method, requiring a large amount of training plots, such as forest inventory data. Future research at the CIEFAP will include the extension of the forest parameter dataset and the improvement of the established models. Also the integration and analysis of a dataset with high spectral resolution could provide information about suitable spectral regions for parameter retrieval. And finally, an implementation of the k nearest neighbor method would be an interesting task and consequent step in future forest parameter extraction research conducted in Patagonian forests.

8.1.5 LAI Measurement and Determination

LAI measurements of Lenga stands tend to be rather low, LAI values between 1.00 and 2.60 were measured. The number of Andean stands for which LAI has been measured is very small. Comparable values were measured for Lenga in Tierra del Fuego with values between 1.70 and 2.80 [70]. In this study all calculations were actually performed with the plant area index, instead of the effective LAI, as the LAI calculation software [194] did not yet account for foliage clumping and non-photosynthetic material. Future research should investigate the influences of foliage and non-photosynthetic material on LAI determination of Lenga stands.

Determination of LAI performed best with a vegetation index based on mir_1 and nir reflectances such as MVI A and $mNDVI_{(A3,A4)}$. LAI was estimated with ASTER data at relative RMSE around 12% for Lenga forest stands. Working with Landsat ETM+ data lead to slightly higher RMSE due to different radiometric configuration and lower geometric resolution.

Vegetation indices that account for canopy or soil background or atmospheric influences did not improve the RMSE.

8.1.6 Forest Parameter Determination

Determination of **tree density** worked best with the soil adjusted vegetation index PVI. It is based on *nir* and *red* reflectances and accounts for soil background effects. Lenga trees are growing in loose stands if they are cultivated or are growing in harsh conditions and the soil coverage can be very variable. Some Lenga stands are hardly covered by a herb layer and soils are bare and some have dense bushes and shrubs growing in the understory. These characteristics seem to be detected by the satellite data and thus the best approximation of the measured Lenga plots was achieved with a soil adjusted vegetation index.

Tree density can be estimated with Landsat ETM+ data at relative RMSE around 45% for Lenga forest stands. Working with other suitable vegetation indices and satellite data can lead to much higher RMSE as the results in Tab. 7.7 have shown. The model can be rated as stable, it explains 55.8% of the behavior of the dependent variable, tree density. The results are promising if compared to results achieved by other studies and the determination of tree density can be stated as successful.

DBH was best estimated by a model based on the tasselled cap derivative greenness, followed by the soil adjusting vegetation indices PVI and WDVI, all derived from Landsat ETM+ data. Since DBH and tree density are closely related the soil adjusting vegetation indices again achieve good results at estimating DBH. Relative RMSE for DBH estimation of Lenga stands are around 26%. The highest R^2 is low, the model explains only 29.8% of the behavior of the dependent variable, DBH. Even so, when regard is had to the small RMSE, the results are promising. Further research should include the amplification and improvement of the established models.

Determination of **basal area** worked best with ASTER6, a *mir₂* band. Basal area can be estimated with ASTER data at relative RMSE around 30% for Lenga stands if vegetation indices include information from *mir* and *nir* reflectances. But working with data from comparable sensors can lead to higher RMSE. The established model is strong, it explains 61.9% of the behavior of basal area. Compared to results from other studies the determination of basal area for Lenga stands can be considered as successful. As mentioned before, the amplification of the established models could bring some improvements.

The use of vegetation indices and spectral bands from ASTER and Landsat ETM+ was not successful in determining **volume** of Lenga forests. No significant correlation existed. LAI is the most suitable parameter, indirectly definable from remote sensing data, to estimate volume. Relative RMSE of volume determination are around 40%, if LAI is modelled with MVI derived from ASTER data. The R^2 is low, the model explains only 17.6% of the behavior of the dependent variable, volume. The results showed that a logarithmic model can yield slightly better results than a linear model for Lenga forests. Compared to other studies of volume estimation, the achieved relative RMSE is good, however, the model based on modelled LAI is weak and the application of more promising methods such as the *k* nearest neighbor estimation method should be considered.

Determination of **biomass** performs best with modelled basal area, based on ASTER6 and reaches a relative RMSE of 57%. Biomass modelling based on spectral information performed only weakly. The best performing spectral estimators are based on ASTER *mir₂* bands and reach a relative RMSE around 61% for Lenga forest stands. The highest R^2 is rather high, the model explains 75.5% of the behavior of biomass. The highest R^2 was found for the model based on ASTER9, whereas the lowest relative RMSE was achieved with the model based on modelled basal area. Consequently biomass map calculation was performed with the model based on ASTER9 due to higher stability of the model.

With biomass only few determination studies were performed, for example a study conducted

in Canadian boreal forests reached slightly better relative RMSE [106]. Therefore the determination results of biomass for Lenga forests can be rated as moderate. The application of other determination methods should be considered and investigated.

The analysis of the descriptive forest stand parameters in combination with the measured forest parameters confirms that total volume and therefore timber production vary according to site quality, stocking, growth phase and previous land management. Therefore, forest parameter maps were produced by applying the best performing models to the areas classified as Lenga forest. All maps show large-scale or even regional-scale variations, depending on the forest parameter. Reasons for these effects are partially expected to be due to radiometric overcorrection of the remote sensing datasets. However, the dimension of the influence can not be clearly quantified. The forest parameter maps are a valuable, non-replaceable resource, which were integrated into the local GIS of CIEFAP and DGBYP.

8.1.7 Costs and Time Account

Considering the limited funding of this project, cost-effective project planing was essential. The database was established with low-cost satellite data with regard to the spatial resolution and required accuracy. For Patagonian forest applications requirements resolution capabilities of 15 m to 30 m are deemed adequate for forest cover mapping and monitoring as well as collecting forest harvest information. Ground reference data collection was conducted in areas accessible by foot and one-day expeditions. The applied methodologies were chosen with regard to the possibility of integration at the CIEFAP and DGBYP, expenditure of time and accuracy.

Table 8.1 Approximate costs and production time calculation for the main procedure steps of this research project, conducted by experienced staff.

	Fieldwork & labor costs in ARG [US\$]	Labor costs in CH [US\$]	Time [days]
ASTER data (4 scenes) ¹⁾	-		1
Landsat ETM+ data (two scenes) ²⁾	-		1-3 ³⁾
GCP Collection	6476		80
Ground reference Collection	1514		18
Forest Parameter Measurements	2588	16000	25
DEM Generation and Postprocessing (4 scenes)		7680	12
Geometric and Radiometric Preprocessing		3840	6
Thematic Classification		4480	7
Parameter Estimation (6 parameters)		7680	12
Map Production		1920	3
Total Costs in ARG & CH	10578	41600	
Subtotal Costs & Time	52178		165-167

¹⁾ ASTER data provided via ftp by EROS Data Centre cost 55US\$ as of August 12th, 2002.

²⁾ Datasets were provided by CONAE for free. Cost of a system corrected Landsat ETM+ scene (Level 1G) bands 1-8 provided by CONAE or EOS Data Centre is 600 US\$. Prices are valid as of April 2004.

³⁾ Delivery time of EROS Data Centre, data provided via ftp.

The evaluation of the classification results and determined parameters have shown that a balance of accuracy and convenience of the chosen methods and processing steps was achieved.

In Tab. 8.1 the material and labour costs incurred during this research project, and the repetitive production time of the main procedure steps, are listed. Development, implementation and evaluation time are not included in this time calculation. Hardware and software facilities, including digital camera and GPS receivers have also not been included in the cost listing.

The total costs amount to 52178 US\$ for a mapped area of approximately 14400 km², which results in 3.6 US\$ per km². These costs will decrease in future as all continuing work will be done in Argentina, where labor costs are much cheaper than in Switzerland.

Most time during this work was spent waiting for cloudless ASTER data, collecting differentially corrected GCPs and ground reference data in the field as well as the development of the object-oriented classification rule base. Future updates of the produced forest parameter maps will take one day each, provided that the remote sensing data is radiometrically corrected. The best performing vegetation indices in forest parameter estimation can be regarded as stable and should preferably be selected for calculation. However, new correlation and regression analysis should be performed if working with new or other remote sensing data. Vegetation map update will need little adjustments of the classification rule base depending on acquisition date of the scene and spectral characteristics of the sensor.

In drawing final conclusions on the main objectives of this work, the following remarks can be stated:

- The accuracy of the generated DEM mosaic is just sufficient to do atmospheric, topographic and geometric corrections to satellite data with resolutions of up to 15 m. The DEM mosaic as well as the satellite database were successfully integrated into the GIS of CIEFAP and DGBYP.
- It was shown that low-cost ASTER data have a large information content and, with its respective resolution of 15 m and 30 m, are accurate enough to serve as database. They are a great opportunity for low-budget mapping and bio-geographical information extraction.
- The object-oriented classification approach led to an improved tree type classification of Patagonian forests. However, the coniferous Ciprés is still difficult to classify due to high spectral resemblance with Coihue. Fuzzy classification of the transition zone ecotones proved to be expedient and accounted for the difficult discrimination of these vegetation ecotones. The full potential of the object-oriented classification approach is not yet tapped. Integration of additional information layers, such as soil maps and an increased research on the characteristics of these ecotones and their preferred habitats, will further improve the classification result.
- Overall, the retrieval of LAI and other forest parameters from multispectral remote sensing data based on empirical regression analysis was successful. LAI, DBH and basal area estimation are promising and the results are above-average. Tree density, volume and biomass estimation results are moderate.
- All map products, including the DEM mosaic and the remote sensing database were transferred to the CIEFAP and the DGBYP. Know-how was transferred during this work and will continue. Training for the local authorities at CIEFAP took place from October to December 2005.

8.2 Outlook

The CIEFAP and the DGBYP promote the optimization of Patagonian forest management according to the site quality and stand conditions that influence the post-harvesting dynamics and thus the improvement of the yield harvesting system. For a relatively small area of approximately 14400 km² a bio-geographical database was established that will help to achieve this high aimed goal.

The next step of this research project will be the detailed validation of the produced LAI and forest parameter maps by the authorities of CIEFAP and DGBYP. The definition of designated areas of so called protection and production Lenga forests is planned as well as the enlargement of the bio-geographical database. The database already resulted in several new research projects, for example a project focusing on afforestation of the transition zone. The high accuracy and information content of the bio-geographical database established in this work and hence resulting insights lead to a great demand of other Patagonian Province authorities for similar bio-geographical databases.

Improvements of the established database and the produced products are versatile and are listed below:

- The remote sensing database: data of higher geometric resolution would lead to more detailed LAI and forest parameter maps. The integration of airborne laser scanning data would lead to accurate tree height information and improved volume estimates. Drawbacks are the local scale and the high costs of such data.
- Geometric and radiometric preprocessing of higher resolution remote sensing data would also require a DEM of higher geometric resolution and accuracy. It would particularly improve geometric accuracy and account for erroneous artefacts after atmospheric correction. It has to be investigated to what extent the freely available final version of the SRTM elevation model with a pixel size of 90 m resolution is suited to preprocess remote sensing data with a geometric resolution of up to 10 m.
- The full potential of the object-oriented classification approach is not yet tapped. Integration of additional information layers such as an autumn satellite scene, a soil map, geological map, precipitation map or forest cultivation plans could greatly improve vegetation classification concerning improved coniferous-deciduous-evergreen tree type discrimination and accurate transition zone vegetation mapping.
- The influence of foliage and non-photosynthetic material on LAI determination should be investigated in future LAI measurements.
- Forest parameter extraction has been successful. However, forest inventory accuracy requirements for tree density, volume and biomass are slightly below the achieved RMSE. Further research should focus on gathering a larger ground data collection and on alternative estimation methods such as the well-established k nearest neighbor method.
- Another interesting and promising approach is the extraction of forest parameters based on previously segmented images into forest stands. The predictions of the forest stand attributes are based on multiple linear regression models where spectral as well as textural information, calculated per stand, is used as input variables. First promising results applying this method were achieved in the USA [116].

References

- [1] Al-Rousan, N., and Petrie, G., 1998: System calibration, geometric accuracy testing and validation of DEM orthoimage data extracted from SPOT stereopairs using commercially available image processing systems. *International Archives of Photogrammetry & Remote Sensing*, Vol. 34, 8-15.
- [2] Antequera, S., 1999: Estudio comparativo de cuatro tratamientos silvícolas en un bosque de Lengua de la Provincia del Chubut. *Patagonia Forestal*, Vol. 5, 7-10.
- [3] Ardö, J., 1992: Volume quantification of coniferous forest compartments using spectral radiance recorded by Landsat Thematic Mapper. *International Journal of Remote Sensing*, Vol. 13, 1779-1786.
- [4] Baillard, C., and Dissard, O., 2000: A stereo matching algorithm for urban digital elevation models. *Photogrammetric Engineering and Remote Sensing*, Vol. 66, 1119-1128.
- [5] Baltsavias, E., and Stallmann, D., 1993: SPOT stereo matching for digital terrain model generation. *Proceedings of 2nd Swiss Symposium on Pattern Recognition and Computer Vision*, Zurich, Switzerland, 1993, 61-72.
- [6] Baret, F., Guyot, G., Major, D.J., 1989: TSAVI: a vegetation index which minimizes soil brightness effects on LAI and APAR estimation. *Proceedings of the 12th Canadian Symposium on Remote Sensing, IGARRS'89*, Vancouver, BC, Canada, Vol. 3, 1355-1358.
- [7] Baret, F., Guyot, G., 1991: Potentials and limits of vegetation indices for LAI and APAR assessment. *Remote Sensing of Environment*, Vol. 35, 161-173.
- [8] Barros, V., Cordon, V., Moyano, C., Ménéndez, R., Forquera, J., Pizzio, O., 1983: Cartas de precipitación de la zona oeste de las provincias de Rio Negro y Neuquén. Report to the Facultad de Ciencias Agrarias, Universidad Nacional del Comahue, Cinco Saltos, Neuquén Argentina.
- [9] Bava, J.O., Schmalz, J., 1992: Actas Seminario de Manejo Forestal de la Lengua y Aspectos Ecológicos Relacionados. CIEFAP, Publicación Técnica 8, Esquel, Argentina, 85-110.
- [10] Benz, U.C., Hofmann, P., Willhauck, G., Lingenfelder, I., Heynen, M., 2004: Multi-resolution, object-oriented fuzzy analysis of remote sensing data for GIS-ready information. *ISPRS Journal of Photogrammetry & Remote Sensing*, Vol. 58, 239-258.
- [11] Berón, F., Claverie, H., Postler, V., Featherston, S., Rêo, G., 1998: Regulación del rendimiento del bosque nativo productivo del Chubut. In: *Actas Primer Congreso Latinoamericano IUFRO*, Valdivia, Chile, 1998, 13 p.
- [12] Berón, F., 1999: Distribución y uso del Ñire (*Nothofagus antarctica*) en la Provincia del Chubut. *Promer Seminario-Taller: Criterios de utilización de ñirantales*. Trevelin, Argentina, INTA-CIEFAP.
- [13] Böswald, K., Lencinas, J.D., Logercio, G., 2002: Carbon reservoirs in temperate South American *Nothofagus* Forests. *The Scientific World Journal*, Vol.2, 53-75.
- [14] Boyd, D.S., Wicks, T.E., Curran, P.J., 2000: Use of middle infrared radiation to estimate the leaf area index of a boreal forest. *Tree Physiology*, Vol. 20, 755-760.
- [15] Brión, C., Grigera, D., Puntieri, J., Rapoport, E., 1988: Plantas exóticas en bosques de *Nothofagus*. Comparaciones preliminares entre el norte de la Patagonia y Tierra del Fuego. *Monografías de la Acad. Nacional de Ciencias Exactas, Físicas y Naturales*, Buenos Aires, Argentina. Vol. 4, 37-47.

-
- [16] Brown, L., Chen, J.M., Leblanc, S.G., Cihlar, J., 2000: A shortwave infrared modification to the simple ratio for LAI retrieval in boreal forests: an image and model analysis. *Remote Sensing of Environment*, Vol. 71, 16-25.
- [17] Brown, S.L., Schroeder, P., Kern, J.S., 1999: Spatial distribution of biomass in forests of the eastern USA. *Forest Ecology and Management*, Vol. 123, 81-90.
- [18] Bunnik, N.J.J., 1978: The multispectral reflectance of shortwave radiation by agricultural crops in relation with their morphological and optical properties. Thesis, Meded. Landbouwhogeschool Wageningen, Nederlands, Vol. 78-1, 175 p.
- [19] Carabelli, F., Antequera, S., Martin, G., Gómez, M., 2000: Análisis ambiental y social de las cuencas hidrográficas cordileranas de la Provincia del Chubut. CIEFAP-GTZ-DGByP, No. 5, 56 p.
- [20] Carrara, A., 1988: Drainage and divide networks derived from high-fidelity digital terrain models. In: *Quantitative Analysis of Mineral and Energy Resources*, eds. C.F. Chung, A.G. Fabbri and P. Larsen (Dordrecht: NATO-ASI Series, D. Reidel Pub. Co.), ISBN: 9027726353, 581-597.
- [21] Carter, J.R., 1992: The effect of data precision on the calculation of slope and aspect using gridded DEMs. *Cartographica*, Vol. 29, 22-34.
- [22] Chason, J.W., Baldocchi, D.D., Huston, M.A., 1991: Comparison of direct and indirect methods for estimating forest canopy leaf-area. *Agricultural and Forest Meteorology*, Vol. 57, 107-128.
- [23] Chen, J.M., Black, T.A., 1992: Defining leaf-area index for non-flat leaves. *Plant Cell. Environ.*, Vol. 15, 421-429.
- [24] Chen, J.M., Cihlar, J., 1996: Retrieving leaf area index of boreal conifer forests using Landsat TM images. *Remote Sensing of Environment*, Vol. 55, 153-162.
- [25] Chen, X., Lee, V., Rowell, E., DeFelice, T., 2004: Using lidar and effective LAI data to evaluate IKONOS and Landsat 7 ETM+ vegetation cover estimates in a ponderosa pine forest. *Remote Sensing of Environment*, Vol.91, 14-26.
- [26] Civanlar, R., Trussel, H., 1986: Constructing membership functions using statistical data. *IEEE Fuzzy Sets and Systems*, Vol. 18, 1 -14.
- [27] Claverie, A., 1999: Personal communication.
- [28] Clevers, J.G.P.W., 1988: The derivation of a simplified reflectance model for the estimation of leaf area index. *Remote Sensing of Environment*, Vol. 25, 53-69.
- [29] Clevers, J.G.P.W., 1989: The application of a weighted infrared-red vegetation index for estimating leaf area index by correcting for soil moisture. *Remote Sensing of Environment*, Vol. 29, 25-37.
- [30] Cohen, J., 1968: Weighted kappa. *Psychological Bulletin*, Vol. 70, 71-94.
- [31] Cohen, W.B., Spies, T.A., Fiorella, M., 1995: Estimating the age and structure of forests in a multi-ownership landscape of western Oregon, USA. *International Journal of Remote Sensing*, Vol. 16, 721-746.

-
- [32] Colmet Daage, F., 1991: Zonificación del potencial forestal de los suelos de la cordillera y precordillera de la Patagonia. Convenio INTA-ORSTROM. In: Actas del XIII Congreso Argentino de las Ciencias del Suelo. Bariloche, Argentina.
- [33] Colombo, R., Bellingeri, D., Fasolini, D., Marino, C.M., 2003: Retrieval of leaf area index in different vegetation types using high resolution satellite data. *Remote sensing of Environment*, Vol. 86, 120-131.
- [34] Congalton, R.G., 2004: Putting the map back in map accuracy assessment. In: *Remote Sensing and GIS Accuracy Assessment*, eds. R.S. Lunetta & J.G. Lyon, CRC Press, Boca Raton, FL, USA, ISBN: 156670443X, 163-172.
- [35] Crippen, R.E., 1990: Calculating the vegetations index faster. *Remote Sensing of Environment*, Vol. 34, 71-73.
- [36] Crist, E. P., Cicone, R. C., 1984: Application of the Tasseled Cap concept to simulated Thematic Mapper data. *Photogrammetric Engineering and Remote Sensing*, Vol. 50, 343-352.
- [37] Crist, E. P., Laurin, R., Cicone, R. C., 1986: Vegetation and soils information contained in transformed Thematic Mapper data. In: *Proceedings of the IGARSS '86 Symposium*, Zurich, Switzerland, 1465-1470.
- [38] Daida, J., Samadani, R., Vesecky, J.F., 1990: Object-oriented feature-tracking algorithms for SAR image of the marginal ice zone. *IEEE Transactions on Geoscience and Remote Sensing* Vol. 28, No. 4, 573-589.
- [39] Danson, F.M., Curran, P.J., 1993: Factors affecting the remotely sensed response of coniferous forest plantations. *Remote Sensing of Environment*, Vol. 43, 55-65.
- [40] Defossé, G.E., Robberecht, R., 1995: Future ecological and socio-economic strategies for the rangelands of Chubut Province, Patagonia, Argentina. *International Rangeland Development Symposium Proceedings*, Phoenix, USA, 27-38.
- [41] De Wulf, R.R., Goossens, R.E., De Roover, B.P., Borry, F.C., 1990: Extraction of forest stand parameters from panchromatic and multispectral SPOT-1 data. *International Journal of Remote Sensing*, Vol. 11, 1571-1588.
- [42] DGBYP, 1996: *Inventario Forestal de Bosque Nativo de la Provincia del Chubut*. Dirección General de Bosques y Parques de la Provincia del Chubut, Esquel, Argentina.
- [43] Donoso, C., 1993: *Bosques Templados de Chile y Argentina. Variación, Estructura y Dinámica*. Editorial Universitaria, Santiago, Chile.
- [44] Dufrêne, E., Bréda, N., 1995: Estimation of deciduous forest leaf-area index using direct and indirect methods. *Oecologia*, Vol. 104, 156-162.
- [45] Eckert, S., Kellenberger, T., Itten, K., 2004: Accuracy assessment of automatically derived digital elevation models from ASTER data in mountainous terrain. *International Journal of Remote Sensing*, Vol.26, No.9, 1943-1957.
- [46] Earth Observing System Data Gateway, 2004: EOS Data Gateway. <http://redhook.gsfc.nasa.gov/~imswwww/pub/imswelcome/>. Last visit: 28.09.2004.
- [47] Eklund, L., Harrie, L., Kuusk, A., 2001: Investigating relationships between Landsat ETM+ sensor data and leaf area index in a boreal conifer forest. *Remote sensing of Environment*, Vol. 78, 239-251.

-
- [48] Eklund, L., Hall, K., Eriksson, H., Ardö, J., Pilesjö, P., 2003: Investigating the use of Landsat thematic mapper data for estimation of forest leaf area index in southern Sweden. *Canadian Journal of Remote Sensing*, Vol. 29, No. 3, 349-362.
- [49] Ekstrand, S., 1994: Assessment of forest damage with Landsat TM: Correction for varying forest stand characteristics. *Remote Sensing of Environment*, Vol. 47, 291-302.
- [50] Fassnacht, K.S., Gower, S.T., Norman, J.M., McMurtrie, R.E., 1994: A comparison of optical and direct methods for estimating foliage surface area index in forests. *Agricultural and Forest Meteorology*, Vol. 71, 183-207.
- [51] Fassnacht, K.S., Gower, S.T., MacKenzie, M.D., Nordheim, E.V., Lillensand, T.M., 1997: Estimating the leaf area index of north central Wisconsin forests using the Landsat thematic mapper. *Remote Sensing of Environment*, Vol. 61, 229-245.
- [52] Foody, G.M., Palubinskas, G., Lucas, R.M., Curran, P.J., Honzak, M., 1996: Identifying terrestrial carbon sinks: classification of successional stages in regenerating tropical forest from Landsat TM data. *Remote Sensing of Environment*, Vol. 55, 205-216.
- [53] Foody, G.M., 2002: Status of land cover classification accuracy assessment. *Remote Sensing of Environment*, Vol. 80, 185-201.
- [54] Franco-Lopez, H., Ek, A.R., Bauer, M.E., 2001: Estimation and mapping of forest density, volume and cover type using the k-nearest neighbors method. *Remote Sensing of Environment*, Vol. 77, 251-274.
- [55] Franklin, J., 1986: Thematic mapper analysis of coniferous forest structure and composition. *International Journal of Remote Sensing*, Vol. 7, 1287-1301.
- [56] Franklin, S. E., 1991: Satellite remote sensing of mountain geomorphic surfaces. *Canadian Journal of Remote Sensing*, Vol. 17, 218-229.
- [57] Franklin, S.E., 2001: Remote sensing for sustainable forest management. Lewis Publishers, Boca Raton, USA, ISBN: 1566703948, 407 p.
- [58] Franklin, S.E., Hall, R.J., Smith, L., Gerylo, G.R., 2003: Discrimination of conifer height, age and crown closure classes using Landsat-5 TM imagery in the Canadian Northwest Territories. *International Journal of Remote Sensing*, Vol. 24, 1823-1834.
- [59] Franke, R., 1982: Smooth interpolation of scattered data by local thin plate splines. *Computer and Mathematics with Applications*, Vol. 8, No. 4, 273-281.
- [60] Frazer, G.W., Trofymow, J.A., Lertzman, K.P., 1997: A method for estimating canopy openness, effective leaf area index, and photosynthetically active photon flux density using hemispherical photography and computerized image analysis techniques. Information Report BC-X-373. Natural Resources Canada, Canadian Forest Service, Pacific Forestry Centre, Victoria, BC, Canada.
- [61] Fujisada, H., 1998: ASTER level-1 data processing algorithm. *IEEE Transactions on Geoscience and Remote Sensing*, Vol. 36, 1101-1112.
- [62] Gemmel, F.M., 1995: Effects of forest cover, terrain, and scale on timber volume estimation with Thematic Mapper data in a Rocky Mountain site. *Remote Sensing of Environment*, Vol. 51, 291-305.
- [63] Ghassemian, H., Landgrebe, D.A., 1988: Object-oriented feature extraction method for image data compaction. *IEEE Control Systems Magazine*, Vol. 8 No. 3, 42- 48.

-
- [64] Gloaguen, R., 2002: Personal communication.
- [65] Gong, P., Pu, R., Biging, S., Larrieu, M.R., 2003: Estimation of forest leaf area index using vegetation indices derived from Hyperion hyperspectral data. *IEEE Transactions on Geoscience and Remote Sensing*, Vol. 41, 1355-1362.
- [66] Gonzalez, R.C., Wintz, P., 1987: *Digital Image Processing*, 2nd Ed., Addison-Wesley, Reading, MA., USA, ISBN: 0201110261, 503 p.
- [67] Goodenough, D.G., Deguise, J.C., Robertson, M.A., 1990: Multiple expert systems for using digital terrain models. *Geoscience and Remote Sensing Symposium, IGARSS'90*, Washington, D.C., USA, 961-961.
- [68] Gower, S.T., Kucharik, C.J., Norman, J.M., 1999: Direct and indirect estimation of LAI, FAPAR and NPP for terrestrial ecosystems. *Remote Sensing of Environment*, Vol. 70, 29-51.
- [69] Green, K., Congalton, R.G., 2004: An error matrix approach to fuzzy accuracy assessment: The NIMA geocover project. In: *Remote Sensing and GIS Accuracy Assessment*, eds. R.S. Lunetta & J.G. Lyon, CRC Press, Boca Raton, FL, USA, ISBN: 156670443X, 163-172.
- [70] Gutiérrez, E., Vallejo, V.R., Romañá, J, Fons., J., 1991: The subantarctic *Nothofagus* forests of Tierra del fuego: Distribution, Structure and Production. *Oecologia Aquatica*, Vol. 10, 1-14.
- [71] Hardisky, M.A., Klemas, V., Smart, M., 1983: The influence of soil salinity, growth form, and leaf moisture on the spectral radiance of *Spartina Alterniflora* canopies. *Photogrammetric Engineering & Remote Sensing*, Vol. 49, 77-83.
- [72] Heene, G., Gautama, S., 2000: Optimisation of a coastline extraction algorithm for object-oriented matching of multisensor satellite imagery. *Proc. IGARSS*, Vol. 6. IEEE Press, New York, 2632-2634.
- [73] Herbert, T.J., 1986: Calibration of fisheye lenses by inversion of area projections. *Applied Optics*, Vol. 25, 1875-1876.
- [74] Hijazi, J., 2001: Elevation extraction from satellite data using PCI software. In: *First Symposium on Space Observation Technologies for Defence Applications*, Abu Dhabi, United Arab Emirates, August 2001.
- [75] Horler, D.N.H., Ahern, F.J., 1986: Forestry information content of Thematic Mapper data. *International Journal of Remote Sensing*, Vol. 7, 405-428.
- [76] Huang, C., Wylie, B., Yang, L., Homer, C., Zylstra, G., 2002: Derivation of a tasseled cap transformation based on Landsat 7 at-satellite reflectance. *International Journal of Remote Sensing*, Vol. 23, 1741-1748.
- [77] Hueck, K., 1966: *Die Wälder Südamerikas; Ökologie, Zusammensetzung und wirtschaftliche Bedeutung*. Gustav Fischer Verlag, Stuttgart, Germany, ISBN: 3437300857, 422 p.
- [78] Hueck, K., Seibert, P., 1981: *Vegetationskarte von Südamerika*, Gustav Fischer Verlag, Stuttgart, Germany, ISBN: 3437303333, 98 p.
- [79] Huete, A.R., 1988: A soil adjusted vegetation index (SAVI). *Remote Sensing of Environment*, Vol. 25, 295-309.

-
- [80] Huete, A.R., Liu, H.Q., Batchily, K., van Leeuwen, W., 1997: A comparison of vegetation indices over a global set of TM images for EOS-MODIS. *Remote Sensing of Environment*, Vol. 59, 440-451.
- [81] Huete, A.R., Didan, K., Miura, T., Rodriguez, E.P., Gao, X., Ferreira, L.G., 2002: Overview of the radiometric and biophysical performance of the MODIS vegetation indices. *Remote Sensing of Environment*, Vol. 83, 195-213.
- [82] IFONA 1984: Pre Carta Forestal Nacional. Territorio Nacional de Tierra del Fuego.
- [83] IFONA 1986: Pre Carta Forestal Nacional. Provincia del Chubut.
- [84] IFONA 1986: Pre Carta Forestal Nacional. Provincia de Rio Negro.
- [85] IFONA 1986: Pre Carta Forestal Nacional. Provincia de Santa Cruz.
- [86] Jakubauskas, M.E., 1996: Canonical correlation analysis of coniferous forest spectral and biotic relations. *International Journal of Remote Sensing*, Vol. 17, 2323-2332.
- [87] Jarvis, P.G., Leverenz, J.W., 1983: Productivity of temperate, deciduous and evergreen forests. In: *Physiological Plant Ecology IV*. eds. Lange, O.L., Omond, C.B., Zeigler, H., Springer Verlag, New York, USA, ISBN: 3540109072, 133-144.
- [88] Jensen, J.R., 1986: *Introductory Digital Image Processing*. Prentice-Hall, Englewood Cliffs, NJ, USA, ISBN: 0131453610, 544 p.
- [89] Jonckheere, I., Fleck, S., Nackaerts, K., Muis, B., Coppin, P., Weiss, M., Baret, F., 2004: Review of methods for in situ leaf area index determination Part I. Theories, sensors and hemispherical photography. *Agricultural and Forest Meteorology*, Vol. 121, No. 1, 19-35.
- [90] Jordan, C.F., 1969: Derivation of leaf area index from quality of light on the floor. *Ecology*, Vol. 50, 663-666.
- [91] Jovanovski, A., 2000: Comunicación personal. In: *Análisis ambiental y social de las cuencas hidrográficas cordilleranas de la Provincia del Chubut*. Carabelli et al. 2000. CIEFAP-GTZ-DGByP, No. 5, 56 p.
- [92] Jovanovski, A., Manfredi, R., 2000: *Módulo de Tecnología y Unidad de Gestión. Informe Final. Fase de Prefactibilidad. Proyecto Protección de Bosques Nativos Recuperación de Bosques Degradados y Manejo Sostenible en la cuenca de los Lagos La Plata y Fontana en la Precordillera Andino Patagónica*. Prima Klima -weltweit- e.V.. Provincia de Chubut, CIEFAP.
- [93] Jürgens, C., 1997: The modified normalized difference vegetation index (mNDVI) - a new index to determine frost damages in agriculture based on Landsat TM data. *International Journal of Remote Sensing*, Vol. 18, 3583-3594.
- [94] Kalacska, M., Sanchez-Azofeifa, G.A., Rivard, B., Calvo-Alvarado, J.C., Journet, A.R.P., Arroyo-Mora, J.P., Ortiz-Ortiz, D., 2004: Leaf area index measurements in a tropical moist forest: a case study from Costa Rica. *Remote Sensing of Environment*, Vol. 91, 134-152.
- [95] Kanemasu, E.T., 1974: Seasonal canopy reflectance patterns of wheat, sorghum, and soybean. *Remote Sensing of Environment*, Vol. 3, 43-47.
- [96] Kaufman, Y.J., Tanré, D., 1992: Atmospherically resistant vegetation index (ARVI) for EOS-MODIS. *IEEE Transactions on Geoscience and Remote Sensing*, Vol. 30, 261-270.
- [97] Kimes, D. S., 1983: Dynamics of directional reflectance factor distributions for vegetated

- canopies. *Applied Optics*, Vol. 22, 1364-1372.
- [98] Kimes, D. S., Newcomb, W. W., Tucker, C. J., Zonneveld, I. S., van Wijngaarden, W., De Leeuw, J., and Epema, G. F., 1985: Directional reflectance factor distributions for cover types of northern Africa. *Remote Sensing of Environment*, Vol. 18, 1-19.
- [99] King, D., Walsh, P., Ciufredda, F., 1994: Airborne digital frame camera imaging for elevation determination. *Photogrammetric Engineering and Remote Sensing*, Vol. 60, 1321-1326.
- [100] Kneubuehler, M., 2002: Spectral assessment of crop phenology based on spring wheat and winter barley. Dissertation, Department of Geography, University of Zurich. *Remote Sensing Series*, Vol. 38, 149 p.
- [101] Knipling, E.B., 1970: Physical and physiological basis for reflectance of visible and near-infrared radiation from vegetation. *Remote Sensing of Environment*, Vol. 1, 155-159.
- [102] Kriebel, K. T., 1978: Measured spectral bidirectional reflection properties of four vegetated surfaces. *Applied Optics*, Vol. 17, 253-259.
- [103] Kramer, H.J., 2002: *Observation of the Earth and its Environment - Survey of Missions and Sensors*. 4th Edition, Springer, Berlin, Germany, ISBN: 3540423885, 1510 p.
- [104] ———: USGS Landsat Project Website. <http://landsat.usgs.gov/>. Last visit: 13.10.2004.
- [105] ———, 1998: *Landsat 7 Data User Handbook*. http://ltpwww.gsfc.nasa.gov/IAS/handbook/handbook_toc.html. Last visit: 13.10.2004.
- [106] Labrecque, S., Fournier, R.A., Luther, J.E., Piercey, D.E., 2003: A comparison of three approaches to map forest biomass from Landsat TM and inventory data in Western Newfoundland. *Proceedings, 25th Canadian Symposium on Remote Sensing*, Montréal, Canada.
- [107] Lang, A.R.G., Xiang, Y., 1986: Estimation of leaf area index from transmission of direct sunlight in discontinuous canopies. *Agricultural and Forest Meteorology*, Vol. 37, 229-243.
- [108] Leberl, F., Maurice, K., Thomas, J.K., Millot, M., 1994: Automated Radar Image Matching Experiment. *ISPRS Journal of Photogrammetry and Remote Sensing*, Vol. 49 No. 3, 19-33.
- [109] Lee, N.J., Nakane, K., 1997: Forest vegetation classification and biomass estimation based on Landsat TM data in a mountainous region of west Japan. In: *The use of remote sensing in the modeling of forest productivity*. eds. H.L. Gholz., K. Nakane, H. Shimoda, Kluwer, Dordrecht, The Netherlands, ISBN: 079234278X, 336 p.
- [110] Lee, K., Cohen, W.B., Kennedy, R.E., Maiersperger, T.K., Gower, S.T., 2004: Hyperspectral versus multispectral data for estimating leaf area index in four different biomes. *Remote Sensing of Environment*, Vol. 91, 508-520.
- [111] Lefsky, M.A., Cohen, W.B., Spies, T.A., 2001: An evaluation of alternate remote sensing products for forest inventory, monitoring, and mapping of Douglas-fir forests in western Oregon. *Canadian Journal of Forest Research*, Vol. 31, 78-87.
- [112] Lencinas, J.D., 2001: *Untersuchungen zur Entwicklungsplanung für die Naturwaldbestände an den Seen La Plata und Fontana in den patagonischen Anden*. Dissertation, Fakultät für Forstwissenschaften und Waldökologie der Georg-August-Universität Göttingen. Cuvillier Verlag, Göttingen, Germany, 134 p.

-
- [113] Lencinas, J.D.: 2003: Personal communication.
- [114] Light, D.L., Brown, D., Colvocoresses, A., 1980: Satellite Photogrammetry. In: Chapter XVII of the Manual of Photogrammetry, American Society of Photogrammetry, 883-977.
- [115] Lillesand, T. M., Kiefer, R. W., 1994: Remote sensing and image interpretation. 3rd Edition, Wiley, New York, USA, ISBN: 0471577839, 750 p.
- [116] Loeffelholz, B., 2005: Personal communication.
- [117] Loguercio, G.A., 1997: Die Erhaltung der Baumart Ciprés de la Cordillera, *Austrocedrus chilensis* (D. DON) FLORIN ET BOUTELJE, durch nachhaltige Nutzung. Dissertation, Forstwissenschaftliche Fakultät der Ludwig-Maximilians-Universität, München, Germany, 212 p.
- [118] Loguercio, G.A., 2001: Evaluación de los bosques de Lengua de Tierra del Fuego como sumideros de carbono. Fundación para el desarrollo forestal, ambiental y del ecoturismo Patagónico. Project Report, CIEFAP, Esquel, Argentina.
- [119] Lomagno, J., 1999: Comunicación personal. In: Análisis ambiental y social de las cuencas hidrográficas cordilleranas de la Provincia del Chubut. Carabelli et al. 2000. CIEFAP-GTZ-DGBYP.
- [120] Lu, D., Mausel, P., Brondizio, E., Moran, E., 2004: Relationships between forest stand parameters and Landsat TM spectral responses in the Brazilian Amazon basin. *Forest Ecology and Management*, Vol. 198, 149-167.
- [121] Maltamo, M., Eerikäinen, K., Pitkänen, J., Hyypä, J., Vehmas, M., 2004: Estimation of timber volume and stem density based on scanning laser altimetry and expected tree size distribution functions. *Remote Sensing of Environment*, Vol. 90, 319-330.
- [122] Manjunath, B., Chellappa, R., 1991: Unsupervised texture segmentation using Markov random field models. *IEEE Transactions on Pattern Analysis and Machine Intelligence*, Vol. 13 No. 5, 478– 482.
- [123] Mao, J., Jain, A., 1992: Texture classification and segmentation using multiresolution simultaneous autoregressive models. *Pattern Recognition*, Vol. 25 No. 2, 173– 188.
- [124] McIver, D.K., Friedl, M.A., 2002: Using prior probabilities in decision-tree classification of remotely sensed data. *Remote Sensing of Environment*, Vol. 81, 253-261.
- [125] McQueen, D.R., 1976: The ecology of *Nothofagus* and associated vegetation in South America. *Tuatara*, Vol. 22, 38-68.
- [126] Meyer, P., 1992: Segmentation and symbolic description for a classification of agricultural areas with multispectral scanner data. *IEEE Transactions on Geoscience and Remote Sensing*, Vol. 30, 673–679.
- [127] Miller, A., 1976: The climate of Chile. In: *World Survey of Climatology*. ed. W. Schwerdtfeger, Elsevier, Amsterdam, The Netherlands, ISBN: 0444412719, 113-145.
- [128] Moll, U.A., 1981: Struktur- und Zuwachsuntersuchung in Magellanischen *Nothofagus Pumilio*-Urwäldern. Dissertation, Forstliche Fakultät der Georg-August-Universität Göttingen, 127 p.
- [129] Nackaerts, K., Wagendorp, T., Coppin, P., Muys, B., Gombeer, R., 1999: A correction of indirect LAI measurements for a non-random distribution of needles on shoots. In: Pro-

- ceedings of ISSSR 1999, Systems and Sensors for the New Millennium, Las Vegas, NV, USA. 31 October–4 November, 413–424.
- [130] Nemani, R., Pierce, L., Running, S., Band, L., 1993: Forest ecosystem processes at the watershed scale: sensitivity to remotely-sensed leaf area index estimates. *International Journal of Remote Sensing*, Vol. 14, 2519–2534.
- [131] Neumann, H.H., Den Hartog, G.D., Shaw, R.H., 1989: Leaf-area measurements based on hemispheric photographs and leaf-litter collection in a deciduous forest during autumn leaf-fall. *Agricultural and Forest Meteorology*, Vol. 45, 325–345.
- [132] Nilson, T., 1971: A theoretical analysis of the frequency gaps in plant stands. *Agricultural and Forest Meteorology*, Vol. 8, 25–28.
- [133] Norman, J.M., Campbell, G.S., 1989: Canopy structure. In: *Plant physiological ecology: field methods and instrumentation*. eds. Pearcy, R.W., Ehleringer, J., Mooney, H.A., Rundel, P.W., Chapman & Hall, London, UK, ISBN: 0412232308, 301–325.
- [134] Ochsner, P., 2003: Waldbestandesklassifikation mit Landsat-7 ETM+ Daten in Chubut, Patagonien. Diplomarbeit, Geographisches Institut der Universität Zürich, 70 p.
- [135] Olsson, L., Carlsson, K., Grip, H., Perttu, K., 1982: Evaluation of forest-canopy photographs with diode-array scanner OSIRIS. *Canadian Journal of Forest Research*, Vol. 12, 822–828.
- [136] Päivinen, R., Anttila, P., 2001: How reliable is a satellite forest inventory?. *Silva Fennica*, Vol. 35, 125–127.
- [137] Panjwani, D., Healey, G., 1995: Markov random field models for unsupervised segmentation of textured color images. *IEEE Transactions on Pattern Analysis and Machine Intelligence*, Vol. 17, 939–954.
- [138] PCI, 2001a, OrthoEngine Satellite Projects Manual, Version 8.2. PCI Inc, Ontario, Canada, L4B 1M5.
- [139] PCI, 2001b, OrthoEngine Online Help, Version 8.2. PCI Inc, Ontario, Canada, L4B 1M5.
- [140] Pierce, L.L., Running, S.W., 1988: Rapid estimation of coniferous forest leaf area index using a portable integrating radiometer. *Ecology*, Vol. 69, 1762–1767.
- [141] Premoli, A.C., 1991: Morfología y capacidad germinativa en poblaciones de *Nothofagus antarctica* (Foster) Oerst. del noroeste andino patagónico. *Bosque*, Vol. 12, 53–59.
- [142] Pickett, S.T.A., Thompson, J.N., 1978: Patch dynamics and the size of nature reserves. *Biological Conservation*, Vol. 13, 27–37.
- [143] Pittock, A.B., 1980: Patterns of climatic variation in Argentina and Chile. I. Precipitation, 1931–60. *Monthly Weather Review*, Vol. 108, 1347–1361.
- [144] Pocewicz, A.L., Gessler, P., Robinson, A.P., 2004: The relationship between effective plant area index and Landsat spectral response across elevation, solar insolation, and spatial scales in a northern Idaho forest. *Canadian Journal of Forest Research*. Vol. 34, 465–480.
- [145] Poso, S., Wang, G., Tuominen, S., 1999: Weighting alternative estimates when using multi-source auxiliary data for forest inventory. *Silva Fennica*, Vol. 33, 41–50.
- [146] Puhr, C.B., Donoghue, D.N.M., 2000: Remote sensing of upland conifer plantations using Landsat TM data: a case study from Galloway, south-west Scotland. *International Journal*

- of Remote Sensing, Vol. 21, 633-646.
- [147] Reithmaier, L.M., Barbosa, P., San-Miguel-Ayanz, J., 2005: Assessment of Quickbird images to monitor early post-fire vegetation dynamics applying spectral mixture analysis. In: Proceedings of ForestSat 2005, Borås, Sweden, May 31-June 3, Rapport 8b, 36-40.
- [148] Reese, H., Nilsson, M., Granqvist Pahlén, T., Hagner, O., Joyce, S., Tingelöf, U., Egberth, M., Olsson, H., 2003: Countrywide estimates of forest variables using satellite data and field data from the national forest inventory. *Ambio*, Vol. 32, 542-548.
- [149] Rich, P.M., 1988: Video image analysis of hemispherical canopy photography. Proceedings of the First Special Workshop on Videography. eds. Mausel, P.W., American Society for Photogrammetry and Remote Sensing, Terre Haute, IN, USA, 84-95.
- [150] Rich, P.M., 1990: Characterizing plant canopies with hemispherical photographs. *Remote Sensing Reviews*, Vol. 5, 13-29.
- [151] Rich, P.M., Clark, D.B., Clark, D.A., Oberbauer, S.F., 1993: Long-term study of solar radiation regimes in a tropical wet forest using quantum sensors and hemispherical photography. *Agricultural and Forest Meteorology*, Vol. 65, 107-127.
- [152] Richter, R., 1996a: A spatially adaptive fast atmospheric correction algorithm. *International Journal of Remote Sensing*, Vol. 17, 1201-1214.
- [153] Richter, R., 1996b: Atmospheric correction of satellite data with haze removal including a haze/clear transition region. *Computers & Geosciences*, Vol. 22, 675-681.
- [154] Richter, R., 1998: Correction of satellite imagery over mountainous terrain. *Applied Optics*, Vol. 37, 4004-4015.
- [155] Richter, R., 2001: Atmospheric and Topographic Correction: Model ATCOR., DLR-IB 564-03/01, DLR Wessling, Germany.
- [156] Rodríguez, D., Sourrouille, A., Gallopín, G.C., Montaña, C., 1978: Estudio ecológico integrado de la cuenca del Rio Manso Superior (Rio Negro, Argentina). II. Tipos de vegetación. *An. Parq. Nacion. (Argentina)*, Vol. 14, 231-248.
- [157] Rondeaux, G., Steven, M., Baret, F., 1996: Optimization of soil adjusted vegetation indices. *Remote Sensing of Environment*, Vol. 55, 95-107.
- [158] Rosenfeld, A., Kak, A.C., 1976: *Digital Picture Processing*. Academic Press, New York, USA, ISBN: 0125973608, 475 p.
- [159] Rouse, J.W., Haas, R.H., Schell, J.A., Deering, D.W., 1973: Monitoring vegetation systems in the great plains with ERTS. Third ERTS Symposium, NASA SP-351, NASA, Washington, DC, Vol. 1, 309-317.
- [160] Salvador, R., Pons, X., 1998: On the applicability of Landsat TM images to Mediterranean forest inventories. *Forest Ecology and Management*, Vol. 104, 193-208.
- [161] Schaaf, C. B., Li, X., and Strahler, A. H., 1994: Topographic effects on bidirectional and hemispherical reflectances calculated with a geometric-optical canopy model. *IEEE Transactions on Geoscience and Remote Sensing*, Vol. 32, 1186-1193.
- [162] Schenk, F.A., 1996: Digital Elevation Model Extraction. In: *Digital Photogrammetry: An addendum to the manual of photogrammetry*. American Society for Photogrammetry and Remote Sensing. ed. C. Greve, Bethesda, USA, ISBN: 1570830371, 247 p.
- [163] Schowengerdt, R.A., 1997: *Remote Sensing, Models and Methods for Image Processing*.

- 2nd Edition, Academic Press, San Diego, USA, ISBN: 0126289816, 522 p.
- [164] Seibert, P., 1982: Carta de vegetación de la región de El Bolsón, Rio Negro y su aplicación a la planificación del uso de la tierra. *Documenta Phytosociologica*, Vol. 2, 1-120.
- [165] Seibert, P., 1996: *Farbatlas Südamerika, Landschaften und Vegetation*. Eugen Ulmer GmbH & Co., Stuttgart, Germany, ISBN: 3800133571, 288 p.
- [166] Schlerf, M., Atzberger, C., Hill, J., 2005: Remote sensing of forest biophysical variables using HyMap imaging spectrometer data. *Remote Sensing of Environment*, Vol. 95, 177-194.
- [167] Schmalz, J., 1992: Die Zerstörung der natürlichen Wälder im argentinischen Patagonien. *Forst und Holz*, Vol. 47, No. 11.
- [168] Schmidt, H., Urzúa, A., 1982: Transformación y manejo de los bosques de Lengua en Magallanes. *Ciencias Agrícolas*, Universidad de Chile, Santiago, No. 11, 1-62.
- [169] Schwerdtfeger, W. 1976: Introduction. In: *World Survey of Climatology*, ed. W. Schwerdtfeger, Elsevier, Amsterdam, The Netherlands, ISBN: 0444412719, 1-12.
- [170] Spanner, M.A., Pierce, L.L., Peterson, D.L., Running, S.W., 1990: Remote sensing of temperate coniferous forest leaf area index. The influence of canopy closure, understorey vegetation and background reflectance. *International Journal of Remote Sensing*, Vol. 11, 95-111.
- [171] Story, M., Congalton, R.G., 1986: Accuracy assessment: a user's perspective. *Photogrammetric Engineering and Remote Sensing*, Vol. 52, 397-399.
- [172] ———: JPL - Shuttle Radar Topography Mission, Mission Statistics. <http://www2.jpl.nasa.gov/srtm/statistics.html>. Last visited: 26.10.2004.
- [173] ———: DEM's Overview, Shuttle Radar Topography Mission. http://www.geoimage.com.au/geoweb/dems/dems_overview.htm. Last visited: 26.10.2004.
- [174] Taljaard, J.J., 1972: Synoptic meteorology of the Southern Hemisphere. *Meteorological Monographs*, Vol. 13, 139-213.
- [175] Tompoo, E., 1993: Multi-source national forest inventory of Finland. In: *Proceedings of Ilvessalo Symposium on National Forest Research Institute Research Papers*. eds. A. Nyysönen, S. Poso, & J. Rautala, Vol. 444, 52-60.
- [176] Tortorelli, L.A., 1956: *Maderas y bosques argentinos*. Editorial ACME, Buenos Aires, 910 p.
- [177] Toutin, T., 1985: *Analyse mathématique des possibilités cartographiques du système SPOT*, Thèse de Docteur-Ingénieur, École Nationale des Sciences Géodésiques, St-Mandé, France.
- [178] Toutin, T., 2001: Elevation Modelling from Satellite Data. *International Journal of Remote Sensing*, Vol. 22, 1097-1125.
- [179] Toutin, T., Cheng, P., 2002: Comparison of automated digital elevation model extraction results using along-track ASTER and across-track SPOT stereo images. *Optical Engineering*, Vol. 41, 2102-2106.
- [180] Trotter, C.M., Dymond, J.R., Goulding, C.J., 1997: Estimation of timber volume in a coniferous plantation forest using Landsat TM. *International Journal of Remote Sensing*, Vol. 18, 2209-2223.

- [181] Tsu, H., 1996: Algorithm Theoretical Basis Document for ASTER Level-1 Data Processing (Ver. 3.0). ERSDAC. http://eosps0.gsfc.nasa.gov/eos_homepage/for_scientists/atbd/viewInstrument.php?instrument=4. Last visited: 30.09.2004.
- [182] Tucker, C. J., 1979: Red and photographic infrared linear combinations for monitoring vegetation. *Remote Sensing of Environment*, Vol. 8, 127–150.
- [183] Tuominen, S., Pekkarinen, A., 2005: Performance of different spectral and textural aerial photograph features in multi-source forest inventory. *Remote Sensing of Environment*, Vol. 94, 256–268.
- [184] ——— 2003: User Guide eCognition. http://www.definiens_imaging.com. Last visited 24.04.2003.
- [185] Veblen, T.T., 1982: Growth patterns of *Chusquea* bamboos in the understory of Chilean *Nothofagus* forests and their influences in forest dynamics. *Bulletin of the Torrey Botanical Club*, Vol. 109, 474–487.
- [186] Veblen, T.T., Donoso, C., Kitzberger, T., Rebertus, A.J., 1996: Ecology of Southern Chilean and Argentinean *Nothofagus* Forests. In: *The Ecology and Biogeography of Nothofagus Forests*, eds. T.T. Veblen, R.S. Hill, and J. Read. Yale University Press, New Haven, USA. 293–353.
- [187] Veblen, T.T., Kitzberger, T., Raffaele, E., Lorenz, D.C., 2003: Fire history and vegetation changes in northern Patagonia, Argentina. In: *Fire and Climatic Change in Temperate Ecosystems of the Western Americas*, Springer, New York, ISBN: 0387954554, 444 p.
- [188] Villalba, R. 1990: Latitude of the surface high-pressure belt over western South America during the last 500 years as inferred from tree-ring analysis. *Quaternary of South America and Antarctic Peninsula*, Vol. 7, 273–303.
- [189] Vogelmann, J.E., 1990: Comparison between two vegetation indices for measuring different types of forest damage in the northeastern United States. *International Journal of Remote Sensing*, Vol. 35, 675–686.
- [190] Wang, Q., Adiku, S., Tenhunen, J., Granier, A., 2004: On the relationship of NDVI with leaf area index in a deciduous forest site. *Remote Sensing of Environment*, Vol. 94, 244–255.
- [191] Waring, R.H., Law, B.E., Goulden, M.L., Bassow, S.L., McCreight, R.W., Wofsey, S.C., Bazzaz, F.A., 1995: Scaling gross ecosystem productivity at Harvard Forest using remote sensing: a comparison of estimates from a constrained quantum-use efficiency model and eddy correlation. *Plant, Cell and Environment*, Vol. 18, 1201–1213.
- [192] Waring, R.H., Running, S.W., 1998: *Forest Ecosystems: Analysis at Multiple Scales*. 2nd Edition, Academic Press, San Diego, USA, ISBN: 0127354433, 370 p.
- [193] Watson, D.J., 1947: Comparative physiological studies in the growth of field crops. I. Variation in net assimilation rate and leaf area between species and varieties, and within and between years. *Annals of Botany*, Vol. 11, 41–76.
- [194] Weiss, M., 2002. EYE-CAN User Guide. NOV-3075-NT-1260. NOVELTIS, Toulouse, France.
- [195] Welles, J.M., 1990: Some indirect methods of estimating canopy structure. *Remote Sensing Reviews*, Vol. 5, 31–43.
- [196] Welles, J.M., Norman, J.M., 1991: Instrument for indirect measurement of canopy archi-

-
- tecture. *Agricultural Journal*, Vol. 83, 818–825.
- [197] Wulder, M.A., Franklin, S.E., 2003: *Remote Sensing of Forest Environments. Concepts and Case Studies*. Kluwer Academic Publishers, Boston, USA, ISBN: 1402074050, 519 p.
- [198] Yamaguchi, Y., Kahle, A., Tsu, H., Kawakami, T., Pniel, M., 1998: Overview of advanced spaceborne thermal emission and reflection radiometer (ASTER). *IEEE Transactions on Geoscience and Remote Sensing*, Vol. 36, 1062-1071.
- [199] Zheng, D., Rademacher, J., Chen, J., Crow, T., Bresee, M., LeMoine, J., Ryu, S.-R., 2004: Estimating aboveground biomass using Landsat 7 ETM+ data across a managed landscape in northern Wisconsin, USA. *Remote sensing of Environment*, Vol. 93, 402-411.
- [200] Zomer, R., Ustin, S., and Ives, J., 2002: Using satellite remote sensing for DEM extraction in complex mountainous terrain: landscape analysis of the Makalu Barun National Park of eastern Nepal. *International Journal of Remote Sensing*, 23, 125-143.

Appendix

a) Developed classification rule base

Table 1 Overview of classification mode, applied feature and shape of fuzzy rule for class separation.

Class	Inheritance Level & Class	Features & Rule				
		St. NN	Membership Functions			
			Feature	Min.	Max.	Shape
Low Vegetation	1	x				
Grass/Neneo/ Bushes/Caña Colihue/Ñire/NDVI > 120	2 (Low Vegetation ->)		NDVI	114.5	125.5	
Rock/NDVI > 120	2 (Low Vegetation ->)		NDVI DEM	120 450	140 2650	 
Bushland/Rangeland	2 (Low Vegetation ->)		NDVI DEM	120 0	140 2350	 
Caña Colihue/Ñire/ Arbustivos	2 (Low Vegetation ->)		NDVI DEM	140 300	185 2500	 
Tendential Arbustivos	3 (Caña Colihue/Ñire/ Arbustivos ->)		Ratio ASTER4	0.0105	0.04	
Tendential Ñire	3 (Caña Colihue/Ñire/ Arbustivos ->)		Ratio ASTER4 DEM	0.015 450	0.02199 1550	 
Tendential Caña Colihue	3 (Caña Colihue/Ñire/ Arbustivos ->)		Ratio ASTER4 DEM	0.000 450	0.01849 1100	 
Shrublenga/Ñire	3 (Grass/Neneo/Bushes/ Caña Colihue/Ñire/NDVI > 120 ->)		NDVI DEM	181 400	255 2500	 
Dense Bushes/Mixed Forest	3 (Grass/Neneo/Bushes/ Caña Colihue/Ñire/NDVI > 120 ->)		NDVI DEM	180 400	255 1400	 
Rock/Bare Soil/Dry Grass/NDVI < 120	2 (Low Vegetation ->)		NDVI	110	130	
Rock	3 (Rock/Bare Soil/Dry Grass/NDVI < 120 ->)		DEM	175	2475	
Spare/Dry Grass	3 (Rock/Bare Soil/Dry Grass/NDVI < 120 ->)		DEM	90	2390	
High Vegetation	1	x				

Table 1 Overview of classification mode, applied feature and shape of fuzzy rule for class separation.

Class	Inheritance Level & Class	Features & Rule				
		St. NN	Membership Functions			
			Feature	Min.	Max.	Shape
Shrubs/Bushes/ Mountain Meadows	2 (High Vegetation ->)		NDVI	130	167	
Dense Vegetation	2 (High Vegetation ->)		NDVI	163	255	
Intense Grassland/ Mixed Trees	3 (Dense Vegetation ->)	x	DEM	600	1220	
Grass/Bushes/ Shrublenga/Ñire	3 (Dense Vegetation ->)		NDVI DEM ETM5	163 10 57	235 1310 177	  
Grass/Bushes < 1000m asl	4 (Grass/Bushes/ Shrublenga/Ñire ->)		NDVI DEM	163 425	255 1025	 
Lenga/Ñire Arbustivos	4 (Grass/Bushes/ Shrublenga/Ñire ->)		NDVI DEM	163 1030	255 1530	 
Forest/Caña Colihue	3 (Dense Vegetation ->)		NDVI ETM5 DEM	165 3 330	245 77.2 1700	  
Lenga	4 (Forest/Caña Colihue ->)		ASTER2 ASTER4 WETN DEM	11 13 138 915?	52.7 40 169.8 1900	   
Coihue	4 (Forest/Caña Colihue ->)		ASTER1 ASTER2 ASTER4 ETM7 WETN DEM	54 25.1 1.5 2 149.7 450	86.8 46.8 24.65 20 166.99 1000	     

Table 1 Overview of classification mode, applied feature and shape of fuzzy rule for class separation.

Class	Inheritance Level & Class	Features & Rule				
		St. NN	Membership Functions			
			Feature	Min.	Max.	Shape
Ñire	4 (Forest/Caña Colihue ->)		ASTER1	77	108	
			ASTER2	40	80	
			ASTER4	24	35	
			ASTER5	26	36.5	
			WETN	143	152.3	
			DEM	470	1450	
Ciprés	4 (Forest/Caña Colihue ->)		ASTER2	41	61.5	
			ASTER4	11	26	
			ETM5	20	44	
			BRIGHT	13.8	31.5	
			DEM	405	1105	
Caña Colihue	4 (Forest/Caña Colihue ->)		ASTER2	38	59	
			ASTER4	17	29	
			ASTER5	21.17	28.5	
			ETM5	40	56	
			ETM7	15.5	28	
			BRIGHT	27	43	
			WETN	142.9	159.1	
			DEM	460	1100	
Plantations	1		PLANTATION	114	255	
Water	1		ASTER3	0	50	
			not DEM	-270	90	
			SLOPE	1	31	
Snow/Bright Rocks	1	x				
Border	1		ASTER5	-0.5	9.7	
			DEM	-270	90	
			DEM	-1	+1	

b) Correlation coefficients for the linear relationships between LAI and the spectral bands
Table 2 Correlation coefficients for linear relationships between LAI and the spectral bands, derivatives and vegetation indices as well as selected forest parameters (n = 38).

Parameter	VI/Parameter	r	Sig. (2-tailed)
LAI	ASTER3	0.685	0.000
	ASTER5	-0.75	0.000
	SAVI A	0.485	0.002
	WDVI A	0.688	0.000
	SR A	0.499	0.001
	NDVI A	0.483	0.002
	mNDVI(A3,A4)	0.713	0.000
	MVI A	0.706	0.000
	GR A	0.662	0.000
	OSAVI A	0.483	0.002
	IPVI A	0.483	0.002
	ETM2	-0.466	0.003
	ETM3	-0.571	0.000
	ETM4	0.548	0.000
	SR E	0.651	0.000
	NDVI E	0.701	0.000
	EVI E	0.445	0.005
	mNDVI(E4,E5)	0.659	0.000
	MVI E	0.665	0.000
	MSI A	-0.713	0.000
	mNDVI(A3,A5)	-0.810	0.000
	A4-3	0.742	0.010
	A5-4	-0.414	0.000
	PVI A	0.688	0.000
	PVI E	0.579	0.000
	SRC A	0.511	0.001
	SRC E	0.653	0.000
	NDVIC A	0.501	0.001
	NDVIC E	0.626	0.000
	Basal area	0.488	0.002
	Biomass	0.513	0.001

c) Correlation coefficients for the linear relationship between the forest parameters and LAI

Table 3 Correlation coefficients for linear relationships between the forest parameters and LAI, the spectral bands, the derivatives and vegetation indices (n = 38).

Parameter	VI/Parameter	r	Sig. (2-tailed)
Tree density	SAVI A	0.443	0.005
	SR A	0.482	0.002
	NDVI A	0.442	0.005
	mNDVI(A3,A4)	0.445	0.005
	MVI A	0.457	0.004
	OSAVI A	0.443	0.005
	GRVI A	0.437	0.006
	IPVI A	0.442	0.005
	ETM4	0.657	0.000
	ETM PAN	0.535	0.001
	SR E	0.447	0.005
	NDVI E	0.455	0.004
	mNDVI(E4,E5)	0.579	0.000
	MVI E	0.611	0.000
	GR E	0.489	0.002
	Greenness	0.56	0.000
	OSAVI E	0.456	0.004
	IPVI E	-0.455	0.004
	MSI E	-0.554	0.000
	MSI A	-0.440	0.006
A4-3	-0.440	0.006	
DBH	-0.751	0.000	
Dominant Height	Dominant Height	-0.448	0.005
	Biomass	0.415	0.009
Dominant Height	Tree Density	-0.448	0.005
	Volume	0.434	0.007
DBH	ETM4	-0.491	0.002
	mNDVI(E4,E5)	-0.431	0.007
	MVI E	-0.441	0.006
	Greenness	-0.502	0.001
	MSI E	0.424	0.008
	PVI E	-0.496	0.002
	Tree Density	-0.751	0.000
	Volume	0.456	0.004
Basal Area	ASTER5	-0.49	0.002
	mNDVI(A3,A5)	0.481	0.002
	LAI	0.488	0.002
	LAIuwdw	0.605	0.000
	Volume	0.803	0.000
	Biomass	0.833	0.000

Table 3 Correlation coefficients for linear relationships between the forest parameters and LAI, the spectral bands, the derivatives and vegetation indices (n = 38).

Parameter	VI/Parameter	r	Sig. (2-tailed)
Volume	LAIuwdw	0.511	0.001
	Basal Area	0.803	0.000
	DBH	0.456	0.004
	Dominant Height	0.434	0.007
	Biomass	0.796	0.000
Biomass	ASTER5	-0.498	0.001
	SAVI A	0.429	0.007
	SR A	0.429	0.007
	NDVI A	0.428	0.007
	mNDVI(A3,A4)	0.502	0.001
	MVI A	0.492	0.002
	GR A	0.444	0.005
	OSAVI A	0.428	0.007
	IPVI A	0.428	0.007
	ETM PAN	0.422	0.008
	GR E	0.517	0.001
	MSI A	-0.504	0.001
	A4-3	-0.476	0.003
	mNDVI(A3,A5)	0.505	0.001
	LAI	0.513	0.001
	LAIuwdw	0.515	0.001
	Tree Density	0.415	0.009
	Basal Area	0.833	0.000
	Volume	0.796	0.000

d) Land cover classification map and forest parameter maps in A3 map format (see addendum)

Acknowledgements

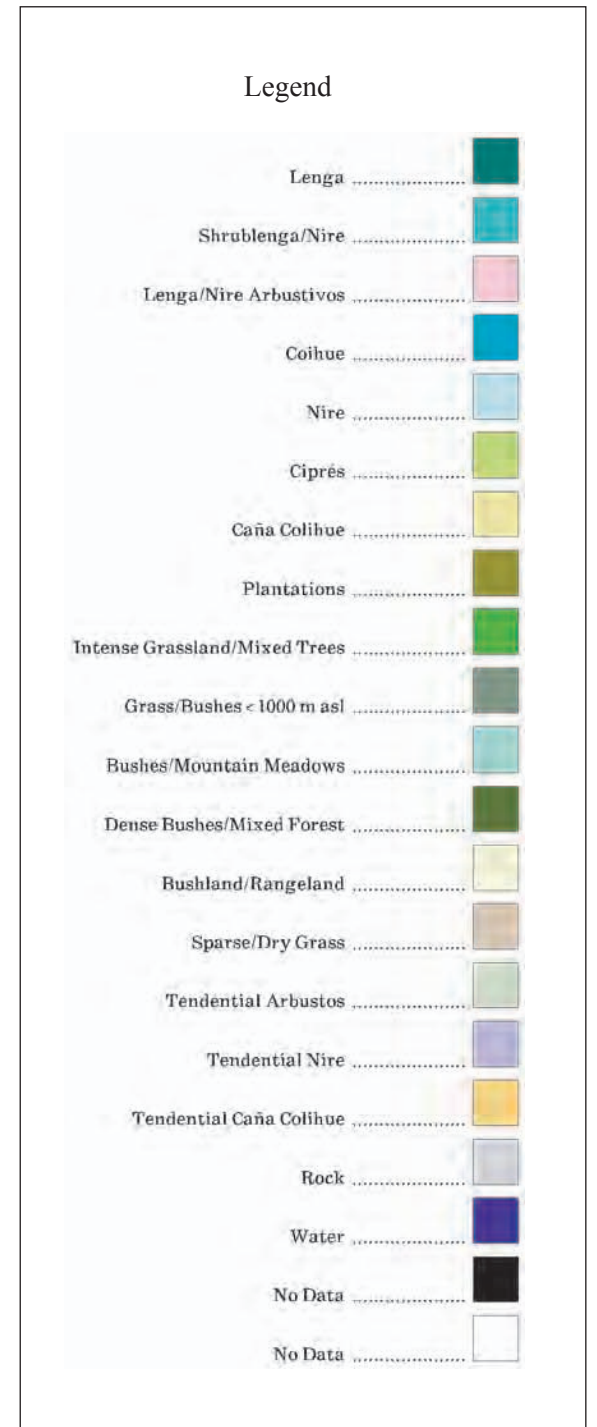
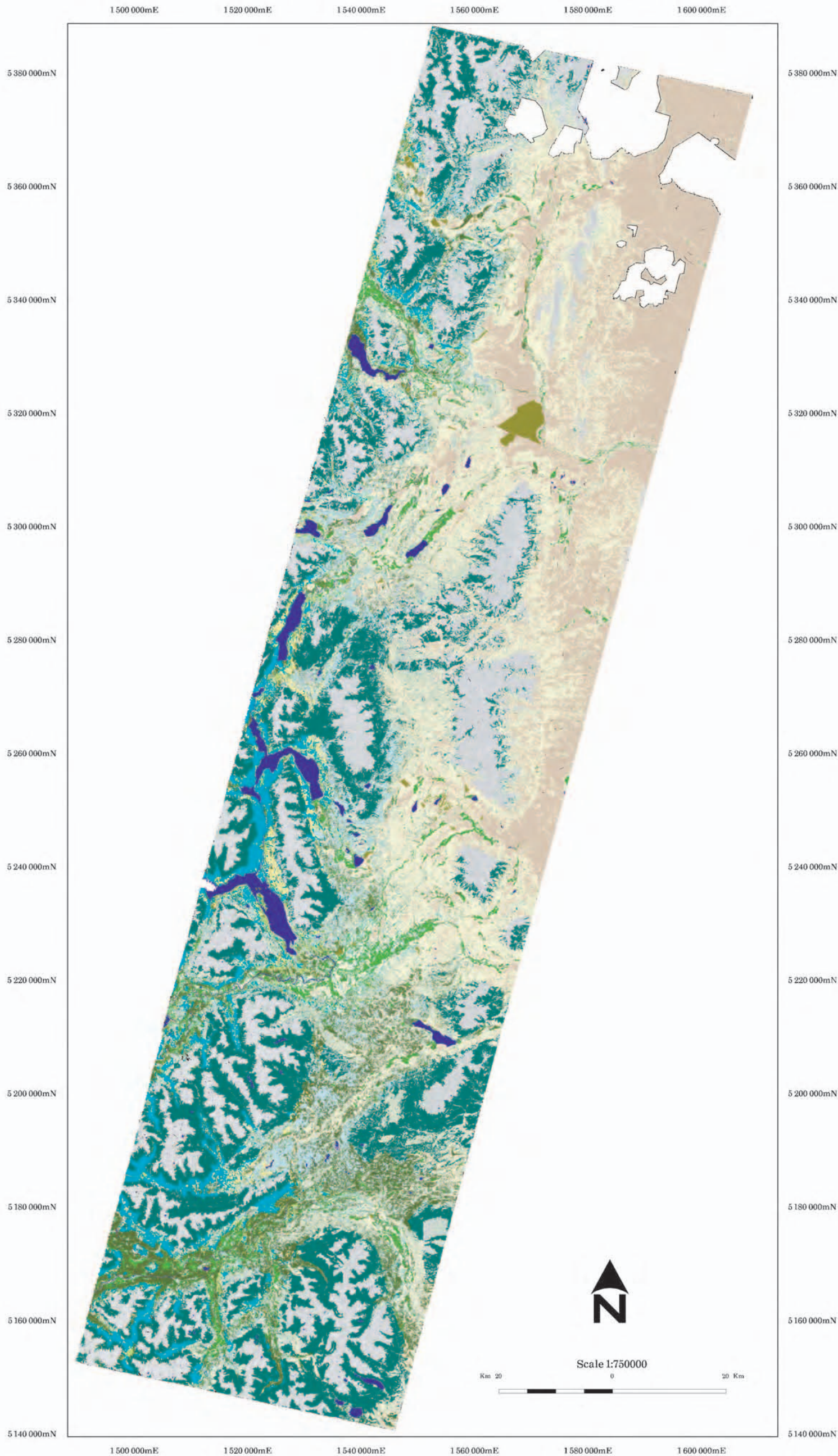
I would like to acknowledge the following persons for their highly appreciated support during the time of this research project:

- Prof. Dr. Klaus I. Itten for his continuous support, interest and trust in this work and his generous and uncomplicated support in my fieldwork activities.
- The Co-Investigator, Dr. Thomas Schneider from TU Munich, for the proof-reading and his inspiring discussions.
- My supervisor, colleague and friend, Tobias Kellenberger for his belief in this research project, his methodological support and personal encouragements as well as for proof-reading of this work.
- My research partner at CIEFAP, Patagonia, José D. Lencinas for his unbelievable enthusiasm and belief in achieving sustainable forest management in Patagonia; for his support in behalf of technical and silvicultural questions, planning and conducting fieldwork, organizing software, hardware, staff and funding; and last but not least for being a precious friend.
- The fieldwork team in Esquel: Antje, Daniel, Dante, Fernanda and Florencia for spending a lot of time in the field, e.g. collecting GPS points, mapping ground truth data and measuring forest parameters in the Lengua forests of Province of Chubut, and being good friends while my unforgettable stay in Esquel.
- Dante, José and the *Plan Nacional de Manejo del Fuego* for organizing two helicopter flights to acquire ground truth data.
- Andi Kääb and Erich Meier for their support and comments on theoretical questions concerning DEM generation from ASTER data and ASTER specific problems.
- My dear friend Mariana Louw for proof-reading of this work.
- My colleagues at RSL and the Department of Geography with whom I spent, besides many working hours, inspiring and most of all relaxing coffee and lunch breaks.
- My parents and my sister in believing in me.

Sandra Eckert

Baden, Autumn 2005

LAND COVER MAP OF NORTH-WESTERN CHUBUT



Map Information:

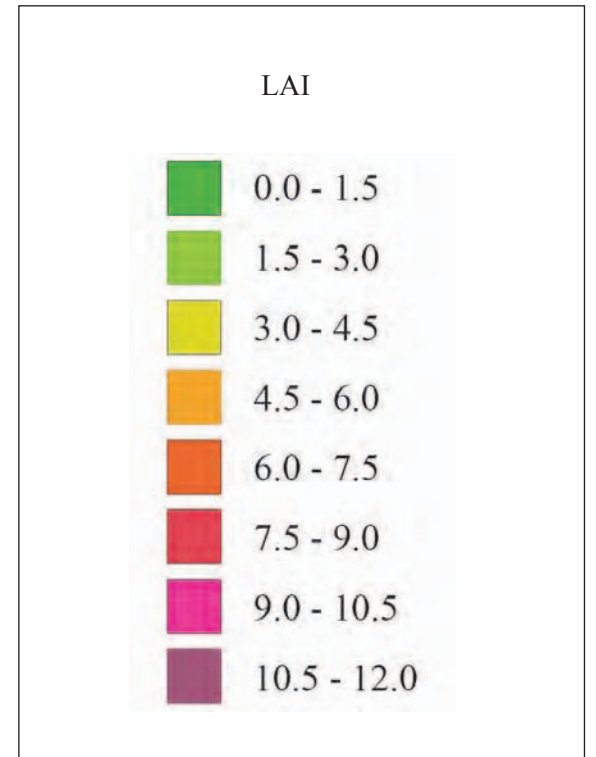
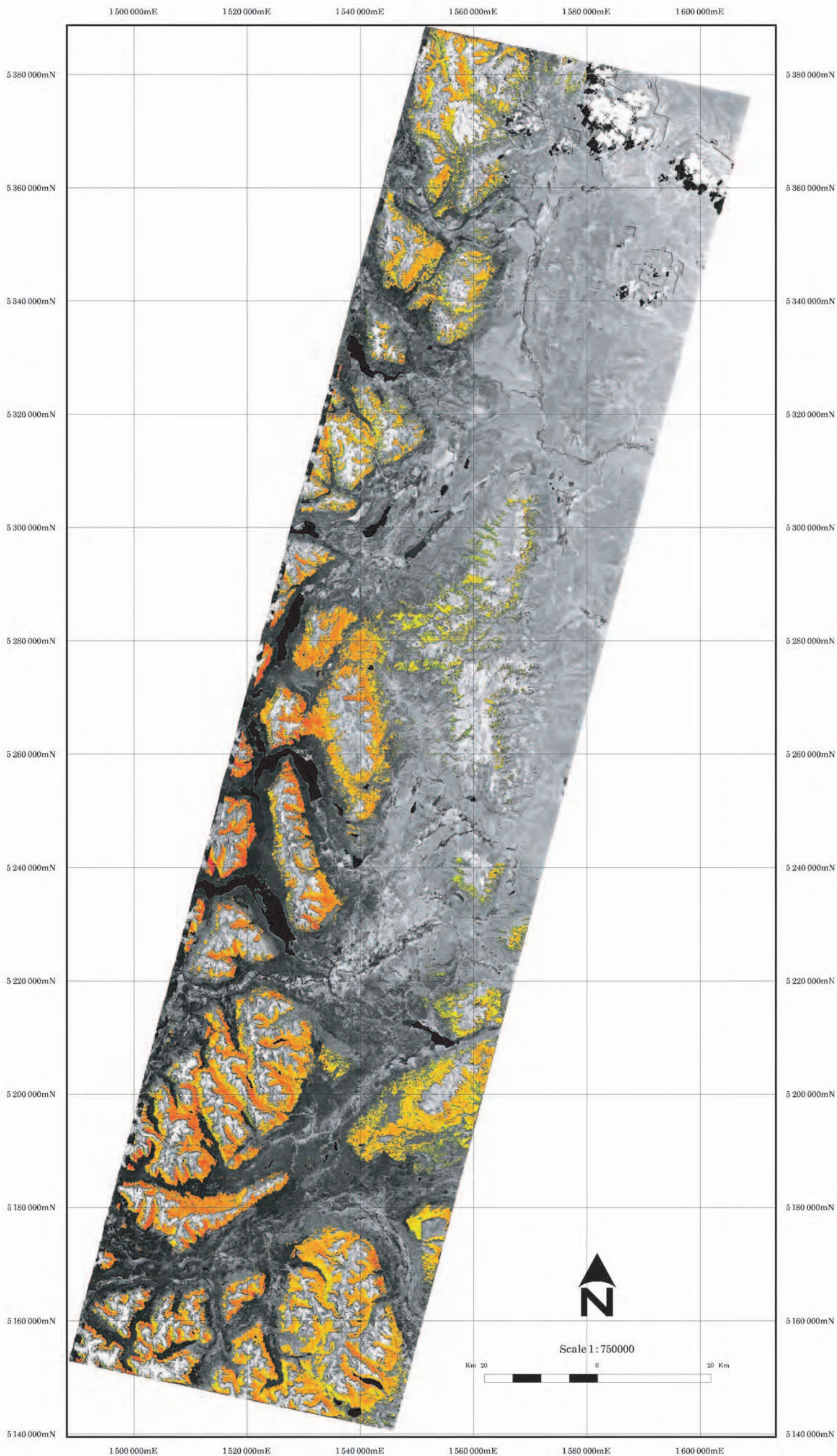
Date: 18. Jan. 2002
 Datum: Campo Inchauspe
 Ellipsoid: International 1924

Object-oriented classification
 Software: eCognition
 Database: ASTER, Landsat ETM+

Author: S. Eckert



LEAF AREA INDEX (LAI) MAP OF NORTH-WESTERN CHUBUT



Map Information:

Date: 18. Jan. 2002

Datum: Campo Inchauspe

Ellipsoid: International 1924

$$LAI = -0.8965 + 0.96922 * MVI \text{ ASTER}$$

$$R^2 = 0.707, RMSE = 11.281 \%$$

Database: ASTER

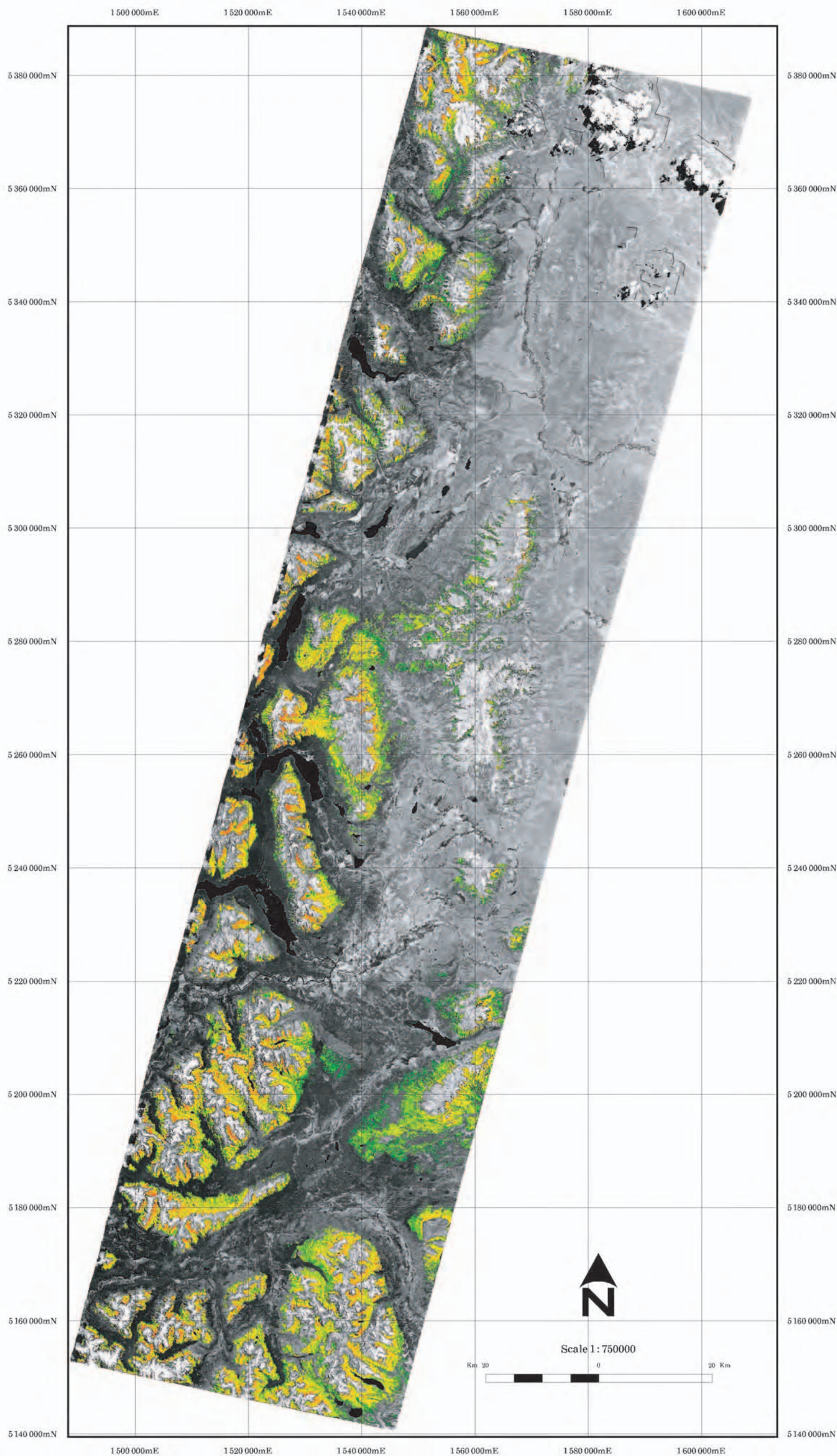
Background Layer: ASTER Band 2 (red)

Author: S. Eckert

REMOTE SENSING LABORATORIES **RSL**

CIEFAP
Centro de Investigación y Extensión Forestal Andino Patagónico

TREE DENSITY MAP OF NORTH-WESTERN CHUBUT



TREE DENSITY [trees/ha]



Map Information:

Date: 18. Jan. 2002
 Datum: Campo Inchauspe
 Ellipsoid: International 1924

$$\text{TREE DENSITY} = -491.515378 + 32.164082 * \text{PVI E}$$

$$R^2 = 0.558, \text{RMSE} = 44.607 \%$$

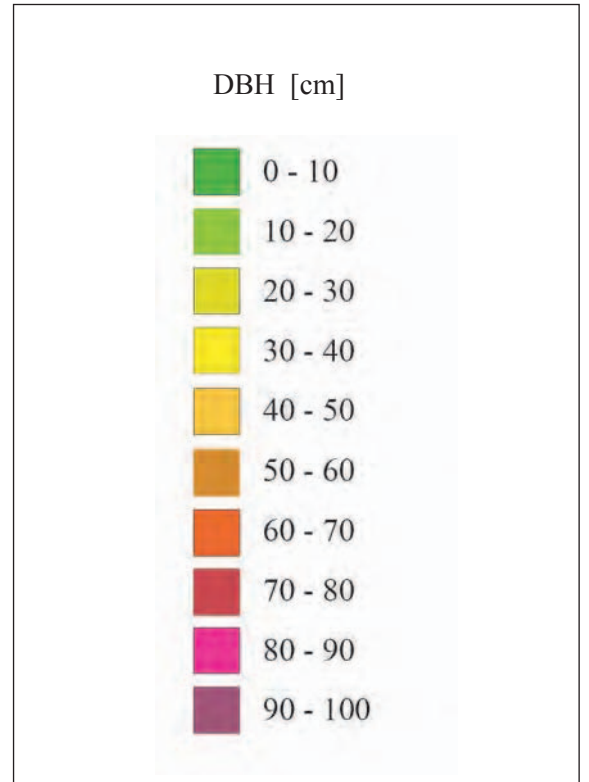
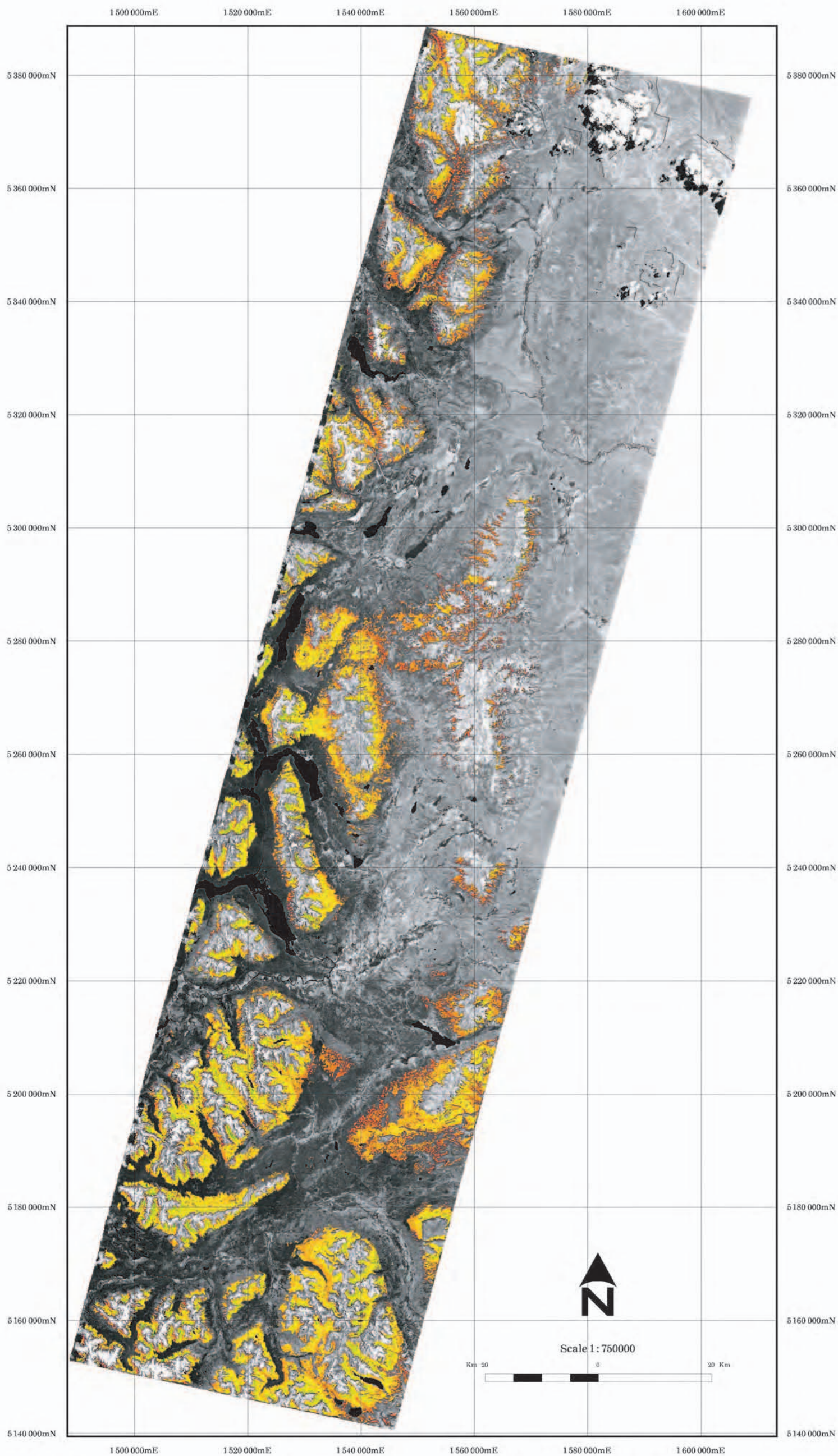
Database: ASTER
 Background Layer: ASTER Band 2 (red)

Author: S. Eckert

REMOTE SENSING LABORATORIES **RSL**

CIEFAP
 Centro de Investigación y Extensión Forestal Andino Patagónico

DIAMETER AT BREAST HEIGHT (DBH) MAP OF NORTH-WESTERN CHUBUT



Map Information:

Date: 18. Jan. 2002

Datum: Campo Inchauspe

Ellipsoid: International 1924

DBH = 366.468593 - 1.872857 * GREENESS

$R^2 = 0.365$, RMSE = 25.414 %

Database: ASTER

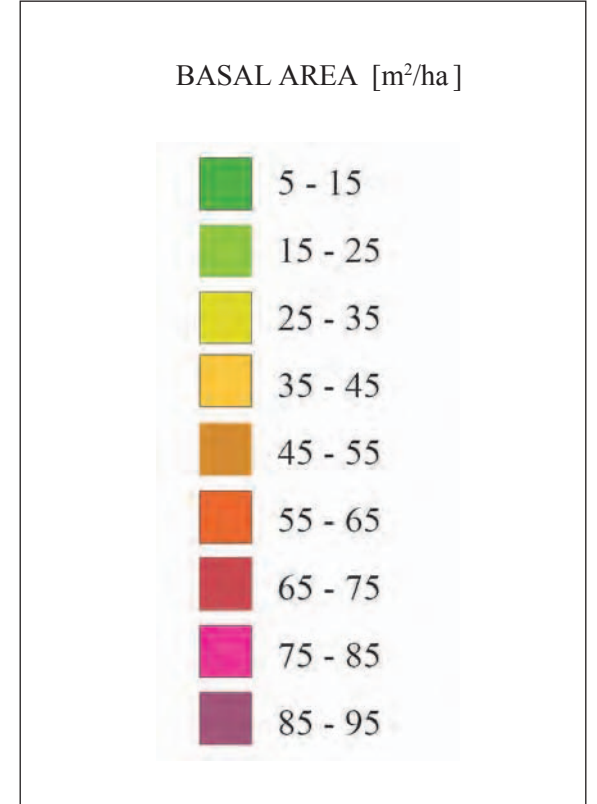
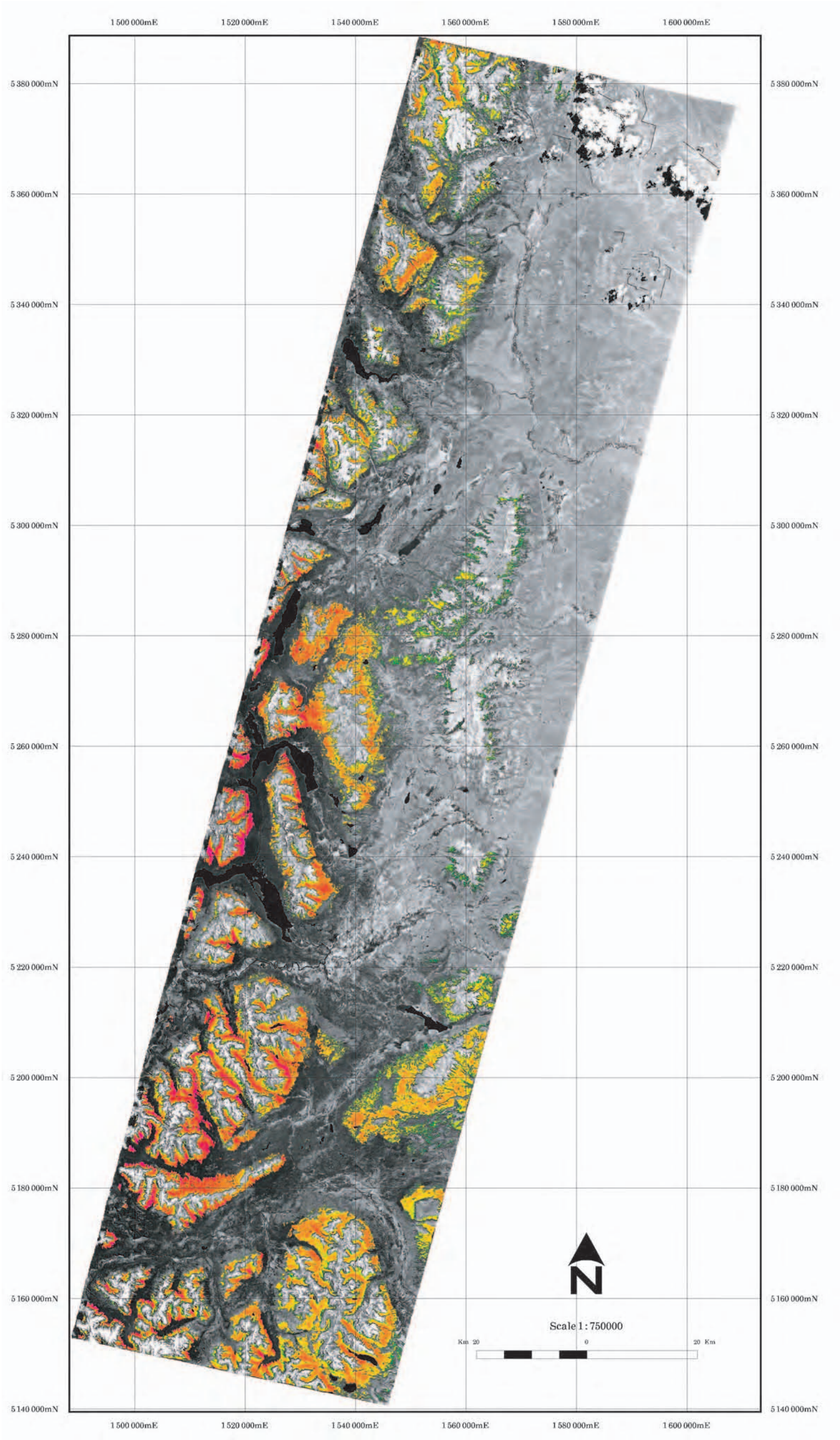
Background Layer: ASTER Band 2 (red)

Author: S. Eckert

REMOTE SENSING LABORATORIES **RSL**

CIEFAP
Centro de Investigación y Extensión Forestal Andino Patagónico

BASAL AREA MAP OF NORTH-WESTERN CHUBUT



Map Information:

Date: 18. Jan. 2002
 Datum: Campo Inchauspe
 Ellipsoid: International 1924

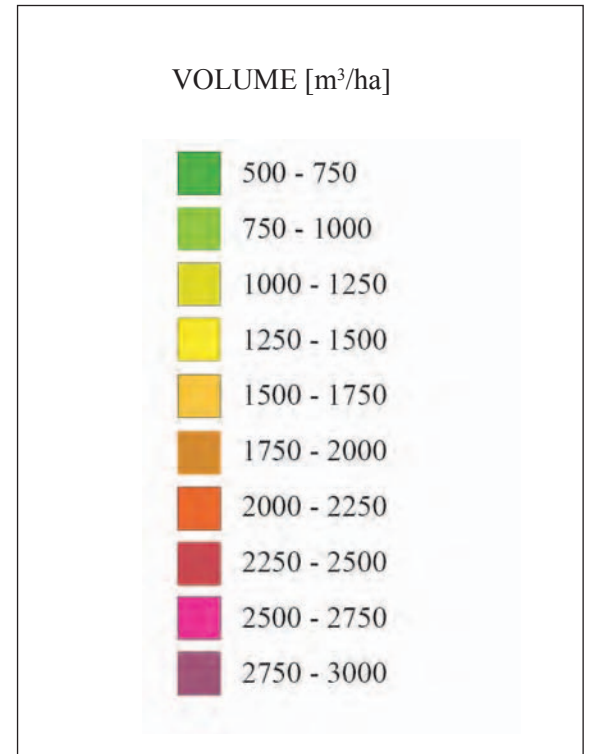
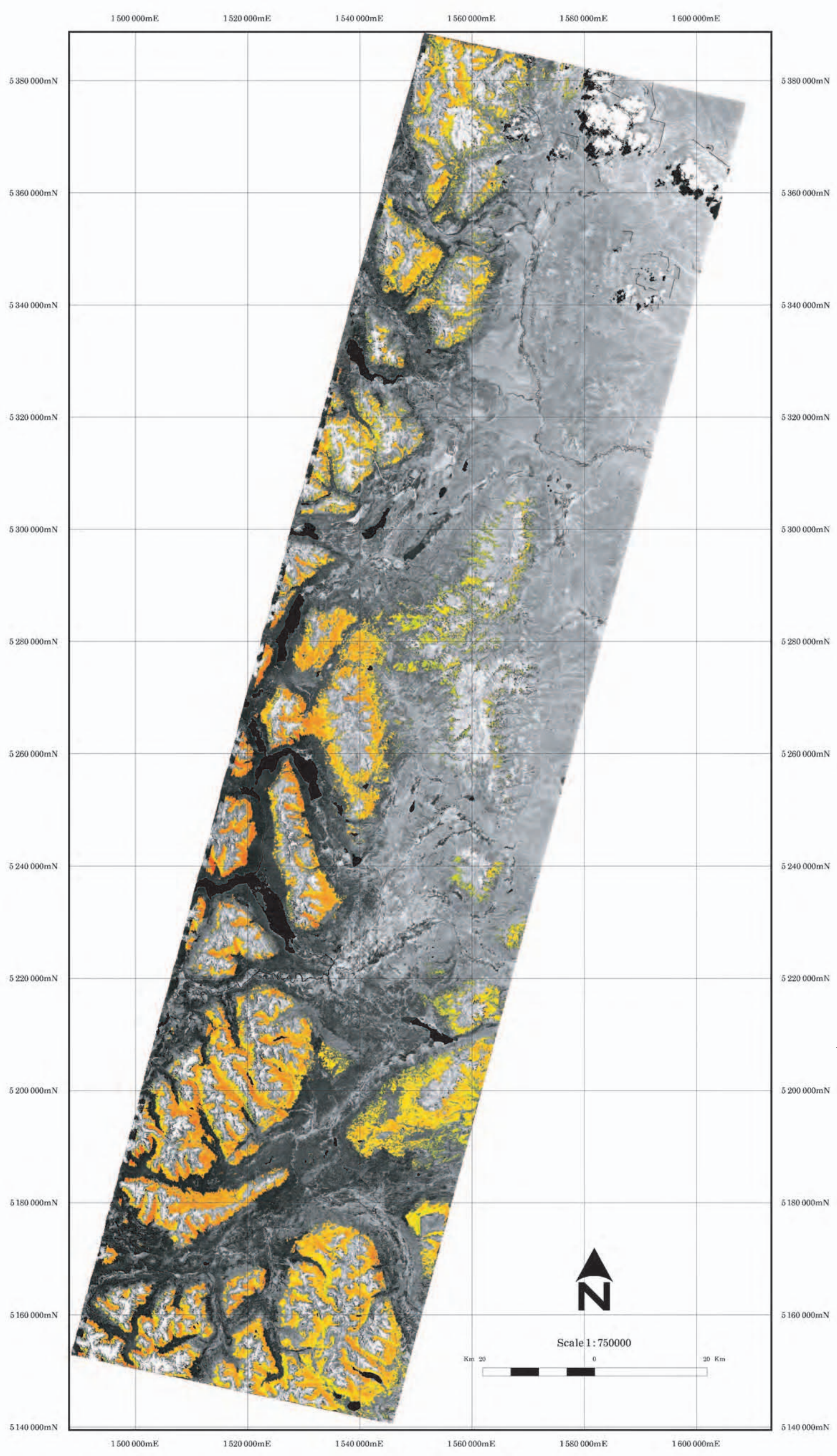
BASAL AREA = 174.03713 - 5.713072 * ASTER6
 R² = 0.619, RMSE = 28.765 %

Database: ASTER
 Background Layer: ASTER Band 2 (red)

Author: S. Eckert



VOLUME MAP OF NORTH-WESTERN CHUBUT



Map Information:

Date: 18. Jan. 2002
 Datum: Campo Inchauspe
 Ellipsoid: International 1924

$VOLUME = 177.837909 + 161.138929 * LAI$ (modelled)
 $R^2 = 0.176$, RMSE = 38.48 %

Database: ASTER
 Background Layer: ASTER Band 2 (red)

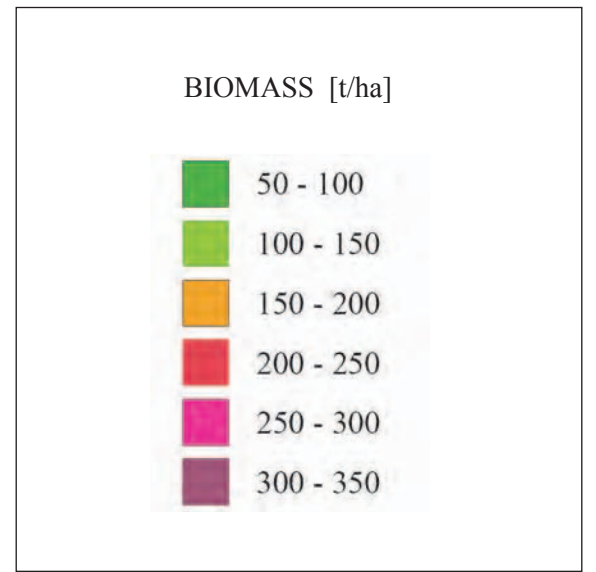
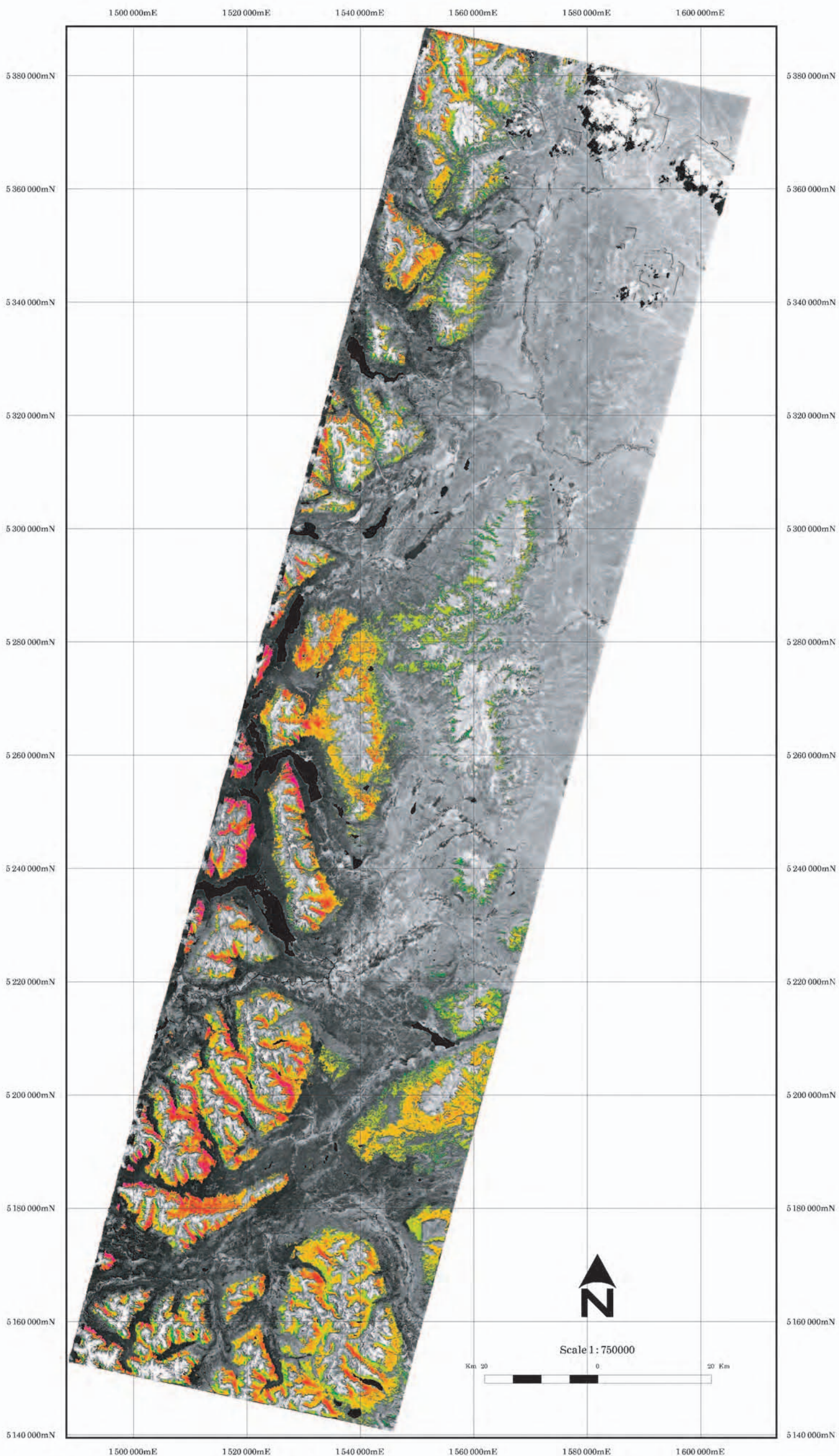
Author: S. Eckert



Scale 1:750000



BIOMASS MAP OF NORTH-WESTERN CHUBUT



Map Information:

Date: 18. Jan. 2002
 Datum: Campo Inchauspe
 Ellipsoid: International 1924

BIOMASS = 555226.487 - 12737.841 * ASTER9
 R² = 0.500, RMSE = 61.695 %

Database: ASTER
 Background Layer: ASTER Band 2 (red)

Author: S. Eckert

